Search for Neutrino Non-Standard Interactions with the KM3NeT/ORCA 6 lines detector

Author:
Jerzy Mikołaj Mańczak

Supervisors:
Dr. Juan José HERNÁNDEZ REY
Dr. Juan de Dios ZORNOZA GÓMEZ

*A thesis submitted in partial fulfillment of
the requirements for the degree of*

Doctor of Philosophy

in the

Departamento de Física Atómica, Molecular y Nuclear
Instituto de Física Corpuscular (UV – CSIC)

València, November 2022

Title:

Search for Neutrino Non-Standard Interactions with the KM3NeT/ORCA 6 lines detector

Author:

Jerzy Mikołaj Mańczak
Departamento de Física Atómica, Molecular y Nuclear
Instituto de Física Corpuscular (IFIC)
Universitat de València, Spain

Supervisors:
Dr. Juan José HERNÁNDEZ REY
Instituto de Física Corpuscular (IFIC)
Consejo Superior de Investigaciones Científicas (CSIC), Spain
and

Dr. Juan de Dios ZORNOZA GÓMEZ
Departamento de Física Atómica, Molecular y Nuclear
Instituto de Física Corpuscular (IFIC)
Universitat de València, Spain

Typeset by the author using the Thesis-LaTeX class developed by Vel.
https://www.latextemplates.com/template/masters-doctoral-thesis

Dr. Juan José HERNÁNDEZ REY, Profesor de Investigación del Consejo Superior de Investigaciones Científicas y **Dr. Juan de Dios ZORNOZA GÓMEZ**, Profesor Titular del Departamento de Física Atómica, Molecular y Nuclear de la Facultad de Física de la Universidad de Valencia,

CERTIFICAN,

Que la presente memoria, *"Search for Neutrino Non-Standard Interactions with the KM3NeT/ORCA 6 lines detector"*, ha sido realizada bajo su dirección en el Instituto de Física Corpuscular (Centro Mixto Universidad de Valencia - CSIC) por **Jerzy Mikołaj Mańczak** y constituye su Tesis Doctoral para optar al título de Doctor por la Universitat de València una vez cursados los estudios en el Doctorado en Física.

Y para que conste, en cumplimiento de la legislación vigente, firman el presente certificado en Paterna, el 31 de julio de 2022.

Dr. Juan José HERNÁNDEZ REY

Dr. Juan de Dios ZORNOZA GÓMEZ

*Las firmas están en el archivo de la Escuela de Doctorat.

Abstract

Departamento de Física Atómica, Molecular y Nuclear

Instituto de Física Corpuscular (UV – CSIC)

UNIVERSITAT DE VALÈNCIA

Search for Neutrino Non-Standard Interactions with the KM3NeT/ORCA 6 lines detector

by Jerzy Mikołaj Mańczak

The KM3NeT neutrino telescope has already gathered the first data and proven its capability for measuring atmospheric neutrino oscillations with the KM3NeT/ORCA detector. The first stage of the KM3NeT/ORCA detector, ORCA6, was operating for almost two years until it was extended with additional detection lines. This thesis presents the first attempt to measure Neutrino Non-Standard Interactions with the data gathered by the ORCA6 detector. The same data sample is exploited as the one used for the study of standard oscillations of atmospheric neutrinos. The data taking period spans over more than one year from January 2020 until March 2021. Effectively, the analysis seeks for sub-leading effects in the well-established neutrino standard oscillations in the Earth's matter. The limits of the similar order of magnitude to the current world-leading measurements are reported providing very promising prospects for the future research with the KM3NeT/ORCA detector. The reliability of the obtained results is tested thoroughly using various statistical methods and verifying the assumptions commonly made in the explored field of research.

Contents

Introduction

The thesis presents the first attempt to measure Neutrino Non-Standard Interactions (NSIs) with the early stage of the KM3NeT/ORCA detector (further referred to as ORCA), called ORCA6. The content of this dissertation is organised as follows:

Chapter 1 describes the theory of neutrino physics with a focus on experimental consequences. Neutrino Non-Standard Interactions are introduced together with the details of their potential implications for neutrino oscillations in matter.

Chapter 2 introduces the detector technology and the neutrino detection principle. All the detector components are briefly described. Peculiarities of the seawater environment in the context of light propagation are discussed. Signal and background signatures are discussed together with the data taking procedure.

Chapter 3 discusses subsequent stages of the Monte Carlo simulations essential for the modelling of the ORCA detector. The concept of a response matrix is presented. Parameters accounting for the systematic uncertainties in the models used in the analysis are also described. The whole detector modelling chain is summarised in the context of the reconstructed event rate predictions.

Chapter 4 presents the experimental results on the search for NSIs with 355 days of ORCA6 data. The statistical procedures are thoroughly discussed. The impact of the systematic uncertainties is investigated. The obtained results are compared to the world's best measurements.

An overview of the thesis is presented in the form of a Summary.

1   Physics of Neutrinos

Contents

In this chapter, neutrino interactions and mass-induced oscillations are reviewed. First, in Section 1.1.1, the Standard Model (SM) theory is introduced within its context and implications for the physics of neutrino interactions. A phenomenological consequence in the form of Neutrino Non-Standard Interactions (NSIs) of a possible theoretical detour beyond the Standard Model is briefly described in Section 1.1.2. In Section 1.2 neutrino oscillations are introduced for the vacuum propagation case, which is then extended by the influence of matter effects and NSIs in Sections 1.2.2 and 1.2.3. The neutrino oscillation description is summarised with the current status of the experimental bounds on the standard neutrino oscillations and the NSI parameters. In the final part of this Chapter, the oscillograms with different neutrino oscillation model assumptions and parameter values are depicted to highlight the observable consequences of the introduced theory and the potential signatures of new physics to be searched for in the experimental data.

1.1   Neutrinos and their interactions

The neutrino is an elementary particle historically first proposed in 1930 by Wolfgang Pauli as a solution to the continuous energy spectrum of the outgoing electron in the beta decay. In 1914, Chadwick gave compelling evidence that the electrons from β decays have a continuous energy distribution [1]. After a long controversy about the possibility that this continuous spectrum was due to energy losses of the electron when traversing matter, a key experiment by Wooster and Ellis in 1927 demonstrated that the electrons emitted by the nuclei had indeed a continuous distribution of energy [2].

The name "neutrino" (the Italian diminutive for neutron) was proposed by Enrico Fermi, who incorporated this elusive particle into his early theory of weak interactions in 1933 [3]. For the experimental proof of this at the time extravagant concept, physicists had to wait more than 20 years until in 1956 Frederick Reines and Clyde Cowan finally confirmed the existence of a particle, which clearly exhibited all of the postulated neutrino attributes: no mass, very low interaction cross section and lack of electric charge [4].

In 1962, it was experimentally demonstrated that there were at least two kinds ("flavours" or "families") of neutrinos [5]. In 1968 the first neutrinos from the Sun were detected, and the first hints of a deficit of neutrinos with respect to expectations were observed [6]. This "solar neutrino problem" motivated a variety of theories and experiments but it was not until 2001 when the SNO experiment measured the flux of the three neutrino flavours from the Sun [7] that the problem was resolved. SNO established that the total flux agreed with expectations and that previous results were due to the transformation of neutrinos between families. Similarly, the observation of a muon-neutrino deficit in the flux of atmospheric neutrinos by several experiments was clarified by the Super-Kamiokande experiment as due to the transformation between neutrino flavours [8].

So far three neutrino flavours have been detected, which is in compliance with the predictions from another milestone experimental result: the Z^0 boson width measurement in LEP [9]. The first observation of tau neutrino by DONUT collaboration in Fermilab in 2000 [10] put the final sentence in the story of neutrinos in the frame of the Standard Model.

According to our present understanding, there are three-flavours/families of active neutrinos that oscillate among each other. However, some of the experimental neutrino features still remain unresolved. Questions like whether the neutrino is a Majorana particle, what is the hierarchy of the neutrino masses or what is the absolute neutrino mass scale are the main pending topics in the current particle physics research. At the moment, an enormous effort is being put by the international scientific community into the preparation and construction of a new generation of neutrino experiments which are foreseen to provide answers to at least some of these questions within the coming decade.

1.1.1   Within the Standard Model

The Standard Model is the state-of-the-art theory which combines all the fundamental interactions (excluding gravity) among the known elementary particles. It comprises:

- twelve particles with spin $\frac{1}{2}$ (fermions): 6 quarks and 6 leptons,

- four force intermediate vector bosons with integer spin: $W^\pm, Z^0$, photon γ and gluon g,

- one scalar boson (spin 0) known as the Higgs boson.

A summary of the SM particles is shown in Table 1.1. All the fermions have their corresponding anti-particles, which are obtained via the CP (Charge-Parity) transformation. Each of the constituent particles of the SM responds to at least one of the fundamental forces:

1. **The weak force** distinguishes between two interaction types: charged current (CC) mediated by $W^\pm$ bosons and neutral current (NC) involving the Z^0 boson. A Neutrino is changed into its flavour-corresponding charged lepton when involved

in CC interactions, while in the case of NC interactions, the neutrino remains the same.

2. **The electromagnetic force** acts with an exchange of a photon γ. Electromagnetic interactions dominate above the nuclear scale distances, but they affect only the particles carrying the electric charge. Neutrinos are neutral particles and therefore they do not directly undergo the electromagnetic interactions.

3. **The strong force**, as the name suggests, is by far the strongest of all: $\simeq 137$ times stronger than the electromagnetic force and $\simeq 10^6$ stronger than the weak force. Via the exchange of gluons, the strong interaction confines quarks inside nucleons.

The Standard Model does not include gravity as at the quantum scale its impact is completely negligible compared to the other forces (10^{-31} compared with the strong force coupling). Quantum gravity within the scope of the SM postulates the existence of an additional yet-unobserved spin-2 mediating massless boson called graviton.

	Fermions (spin 1/2)			Vector Bosons (spin 1)	Higgs Boson (spin 0)
Leptons	e ν_e	μ ν_μ	τ ν_τ	$W^\pm, Z^0$ γ	H
Quarks	u d	s c	b t	g	

Table 1.1: Elementary particles of the standard model

Quarks are characterised by their fractional electric charge and confinement inside hadrons (quarks do not exist as free states). They are the only elementary particles which undergo all of the known fundamental forces. Leptons are defined as particles which respond to the weak force, but do not participate in the strong interactions. Charged leptons (electron e, muon μ and tau (or tauon) τ) carry a ± 1 electric charge and a flavour associated with the weak interactions. In fact, the electric charge unit is defined by the charge of an electron (elementary charge). Each charged lepton has a corresponding neutral lepton (neutrino) related by the same flavour. Due to the lack of electric charge, neutrinos interact with other particles only via weak currents. Because of their lack of mass, in the SM, neutrinos exist only in one helicity state: left-handed neutrinos and right-handed anti-neutrinos. This peculiar characteristic was experimentally confirmed by Goldhaber in 1957 [11].

The interactions in the Standard Model are described by gauge symmetries. The gauge group of the Standard Model is $SU(3) \otimes SU(2) \otimes U(1)$ where $SU(2) \otimes U(1)$ defines the electroweak group and $SU(3)$ is the strong gauge group. The electroweak symmetry is broken spontaneously [12, 13, 14] by the Brout-Englert-Higgs mechanism [15, 16], which causes the weak bosons and the charged fermions to gain mass. The existence of the Higgs field gives rise to a massive, spin-0 boson, the Higgs boson, first detected in 2012 [17][18]. The electroweak interactions among the particles of the leptonic sector are

given by the following Lagrangian density $\mathcal{L}$:

$$
\begin{aligned}
\mathcal{L} = {} & eA_\mu \bar{l}_\alpha \gamma^\mu l_\alpha && \text{(EM interaction)} \\
& - \frac{g}{\sqrt{2}} [W_\mu^+ \bar{\nu}_{\alpha L} \gamma^\mu l_{\alpha L} + W_\mu^- \bar{l}_{\alpha L} \gamma^\mu \nu_{\alpha L}] && \text{(CC weak interaction)} \\
& - \frac{g}{2\cos\theta_W} [Z_\mu(\bar{\nu}_{\alpha L}\gamma^\mu \nu_{\alpha L} - \bar{l}_{\alpha L}\gamma^\mu l_{\alpha L} - sin^2\theta_W \bar{l}_\alpha \gamma^\mu l_\alpha)], && \text{(NC weak interaction)}
\end{aligned}
$$

$$(1.1)$$

where

- $l_\alpha = l_{\alpha L} + l_{\alpha R}$ are the charged lepton fields for flavour α and (L)eft/(R)ight handed states,

- ν_α are the neutrino fields for flavour α,

- $W_\mu^\pm$ and Z_μ are the weak bosons fields,

- θ_W is the Weinberg's angle,

- A_μ is the photon field and

- γ^μ are the Dirac matrices.

The symbol μ is the Lorentz index.

The discovery of neutrino masses is considered the first measured phenomenon departing from the frame of the SM. It serves as a strong evidence that Beyond Standard Model (BSM) physics is there to be found, but does not provide many clues on what the new theory should look like. A possible measurement of Neutrino Non-Standard Interactions would channel the efforts of theoreticians in their search for a proper extension of the well-established theory. More details about the phenomenology and the potential consequences of NSIs will be given in sections 1.1.2 and 1.2.3.

1.1.1.1   Neutrino-electron charged current interactions

Possible charged current neutrino-electron scattering configurations can be illustrated by the following reactions:

$$\nu_e + e^- \rightarrow \nu_e + e^-, \tag{1.2}$$

$$\bar{\nu}_e + e^- \rightarrow \bar{\nu}_e + e^-, \tag{1.3}$$

which are described by the Feynmann diagrams shown in Fig. 1.1. As a consequence of the V-A (vector minus axial-vector) character of the weak interactions, whether a particle can undergo a CC interaction depends on its chirality: only left-handed fermions and right-handed anti-fermions couple to W bosons. For massless particles chirality is identical to helicity. To a very good approximation, for ultra-relativistic electrons helicity converges to be the same as chirality. With this assumption, when an anti-neutrino scatters from an electron, conservation of the total angular momentum along the collision axis $J_z = 1$ suppresses backward scattering of the electron. The differential cross sections then become [19]

$$\frac{d\sigma(\nu e)}{d\cos(\theta)} = \frac{G_F^2 s}{\pi}, \tag{1.4}$$

$$\frac{d\sigma(\bar{\nu}e)}{d\cos(\theta)} = \frac{G_F^2 s}{8\pi}(1 + \cos(\theta))^2, \tag{1.5}$$
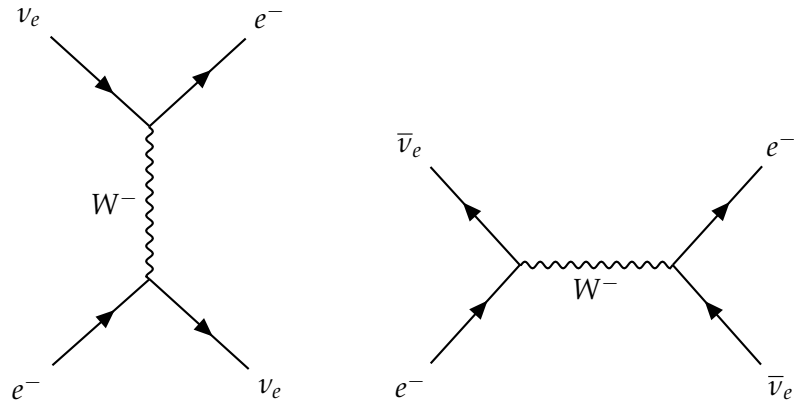
Figure 1.1: Feynmann diagrams for neutrino (left) and anti-neutrino (right) CC scattering from electrons.

where G_F is the Fermi constant and $s \simeq 2m_e E_\nu$ is the center-of-mass energy. The reader should mind the fact that the angle definition is different for t-channel and s-channel diagrams or alternatively for swapped helicity configuration between the incoming and the outgoing states. Equation 1.5 can also be expressed by a dimensionless Bjorken-y variable or the so-called inelasticity:

$$y = \frac{q \cdot p_t}{p_\nu \cdot p_t}, \quad y \in [0, 1], \tag{1.6}$$

$$\left(\frac{1 + \cos(\theta)}{2}\right)^2 = (1 - y)^2, \tag{1.7}$$

where q is the momentum transfer, p_t and p_ν are the target fermion and the incident neutrino four-momenta. It is defined as the fraction of energy of the primary neutrino which is transferred to the target. Eq 1.5 parameterized in y turns into

$$\frac{\mathrm{d}\sigma(\bar{\nu}e)}{\mathrm{d}y} = \frac{G_F^2 s}{\pi}(1 - y)^2 \Rightarrow \int \frac{\mathrm{d}\sigma(\bar{\nu}e)}{\mathrm{d}y}\mathrm{d}y = \frac{G_F^2 s}{3\pi}. \tag{1.8}$$

In the case of the s-channel diagram from Fig 1.1 ($\bar{\nu}_e e^- \rightarrow \bar{\nu}_e e^-$ scattering), in the laboratory frame of the electron at rest, y simply denotes the fraction of the primary neutrino energy transferred to the outgoing electron $y = E_l / E_\nu$.

The neutrino-electron scattering example can be extended to any neutrino interaction with a point-like fermion. As can be derived from Eq 1.5, the cross section is proportional to the neutrino energy and the target mass. For that reason, neutrino-electron scattering plays a marginal role in composite nuclear targets compared to neutrino-nucleon contribution. The energy proportionality breaks down when the center-of-mass energy approaches the mediating boson mass and the propagator effects start to become important.

1.1.1.2 Neutrino-fermion neutral current interactions

Examples of neutrino interactions allowed only via the exchange of the Z^0 boson are

$$\begin{aligned} \nu_\mu + e^- &\rightarrow \nu_\mu + e^-, \\ \bar{\nu}_\mu + e^- &\rightarrow \bar{\nu}_\mu + e^-. \end{aligned} \tag{1.9}$$

Unlike charged currents, neutral currents couple to both the left and right-handed helicity component of a fermion so that the cross sections become

$$\frac{d\sigma(\nu_\mu e)}{dy} = \frac{G_F^2 s}{\pi}[g_L^2 + g_R^2(1-y)^2], \tag{1.10}$$

$$\frac{d\sigma(\bar{\nu}_\mu e)}{dy} = \frac{G_F^2 s}{\pi}[g_R^2 + g_L^2(1-y)^2], \tag{1.11}$$

where g_L and g_R are the couplings to the left-handed and right-handed states, respectively. These couplings are generally characterised by the weak isospin and the Weinberg's angle θ_W. Table 1.2 shows the values of g_L and g_R depending on the type of the coupling fermion. A similar table exists for the CC interactions, but, following the arguments from section 1.1.1.1, the outcome is simplified to $g_L^{CC} = 1(0)$ and $g_R^{CC} = 0(1)$ for all the fermions (anti-fermions). In the case of $\nu_e e$ scattering, the final states are

Fermion	g_L	g_R
ν_e, ν_μ, ν_τ	$\frac{1}{2}$	0
e, μ, τ	$-\frac{1}{2} + \sin^2\theta_W$	$\sin^2\theta_W$
u, c, t	$\frac{1}{2} - \frac{2}{3}\sin^2\theta_W$	$-\frac{2}{3}\sin^2\theta_W$

Table 1.2: Weak neutral current Z^0 couplings g_L and g_R. Weinberg's angle value is $\sin(\theta_W)^2 \simeq 0.231$ [20]. The couplings for the corresponding anti-particles are obtained by swapping $g_L \leftrightarrow g_R$.

indistinguishable for NC and CC currents, so their amplitudes interfere. The combined CC and NC cross section for the example of $\nu_e e^-$ become

$$\frac{d\sigma(\nu_e e^-)}{dy} = \frac{G_F^2 s}{\pi}[g_L^2 + g_R^2(1-y)^2] \tag{1.12}$$

$$= \frac{G_F^2 s}{\pi}[(g_L^{CC} + g_L^{NC})^2 + (g_R^{CC} + g_R^{CC})^2(1-y)^2]$$

$$= \frac{G_F^2 s}{\pi}[(1 - \frac{1}{2} + \sin^2(\theta_W))^2 + (0 + \sin^2(\theta_W))^2(1-y)^2]$$

$$\sigma(\nu_e e^-) = \int \frac{d\sigma(\nu_e e^-)}{dy}dy = \frac{G_F^2 s}{\pi}(\frac{1}{2} + \sin^2(\theta_W))^2 + \frac{G_F^2 s}{3\pi}\sin^4(\theta_W) \tag{1.13}$$

$$= \frac{G_F^2 s}{\pi}(\frac{1}{4} + \sin^2(\theta_W) + \frac{4}{3}\sin^4(\theta_W)).$$

Once again, the formulas 1.10 and 1.11 can be extended to other neutrino-fermion interactions.

1.1.1.3 Neutrino-nucleon interactions

In neutrino detection, the most important neutrino interaction is the neutrino-nucleon scattering, which can be directly generalised to an isoscalar target. When interacting with particles with inner structure, like nucleons, different categories of neutrino interactions can also be distinguished based on the final state:

- Quasi-elastic (QE) - the neutrino scatters off a nucleon as a whole. The prefix quasi takes into account that nucleons cannot be treated as entirely free inside a nucleus. Depending on the weak current type, the nucleon changes its isospin while the neutrino turns into the corresponding charged lepton (CC) or the neutrino keeps its

state (NC) and the interaction becomes truly elastic. In the case of heavier nuclear targets, other subtle effects can play a role resulting in emitting more than one nucleon in the final state [20]. This is why these interactions are sometimes referred to as QE-like (or CC 0π) when a pion gets reabsorbed [21]. Quasi-elastic interactions dominate for the neutrino energies below 1 GeV, but they can still appear up to approximately 10 GeV (see Fig. 1.2).

- Resonance production (RES) - the neutrino interacts with a nucleon and creates a baryon resonant state, for example $\Delta(1232)$, which then decays accordingly. The most frequent result of a resonance decay is single-pion production.

- Deep Inelastic Scattering (DIS) - when the neutrino energy is high enough (>10 GeV), the interaction can happen directly with quarks inside a nucleon. DIS starts dominating the total neutrino-nucleon cross section for neutrino energies higher than $\sim$5 GeV and becomes the only relevant contribution above $\sim$100 GeV.

Cross section calculations with the specified contributions from the aforementioned process classes are depicted on top of some example experimental measurements in Fig. 1.2

(a) Neutrinos   (b) Anti-neutrinos
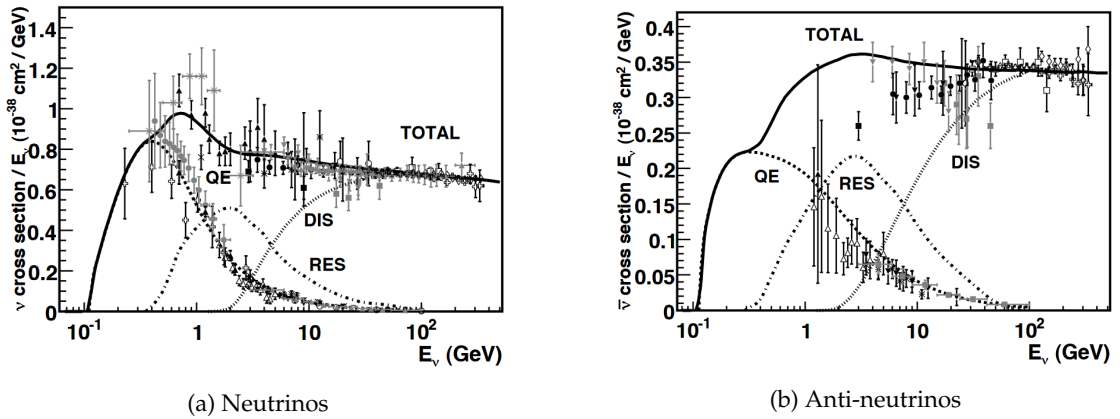
Figure 1.2: Total neutrino-nucleon cross section predictions according to the interaction type. The points with error bars example are the experimental measurements. Notice the different scales on the y-axis. Plots taken from [22].

The ORCA detector is designed to focus on neutrino energies between $\sim$3–100 GeV, so the vast majority of detectable interactions are expected to come from DIS. In this case, the neutrino-nucleon interaction can be considered similarly to the neutrino-electron processes, but happening on the constituent quarks of the nucleon target:

$$\frac{\mathrm{d}^2\sigma(\nu N)}{\mathrm{d}y\mathrm{d}x} = \frac{G^2 xs}{2\pi}[(u(x) + d(x)) + (\bar{u}(x) + \bar{d}(x))(1-y)^2], \tag{1.14}$$

$$\frac{\mathrm{d}^2\sigma(\bar{\nu} N)}{\mathrm{d}y\mathrm{d}x} = \frac{G^2 xs}{2\pi}[(u(x) + d(x))(1-y)^2 + (\bar{u}(x) + \bar{d}(x))], \tag{1.15}$$

where x is a Bjorken scaling variable, which can be interpreted as the fraction of the nucleon's momentum carried by the interacting parton, y is the inelasticity introduced in Eq. 1.6 and $u(x)(\bar{u}(x))$, $d(x)(\bar{d}(x))$ are the quark (anti-quark) probability distribution

functions inside the nucleon. The nucleon structure functions are then defined as

$$\frac{F_2^{\nu N}(x)}{x} = u(x) + d(x) + \bar{u}(x) + \bar{d}(x), \tag{1.16}$$

$$F_3^{\nu N}(x) = u(x) + d(x) - \bar{u}(x) - \bar{d}(x), \tag{1.17}$$

where we neglect a very small contribution from the second and third generation quarks. The total cross sections integrated over y and x (both from 0 to 1) become

$$\sigma(\nu N) = \frac{G_F^2 M E}{\pi}(Q + 1/3\bar{Q}), \tag{1.18}$$

$$\sigma(\bar{\nu} N) = \frac{G_F^2 M E}{\pi}(\bar{Q} + 1/3Q), \tag{1.19}$$

with the average x for quarks and anti-quarks:

$$Q = \int x(u(x) + d(x))\mathrm{d}x, \tag{1.20}$$

$$\bar{Q} = \int x(\bar{u}(x) + \bar{d}(x))\mathrm{d}x. \tag{1.21}$$

Ordinary matter contains almost exclusively fermions (as opposed to anti-fermions), so the expected total cross section ratio would be very close to $\sigma_\nu^{tot}/\sigma_{\bar{\nu}}^{tot} \simeq 3$. However, the actual experimentally derived ratio is $\sigma(\nu N)/\sigma(\bar{\nu} N) \simeq 2$, which leads to the conclusion that a nucleon contains a non-negligible portion of anti-quarks. Figure 1.3 shows the cross section measurements from various experiments of neutrino and anti-neutrino scattering from nucleons.
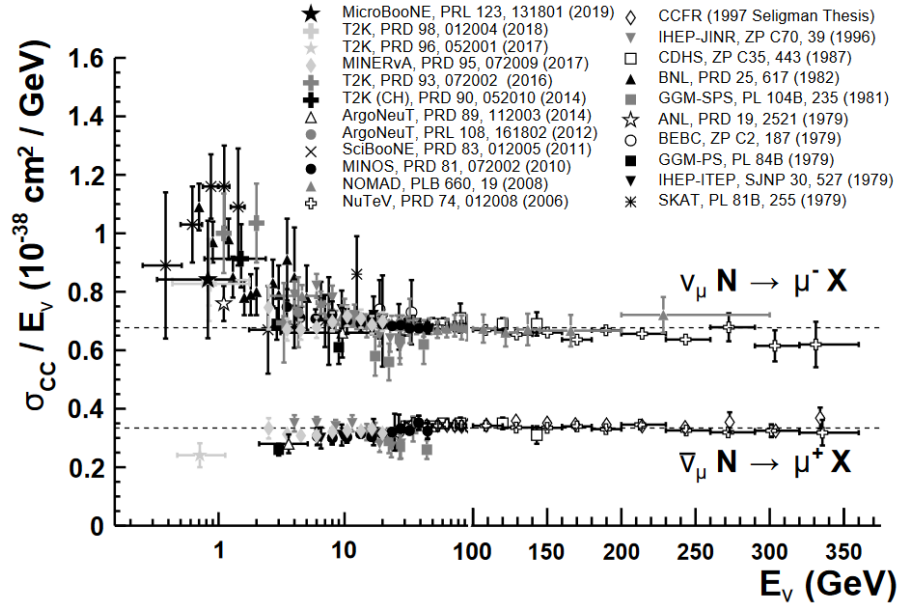
Figure 1.3: Total neutrino-nucleon CC interaction cross section measurements performed by various experiments. The dashed lines show the world-averaged cross sections $\sigma_\nu/E_\nu = (0.677 \pm 0.014) \cdot 10^8 \mathrm{cm}^2$ for neutrinos and $\sigma_{\bar{\nu}}/E_{\bar{\nu}} = (0.334 \pm 0.008) \cdot 10^8 \mathrm{cm}^2$ for anti-neutrinos. Adapted from [20].

For the t-channel DIS diagrams, in the target rest frame y becomes

$$y = \frac{E_\nu - E_l}{E_\nu}, \tag{1.22}$$

where E_l is the energy of the outgoing lepton. Here, low inelasticity means more energy carried away by the lepton, which in the case of a neutrino telescope such as ORCA is especially preferred for ν_μ-CC interactions, where the effective detection volume depends on the range of the muon. More details about the ORCA design and detection principle will be given in Chapter 2. Figure 1.4 shows the distribution of the Bjorken-y variable for neutrinos and anti-neutrinos interacting with an iron nucleus. As can be seen, the y distribution for anti-neutrinos prefers lower values due to the $(1-y)^2$ factor and the distribution for neutrinos is almost flat as expected from the formulas for scattering off point-like particles.
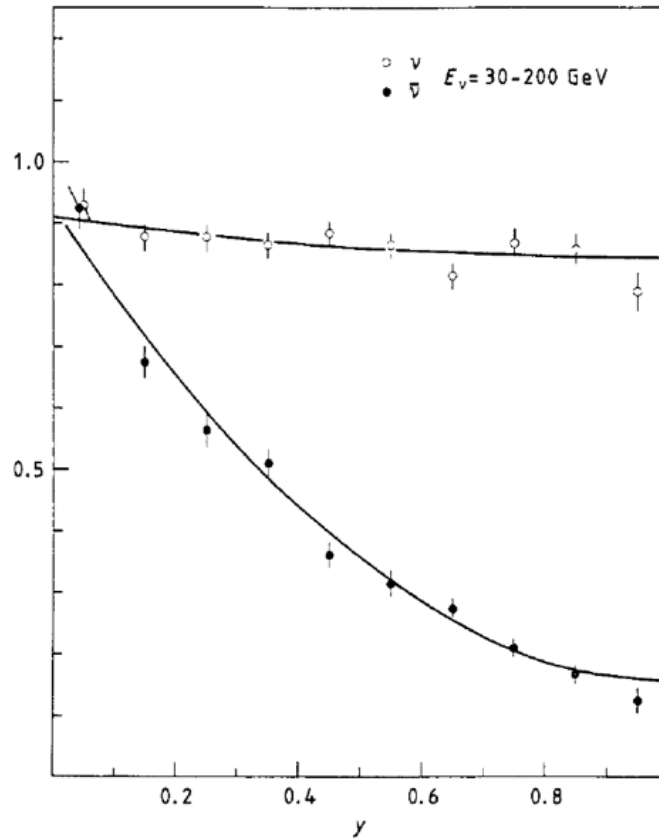
Figure 1.4: Differential cross section for different values of Bjorken-y inelasticity measured for ν and $\bar{\nu}$ scattering from iron nuclei. Adapted from [23].

The discovery of neutrino-nucleon NC interactions was the first experimental proof of the existence of neutral currents. The experimentally measured ratios are [24]

$$\frac{\sigma^{NC}(\nu)}{\sigma^{CC}} = \frac{\sigma(\nu_\mu N \to \nu_\mu X)}{\sigma(\nu_\mu N \to \mu^- X)}) \simeq 0.31, \tag{1.23}$$

$$\frac{\sigma^{NC}(\bar{\nu})}{\sigma^{CC}} = \frac{\sigma(\bar{\nu}_\mu N \to \nu_\mu X)}{\sigma(\bar{\nu}_\mu N \to \mu^+ X)}) \simeq 0.38, \tag{1.24}$$

where X represents any possible final state. In reality, the full picture is more complicated and the ratio would strongly depend on the type of the interaction (QE, RES or DIS), the energy and the momentum transfer [25]. However, the given ratios provide a good approximation for the energy range of atmospheric neutrinos. The situation gets more complicated again for astrophysical neutrinos, where the energies can reach up to the PeV scale [26][27].

Neutrino cross section uncertainties contribute to the systematic uncertainty of the neutrino oscillation measurements performed with experiments like ORCA. The precision of the ν_μ and ν_e DIS CC cross section measurement and modelling is relatively high in the energy range of our interest. However, the experimental challenges in separating events with a high likelihood lead to significantly lower statistics in all-flavour neutrino NC and ν_τ-CC interaction cross section measurements. Therefore, the normalisation needs to be accounted for with a wider margin [28][29]. More information about the treatment of systematic uncertainties will be given in Chapter 3.

Figure 1.5 depicts the total neutrino cross section values separated by the flavour, polarisation and weak current type. All the characteristics discussed in this section are well portrayed:

- $\nu/\bar{\nu}$ cross section ratio is of the order of 2,

- CC/NC cross section ratio is around 3,

- In a broad spectrum of energy the cross section is proportional to the neutrino energy. In the case of ν_τ there is a threshold effect related to the relatively high τ lepton mass of $\sim 1.7\,\mathrm{GeV}$.

A detailed overview of neutrino cross sections and interactions can be found in [22] and [30].
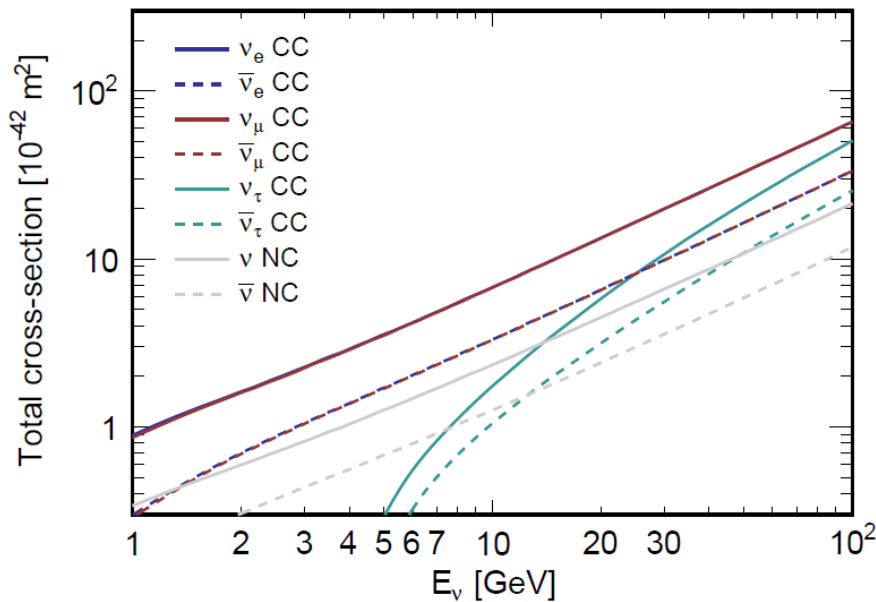
Figure 1.5: Total cross section per nucleon for neutrino interactions with water molecules calculated using GENIE [31]. Plot taken from ref. [32].

1.1.2 Non-Standard Interactions

Historically the so-called Neutrino Non-Standard Interactions were first proposed in a seminal paper by Wolfenstein [33] as a possible explanation for the oscillations of massless neutrinos. Nevertheless, even after the establishment of neutrino masses as the origin of neutrino oscillations, the current status of neutrino oscillation parameters measurements (see Section 1.2.5) still allows NSIs to contribute as a sub-leading effect, which can raise to the first order importance with high energy neutrinos crossing the

Earth. This scenario will be discussed further in Section 1.2.3. Most of the new physics models providing an explanation to massive neutrinos imply the existence of NSIs (reviews of the subject can be found in [34, 35, 36]). Putting experimental constraints on the NSI strength could shed a new light on which of the possible Standard Model extensions are worth to pursue. From a phenomenological point of view, this new type of interactions can be described as model-independent effective terms (operators) in the Lagrangian:

$$\mathcal{L}_{NSI}^{CC} = -2\sqrt{2}G_F \sum_{f,f',P,\alpha,\beta} \epsilon_{\alpha\beta}^{CC,ff'P}[\bar{\nu}_\alpha \gamma_\rho P_L l_\beta][\bar{f}\gamma^\rho P f'], \tag{1.25}$$

$$\mathcal{L}_{NSI}^{NC} = -2\sqrt{2}G_F \sum_{f,P,\alpha,\beta} \epsilon_{\alpha\beta}^{NC,fP}[\bar{\nu}_\alpha \gamma_\rho P_L \nu_\beta][\bar{f}\gamma^\rho P f], \tag{1.26}$$

where G_F is the Fermi constant, ϵ quantifies the relative strength of NSI to the weak interactions and $P \in P_L = (1 + \gamma^5), P_R = (1 - \gamma^5)$ are the projection operators of chirality. The sum goes over lepton flavours $\alpha, \beta \in \{e, \mu, \tau\}$ and interacting fermions, for ordinary matter $f, f' \in \{e, u, d\}$.

As the superscripts of the operators from Eq. 1.25 and 1.26 indicate, and similarly to the weak interactions, there are two types of NSIs: Charged Currents and Neutral Currents. The production and detection of neutrinos can be affected by CC NSIs, therefore in the literature they are often referred to as production or detection NSIs. In the presence of CC NSIs the neutrino states produced in the source or observed at the detector are superpositions of pure orthonormal flavour eigenstates. Therefore, the effects on neutrino oscillation experiments become more intricate, for instance, zero-distance flavour transitions are possible [35]. Nevertheless, CC NSIs are strongly constrained by a variety of standard processes, such as muon decay (via their impact on the Fermi constant), the unitarity of the CKM matrix, pion decays, results of the oscillation experiments and others [37, 38, 34, 39]. On the contrary, present data constrain NC NSIs only to be a sub-leading effect, but the bounds on their contribution to neutrino flavour transitions are relatively feeble. In this work, only NC NSIs will be studied. NC NSIs are frequently called matter NSIs as they are able to impact neutrino propagation through matter. A complete picture of neutrino oscillations in the Earth's matter under the influence of NC NSIs will be presented in Section 1.2.3. Assuming that the Standard Model is a low-energy approximation of a more complete theory, NSIs would originate from new physics above the electroweak scale. The coupling strength of this new type of interactions is expected to be of the order of

$$\epsilon \propto \frac{m_W^2}{m_X^2}, \tag{1.27}$$

where m_W denotes the mass of the W boson and m_X is the scale of the new physics, e.g. of the particles that mediate the new interactions. In the case of new physics being within the order of $1 - 10$ TeV, the expected values of the effective NSI parameters are between $\epsilon \sim 10^{-2} - 10^{-4}$.

1.2 Neutrino oscillations

Neutrino mass eigenstates are not equal to their flavour eigenstates and therefore neutrinos undergo oscillations. The transition between the mass states $|\nu_{1,2,3}\rangle$ basis to the flavour states $|\nu_{e,\mu,\tau}\rangle$ basis is defined by the Pontecorvo-Maki-Nakagawa-Sakata (PMNS)

unitary matrix U [40]:

$$\begin{pmatrix} \nu_e \\ \nu_\mu \\ \nu_\tau \end{pmatrix} = \begin{bmatrix} U_{e1} & U_{e2} & U_{e3} \\ U_{\mu 1} & U_{\mu 2} & U_{\mu 3} \\ U_{\tau 1} & U_{\tau 2} & U_{\tau 3} \end{bmatrix} \begin{pmatrix} \nu_1 \\ \nu_2 \\ \nu_3 \end{pmatrix}. \tag{1.28}$$

The most common parametrisation of the PMNS matrix involves three mixing angles θ_{ij} and one complex phase δ_{CP}, which accounts for the possibility of CP violation in the neutrino sector:

$$U = \begin{bmatrix} 1 & 0 & 0 \\ 0 & c_{23} & s_{23} \\ 0 & -s_{23} & c_{23} \end{bmatrix} \begin{bmatrix} c_{13} & 0 & e^{-i\delta_{CP}} s_{13} \\ 0 & 1 & 0 \\ -s_{13} e^{i\delta_{CP}} & 0 & c_{13} \end{bmatrix} \begin{bmatrix} c_{12} & -s_{12} & 0 \\ -s_{12} & c_{12} & 0 \\ 0 & 0 & 1 \end{bmatrix}, \tag{1.29}$$

where s_{ij} and c_{ij} stand for the sine and cosine functions of θ_{ij}. The time evolution of a neutrino mass state is defined by Schrödinger's equation:

$$i\frac{d}{dt} \left| \nu_i(t) \right\rangle = H \left| \nu_i \right\rangle, i = 1, 2, 3. \tag{1.30}$$

When the Hamitonian H does not depend on time, Eq. 1.30 has a plane wave solution[1]:

$$\left| \nu_i(t) \right\rangle = e^{-i(Et - px)} \left| \nu_i(0) \right\rangle, i = 1, 2, 3, \tag{1.31}$$

where E is the neutrino energy and $\vec{p}$ is its momentum vector. Considering a negligible neutrino mass ($m \ll E$) and $x \simeq ct = L$ we get

$$p_i = \sqrt{E_i^2 + m_i^2} = E\sqrt{1 + \frac{m_i^2}{E^2}} \approx E_i + \frac{m_i^2}{2E_i} \tag{1.32}$$

and in the case of a transition between mass states

$$\phi_i - \phi_j = (E_j - E_i)t - (p_j - p_i)x = -\left(\frac{m_j^2}{2E_j} - \frac{m_i^2}{2E_i} \right) L = \frac{\Delta m_{ij}^2 L}{2E}, \tag{1.33}$$

where ϕ_i is the propagation phase of a given mass state i and the mass states are created with the same energy $E_i = E_j$[2]. With the above definitions, the neutrino flavour transition probabilities are given by the formula:

$$P_{\nu_\alpha \to \nu_\beta}(t) = P_{\alpha\beta} = \sum_{i,j} U_{\alpha i}^* U_{\beta i} U_{\alpha j} U_{\beta j}^* \exp\left\{ -i\frac{\Delta m_{ij}^2 L}{2E} \right\}, \tag{1.34}$$

where L is the distance travelled by the neutrino and $E \approx |\vec{p}|$ is its energy. Δm_{ij}^2 denotes the difference between squared masses of two neutrino mass eigenstates. For oscillations to be possible, at least two neutrino masses are required to be different from each other. The observation of neutrino oscillations between all of the three flavours was a proof that neutrinos are indeed massive particles and at least two of the neutrino masses are

---

[1] The convention used in this Chapter assumes the natural units framework where the speed of light $c = 1$ and Dirac's constant $\hbar = 1$.

[2] This assumption would not be needed if the neutrino states were more precisely expressed as wave packets [41]. However, the plane wave approximation with $E_i = E_j$ leads to the same result.

non-zero. It is useful to separate the real and the imaginary part of the oscillation formula in Eq. 1.34:

$$P_{\nu_\alpha \to \nu_\beta} = \delta_{\alpha\beta} - 4 \sum_{i>j} \mathbb{R}e[U_{\alpha i}^* U_{\beta i} U_{\alpha j} U_{\beta j}^*] \sin^2\left(\frac{\Delta m_{ij}^2 L}{4E_\nu}\right)$$

$$\pm 2 \sum_{i>j} \mathbb{I}m[U_{\alpha i}^* U_{\beta i} U_{\alpha j} U_{\beta j}^*] \sin\left(\frac{\Delta m_{ij}^2 L}{4E_\nu}\right),$$

(1.35)

where the sign varies for neutrinos($+$) and anti-neutrinos($-$). The real part does not depend on the mass-squared difference sign, because the $\sin^2(x)$ function is symmetric around the ordinate. On the other hand, the imaginary part is sensitive to the sign of the mass-squared difference, but can contribute to the oscillation probability only in the presence of CP violation (δ_{CP} different from 0 or π). If all masses are equal, the formula is reduced to $P_{\alpha\beta} = \delta_{\alpha\beta}$. Overall, the oscillation amplitude depends on the mixing angles and the oscillation phase depends on the combination of the mass-squared difference, the neutrino energy and the travelled distance. The transition oscillation probabilities with $\alpha \neq \beta$ are associated with *appearance* channels and the probabilities with $\alpha = \beta$ are frequently called survival probabilities referring to *disappearance* channels.

To gain more intuition about the relation between the model parameters and the actual probability values, the rather cumbersome formulas defined in Eq. 1.34 can be simplified to a two-flavour approximation, which in many realistic experimental setups provides a sufficient theoretical picture. In such a case, the oscillation model is reduced to two parameters θ_{2f} and Δm_{2f}^2 and the PMNS matrix becomes a simple rotation matrix. The two-flavour neutrino oscillation probabilities read

$$P_{\alpha\beta}^{2f} = \sin^2(2\theta_{2f}) \sin^2\left(\frac{\Delta m_{2f}^2 L}{4E_\nu}\right)$$

(1.36)

$$P_{\alpha\alpha}^{2f} = 1 - P_{\alpha\beta}^{2f},$$

(1.37)

where the interplay between the mixing angle and mass-squared difference is clearly visible.

1.2.1 Neutrino Mass Ordering

There are at least three neutrino mass states, which implies three differences Δm_{21}^2, Δm_{31}^2 and Δm_{32}^2. Effectively, it leaves two free parameters in the model as the third mass difference can be unambiguously derived from the other two. The positive sign of Δm_{21}^2 is a matter of convention as with the observation of solar matter effects the quantity $\Delta m_{21}^2 \cdot \cos(2\theta_{12})$ was found to be positive [42][43]. This common convention choice restricts the range of θ_{12} to the first octant $[0, \pi/4]$. The yet unconstrained question whether Δm_{31}^2 is greater or smaller than Δm_{21}^2 is known as the Neutrino Mass Ordering (NMO) problem with the two possible scenarios defined as Normal Ordering (NO), $m_3 > m_2$, and Inverted Ordering (IO), $m_3 < m_1$. The two orderings are illustrated in Fig. 1.6. Oscillations in vacuum are not sensitive to NMO, however it can the studied thanks to the modification of Eq 1.34 induced by the presence of matter.

1.2.2 Matter effects

Neutrino oscillation patterns can be affected by the presence of matter, which introduces charged current coherent forward scattering of electron neutrinos off electrons bounded
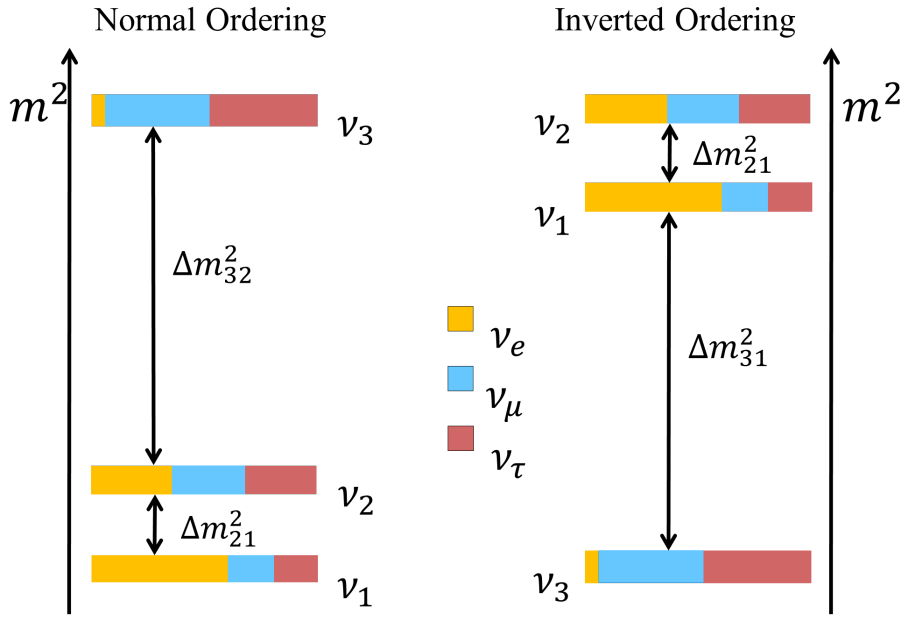
Figure 1.6: Neutrino mass ordering scenarios: Normal Ordering (left) and Inverted Ordering (right). The colours represent the relative contribution of the given flavour states to the mass states.

in atoms (see the Feynman diagrams in Fig. 1.1). This experimental fact leads to a set of matter effects such as resonance enhancement in transition probabilities or a phenomenon known as Mikheyev-Smirnov-Wolfenstein (MSW) effect [33][44]. In the presence of matter, the three-flavour vacuum Hamiltonian H_{vac} from Eq. 1.30 is modified by an additional perturbation H_{mat}, which leads to the combined effective Hamiltonian H_{eff}, which is simply expressed in the flavour basis as

$$H_{eff} = H_{vac} + H_{mat} = \frac{1}{2E} U_{PMNS} \begin{bmatrix} 0 & 0 & 0 \\ 0 & \Delta m_{21}^2 & 0 \\ 0 & 0 & \Delta m_{31}^2 \end{bmatrix} U_{PMNS}^\dagger + \begin{bmatrix} V_{CC} & 0 & 0 \\ 0 & 0 & 0 \\ 0 & 0 & 0 \end{bmatrix}, \quad (1.38)$$

where the effective potential $V_{CC} = \pm\sqrt{2}G_F N_e(x)$ depends on the electron number density $N_e(x)$ along the neutrino path x and the Fermi constant, G_F. The positive (negative) sign in the potential applies for neutrinos (anti-neutrinos). The transition matrix to the matter-modified mass basis can be found after diagonalisation of H_{eff}. This gives rise to the modification of the effective neutrino mixing parameters. In the two-flavour approximation, the new effective values $\theta_{13} \rightarrow \theta_{13}^m$ and $\Delta m_{31}^2 \rightarrow \Delta m_{31m}^2$ can be defined as

$$\sin^2(2\theta_{13}^m) = \frac{\sin^2(2\theta_{13})}{(\cos 2\theta_{13} - V_{CC}2E_v/\Delta m_{31}^2)^2 + \sin^2(2\theta_{13})}, \quad (1.39)$$

$$\Delta m_{31m}^2 = \Delta m_{31}^2 [(\cos 2\theta_{13} - V_{CC}2E_v/\Delta m_{31}^2)^2 + \sin^2(2\theta_{13})], \quad (1.40)$$

where the m sub- and superscript indicates the matter-induced modification. A resonance appears at

$$V_{CC}2E_v = \Delta m_{31}^2 \cos(2\theta_{13}) \Rightarrow E_v = \frac{\Delta m_{31}^2 \cos(2\theta_{13})}{2V_{CC}}, \quad (1.41)$$

either for neutrinos ($\Delta m^2_{31} > 0$) or anti-neutrinos ($\Delta m^2_{31} < 0$). It is important to notice that for the resonance to occur the electron density, N_e, has to be either constant or undergo adiabatic (or at least partially adiabatic) changes (MSW effect). For neutrinos crossing the Earth, the matter density varies between the Earth layers and the average N_e felt by a neutrino depends on its incident direction. Therefore, when studying atmospheric neutrinos, the resonance energy will differ depending on the amount of matter present on the neutrino's path. The relation between the direction of an atmospheric neutrino crossing the Earth and the thickness of the consecutive layers on its path is shown in Fig. 1.7. A detailed discussion of the formulas for the three flavour neutrino oscillation in
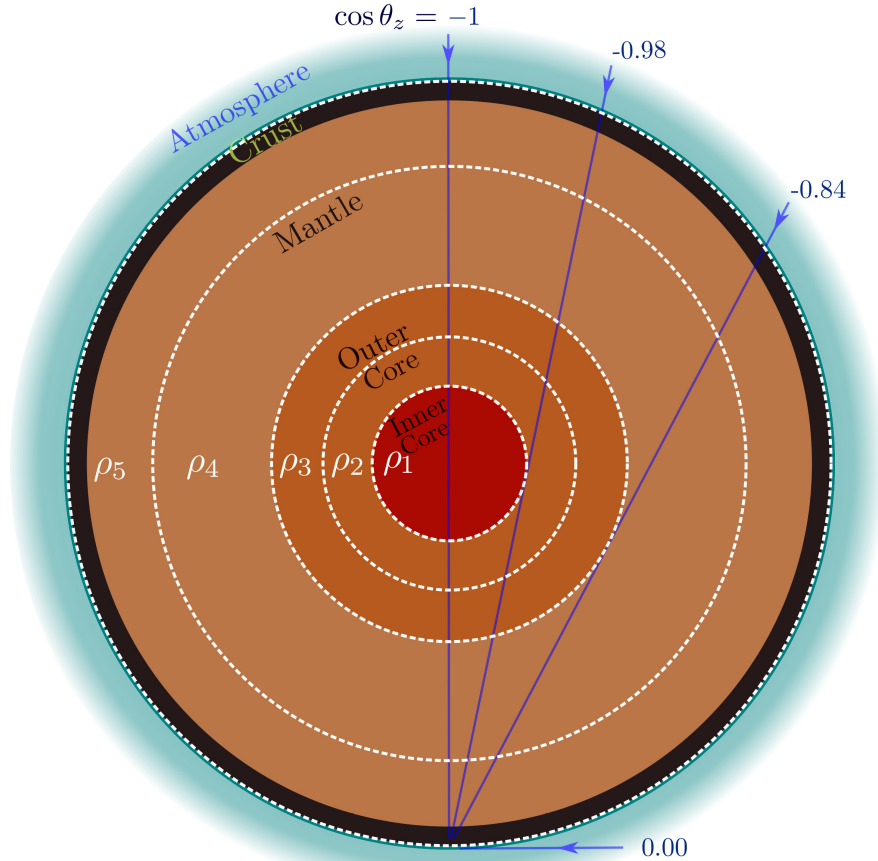
Figure 1.7: Earth cross section showing a simplified Earth layers' density profile. Blue lines correspond to the possible trajectories of the neutrinos produced in the atmosphere. Adapted from ref. [45].

matter can be found in [46]. A good description of the MSW effect with its analogies to classical optics (giving rise to the term *neutrino optics*) is presented in [47].

1.2.3 Oscillations in the presence of Non-Standard Interactions

Neutral current NSIs extend the Hamiltonian from Eq. 1.38 with an additional term

$$H_{eff} = \frac{1}{2E} U_{PMNS} \begin{bmatrix} 0 & 0 & 0 \\ 0 & \Delta m^2_{21} & 0 \\ 0 & 0 & \Delta m^2_{31} \end{bmatrix} U^\dagger_{PMNS} + V_{CC} \begin{bmatrix} 1 + \epsilon_{ee} & \epsilon_{e\mu} & \epsilon_{e\tau} \\ \epsilon^*_{e\mu} & \epsilon_{\mu\mu} & \epsilon_{\mu\tau} \\ \epsilon^*_{e\tau} & \epsilon^*_{\mu\tau} & \epsilon_{\tau\tau} \end{bmatrix}, \qquad (1.42)$$

where the "1" term in the 1-1 matrix element corresponds to the standard matter effect in Eq. 1.38. The NSI parameters $\epsilon_{\alpha\beta}$ at the Hamiltonian level are related to the coupling

strengths $\epsilon_{\alpha\beta}^{fP}$ from Lagrangian terms in Eq. 1.26 by (the NC superscript omitted):

$$\epsilon_{\alpha\beta} = \sum_{f \in \{e,u,d\}} \frac{N_f(x)}{N_e(x)} \epsilon_{\alpha\beta}^{fV}, \tag{1.43}$$

$$\epsilon_{\alpha\beta}^{fV} = \epsilon_{\alpha\beta}^{fP_L} + \epsilon_{\alpha\beta}^{fP_R}, \tag{1.44}$$

where $N_f(x)$ and $N_e(x)$ are the number densities of fermions f and electrons at the position x. In this thesis all the oscillation probabilities modified by NSIs are calculated with NSI coupling to d-quarks only. Assuming the Earth density profile with a stable relation $N_d \simeq 3N_e$ and electric neutrality of the Earth's matter, results for d-quarks can be simply re-scaled to obtain the NSI coupling strengths to the other fermions. Some NSI results obtained with neutrinos crossing the Earth [48][49] fix the average $N_n/N_e = 1.012$ in the mantle and $N_n/N_e = 1.137$ in the core resulting in a mass weighted average of $\langle N_n/N_e \rangle = 1.051 \Rightarrow \langle N_d/N_e \rangle = 3.102$, where N_n is the number density of neutrons. Other analyses, like for example those in refs [50] or [51][3], choose to use an exact factor of $N_d/N_e = 3$. It is important to be aware of these differences when comparing results. In our approach, a full 44-layer PREM model [52] is used to account for the varying density and $N_d(x)/N_e(x)$, which effectively introduces only a small correction to the aforementioned core/mantle neutron-to-electron ratio single step variation. For further details see Chapter 3.

If $\epsilon_{\alpha\beta} \neq 0$ for $\alpha \neq \beta$ lepton flavour conservation is violated. When $\epsilon_{\alpha\alpha} - \epsilon_{\beta\beta} \neq 0$ then NSIs introduce lepton flavour non-universality. Generally the off-diagonal NSI parameters also carry a complex phase — a more detailed discussion of this issue will be presented in Section 1.2.4.3. In analogy to the absolute neutrino mass scale, oscillation experiments cannot measure the absolute value of the diagonal NSI parameters. Without any effect on oscillations, the matrix $\epsilon_{\mu\mu} \times I(3 \times 3)$ can be subtracted from the Hamiltonian in Eq. 1.42 and the diagonal part of the NSI matrix becomes $diag(1 + \epsilon_{ee} - \epsilon_{\mu\mu}, 0, \epsilon_{\tau\tau} - \epsilon_{\mu\mu})$. This degeneracy can only be resolved by neutrino scattering experiments, which are capable of measuring directly the individual diagonal terms.

The evolution equation with the Hamiltonian from Equation 1.42 is invariant under the following transformation [53]:

$$\begin{aligned}
&\theta_{12} \to \pi - \theta_{12}, \; \epsilon_{ee} \to -\epsilon_{ee} - 2 \\
&\delta_{CP} \to \pi - \delta_{CP}, \; \epsilon_{\alpha\beta} \to -\epsilon_{\alpha\beta} \; (\alpha\beta \neq ee) \\
&\Delta m_{31}^2 \to -\Delta m_{31}^2 + \Delta m_{32}^2
\end{aligned} \tag{1.45}$$

Considering the lack of sensitivity of ORCA to θ_{12} and δ_{CP}, $\epsilon_{\alpha\beta}$ sensitivities are expected to be symmetrical if the neutrino mass hierarchy is profiled over in the fit. However, the degeneracy is not exact due to the presence of the standard matter potential — the condition on ϵ_{ee} shift is not symmetric around 0 so neglecting this parameter in the tested models (fixing $\epsilon_{ee} = 0$) actually breaks the degeneracy.

The calculation of the NSI-affected neutrino oscillation probabilities in matter for the full 3-flavour model is overwhelmingly complicated. Nevertheless, the leading order effects can be usually expressed analytically when certain approximations are made. For that reason, similarly to standard oscillations in vacuum (Eq. 1.36) and in matter (Eq. 1.39 and 1.40), in Section 1.2.4 a simplified two-flavour NSI model is discussed, where effectively

---

[3]In this IceCube paper from January 2022 the scaling factor is not stated explicitly, but it was obtained from private communications.

the NSI potential matrix is reduced to 2 parameters. A detailed discussion of the formulas for oscillation probabilities in the presence of NSIs can be found in [54] and [55].

1.2.4 Two flavour approximation

For a better understanding it is often convenient to simplify the NSI neutrino oscillation formulas to a two-flavour approximation. The atmospheric neutrino flux above the energies of a few GeV is dominated by muon neutrinos (see section 2.3.1) and the most important ν_μ disappearance channel comes from the $\nu_\mu \to \nu_\tau$ transition, so it is the most informative to look into the oscillations only in the $\mu - \tau$ sector. From the perspective of oscillations in vacuum, this choice is equivalent to setting $\Delta m^2_{21} = \theta_{12} = \theta_{13} = 0$. In the literature, this set of assumptions is sometimes called the *two-flavour hybrid model* [56]. In this case, the Hamiltonian becomes:

$$H^{2\nu}_{NSI} = \frac{\Delta m^2_{31}}{2E} \begin{bmatrix} c_{23} & -s_{23} \\ s_{23} & c_{23} \end{bmatrix} \begin{bmatrix} 0 & 0 \\ 0 & 1 \end{bmatrix} \begin{bmatrix} c_{23} & s_{23} \\ -s_{23} & c_{23} \end{bmatrix} + V_d \begin{bmatrix} \epsilon_{\mu\mu} & \epsilon_{\mu\tau} \\ \epsilon^*_{\mu\tau} & \epsilon_{\tau\tau} \end{bmatrix}, \qquad (1.46)$$

where the full PMNS matrix is reduced to a rotation matrix with one angle θ_{23}. If we consider only the real part of the non-diagonal NSI parameters and subtract $\epsilon_{\mu\mu} \cdot I(2 \times 2)$ from the Hamiltonian then only two effective parameters are left in the model: $\epsilon_{\mu\tau} = \epsilon^*_{\mu\tau}$ and $\epsilon' = \epsilon_{\tau\tau} - \epsilon_{\mu\mu}$. This assumption does not introduce any loss of generality as basically no sensitivity is expected to the NSI complex phases. However, the existence of the imaginary part in the NSI non-diagonal part can effectively deteriorate the sensitivity to the modulus. This possibility will be discussed in Section 1.2.4.3.

The absence of the Standard Model potential in the equation can be justified by the fact that under the assumption of $\mu - \tau$ NSI only ($\epsilon_{ee} = \epsilon_{e\tau} = \epsilon_{e\mu} = 0$), above the first matter resonance $E_\nu \simeq 20\,\text{GeV}$, the ν_e state practically separates from the evolution of the other flavours. The separation happens for even lower energies if we consider only the long baselines of the very up-going Earth-crossing neutrino directions. Moreover, in the atmospheric neutrino flux, only minimal amounts of electron neutrino are expected for $E_\nu \geq 10\,\text{GeV}$ in these up-going directions as atmospheric muons get suppressed by the Earth's matter before they have a chance to decay (more information on the atmospheric neutrino flux will appear in Section 2.3.1). The ORCA detector is in fact designed to reconstruct primary neutrino energies down to a few GeV and the above assumption would not exactly apply. However, as it will be shown in Chapter 3, the early stage ORCA6 does not yet provide a sufficient energy and direction resolution in a low energy regime and has to rely on the muons originating from high energy neutrinos. The ORCA6 threshold for a reliable reconstruction is just around $E_\nu \approx 10\,\text{GeV}$. The event selection used for the NSI analysis in this dissertation was optimised for muon neutrinos to look at their disappearance channel (further explanation will be given in Chapters 3 and 4). Therefore, the approximation discussed in this section is believed to accurately explain the oscillation physics affecting our analysis in the $\mu - \tau$ sector.

With NSIs coupling to *d*-quarks only (assumption already introduced in Section 1.2.3) and the lack of the standard matter potential, the normalisation factor from Eq. 1.43 can be omitted and we set $V_d = \sqrt{2}G_F N_d$. If we assume also constant matter density on the

neutrino path, the probabilities become

$$P_{\mu\tau} = \sin(2\Theta_m)\sin^2\left(\frac{\Delta m_{31}^2 L}{4E_\nu}R\right),$$ (1.47)

$$P_{\mu\mu} = 1 - \sin(2\Theta_m)\sin^2\left(\frac{\Delta m_{31}^2 L}{4E_\nu}R\right),$$ (1.48)

where the resonance factor

$$R^2 = 1 + R_0^2 + 2R_0\cos\left(2(\theta_{23} - \xi)\right)$$ (1.49)

and the effective mixing angle Θ_m

$$\sin(2\Theta_m) = \frac{\sin(2\theta_{23} - R_0)\sin(2\xi)}{R^2}$$ (1.50)

depend on the strength of the matter contribution relative to the vacuum part [57]

$$R_0 = \phi_{mat}/\phi_{vac} = \frac{V_{NSI}L/2}{\Delta m_{31}^2 L/4E_\nu}$$ (1.51)

$$V_{NSI} = V_d\sqrt{4\epsilon_{\mu\tau}^2 - \epsilon'^2} = \frac{2E_\nu V_{NSI}}{\Delta m_{31}^2},$$ (1.52)

where ϕ_{vac} and ϕ_{mat} denote respectively the vacuum oscillation phase and the oscillation phase induced by the presence of matter NSIs, and the effective NSI mixing angle obtained from the diagonalisation of the Hamiltonian perturbation due to NSIs

$$\sin(2\xi) = \frac{2\epsilon_{\mu\tau}}{\sqrt{4\epsilon_{\mu\tau}^2 + \epsilon'^2}},$$ (1.53)

so that the Hamiltonian from Eq. 1.46 can be rewritten as

$$H_{NSI}^{2\nu} = \frac{\Delta m_{31}^2}{2E}U(\theta_{23})\begin{bmatrix}0 & 0 \\ 0 & 1\end{bmatrix}U(\theta_{23})^\dagger + R_0 U(\xi)\begin{bmatrix}0 & 0 \\ 0 & 1\end{bmatrix}U(\xi)^\dagger.$$ (1.54)

The minimal value of the resonance factor appears for

$$R_0 = -\cos(2\theta_{23} - \xi) \rightarrow E_\nu^R = -\frac{\Delta m_{31}^2}{2V_{NSI}}\cos(2\theta_{23} - \xi),$$ (1.55)

where E_ν^R is the resonance energy, whose appearance for a fixed mass ordering depends on the sign of $\epsilon_{\mu\tau}$ and the neutrino/anti-neutrino channel. With the epsilons of the order of 10^{-2}, the resonance energy becomes $E_\nu^R \approx 100$ GeV assuming the trajectory corresponding to $\cos\theta_z = -1$. In the resonance region, the amplitude factor is reduced to

$$\sin(2\Theta_m) = \cos^2(2\xi)$$ (1.56)

and can completely vanish for a combination of $\epsilon_{\mu\tau}$ and ϵ' fulfilling the condition $\xi = \pi/4$. The resonance energy, for which the NSI effects are the most prominent, increases with decreasing values of the NSI epsilons. Therefore, the study of NSIs in the $\mu - \tau$ sector greatly benefits from the experimental capability to measure very high energy neutrinos crossing the Earth.

For very high energies, the vacuum term of the Hamiltonian in Eq. 1.46 vanishes due to the $1/E_\nu$ factor and the oscillation formula from Eq. 1.47 is reduced to

$$P_{\mu\tau} = \sin^2(2\xi) \sin^2 \left(\frac{V_d L}{2} \sqrt{4\epsilon_{\mu\tau}^2 + \epsilon'^2} \right), \tag{1.57}$$

where we still assume constant matter density and constant potential. In this particular case, without loss of generality, the potential can be also substituted with an average over the neutrino path $\overline{V}_d$. With the NSI parameters (and as a consequence the oscillation phase) close to zero, Eq. 1.57 can be approximated as

$$P_{\mu\tau} \approx (\epsilon_{\mu\tau} V_d L)^2, \tag{1.58}$$

with vanishing dependence on ϵ' and a straightforward sensitivity estimation

$$\epsilon_{\mu\tau} = \frac{1}{V_d L} \sqrt{P_{\mu\tau}}, \tag{1.59}$$

which depends on the resolution of the $P_{\mu\tau}$ measurement of a given experiment. Eq. 1.58 reveals some interesting features in the high energy limit:

1. the oscillation probabilities do not depend neither on ϵ' nor the sign of $\epsilon_{\mu\tau}$,

2. the dependence on Δm^2 disappears and therefore NMO does not play a role anymore,

3. as the probability now depends on V_d^2, the same outcome is expected for neutrinos and anti-neutrinos.

All the aforementioned observations are portrayed in Section 1.3, where precise numerical calculations of the oscillation probabilities are presented. The asymptotic behaviour of the NSI-matter oscillation phase becomes very useful for the $\epsilon_{\mu\tau}$ study with neutrino telescopes as they are not able to distinguish neutrinos from anti-neutrinos and, due to this fact, in the lower energy regime ($E_\nu < 100$ GeV) the NSI effects get partially cancelled out. Moreover, the reconstructed energy resolution does not have to be very precise for high neutrino energies where the $\nu_\mu / \bar{\nu}_\mu$ disappearance probability approaches the same asymptotic value. The disadvantage of using the asymptotic region for the measurement of $\epsilon_{\mu\tau}$ is that its sign cannot be resolved.

It is worth to investigate two separate cases with only one parameter at a time to find out where the sensitivity for a given parameter should come from in the observable phase space.

1.2.4.1 Flavour violating NSIs

In this scenario we take $\epsilon_{\mu\tau} \neq 0, \epsilon' = 0$, so $\sin(\xi) = 1$. The mixing angle now reads

$$\sin(2\Theta_m) = \frac{1}{1 + \cos^2(\theta_{23})(R_0 + \sin(2\theta_{23}))^{-2}}, \tag{1.60}$$

so it becomes maximal for large values of R_0. Away from the resonance region, the oscillation phase from Eq. 1.47 can be approximated (with $2R_0 \sin(2\theta_{23}) \approx 2R_0$) as

$$\frac{\Delta m_{31}^2 L}{4E_\nu} R \approx \frac{\Delta m_{31}^2 L}{4E_\nu}(1 + R_0) = \phi_{vac} + \phi_{mat} = \frac{\Delta m_{31}^2 L}{4E_\nu} + V_d L \epsilon_{\mu\tau} \tag{1.61}$$

and the NSI-induced modification does not depend on the neutrino energy. Figure 1.8 shows the impact of an example values of $\epsilon_{\mu\tau} = \pm0.01$ on the ν_μ disappearance probability. The values, already excluded by other experiments, corresponds to the sensitivity of ORCA6, which will be discussed in Chapter 4. As can be seen, the behaviour is symmetric under a simultaneous change $\nu \leftrightarrow \bar{\nu}$ and $\epsilon_{\mu\tau} \leftrightarrow -\epsilon_{\mu\tau}$. The variation in amplitude is visible, but very small. The resonance can be observed at the energy

$$E_R = -\frac{\Delta m_{31}^2}{4\epsilon_{\mu\tau} V_{NSI}(\theta_z)} \sin(2\theta_{23}), \tag{1.62}$$

which for the depicted value of $\cos\theta_z = -1$ lands at $E_R \simeq 60$ GeV. For energies above

(a) Neutrinos

(b) Anti-neutrinos
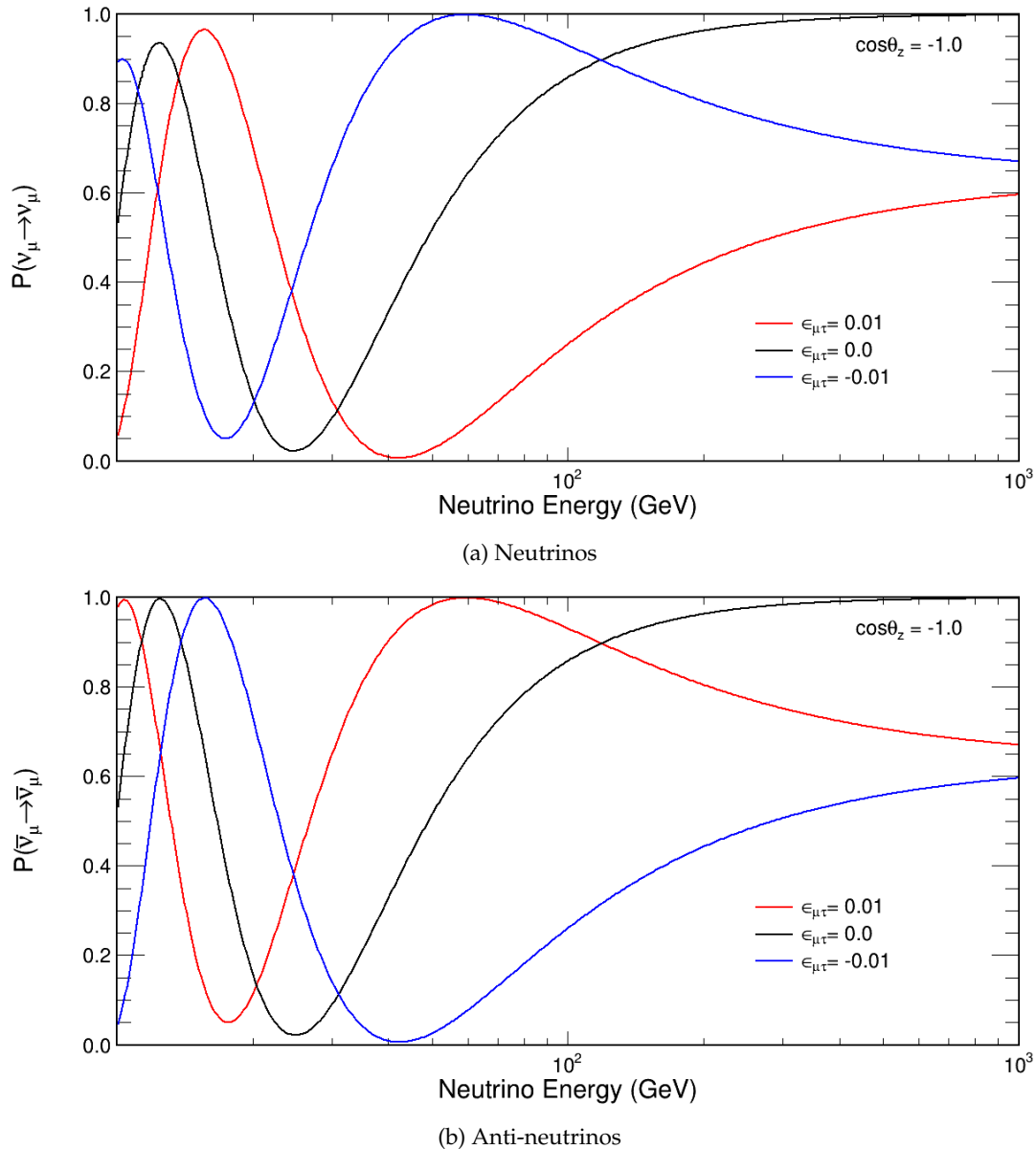
Figure 1.8: $P(\nu_\mu \rightarrow \nu_\mu)$ (a) and $P(\bar{\nu}_\mu \rightarrow \bar{\nu}_\mu)$ (b) survival probabilities for $\epsilon_{\mu\tau} = \pm0.01$. The calculations are done with OscProb [58] using the full 3-flavour oscillation scenario.

$E_\nu \sim 100$ GeV, where the vacuum phase ϕ_{vac} can be neglected, the muon survival

probability is reduced to its minimum in a realistic Earth-crossing trajectory case when

$$V_d L \epsilon_{\mu\tau} = \pi/2 \Rightarrow -2V_d(\theta_z) R_\oplus \cos\theta_z \epsilon_{\mu\tau} = \pi/2, \tag{1.63}$$

where $R_\oplus$ is the Earth's radius and V_d depends on the incident neutrino direction. The maximum possible $L = 2R_\oplus$ defines the minimum $\epsilon_{\mu\tau} \approx 2 \cdot 10^{-2}$ for which the condition in Eq. 1.63 can be fulfilled in Earth's matter with atmospheric neutrinos. Figure 1.9 shows the expected behaviour in the ν_μ survival probability with $\epsilon_{\mu\tau} = 0.02$ and $\epsilon_{\mu\tau} = -0.02$. The condition in Eq. 1.63 is independent of the sign of $\epsilon_{\mu\tau}$ as sine square is an even function. For $E_\nu > 100$ GeV and given that $\epsilon_{\mu\tau}$ is small then $\sin^2(V_d L \epsilon_{\mu\tau}) \simeq (V_d L \epsilon_{\mu\tau})^2$ and the probabilities converge to the asymptotic value following the discussion in Section 1.2.4. The sensitivity to the absolute value of of $\epsilon_{\mu\tau}$ would benefit from a good

(a) Neutrinos
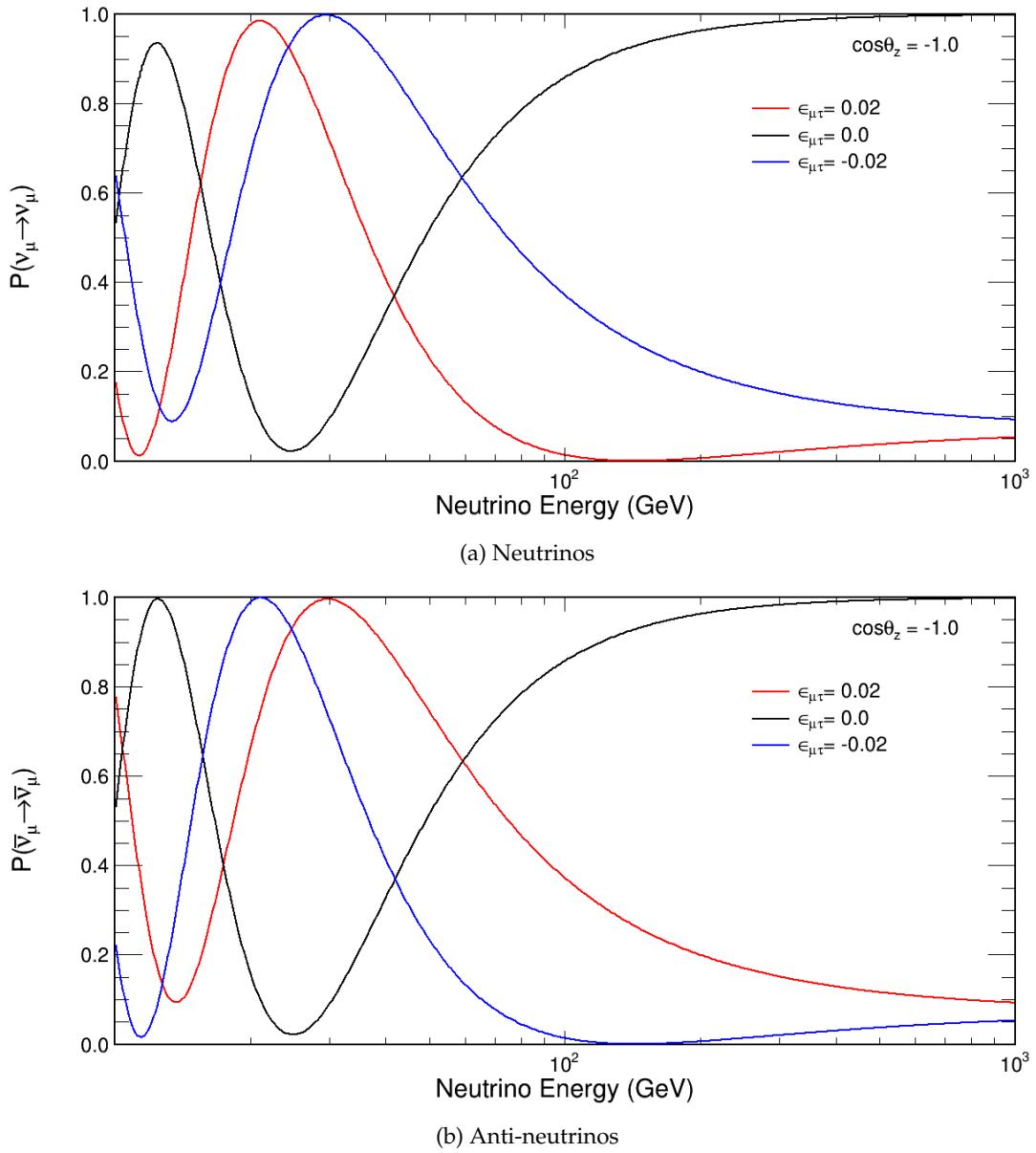
(b) Anti-neutrinos

Figure 1.9: $P(\nu_\mu \rightarrow \nu_\mu)$ (a) and $P(\bar{\nu}_\mu \rightarrow \bar{\nu}_\mu)$ (b) survival probabilities for $\epsilon_{\mu\tau} = \pm 0.02$. The calculations are done with OscProb [58] using the full 3-flavour oscillation scenario.

energy resolution at the resonance region and below, but only given that neutrinos and

anti-neutrinos can be separated or the measured interaction rate is asymmetric in $\nu_\mu/\bar{\nu}_\mu$ ratio. To be able to measure the sign of $\epsilon_{\mu\tau}$ would additionally require the mass ordering to be known. Since the mass ordering is not resolved, usually the results on $\epsilon_{\mu\tau}$ are presented for NO assuming a mirrored behaviour for IO. Energies below $E_\nu < 10$ GeV are not presented in the plots, because rapid changes in the fast oscillations regions are very challenging to measure in a neutrino telescope like ORCA.

1.2.4.2 Non-universal NSIs

For flavour non-universal NSIs, we assume $\epsilon_{\mu\tau} = 0, \epsilon' \neq 0$. In this case, the formulas for the effective mixing angle and the oscillation phase are the same as in the standard matter effect, but the standard matter potential turns into $V_{NSI} = V_d \epsilon'$. After changing $\theta_{13} \to \theta_{23}$ and one of the signs in Eq. 1.39 (here the two flavours in consideration are $\mu - \tau$ instead of $e - \mu$) we end up with

$$\sin^2(\Theta_m) = \frac{\sin^2(2\theta_{23})}{(R_0 + \cos(2\theta_{23}))^2 + \sin^2(\theta_{23})} = \frac{\sin^2(2\theta_{23})}{(\frac{2E_\nu V_d \epsilon'}{\Delta m_{31}^2} + \cos(2\theta_{23}))^2 + \sin^2(\theta_{23})}, \quad (1.64)$$

$$\Delta m_{31\epsilon'}^2 = \Delta m_{31}^2 \sqrt{\left(\frac{2E_\nu V_d \epsilon'}{\Delta m_{31}^2} + \cos(2\theta_{23})\right)^2 + \sin^2(\theta_{23})} \quad (1.65)$$

and the resonance condition is found at

$$E_R = -\frac{\Delta m_{31}^2 \cos(2\theta_{23})}{2V_d \epsilon'}, \quad (1.66)$$

which for a given sign of ϵ' appears only for neutrinos (ϵ' negative) or anti-neutrinos (ϵ' positive) assuming that the NO mass ordering is realised in nature. Due to the $\cos(2\theta_{23})$ dependence, a sign degeneracy also appears in the octant of θ_{23}, which is so far preferred to be the same for NO and IO in the global fits. However, as it is depicted in Section 1.2.5, the θ_{23} octant is not yet precisely measured and both scenarios, $\theta_{23} \in [0, \pi/4]$ and $\theta_{23} \in [\pi/4, \pi/2]$, are consistent with the current data. For an ϵ' value of the order of 10^{-2}, the resonance energy would be found, depending on the neutrino path, between 3 GeV and 30 GeV, which is a region where the standard vacuum mixing is already substantial. Hence, the most significant effect induced by the presence of ϵ' is expected to originate from the oscillation suppression for the energies higher than E_R. The oscillation phase

$$\phi_m = \phi_{vac}\sqrt{1 + 2\cos(2\theta_{23})R_0 + R_0^2},$$
$$= \frac{\Delta m_{31}^2 L}{4E_\nu}\sqrt{1 + 2\cos(2\theta_{23})\frac{2V_d E_\nu \epsilon'}{\Delta m_{31}^2} + \left(\frac{2V_d E_\nu \epsilon'}{\Delta m_{31}^2}\right)^2}, \quad (1.67)$$

can be affected linearly in ϵ', but only when 2-3 mixing is not maximal and with the neutrino energies away from the resonance. For a typical consideration of small ϵ', the quadratic terms can be neglected. All things considered, the main effect from ϵ' is expected rather in the change of the amplitude than in the phase shift. With growing neutrino energies, the oscillations get suppressed due to the $\sin(\Theta_m) \approx 1/R_0 \sin(2\theta_{23})$ dependence to finally converge to the vacuum case. Figure 1.10 depicts the impact of $\epsilon' = \epsilon_{\tau\tau} - \epsilon_{\mu\mu}$ on the muon neutrino survival probability. As expected, the most important change induced by ϵ' is the depth variation of the last oscillation minimum. Moreover, below the ν_e decoupling threshold of $E_\nu \simeq 20$ GeV, the standard matter resonance gets modified by the presence of ϵ'.

(a) Neutrinos

(b) Anti-neutrinos
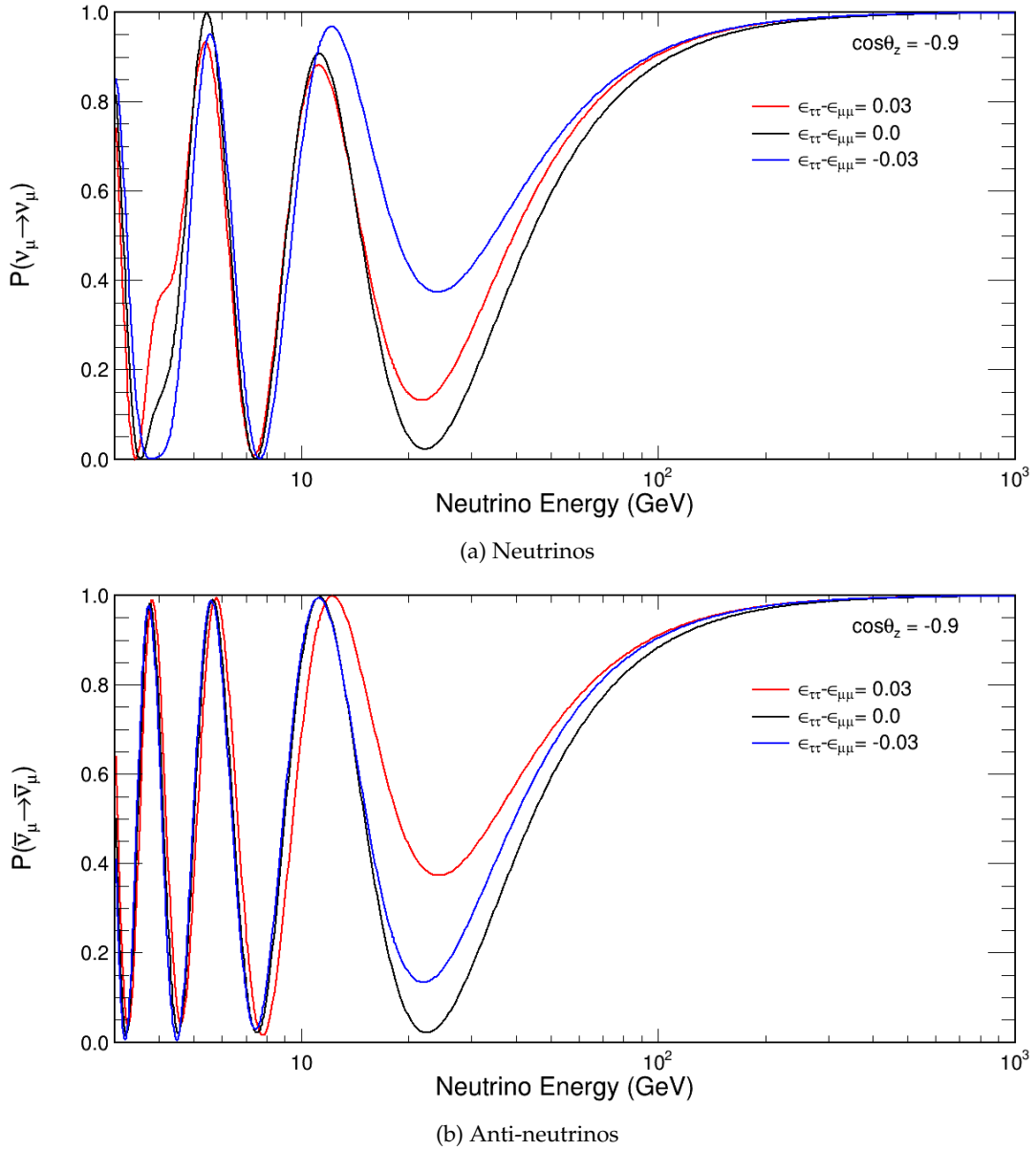
Figure 1.10: $P(\nu_\mu \rightarrow \nu_\mu)$ (a) and $P(\bar{\nu}_\mu \rightarrow \bar{\nu}_\mu)$ (b) survival probabilities for $\epsilon' = \epsilon_{\tau\tau} - \epsilon_{\mu\mu} = \pm 0.03$. The calculations are done with OscProb [58] using the full 3-flavour oscillation scenario.

A comprehensive study of the theory behind probing NSIs in the $\mu - \tau$ sector with atmospheric neutrinos is presented in [57] and [59]. A similar exercise can be done including only NSIs in the $e - \tau$ sector. In such a case, the dominant oscillation channel for atmospheric neutrino experiments, ν_μ disappearance, is still indirectly affected by the rotation of the ν_τ flavour state. Moreover, when the electron-flavour NSIs come into play, the standard matter oscillation picture is distorted and the sensitivity might appear at the lower energies ($E_\nu < 10$ GeV). A detailed discussion with analytical formulas for two-flavour approximation in the $e - \tau$ NSI sector can be found in [60] and [61].

1.2.4.3   Complex phase

Even though the complex phases of the non-diagonal NSI parameters are not yet measurable with the current experiments, their realisation in nature would introduce a reduction in the sensitivity to the modulus. The first order approximation of the ν_μ survival probability in the presence of a complex $\epsilon_{\mu\tau}$ matter NSIs reads [62, 63, 64]

$$
\begin{aligned}
P_{\mu\mu} \approx P^0_{\mu\mu} &- A|\epsilon_{\mu\tau}|\cos\left(\delta_{\mu\tau}\right)[\sin^3(2\theta_{23})\frac{L}{2E}\sin\left(2\Delta m^2_{31}L\right) \\
&+ 4\sin(2\theta_{23})\cos^2(2\theta_{23})\frac{1}{\Delta m^2_{31}}\sin^2(\Delta m^2_{31}L)] \\
&- A\epsilon' c^2_{23}s^2_{23}(c^2_{23}-s^2_{23})\left(\frac{L}{8E}\sin\left(\frac{2\Delta m^2_{31}L}{4E}\right)-\frac{1}{\Delta m^2_{31}}\sin^2\left(\frac{\Delta m^2_{31}L}{4E}\right)\right) \\
&+ O(\epsilon^2),
\end{aligned}
\tag{1.68}
$$

where $A = 2\sqrt{2}G_F N_e E_\nu$ and the assumption is made that $\sqrt{\Delta m^2_{21}/\Delta m^2_{31}} \simeq |\epsilon_{\alpha\beta}| \simeq \sin(\theta_{13})$. From Eq. 1.68, it can be seen that for the special case of $\epsilon' = 0$ and $\delta_{\mu\tau} = \pi/2 \vee \delta_{\mu\tau} = 3\pi/2$:

1. The sensitivity for $|\epsilon_{\mu\tau}|$ is suppressed,

2. The dependence on NMO vanishes if we assume $\delta_{CP} = 0$ (see the vacuum oscillation formula in Eq 1.35),

3. The probabilities for ν_μ and $\bar{\nu}_\mu$ are the same (the probability does not depend on the sign of the potential).

However, the expansion in Eq. 1.68 is not valid in the regions where NSI effects dominate over standard oscillations, which for the Earth's density profile would happen at high energies E_ν. Precise numerical calculations of the oscillation probabilities impacted by the complex NSIs are presented in section 1.3.1.

The complex phases can also be introduced in the $\epsilon_{e\tau}$ and $\epsilon_{e\mu}$ parameters in a similar way to Eq. 1.68. In such a case, it is the $P(\nu_\mu \to \nu_e)$ transition probability which gets affected via factors proportional to $\sin\left(\theta^m_{13}\right)\cos\left(\phi_{e\beta}+\delta_{CP}\right), \beta = \tau, \mu$. The $\sin(\theta_{13})$ terms cannot be neglected anymore.

1.2.5   Current status

Over the years, the combined effort of various research groups [65, 66, 67, 68, 69] has converged into a consistent and widely agreed-upon picture of the neutrino oscillation model. The last review of Particle Data Group [20], where the global best-fit values of the neutrino oscillation parameters are summarised, highlights three of the recent results which agree within 1σ error [70, 71, 72]. However, this review does not include the most recent updates [73, 74]. The global fit values from the latest NuFIT group results [73] provide the most up-to-date picture and therefore were chosen to serve as a reference point for all the neutrino oscillation calculations present in this dissertation. These values are summarised in Table 1.3. Even though the global data generally disfavours the inverted ordering [20], whether NO or IO is realised in nature is still a pending question and therefore both scenarios have to be taken into account in the analysis.

NuFIT 5.1 (2021)

		Normal Ordering (best fit)		Inverted Ordering ($\Delta\chi^2 = 2.6$)	
		bfp $\pm 1\sigma$	3σ range	bfp $\pm 1\sigma$	3σ range
without SK atmospheric data	$\sin^2\theta_{12}$	$0.304^{+0.013}_{-0.012}$	$0.269 \to 0.343$	$0.304^{+0.012}_{-0.012}$	$0.269 \to 0.343$
	$\theta_{12}/°$	$33.44^{+0.77}_{-0.74}$	$31.27 \to 35.86$	$33.45^{+0.77}_{-0.74}$	$31.27 \to 35.87$
	$\sin^2\theta_{23}$	$0.573^{+0.018}_{-0.023}$	$0.405 \to 0.620$	$0.578^{+0.017}_{-0.021}$	$0.410 \to 0.623$
	$\theta_{23}/°$	$49.2^{+1.0}_{-1.3}$	$39.5 \to 52.0$	$49.5^{+1.0}_{-1.2}$	$39.8 \to 52.1$
	$\sin^2\theta_{13}$	$0.02220^{+0.00068}_{-0.00062}$	$0.02034 \to 0.02430$	$0.02238^{+0.00064}_{-0.00062}$	$0.02053 \to 0.02434$
	$\theta_{13}/°$	$8.57^{+0.13}_{-0.12}$	$8.20 \to 8.97$	$8.60^{+0.12}_{-0.12}$	$8.24 \to 8.98$
	$\delta_{\mathrm{CP}}/°$	194^{+52}_{-25}	$105 \to 405$	287^{+27}_{-32}	$192 \to 361$
	$\dfrac{\Delta m^2_{21}}{10^{-5}\ \mathrm{eV}^2}$	$7.42^{+0.21}_{-0.20}$	$6.82 \to 8.04$	$7.42^{+0.21}_{-0.20}$	$6.82 \to 8.04$
	$\dfrac{\Delta m^2_{3\ell}}{10^{-3}\ \mathrm{eV}^2}$	$+2.515^{+0.028}_{-0.028}$	$+2.431 \to +2.599$	$-2.498^{+0.028}_{-0.029}$	$-2.584 \to -2.413$

		Normal Ordering (best fit)		Inverted Ordering ($\Delta\chi^2 = 7.0$)	
		bfp $\pm 1\sigma$	3σ range	bfp $\pm 1\sigma$	3σ range
with SK atmospheric data	$\sin^2\theta_{12}$	$0.304^{+0.012}_{-0.012}$	$0.269 \to 0.343$	$0.304^{+0.013}_{-0.012}$	$0.269 \to 0.343$
	$\theta_{12}/°$	$33.45^{+0.77}_{-0.75}$	$31.27 \to 35.87$	$33.45^{+0.78}_{-0.75}$	$31.27 \to 35.87$
	$\sin^2\theta_{23}$	$0.450^{+0.019}_{-0.016}$	$0.408 \to 0.603$	$0.570^{+0.016}_{-0.022}$	$0.410 \to 0.613$
	$\theta_{23}/°$	$42.1^{+1.1}_{-0.9}$	$39.7 \to 50.9$	$49.0^{+0.9}_{-1.3}$	$39.8 \to 51.6$
	$\sin^2\theta_{13}$	$0.02246^{+0.00062}_{-0.00062}$	$0.02060 \to 0.02435$	$0.02241^{+0.00074}_{-0.00062}$	$0.02055 \to 0.02457$
	$\theta_{13}/°$	$8.62^{+0.12}_{-0.12}$	$8.25 \to 8.98$	$8.61^{+0.14}_{-0.12}$	$8.24 \to 9.02$
	$\delta_{\mathrm{CP}}/°$	230^{+36}_{-25}	$144 \to 350$	278^{+22}_{-30}	$194 \to 345$
	$\dfrac{\Delta m^2_{21}}{10^{-5}\ \mathrm{eV}^2}$	$7.42^{+0.21}_{-0.20}$	$6.82 \to 8.04$	$7.42^{+0.21}_{-0.20}$	$6.82 \to 8.04$
	$\dfrac{\Delta m^2_{3\ell}}{10^{-3}\ \mathrm{eV}^2}$	$+2.510^{+0.027}_{-0.027}$	$+2.430 \to +2.593$	$-2.490^{+0.026}_{-0.028}$	$-2.574 \to -2.410$

Table 1.3: Global best-fit values of the standard neutrino oscillation parameters provided by the latest result of the NuFIT group [73]. For Normal Ordering $\Delta m^2_{3\ell} \equiv \Delta m^2_{31}$ and for Inverted Ordering $\Delta m^2_{3\ell} \equiv \Delta m^2_{32}$. The separation of the cases with and without SK (Super-Kamiokande) atmospheric data is driven by the fact that the SK collaboration did not publish sufficient information to include its analysis in the global likelihood [75]. However, their result in the form of χ^2 tables can still be combined with the NuFIT global result. Taken from [73].

1.2.5.1 Matter NSI parameters

So far, no experiment has provided a statistically significant evidence for a deviation from the standard three-flavour neutrino oscillation model. Nevertheless, a wide variety of experiments have put constraints on matter NSI using solar, atmospheric and long-baseline accelerator neutrino sources. A special place in the NC NSI study is taken by the COHERENT [76] experiment, which provides the experimental setup allowing for measurements of the diagonal terms $\epsilon_{\alpha\alpha}$ independently, whereas oscillation neutrino data can only constrain their difference $\epsilon_{\alpha\alpha} - \epsilon_{\beta\beta}$. At the moment, the most stringent single experiment limits are provided by IceCube and DeepCore with strong competition from ANTARES in the $\mu - \tau$ sector [77]. However, the comparison between results is

sometimes not straightforward as the assumptions about the Earth density layers, the effective NSI coupling strengths and other model parameters can vary between different analyses. Table 1.4 shows the most recent results from the global fit using oscillation data combined with COHERENT neutrino-nucleus scattering sample. In the quoted results it is generally assumed that the flavour structure of the NSI interactions does not depend on the coupling fermion. The table with the most up-to-date experimental limits, which can be directly compared to the results presented in Chapter 4, is shown in Table 1.5.

NSI Couplings	2σ allowed regions
Oscillation data + COHERENT global fit [78]	
ϵ_{ee}	$[-0.004, 0.367]$
$\epsilon_{\mu\mu}$	$[-0.038, 0.060]$
$\epsilon_{\tau\tau}$	$[-0.038, 0.058]$
$\epsilon_{e\mu}$	$[-0.049, 0.018]$
$\epsilon_{e\tau}$	$[-0.084, 0.094]$
$\epsilon_{\mu\tau}$	$[-0.006, 0.006]$
Global fit based on oscillation data only [79]	
$\epsilon_{ee} - \epsilon_{\mu\mu}$	$[-0.084, +0.326]$
$\epsilon_{\tau\tau} - \epsilon_{\mu\mu}$	$[-0.001, 0.018]$
$\epsilon_{e\mu}$	$[-0.051, 0.038]$
$\epsilon_{e\tau}$	$[-0.077, 0.098]$
$\epsilon_{\mu\tau}$	$[-0.006, 0.007]$

Table 1.4: Constraints on the matter propagation NSI at 2σ C.L. for the NSI coupling to d-quarks. Only one NSI parameter is considered at a time. The presented values were obtained after marginalising over the standard oscillation parameters and all the other undisplayed NC NSI parameters while probing only one $\epsilon_{\alpha\beta}$ at a time. The intervals, which allow for the Large Mixing Angle Dark (LMA-D) solution are not shown as this scenario is rarely considered in separate neutrino oscillation experimental results. The COHERENT data sample used to obtain the presented values included the energy and the time information with background estimations provided directly by the COHERENT collaboration [80] (it corresponds to the "Data release t+E" column in Table 3 in the global analysis article addendum in ref. [78]).

NSI Couplings	90% CL allowed regions	Experiment
$\epsilon_{\mu\tau}$ IO assumed	$[-0.0031, 0.0041]$	IceCube [51]
$\epsilon_{\mu\tau}$ NO assumed	$[-0.0041, 0.0031]$	—— ‖ ——
$\epsilon_{ee} - \epsilon_{\tau\tau}$	$[-0.70, -0.40] \cup [-0.23, 0.10]$	DeepCore [81]
$\epsilon_{\tau\tau} - \epsilon_{\mu\mu}$	$[-0.013, 0.013]$	—— ‖ ——
$\epsilon_{\mu\tau}$	$[-0.0055, 0.0043]$	—— ‖ ——
$\epsilon_{\mu\tau}$ IO assumed	$[-0.0029, 0.0047]$	ANTARES [77]
$\epsilon_{\mu\tau}$ NO assumed	$[-0.0047, 0.0029]$	—— ‖ ——
$\epsilon_{\tau\tau} - \epsilon_{\mu\mu}$ IO assumed	$[-0.064, -0.004] \cup [0.014, 0.064]$	—— ‖ ——
$\epsilon_{\tau\tau} - \epsilon_{\mu\mu}$ NO assumed	$[-0.061, -0.014] \cup [0.014, 0.081]$	—— ‖ ——
$\epsilon_{\tau\tau} - \epsilon_{\mu\mu}$	$[-0.049, 0.049]$	Super-K [82]
$\epsilon_{e\tau}$ (for $\epsilon_{ee} = -0.5$)	$[-0.05, 0.05]$	—— ‖ ——
$\epsilon_{e\tau}$ (for $\epsilon_{ee} = 0.5$)	$[-0.019, 0.013]$	—— ‖ ——
Complex flavour violating NSI	90% CL allowed regions	
$|\epsilon_{e\mu}|$	≤ 0.045	DeepCore [81]
$\delta_{e\mu}$	$[0, 2\pi]$	—— ‖ ——
$|\epsilon_{e\tau}|$	≤ 0.054	—— ‖ ——
$\delta_{e\tau}$	$[0, 2\pi]$	—— ‖ ——
$|\epsilon_{\mu\tau}|$	≤ 0.007	—— ‖ ——
$\delta_{\mu\tau}$	$[0, 2\pi]$	—— ‖ ——

Table 1.5: Summary of the limits on NSI couplings from atmospheric neutrino measurements. The top section contains those couplings which are assumed to be real. The bottom section presents the DeepCore measurements where the possible complex nature of the flavour-violating NSI parameters is accounted for. In all cases, unless specified otherwise, Normal Ordering is assumed. The DeepCore results are divided by 3.21 to match the NSI coupling to d-quark only (the explanation for the re-scaling factor will be given in Chapter 4). For complex NSI parameters, the limits on the moduli $|\epsilon_{\alpha\beta}|$ are obtained by profiling over the corresponding phase $\delta_{\alpha\beta}$. None of the experimental results consider the LMA-D solution, because the intervals in this table assume all the other NSI parameters fixed at 0. Even though ANTARES measures a mild preference towards non-zero NSI in the flavour non-universal $\mu - \tau$ parameter, this tension disappears for 95% CL. In the case of the IceCube result (first row), the complex nature of $\epsilon_{\mu\tau}$ was parameterised by fitting the real and imaginary part, but it was found that the limits are almost perfectly circular in the complex plane.

1.3   Oscillograms

The oscillograms presented in this section are two-dimensional oscillation probability maps for neutrinos crossing the Earth as a function of true neutrino energy, E_{true}, and cosine of the neutrino's true zenith angle, $\cos\theta_z$, which translates into the oscillation path length as $L \approx -2R_\oplus \cos\theta_z$, where $R_\oplus$ is the Earth's radius. The dashed lines indicated in the plots correspond to constant L/E_{true}. Oscillation probabilities are calculated with the OscProb software package [58]. The Earth density is based on the PREM model [52] with 44 layers.

Neutrino telescopes like ORCA are in principle not able to distinguish particle from anti-particle. For that reason, the oscillation measurements rely on the presence of matter and the differences in cross sections. Considering the atmospheric neutrino flux flavour and $\nu/\bar{\nu}$ ratios for the energies detectable with ORCA together with the cross section asymmetry, $\sigma_\nu/\sigma_{\bar{\nu}} \simeq 2$, it is most informative to look at oscillograms for summed ν_μ and $\bar{\nu}_\mu$ weighted with the $\nu_\mu/\bar{\nu}_\mu = 2$ flux ratio. The formula for combined and weighted

muon neutrino-anti-neutrino survival probability becomes

$$P_{\mu\mu}^{\nu+0.5\bar{\nu}} = [P(\nu_\mu \to \nu_\mu) + 0.5 \times P(\bar{\nu}_\mu \to \bar{\nu}_\mu)]/1.5 \qquad (1.69)$$

To see where to expect the signal in the observable phase space in terms of excess or deficit of events induced by NSIs with respect to the standard oscillation scenario, it is useful to look at $\Delta P_{\mu\mu}^{\nu+0.5\bar{\nu}}$, defined as the probability difference between $P_{\mu\mu}^{\nu+0.5\bar{\nu}}$ with and without NSIs present in the model. In all the oscillograms presented in the following sections, $\Delta P_{\mu\mu}^{\nu+0.5\bar{\nu}}$ symbol is simplified to $\Delta P_{\mu\mu}$ in the axis titles.

The values of the NSI parameters used in the oscillograms presented in this section are already excluded by experimental results (see Section 1.2.5), but they are chosen to highlight the most important regions in terms of the signal measurable with ORCA6.

The oscillograms in Fig. 1.11 show the effect of $\epsilon_{\mu\tau}$. The oscillograms in Fig. 1.12 show the effect of $\epsilon_{e\tau}$. They are accompanied by one-dimensional oscillation plots for fixed $\cos\theta$ depicted in Fig 1.13. The oscillograms in Fig. 1.14 show the effect of $\epsilon_{e\mu}$. Here, the projected one-dimensional probabilities are not shown since the effect is widely spread in the whole presented phase space. Fig. 1.15 show the effect of $\epsilon_{\tau\tau} - \epsilon_{\mu\mu}$.

Most of the NSI-induced deviation from the standard oscillations is expected for the up-going neutrino directions with $\cos\theta_z < 0.84$ which correspond to the core-crossing neutrino paths (see Fig. 1.7). The high density of the Earth's core amplifies the effects of matter NSIs. The strongest effects are seen in the flavour violating $\epsilon_{\mu\tau}$ due to the fact that the main oscillation channel observed with atmospheric neutrinos in ORCA is the disappearance of muon neutrinos which in the standard oscillations transform mainly into tau neutrinos. Generally, in the neutrino energy dimension, the effect of the NSIs affecting the $\mu - \tau$ sector concentrates in the 20-40 GeV region, because of the shift of the oscillation minimum at around 25 GeV causing a high difference between NSI and SI. Depending on the particular parameter, the phase shift can be accompanied by the amplitude change.

The oscillograms showing all the oscillation channels in the case of standard oscillations in vacuum and in matter together with the ν_μ survival probabilities for all the NSI parameters tested in this work are shown in Appendix B.

Flavour violating $\epsilon_{\mu\tau}$

(a) $\Delta P_{\mu\mu}^{\nu+0.5\bar{\nu}}$ NO + $\epsilon_{\mu\tau} = -0.01$

(b) $\Delta P_{\mu\mu}^{\nu+0.5\bar{\nu}}$ NO, $\epsilon_{\mu\tau} = 0.01$

(c) $\Delta P_{\mu\mu}^{\nu+0.5\bar{\nu}}$ NO, $\epsilon_{\mu\tau} = -0.015$

(d) $\Delta P_{\mu\mu}^{\nu+0.5\bar{\nu}}$ NO, $\epsilon_{\mu\tau} = 0.015$

(e) $\Delta P_{\mu\mu}^{\nu+0.5\bar{\nu}}$ NO, $\epsilon_{\mu\tau} = -0.02$

(f) $\Delta P_{\mu\mu}^{\nu+0.5\bar{\nu}}$ NO, $\epsilon_{\mu\tau} = 0.02$
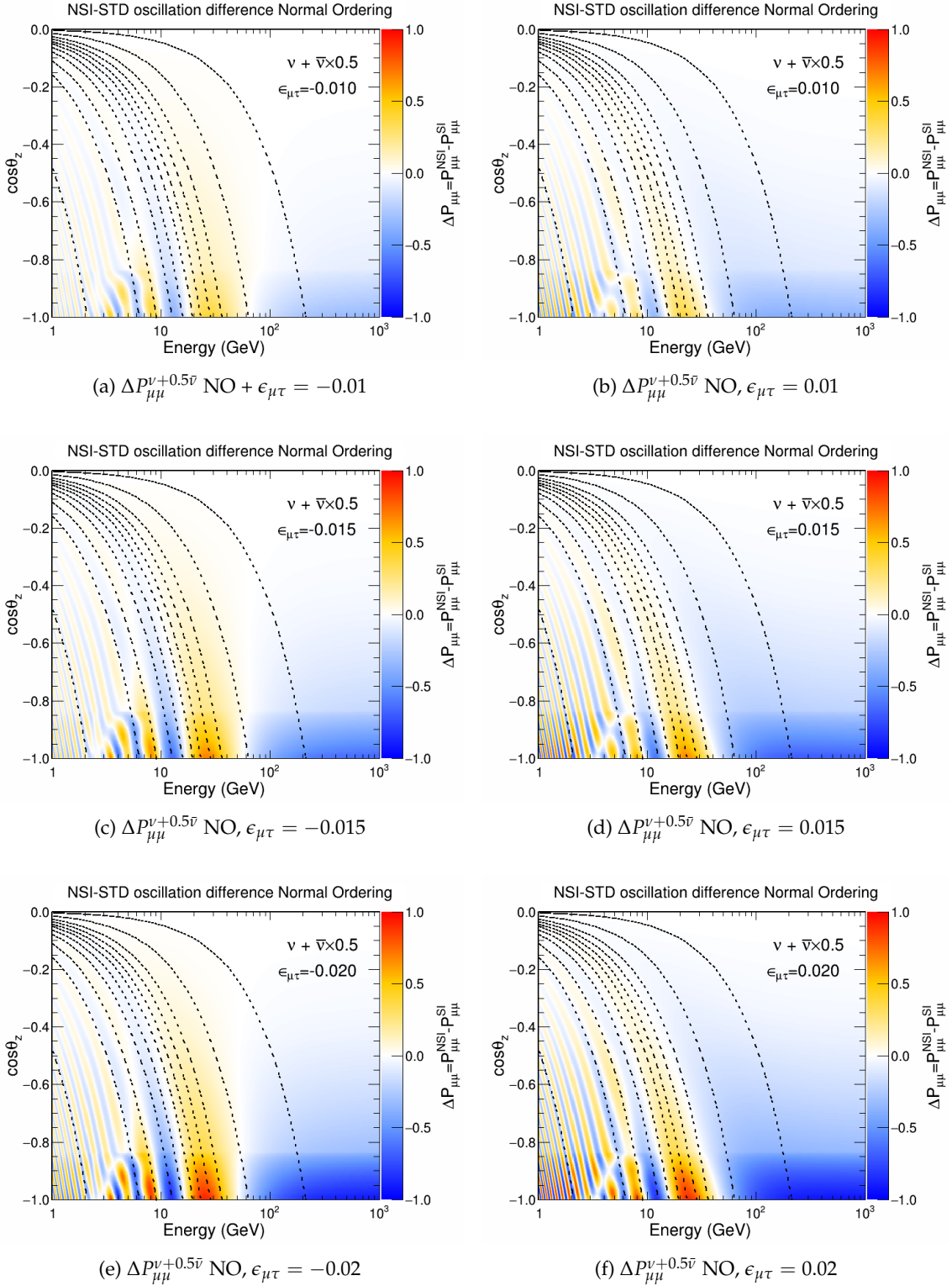
Figure 1.11: Difference in the survival probability for the weighted neutrino-anti-neutrino flux $\Delta P_{\mu\mu}^{\nu+0.5\bar{\nu}}$ between oscillations with NSI and standard oscillations for the parameter value $\epsilon_{\mu\tau} \in \{\pm 0.01, \pm 0.015, \pm 0.02\}$.

Flavour violating $\epsilon_{e\tau}$

(a) $\Delta P_{\mu\mu}^{\nu+0.5\bar{\nu}}$ NO, $\epsilon_{e\tau} = -0.1$

(b) $\Delta P_{\mu\mu}^{\nu+0.5\bar{\nu}}$ NO, $\epsilon_{e\tau} = 0.1$

(c) $\Delta P_{\mu\mu}^{\nu+0.5\bar{\nu}}$ NO, $\epsilon_{e\tau} = -0.15$

(d) $\Delta P_{\mu\mu}^{\nu+0.5\bar{\nu}}$ NO, $\epsilon_{e\tau} = 0.15$

(e) $\Delta P_{\mu\mu}^{\nu+0.5\bar{\nu}}$ NO, $\epsilon_{e\tau} = -0.2$

(f) $\Delta P_{\mu\mu}^{\nu+0.5\bar{\nu}}$ NO, $\epsilon_{e\tau} = 0.2$
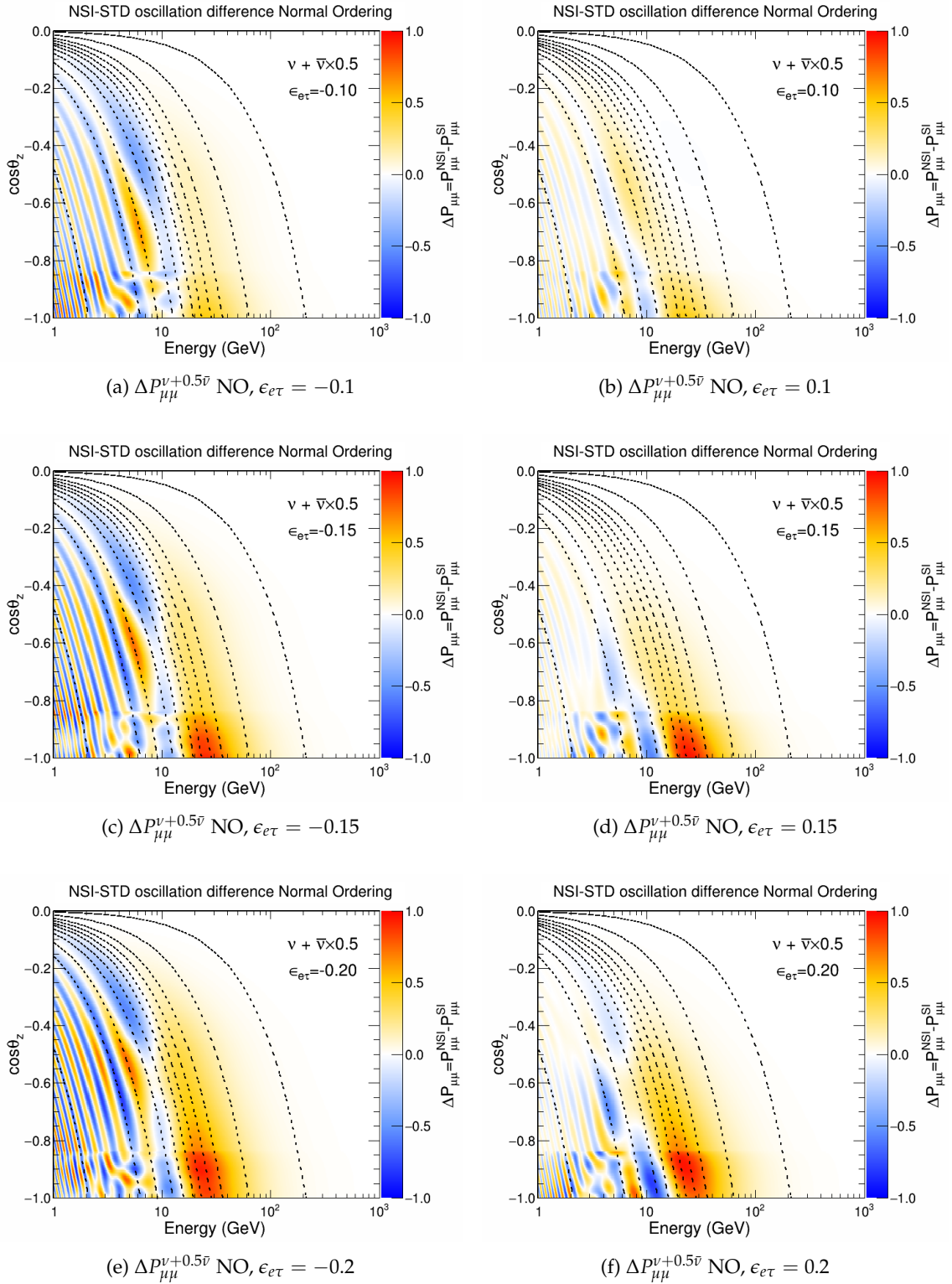
Figure 1.12: Difference in the survival probability for the weighted neutrino-anti-neutrino flux $\Delta P_{\mu\mu}^{\nu+0.5\bar{\nu}}$ between oscillations with NSI and standard oscillations for the parameter values $\epsilon_{e\tau} \in \{\pm 0.1, \pm 0.15, \pm 0.2\}$.

It is more intuitive to have a look at the oscillation plots projected onto the energy dimension. The example is shown in Fig. 1.13.

(a) Neutrinos

(b) Anti-neutrinos
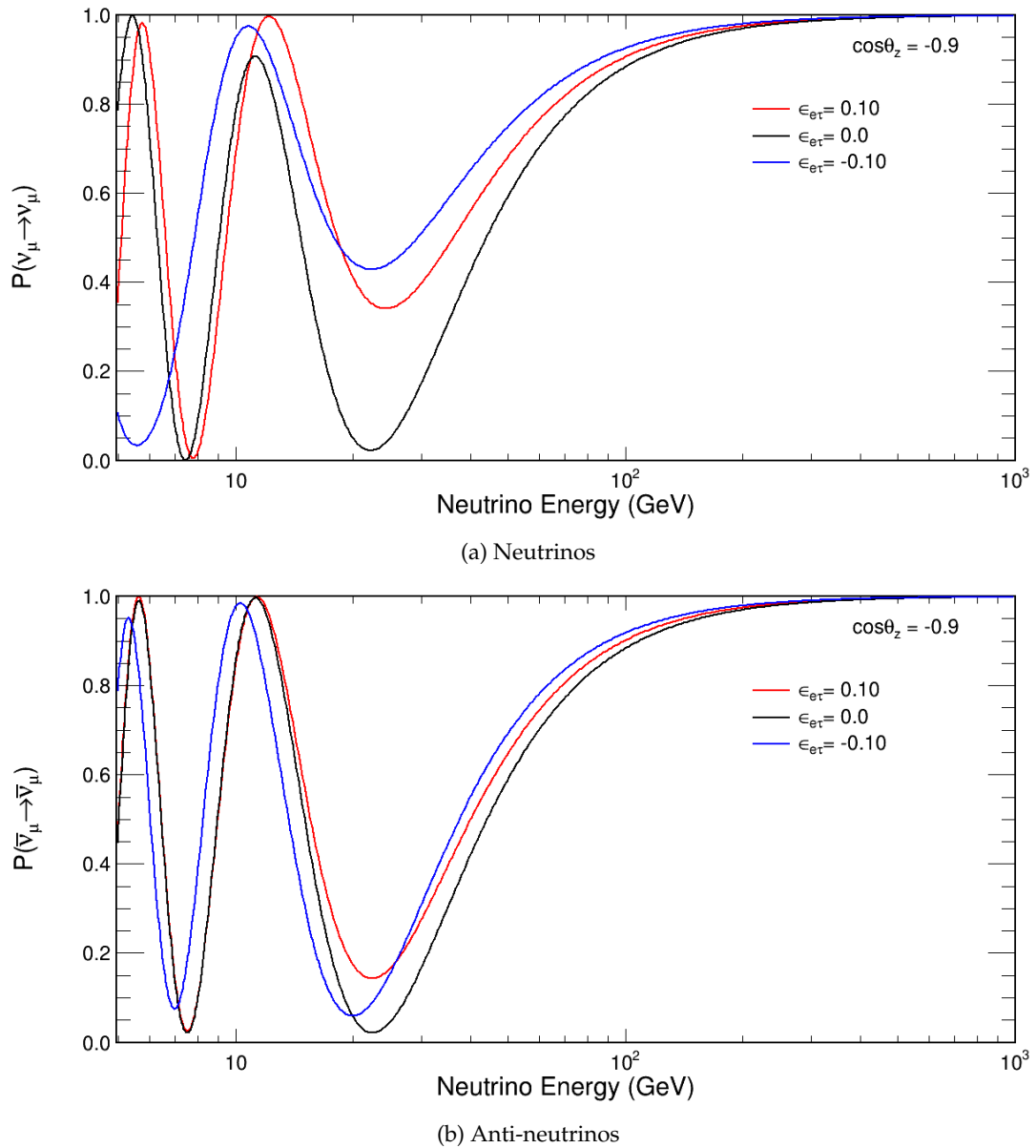
Figure 1.13: $P(\nu_\mu \rightarrow \nu_\mu)$ (a) and $P(\bar{\nu}_\mu \rightarrow \bar{\nu}_\mu)$ (b) survival probabilities for $\epsilon_{e\tau} = \pm 0.1$. The calculations are done with OscProb using the full 3-flavour oscillation scenario. Normal ordering is assumed.

Flavour violating $\epsilon_{e\mu}$

(a) $\Delta P_{\mu\mu}^{\nu+0.5\bar{\nu}}$ NO, $\epsilon_{e\mu} = -0.02$

(b) $\Delta P_{\mu\mu}^{\nu+0.5\bar{\nu}}$ NO, $\epsilon_{e\mu} = 0.02$

(c) $\Delta P_{\mu\mu}^{\nu+0.5\bar{\nu}}$ NO, $\epsilon_{e\mu} = -0.06$

(d) $\Delta P_{\mu\mu}^{\nu+0.5\bar{\nu}}$ NO, $\epsilon_{e\mu} = 0.06$

(e) $\Delta P_{\mu\mu}^{\nu+0.5\bar{\nu}}$ NO, $\epsilon_{e\mu} = -0.1$

(f) $\Delta P_{\mu\mu}^{\nu+0.5\bar{\nu}}$ NO, $\epsilon_{e\mu} = 0.1$
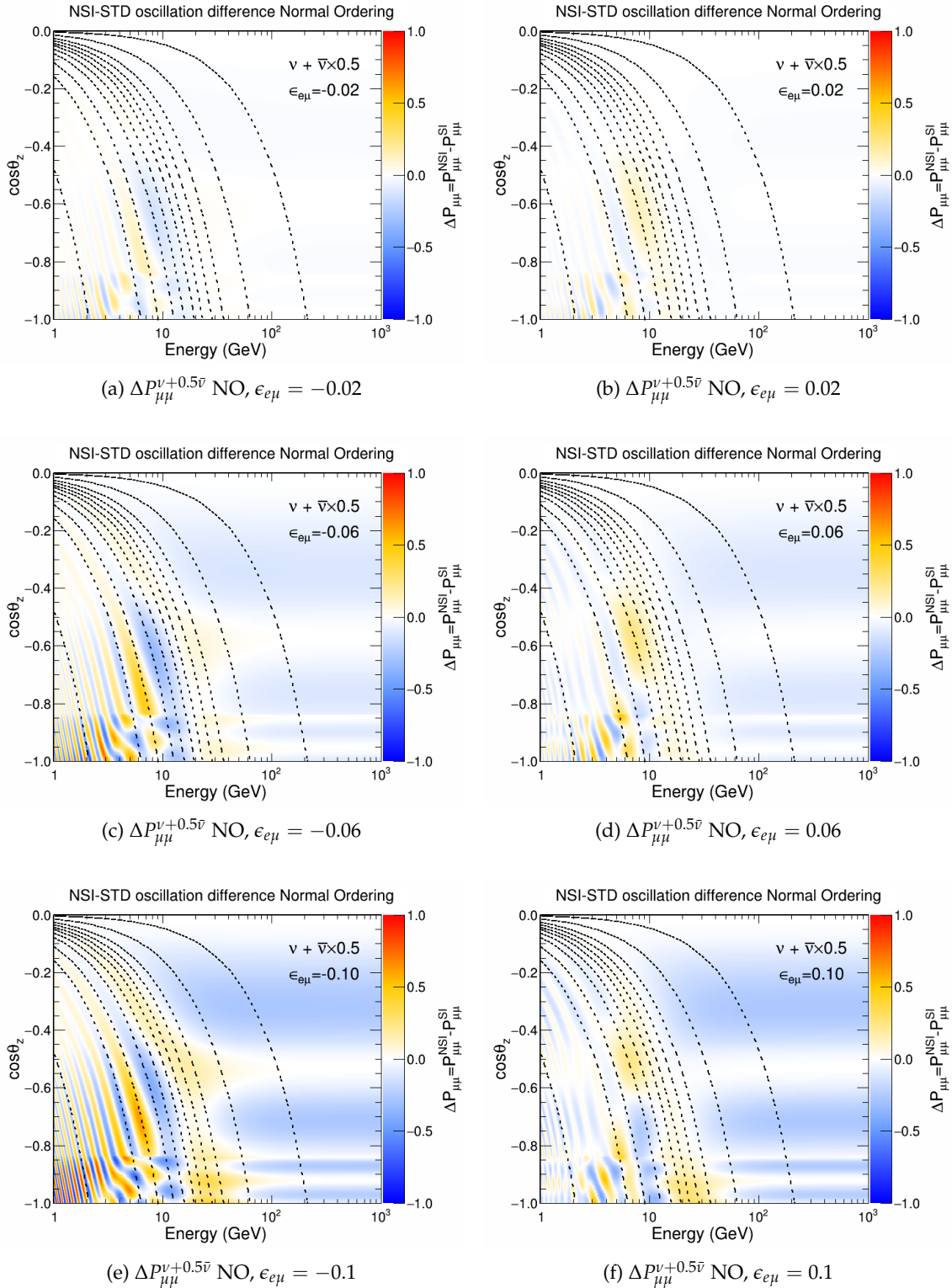
Figure 1.14: Difference in the survival probability for the weighted neutrino-anti-neutrino flux $\Delta P_{\mu\mu}^{\nu+0.5\bar{\nu}}$ between oscillations with NSI and standard oscillations for the parameter values $\epsilon_{e\mu} \in \{\pm 0.02, \pm 0.06, \pm 0.1\}$.

Flavour non-universal $\epsilon_{\tau\tau} - \epsilon_{\mu\mu}$

(a) $\Delta P_{\mu\mu}^{\nu+0.5\bar{\nu}}$ NO, $\epsilon_{\tau\tau} - \epsilon_{\mu\mu} = -0.01$

(b) $\Delta P_{\mu\mu}^{\nu+0.5\bar{\nu}}$ NO, $\epsilon_{\tau\tau} - \epsilon_{\mu\mu} = 0.01$

(c) $\Delta P_{\mu\mu}^{\nu+0.5\bar{\nu}}$ NO, $\epsilon_{\tau\tau} - \epsilon_{\mu\mu} = -0.02$

(d) $\Delta P_{\mu\mu}^{\nu+0.5\bar{\nu}}$ NO, $\epsilon_{\tau\tau} - \epsilon_{\mu\mu} = 0.02$

(e) $\Delta P_{\mu\mu}^{\nu+0.5\bar{\nu}}$ NO, $\epsilon_{\tau\tau} - \epsilon_{\mu\mu} = -0.04$

(f) $\Delta P_{\mu\mu}^{\nu+0.5\bar{\nu}}$ NO, $\epsilon_{\tau\tau} - \epsilon_{\mu\mu} = 0.04$
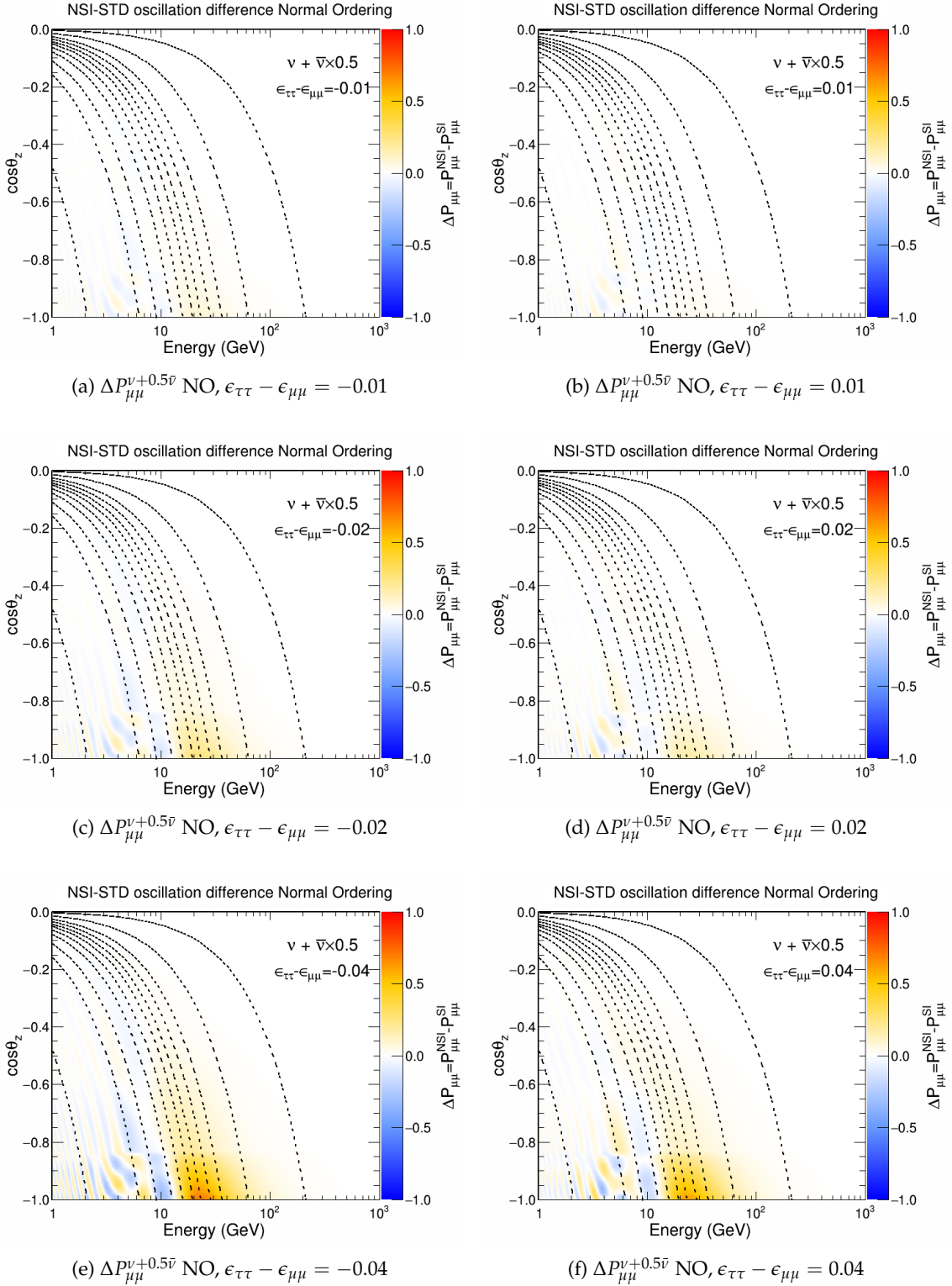
Figure 1.15: Difference in the survival probability for the weighted neutrino-anti-neutrino flux $\Delta P_{\mu\mu}^{\nu+0.5\bar{\nu}}$ between oscillations with NSI and standard oscillations for the parameter values $\epsilon_{\tau\tau} - \epsilon_{\mu\mu} \in \{\pm 0.01, \pm 0.02, \pm 0.04\}$.

1.3.1   Impact of a non-zero complex phase

Figure 1.16 shows the oscillograms for complex values of $\epsilon_{\mu\tau}$ with the modulus fixed to $|\epsilon_{\mu\tau}| = 0.02$ and the phase set to $\delta_{\mu\tau} = \{0, \pi\}$ which correspond to the purely real scenarios with $\epsilon_{\mu\tau} = \{0.02, -0.02\}$ of plots (f) and (e) in Fig. 1.11. In Fig. 1.17, the complex phase is set to $\delta_{\mu\tau} = \{\pi/2, 3\pi/2\}$ so that $\epsilon_{\mu\tau}$ becomes purely imaginary. In compliance with the Eq. 1.68 in Section 1.2.4.3 the impact of NSI and the presence of matter is strongly suppressed for the energies where the matter phase is comparable to the vacuum phase. For high energies, where ϵ^2 terms come into play, the impact of the complex phase is not visible.

(a) $\Delta P_{\mu\mu}^{\nu+0.5\bar{\nu}}$ NO, $|\epsilon_{\mu\tau}| = 0.02$, $\delta_{\mu\tau} = 0$.

(b) $\Delta P_{\mu\mu}^{\nu+0.5\bar{\nu}}$ IO, $|\epsilon_{\mu\tau}| = 0.02$, $\delta_{\mu\tau} = 0$

(c) $\Delta P_{\mu\mu}^{\nu+0.5\bar{\nu}}$ NO, $|\epsilon_{\mu\tau}| = 0.02$, $\delta_{\mu\tau} = \pi$

(d) $\Delta P_{\mu\mu}^{\nu+0.5\bar{\nu}}$ IO, $|\epsilon_{\mu\tau}| = 0.02$, $\delta_{\mu\tau} = \pi$
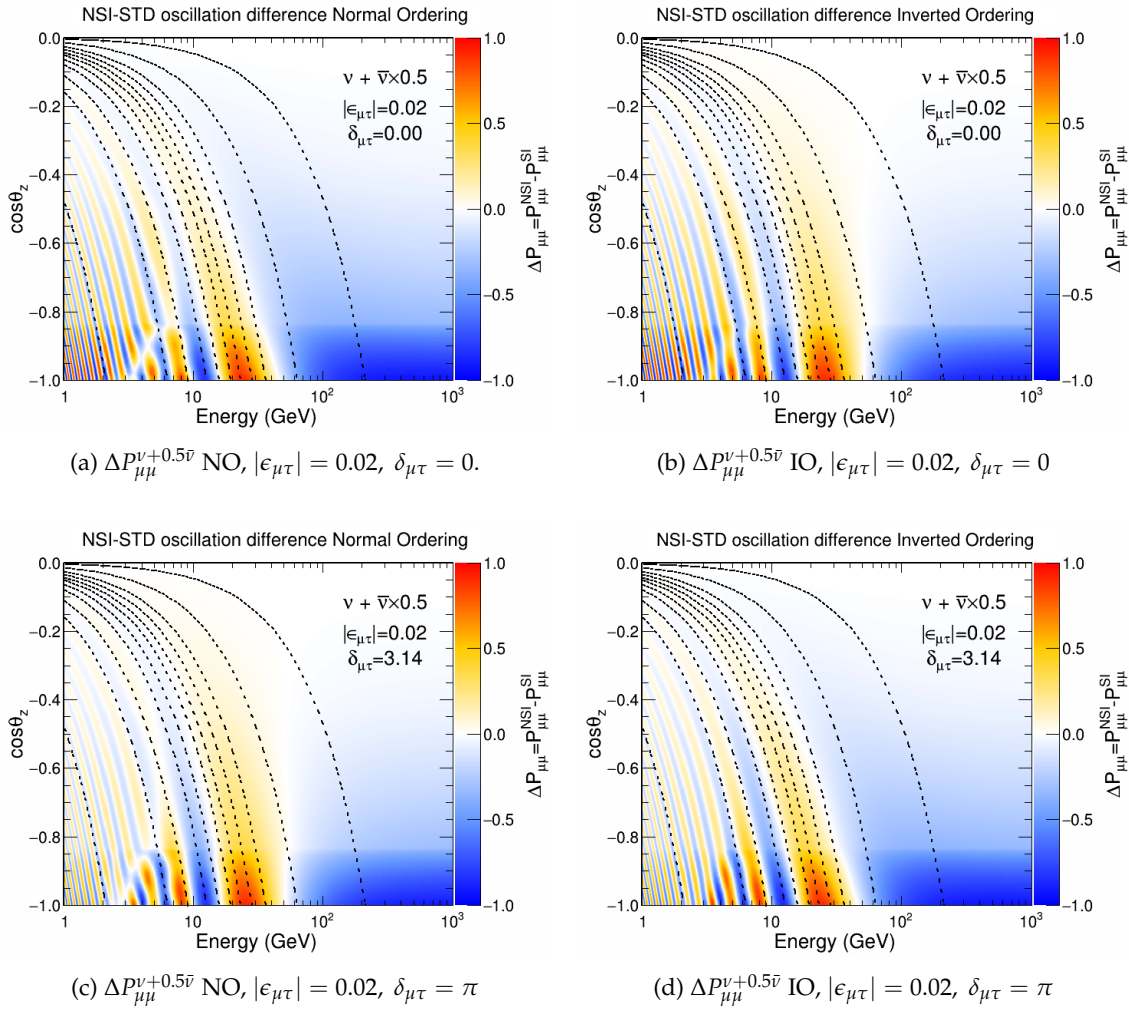
Figure 1.16: Difference in the survival probability for the weighted neutrino-anti-neutrino flux $\Delta P_{\mu\mu}^{\nu+0.5\bar{\nu}}$ between oscillations with NSI and standard oscillations for NSI $|\epsilon_{\mu\tau}| = 0.02$, $\delta_{\mu\tau} = 0$ (top) and $\delta_{\mu\tau} = \pi$ (bottom) for normal (left) and inverted (right) mass orderings. The values correspond to real $\epsilon_{\mu\tau}$.

(a) $\Delta P_{\mu\mu}^{\nu+0.5\bar{\nu}}$ NO, $|\epsilon_{\mu\tau}| = 0.02$, $\delta_{\mu\tau} = \pi/2$

(b) $\Delta P_{\mu\mu}^{\nu+0.5\bar{\nu}}$ IO, $|\epsilon_{\mu\tau}| = 0.02$, $\delta_{\mu\tau} = \pi/2$

(c) $\Delta P_{\mu\mu}^{\nu+0.5\bar{\nu}}$ NO, $|\epsilon_{\mu\tau}| = 0.02$, $\delta_{e\tau} = 3\pi/2$

(d) $\Delta P_{\mu\mu}^{\nu+0.5\bar{\nu}}$ IO, $|\epsilon_{\mu\tau}| = 0.02$, $\delta_{\mu\tau} = 3\pi/2$
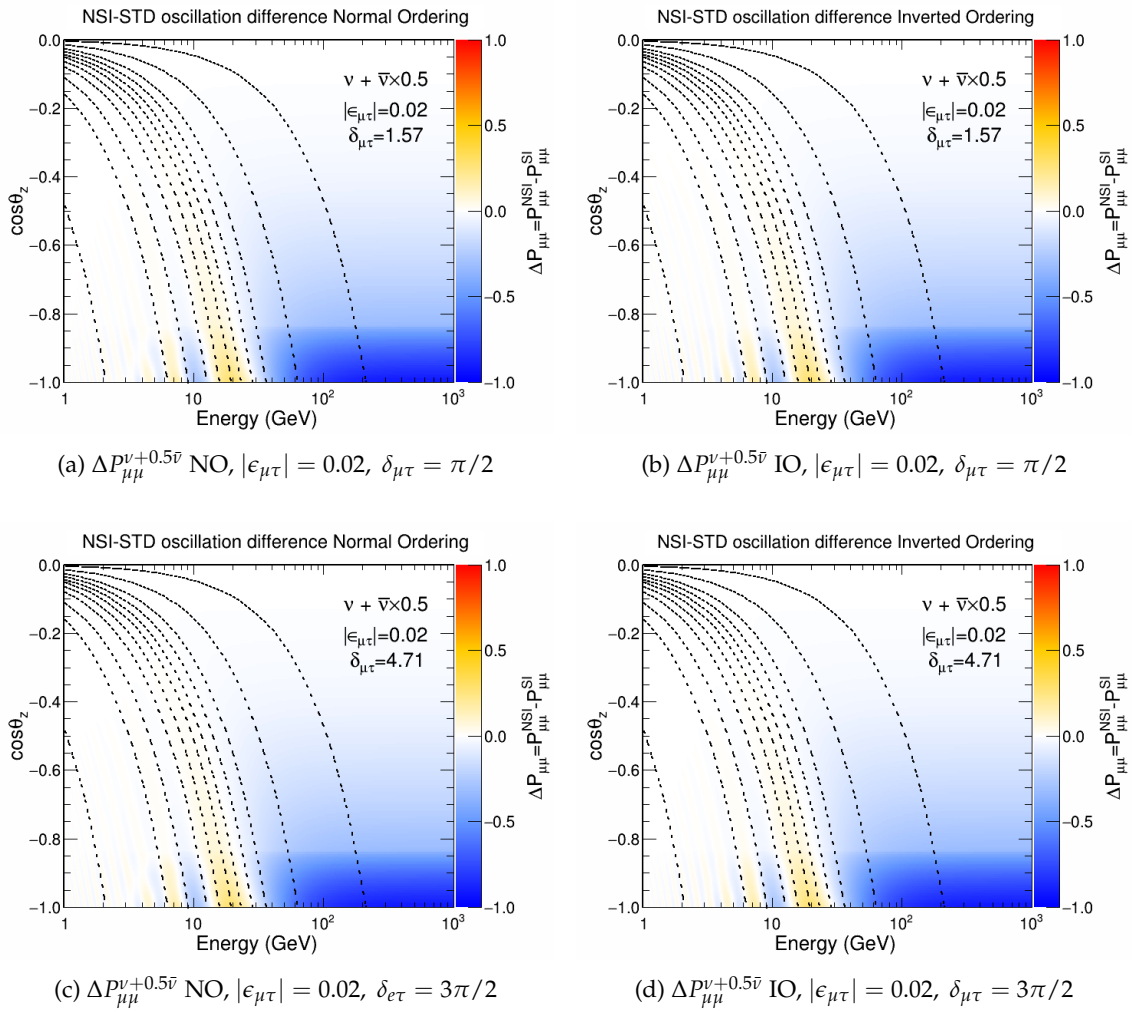
Figure 1.17: Difference in the survival probability for the weighted neutrino-anti-neutrino flux, $\Delta P_{\mu\mu}^{\nu+0.5\bar{\nu}}$, between oscillations with NSI and standard oscillations for NSI $|\epsilon_{\mu\tau}| = 0.02$, $\delta_{\mu\tau} = \pi/2$ (top) and $\delta_{\mu\tau} = \pi/2$ (bottom) for normal (left) and inverted (right) mass orderings. The values correspond to purely imaginary $\epsilon_{\mu\tau}$.

The cases of $\epsilon_{e\tau}$ and $\epsilon_{e\mu}$ are different, because the impact of the corresponding complex phases depends on the shift introduced by the value of the standard δ_{CP}. Therefore the following oscillograms are provided with δ_{CP} fixed at 0. The oscillation probabilities should be affected the most for the values $\delta_{CP} + \delta_{e\mu} = \pi/2 \vee 3\pi/2$, but the difference is not prominent enough to be distinguishable in this particular oscillation channel. Figs. 1.18 and 1.19 show the oscillograms for complex $\epsilon_{e\tau}$ and Figs. 1.20 and 1.21 show the oscillograms for $\epsilon_{e\mu}$

(a) $\Delta P_{\mu\mu}^{\nu+0.5\bar{\nu}}$ NO, $|\epsilon_{e\tau}| = 0.15$, $\delta_{e\tau} = 0$

(b) $\Delta P_{\mu\mu}^{\nu+0.5\bar{\nu}}$ IO, $|\epsilon_{e\tau}| = 0.15$, $\delta_{e\tau} = \pi/2$

(c) $\Delta P_{\mu\mu}^{\nu+0.5\bar{\nu}}$ NO, $|\epsilon_{e\tau}| = 0.15$, $\delta_{e\tau} = \pi$

(d) $\Delta P_{\mu\mu}^{\nu+0.5\bar{\nu}}$ IO, $|\epsilon_{e\tau}| = 0.15$, $\delta_{e\tau} = 3\pi/2$
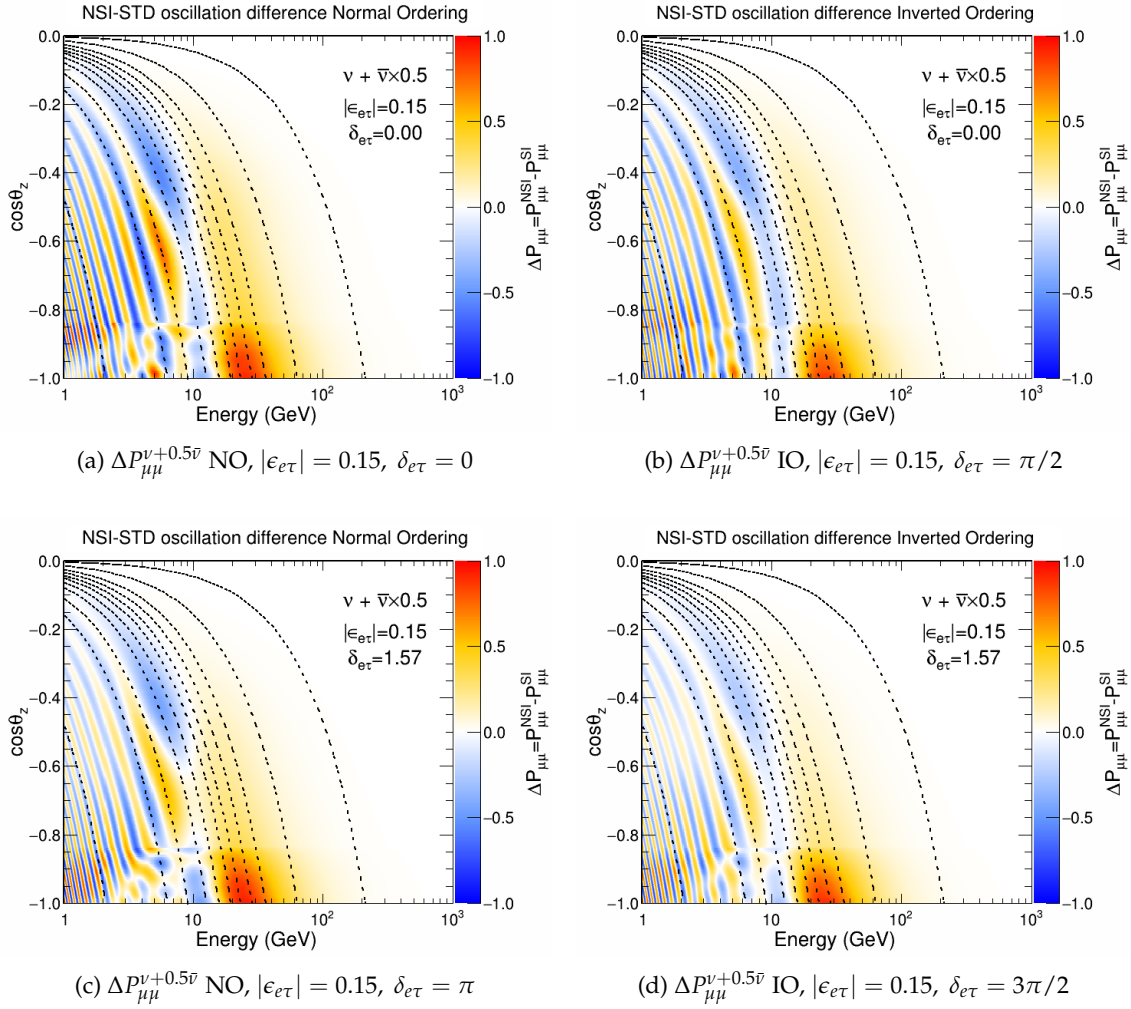
Figure 1.18: Difference in the survival probability for the weighted neutrino-anti-neutrino flux, $\Delta P_{\mu\mu}^{\nu+0.5\bar{\nu}}$, between oscillations with NSI and standard oscillations for $|\epsilon_{e\tau}| = 0.015$, $\delta_{e\tau} = 0$ (top) and $\delta_{e\tau} = \pi$ (bottom) for normal (left) and inverted (right) mass orderings. The values correspond to purely real $\epsilon_{e\tau}$.

(a) $\Delta P_{\mu\mu}^{\nu+0.5\bar{\nu}}$ NO, $|\epsilon_{e\tau}| = 0.15$, $\delta_{e\tau} = \pi/2$

(b) $\Delta P_{\mu\mu}^{\nu+0.5\bar{\nu}}$ IO, $|\epsilon_{e\tau}| = 0.15$, $\delta_{e\tau} = \pi/2$

(c) $\Delta P_{\mu\mu}^{\nu+0.5\bar{\nu}}$ NO, $|\epsilon_{e\tau}| = 0.15$, $\delta_{e\tau} = 3\pi/2$

(d) $\Delta P_{\mu\mu}^{\nu+0.5\bar{\nu}}$ IO, $|\epsilon_{e\tau}| = 0.15$, $\delta_{e\tau} = 3\pi/2$
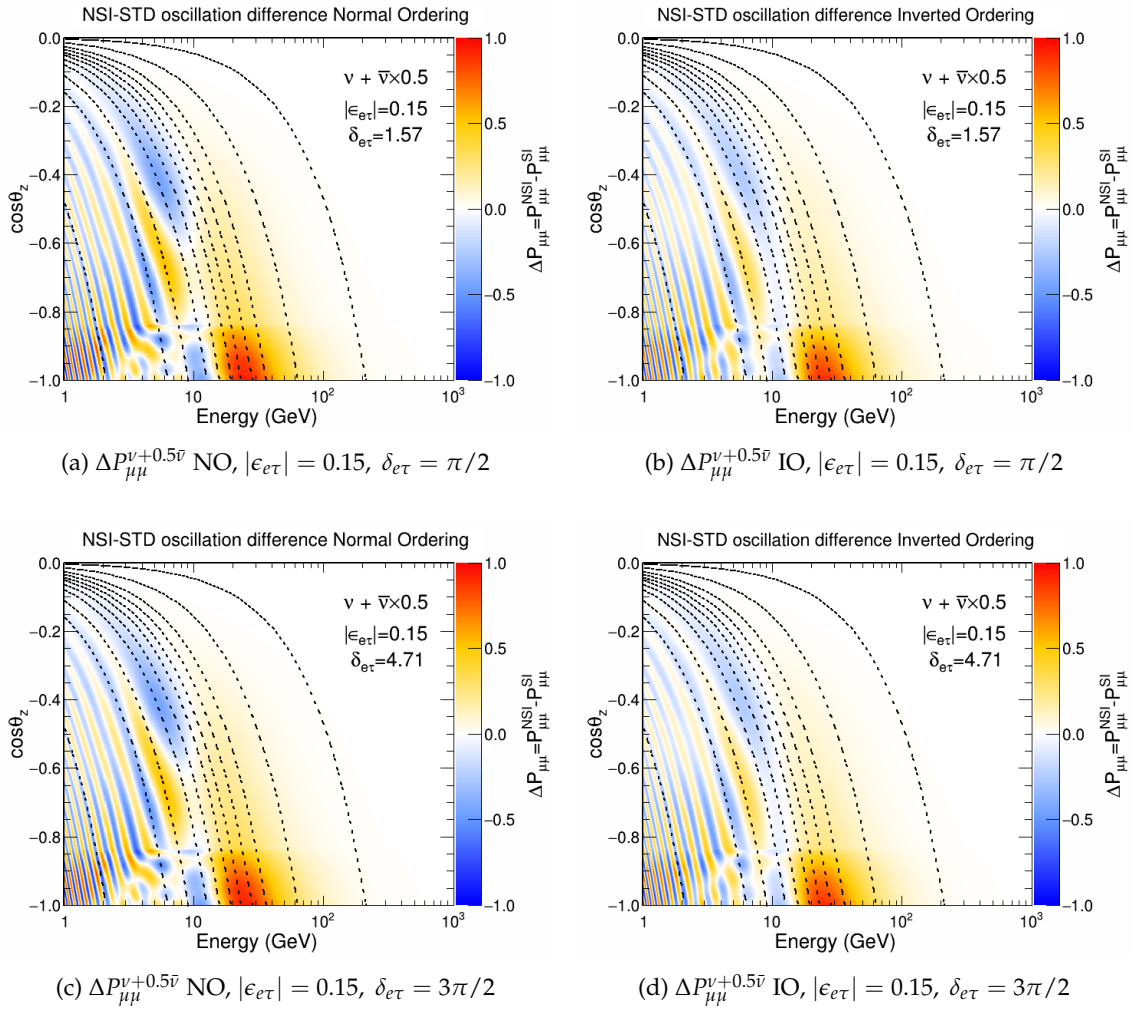
Figure 1.19: Difference in the survival probability for the weighted neutrino-anti-neutrino flux, $\Delta P_{\mu\mu}^{\nu+0.5\bar{\nu}}$, between oscillations with NSI and standard oscillations for $|\epsilon_{e\tau}| = 0.015$, $\delta_{e\tau} = \pi/2$ (top) and $\delta_{e\tau} = 3\pi/2$ (bottom) for normal (left) and inverted (right) mass orderings. The values correspond to purely imaginary $\epsilon_{e\tau}$.

(a) $\Delta P_{\mu\mu}^{\nu+0.5\bar{\nu}}$ NO, $|\epsilon_{e\mu}| = 0.06$, $\delta_{e\tau} = 0$

(b) $\Delta P_{\mu\mu}^{\nu+0.5\bar{\nu}}$ IO, $|\epsilon_{e\mu}| = 0.06$, $\delta_{e\tau} = 0$

(c) $\Delta P_{\mu\mu}^{\nu+0.5\bar{\nu}}$ NO, $|\epsilon_{e\mu}| = 0.06$, $\delta_{e\tau} = \pi$

(d) $\Delta P_{\mu\mu}^{\nu+0.5\bar{\nu}}$ IO, $|\epsilon_{e\mu}| = 0.06$, $\delta_{e\tau} = \pi$
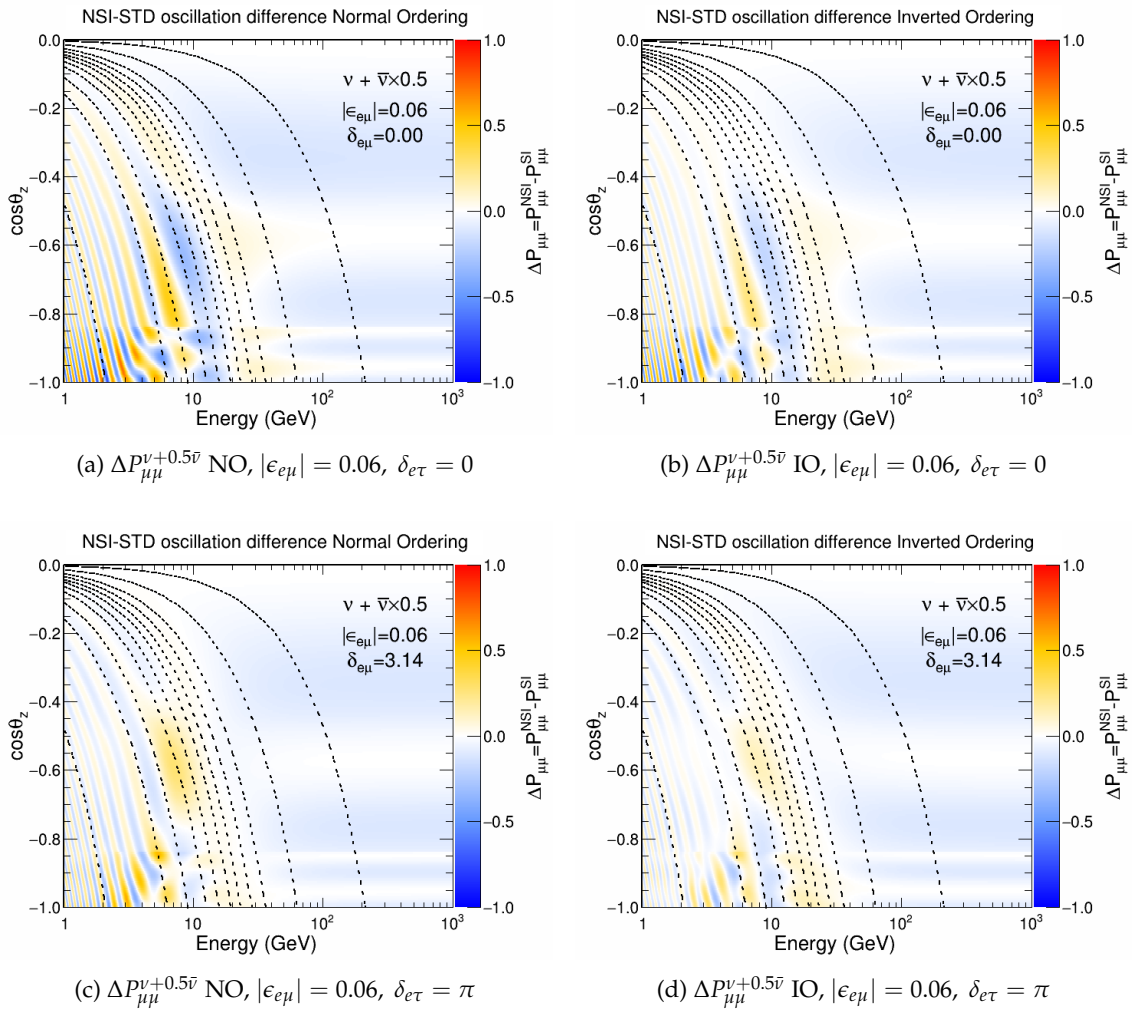
Figure 1.20: Difference in the survival probability for the weighted neutrino-anti-neutrino flux, $\Delta P_{\mu\mu}^{\nu+0.5\bar{\nu}}$, between oscillations with NSI and standard oscillations for $|\epsilon_{e\mu}| = 0.06$, $\delta_{e\tau} = 0$ (top) and $\delta_{e\tau} = \pi$ (bottom) for normal (left) and inverted (right) mass orderings. The values correspond to purely real $\epsilon_{e\mu}$.

(a) $\Delta P_{\mu\mu}^{\nu+0.5\bar{\nu}}$ NO, $|\epsilon_{e\mu}| = 0.06$, $\delta_{e\tau} = \pi/2$

(b) $\Delta P_{\mu\mu}^{\nu+0.5\bar{\nu}}$ IO, $|\epsilon_{e\mu}| = 0.06$, $\delta_{e\tau} = \pi/2$

(c) $\Delta P_{\mu\mu}^{\nu+0.5\bar{\nu}}$ NO, $|\epsilon_{e\mu}| = 0.06$, $\delta_{e\tau} = 3\pi/2$

(d) $\Delta P_{\mu\mu}^{\nu+0.5\bar{\nu}}$ IO, $|\epsilon_{e\mu}| = 0.06$, $\delta_{e\tau} = 3\pi/2$
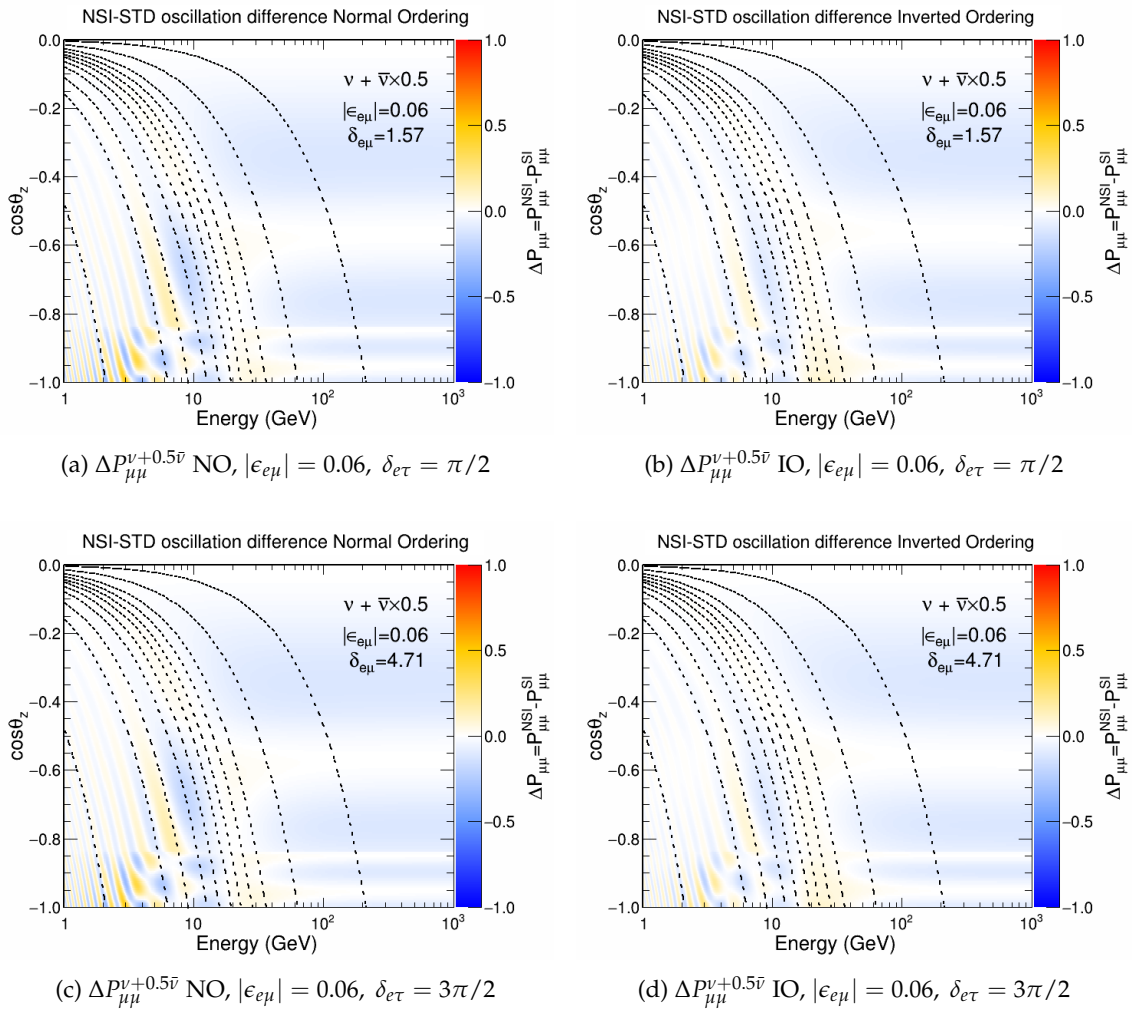
Figure 1.21: Difference in the survival probability for the weighted neutrino-anti-neutrino flux, $\Delta P_{\mu\mu}^{\nu+0.5\bar{\nu}}$, between oscillations with NSI and standard oscillations for $|\epsilon_{e\mu}| = 0.06$, $\delta_{e\mu} = \pi/2$ (top) and $\delta_{e\mu} = 3\pi/2$ (bottom) for normal (left) and inverted (right) mass orderings. The values correspond to purely imaginary $\epsilon_{e\mu}$.

2 The KM3NeT/ORCA neutrino telescope

Contents

This chapter describes the KM3NeT/ORCA detector (further referred to as ORCA): its technology, design, construction components, the neutrino detection mechanism and the features and limitations of its early stage configuration called ORCA6. In the final sections, the data taking procedure is introduced. The atmospheric neutrino production mechanism together with the relevant distributions are presented in Section 2.3.1.

2.1 The KM3NeT project

KM3NeT (Cubic Kilometre Neutrino Telescope) is a next generation neutrino telescope currently under construction in the Mediterranean Sea [83]. It consists of two separate detectors: ARCA (Astroparticle Research with Cosmics in the Abyss) and ORCA (Oscillation Research with Cosmics in the Abyss). The high energy KM3NeT branch with the ARCA detector is focusing on neutrino astronomy and astrophysical neutrino source detection. The ARCA site is located about 100 km from the coast of Sicily at a depth of about 3500 m. ORCA is the low energy branch of KM3NeT, aimed mainly at atmospheric neutrino studies. The ORCA detector is located at a depth of 2450 m about

40 km south from the French city of Toulon. The main differences between ARCA and ORCA sites are their size and density, which translates into different effective volumes and energy thresholds — $\sim 3\,\text{GeV}$ for ORCA and $\sim 1\,\text{TeV}$ for ARCA. These differences in design are driven by the target neutrino fluxes — astrophysical neutrinos are much less abundant and therefore they require a much bigger detector volume to increase the interaction rate. At the same time, their energies are expected to reach far higher than the spectrum of atmospheric neutrinos and only above a certain threshold these two fluxes can be properly distinguished. As of July 2022, 13 out of the final 115 detection units of ORCA and 19 detection units of ARCA have been deployed. Upon completion, KM3NeT will become one of the flagship European research projects in neutrino physics. At the moment it associates more than fifty research institutions from five continents.

This dissertation is exclusively based on the atmospheric neutrino measurements with the ORCA detector and therefore the following part of this chapter does not consider any further the KM3NeT/ARCA site. In any case, the technology used for both sites as well as the physics principles behind the neutrino detection mechanism are exactly the same. Construction-wise the detectors differ only by their size and the spacing of their detector components.

2.2   The ORCA detector

ORCA is designed to focus on the detection of atmospheric neutrinos with energies between 3 and 100 GeV, where the oscillation effects are the most prominent (see Chapter 1). The optimisation for this energy range is reflected in the spacing of the detector components, which leads to a much denser instrumentation with respect to the ARCA detector and therefore a much lower energy threshold. The main goal of the ORCA project is to determine the neutrino mass ordering [84]. Nevertheless, the detector is also capable of probing a wide range of beyond Standard Model physics. The first result on the search for non-standard neutrino interactions based on the ORCA data is the subject of this work. The location of ORCA site is depicted in Fig. 2.1 The technical details of the infrastructure and the sea-floor network necessary for the ORCA detector operation and data transfer to the on-shore processing centre are described in [85].

2.2.1   Detector layout

Once completed, ORCA will comprise 115 Detection Units (DUs) , whose bases are placed roughly on a circle creating a cylindrical structure referred to as a *Building Block*. This structure defines the detector active volume, which corresponds to the volume of seawater being effectively monitored by very sensitive light detectors (in KM3NeT, neutrino detection in done thanks to Cherenkov effect as it will be described in detail in Section 2.3.2). Figure 2.2 shows an artistic impression of the ORCA building block layout.

A DU is a string-like structure anchored at the sea bottom with 18 Digital Optical Modules (DOMs) attached along its entire length with a constant vertical interval. A detailed description of all the detector components and their functions will be given in Section 2.2.2.

2.2.1.1   ORCA6

ORCA6, also referred to as ORCA-Phase1, is the first stage of ORCA, comprising six out of the final 115 DUs. The layout of ORCA6 is presented in Fig. 2.3. This early configuration has been taking data from January 2020 until November 2021
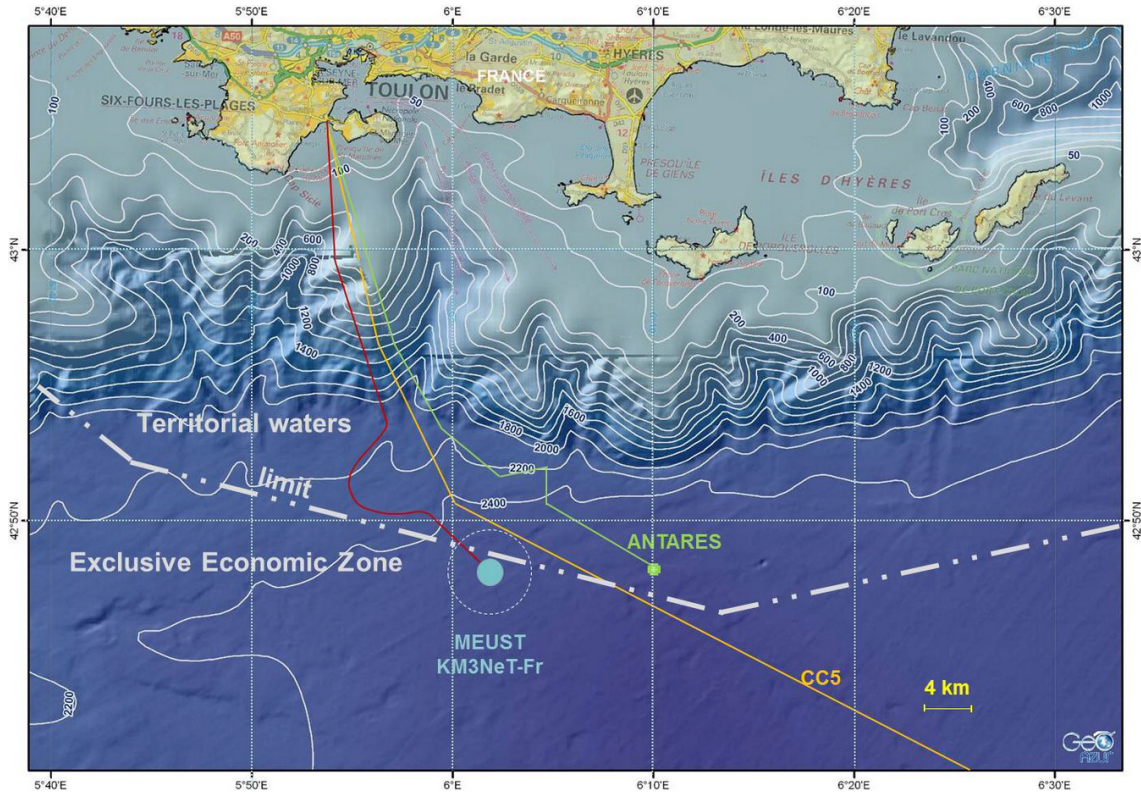
Figure 2.1: Map of the Mediterranean Sea with the location of the KM3NeT/ORCA site indicated as "MEUST KM3NeT-Fr". The acronym MEUST stands for the Mediterranean Eurocentre for Underwater Sciences and Technologies [85]. Taken from ref. [83].
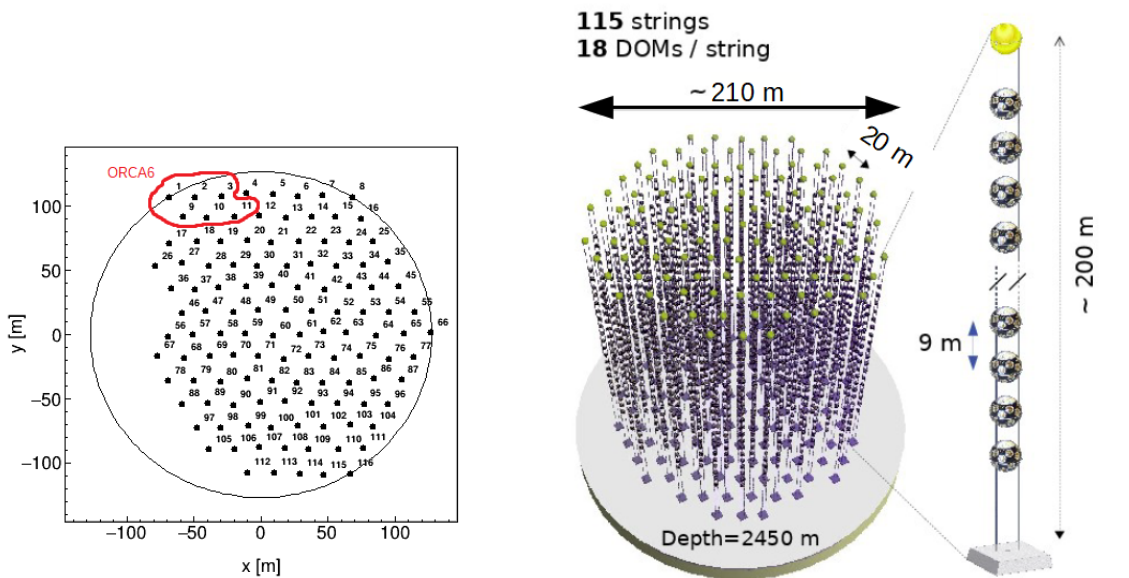
(a) The full ORCA detector footprint. The ORCA6 configuration is indicated by the red contour.

(b) The ORCA detector dimensions. On the right a detection unit is portrayed. On the left, the footprint, which is just an artistic impression not corresponding to the actual relative positions of the strings.

Figure 2.2: The ORCA detector layout.

when 4 additional strings were deployed and ORCA6 turned into ORCA10. Currently ORCA operates with 13 DUs installed at the sea bottom. The first neutrino oscillation

(a) The ORCA6 detector footprint with the smallest enclosing circle roughly corresponding to the detector cylinder base.

(b) ORCA6 in the context of the full ORCA detector planned layout. The red dots indicate the positions of the tripods, which house acoustic beacons for position calibration (more details in Section 2.7).
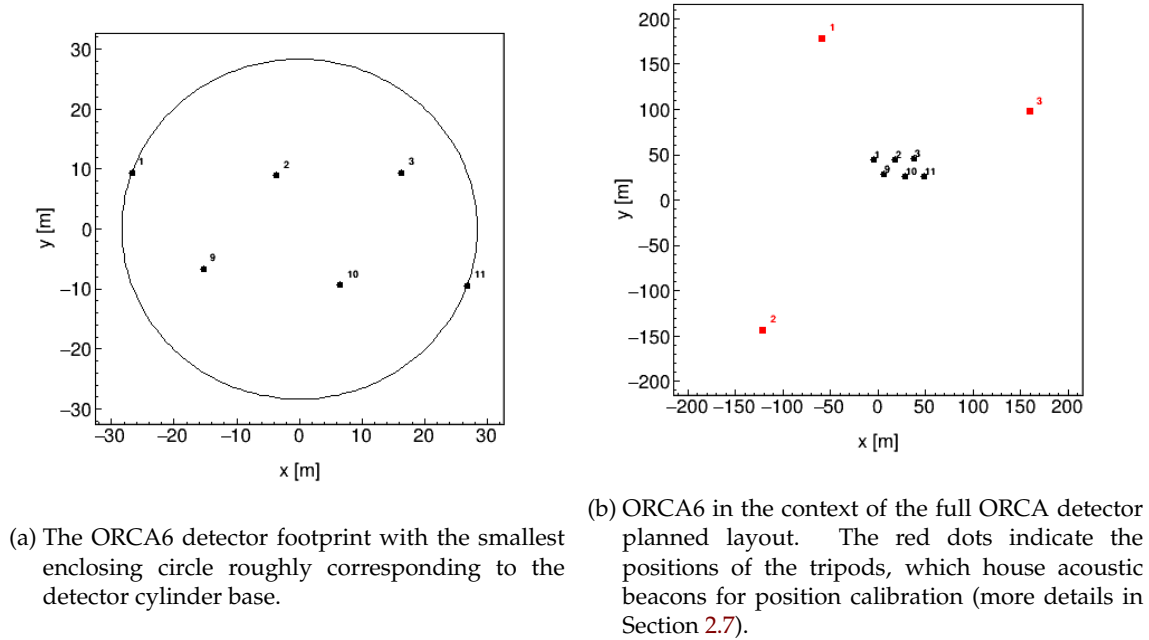
Figure 2.3: ORCA6 footprint

measurement was already performed using the data from ORCA6 [86].

2.2.2   Detector technology

KM3NeT is the successor of the ANTARES neutrino telescope [87]. Taking advantage of the experience gained by 15 years of operation of ANTARES, its predecessor, KM3NeT incorporates a large variety of technological improvements that make it much more performing and cost-effective. The scientific goals of the KM3NeT detectors require stable operation and high resolution neutrino detection for a period of at least 15 years. The intrinsic characteristics of neutrinos such as the very low interaction cross section requires, depending on the flux, from megatonne (ORCA) to gigatonne (ARCA) detector volumes to meet the planned scientific goals.

2.2.2.1   Detection Unit

As it was mentioned in Section 2.2.1, a Detection Unit (DU)[88] is a string-like structure providing support for the actual neutrino-induced light detection devices — Digital Optical Modules (DOMs). The DU has an anchor at the bottom and a buoy at the top to apply the stretching force ensuring stability and preventing horizontal floating of the DOMs. In reality, due to water currents a perfectly vertical orientation is rarely achieved and the deviations can reach up to a few degrees. A set of acoustic and optical position monitoring devices provides real-time information about the actual shape of each DU, which can later be accounted for in the high-level data processing. A dedicated DU deploying device called Launcher of Optical Modules (LOM) was developed to increase the precision and to reduce the cost of the DU deployment process, giving the possibility of deploying several lines in a single sea operations as lines are compacted [89].

2.2.2.2 Digital Optical Module

The core detection component of the KM3NeT telescopes is the Digital Optical Module (DOM) — a pressure-resistant glass orb filled with photosensor detectors called photomultipliers (PMTs), calibration devices and the specialised electronics for the neutrino interaction-induced light detection. The internal components of a DOM are presented in Fig. 2.4. The piezo transducer receives acoustic signals from the sea-bottom emitter to provide information about the current DOM position. The LED nanobeacon [90] is used for the inter-DOM time calibrations. The air inside a DOM provides an adequate buoyancy to stabilise the DU structure. Pressure, temperature and humidity sensors help monitoring the conditions inside the DOM. In order to detect

1. Section of a bottom support structure.
2. Section of a top support structure.
3. Glass hemisphere (bottom).
4. Bottom support structure with PMTs and light collection rings installed.
5. Tray for routing of optical fibres.
6. Cooling and support mechanics (shell with rod mounted).
7. Power board.
8. Central Logic Board.
9. (Three) PMTs with base attached and light collection rings.
10. Pressure gauge.
11. Signal collection boards (2).
12. Nanobeacon (led flasher) on driver board.
13. Penetrator flange (left) and penetrator with temporary fibre/cable routing plate (right).
14. Piezo hydrophone.
15. Laser transceiver.

Figure 2.4: Selection of Digital Optical Module components. Adopted from [90].

light in the dark waters of the abyss, every DOM is equipped with 31 Hamamatsu R12199-02 [91] photomultipliers optimised for Cherenkov light detection and providing almost the full 4π solid angle coverage. Figure 2.5 shows an assembled DOM and a zoomed instance of a single PMT. The bottom hemisphere has more PMTs than the top one because the detector focuses on the up-going particle detection.

The multi-PMT unit is a unique feature of the KM3NeT technology. So far, the other already-operating neutrino telescopes, such as ANTARES [87] or IceCube [92], use a single PMT with a large diameter photocathode, which generally provide less precise information especially concerning the photon arrival direction. The other advantage of a photocathode area segmentation is a superior capability of background rejection based on the single-photon counting capability and coincidence logic. The multi-PMT design also reduces the impact of a single PMT failure on the detection efficiency and increases the potential lifetime of the project. The technical details regarding the DOM integration and testing procedures can be found in [90].

(a) Digital Optical Module; bottom view.

(b) Hamamatsu R12199-02 photomultiplier.
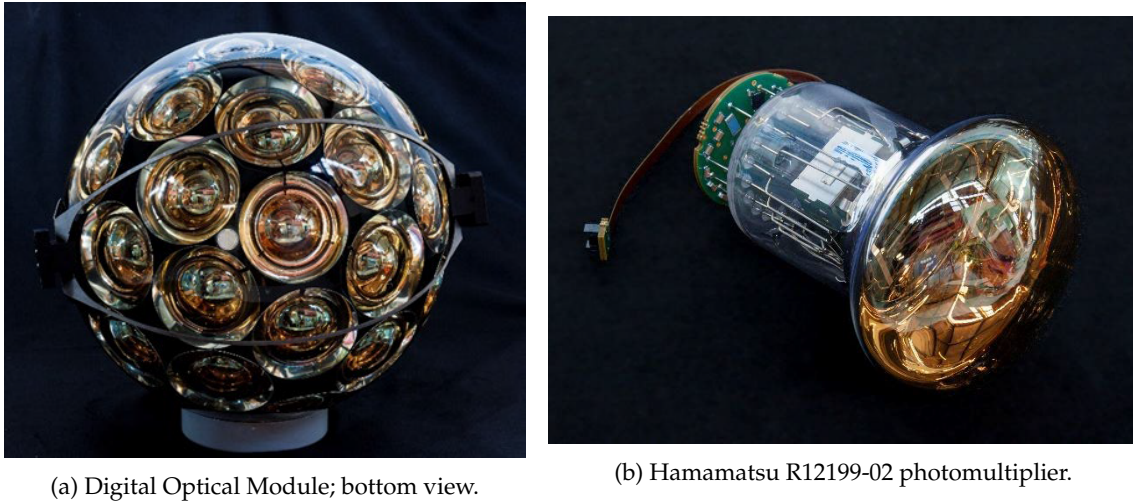
Figure 2.5: An assembled, ready to operate Digital Optical Module (left) and a close-up of a Hamamatsu R12199-02 photomultiplier (right).

2.2.2.3   The Photomultiplier Tube

A photomultiplier tube comprises the following elements:

1. a **photocathode** responsible for the generation (ejection) of free electrons released via the photoelectric effect by the incident photons,

2. a set of **dynodes** with increasing voltage, which generate an avalanche that amplifies the initial signal and

3. an **anode** that is the final electron avalanche target and closes the circuit allowing for a current pulse readout.

All the components are kept in vacuum to assure a clear path for the electrons. To operate, the whole process requires a high voltage (for the Hamamatsu R12199-02 model typically between 1000 V -1400 V to obtain the desired gain of $5 \cdot 10^6$), which stays within the linear gain regime. The electrons are released from the photocathode with a certain wavelength-dependent probability called Quantum Efficiency (QE). The number of Cherenkov photons per unit path released by a particle travelling in a dielectric medium is roughly proportional to the inverse of the photons wavelength $N_\gamma \propto 1/\lambda$. A measurement of the wavelength-dependent quantum efficiency of a Hamamatsu R12199-02 photomultiplier is shown in Fig. 2.6

2.3   Neutrino detection principle

As it was described in Chapter 1, neutrinos do not carry electric charge and therefore the detection happens indirectly. Their passage can only be observed through the light induced by the charged products of neutrino interactions. This light is generated via the Cherenkov radiation process. Before the detection can occur, neutrinos have to be created and reach the detector. The oscillation study with ORCA is using neutrinos produced in the Earth's atmosphere.
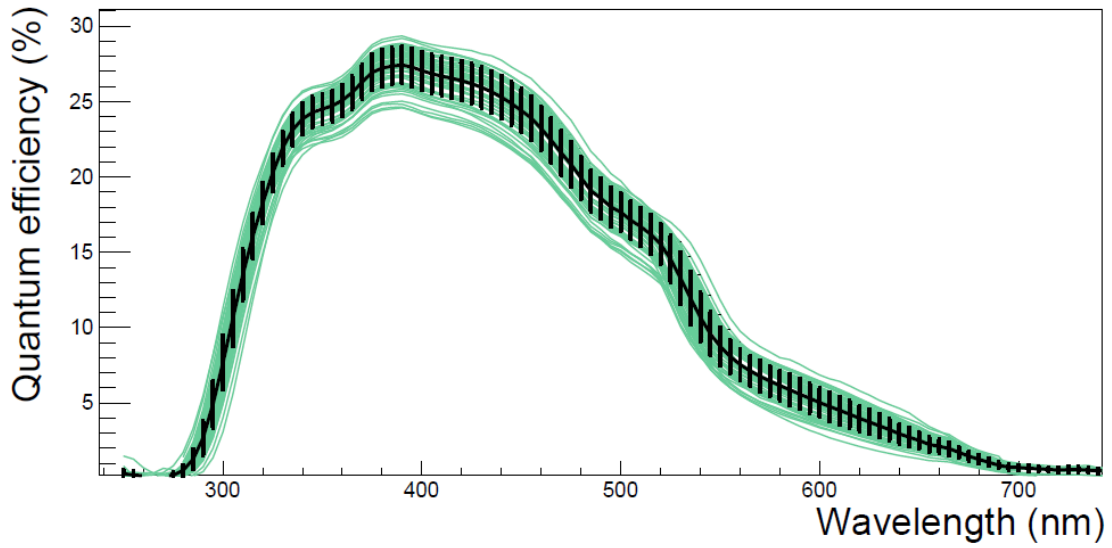
Figure 2.6: Hamamatsu R12199-02 quantum efficiency measured with 54 randomly chosen units from the KM3NeT detector construction batch. From [93].

2.3.1   The atmosphere as a neutrino source

Atmospheric neutrinos are produced in extensive air showers induced by the cosmic ray particles (mostly protons) interacting in the high layers of the atmosphere. Primary hadronic interactions lead to production of pions and kaons, which subsequently decay into muons and neutrinos. The most abundant atmospheric neutrino production chain starts with the dominating (99.9% branching ratio) decay channel of a pion:

$$\pi^\pm \to \mu^\pm + \nu_\mu(\bar{\nu}_\mu)$$
$$\mu^\pm \to e^\pm + \nu_e(\bar{\nu}_e) + \bar{\nu}_\mu(\nu_\mu). \tag{2.1}$$
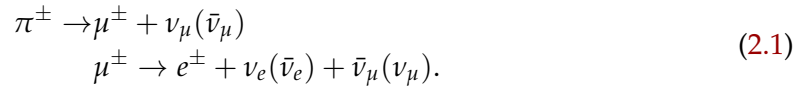
Therefore the expected neutrino flux ratios are $(\nu_\mu + \bar{\nu}_\mu)/(\nu_e + \bar{\nu}_e) \simeq 2$, $\nu_\mu/\bar{\nu}_\mu \simeq 1$ and $\nu_e/\bar{\nu}_e \simeq \mu^+/\mu^-$ [94]. With increasing energy, kaon decays

$$K^\pm \to \mu^\pm + \nu_\mu(\bar{\nu}_\mu) \to e^\pm + \nu_e(\bar{\nu}_e) + \bar{\nu}_\mu(\nu_\mu) + \nu_\mu(\bar{\nu}_\mu) \qquad \text{(BR: 63.6\%)}$$
$$\to \pi^0 + e^\pm + \nu_e(\bar{\nu}_e) \qquad \text{(BR: 5.1\%)}$$
$$\to \pi^0 + \mu^\pm + \nu_\mu(\bar{\nu}_\mu) \qquad \text{(BR: 3.4\%)}$$
$$\tag{2.2}$$
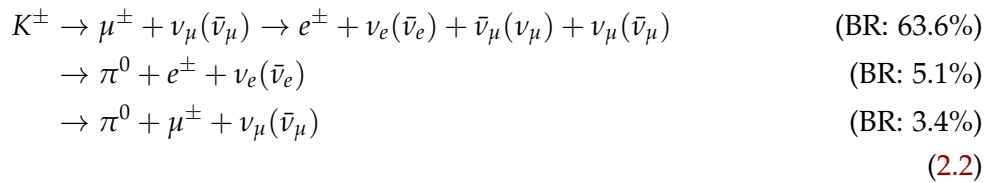
also start to play a significant role in the atmospheric neutrino production. The remaining $\approx 29\%$ of kaons decay into charged pions, so the decay chain goes back to Eq. 2.1. The energy-dependent fractional contributions from pions and kaons to the atmospheric neutrino and muon fluxes are shown in Fig. 2.7. Due to the pion and muon decay kinematics, all the neutrinos produced in the decay chain in Eq. 2.1 end up carrying roughly the same energy. With increasing energy, more and more muons reach the Earth before decaying, effectively leading to a higher ν_μ/ν_e ratio. Low energy charged primary cosmic rays can be deflected by the geomagnetic field and therefore the flux gets suppressed below the GeV energy range. Atmospheric neutrino flux rates calculated from different models are shown in Fig. 2.8. As can be seen, the results can differ up to about 10%. The differences among the models emerge from the choices of hadronic models and uncertainties in the measurements of the primary cosmic-ray
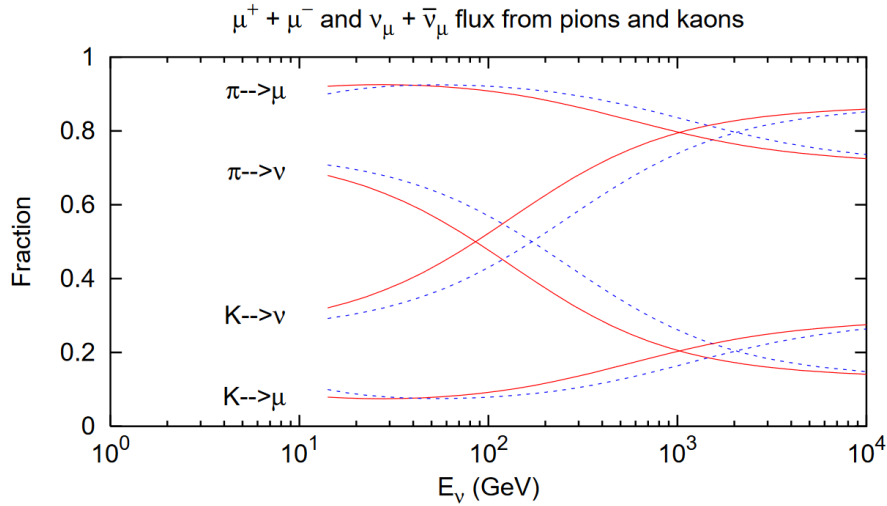
Figure 2.7: Fractions of kaon and pion decays contributing to the flux of muons and neutrinos. The solid lines correspond to the vertical incident direction, the dashed lines depict zenith angle $\theta_z \simeq 60°$. Plot was taken from [94]

spectrum. The zenith-angle dependent flux averaged over the azimuth angle is depicted in Fig 2.9. The uncertainties in the atmospheric neutrino flux ratios and in the flux normalisation contribute to the systematic uncertainty in the ORCA measurements. A detail explanation of these contributions is presented in Chapter 3.
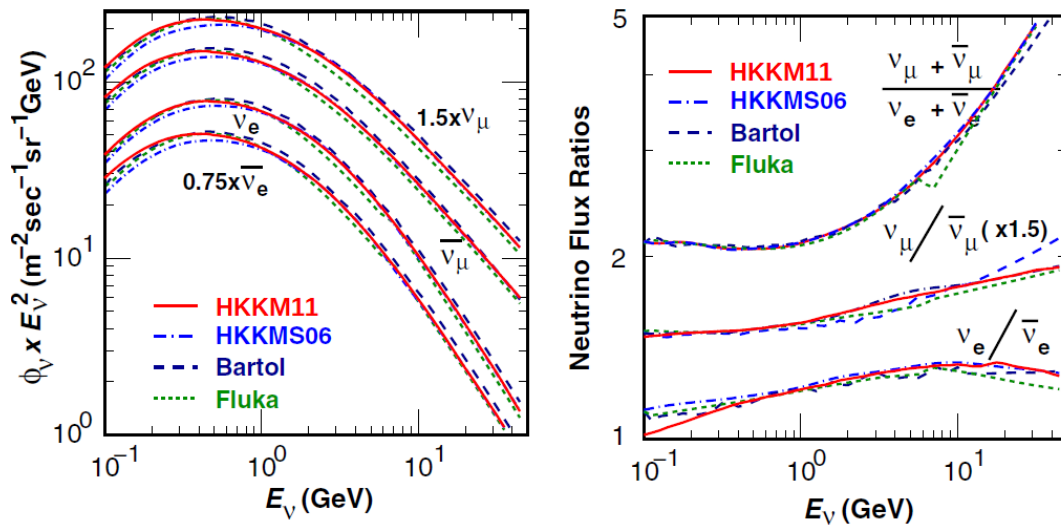
Figure 2.8: Atmoshperic neutrino fluxes averaged over the zenith angle predicted by several research groups: HKKM [95][96], Bartol [97] and Fluka [98]. The calculations differ by the choice of the hadronic model and the primary cosmic ray flux measurements. The factors 1.5 and 0.75 are used to separate the curves and make them more visible. Plot taken from [99].

The aforementioned mechanism is frequently called the conventional flux. No primary tau neutrinos are produced within this model, although they can still appear in the detector due to the oscillation effect. There is an additional atmospheric neutrino production mechanism frequently referred to as the *prompt* flux, which originates from the decays of heavy hadrons. The prompt component in principle contains a small

(a) Energy 3.4 GeV   (b) Energy 5 GeV   (c) Energy 10 GeV
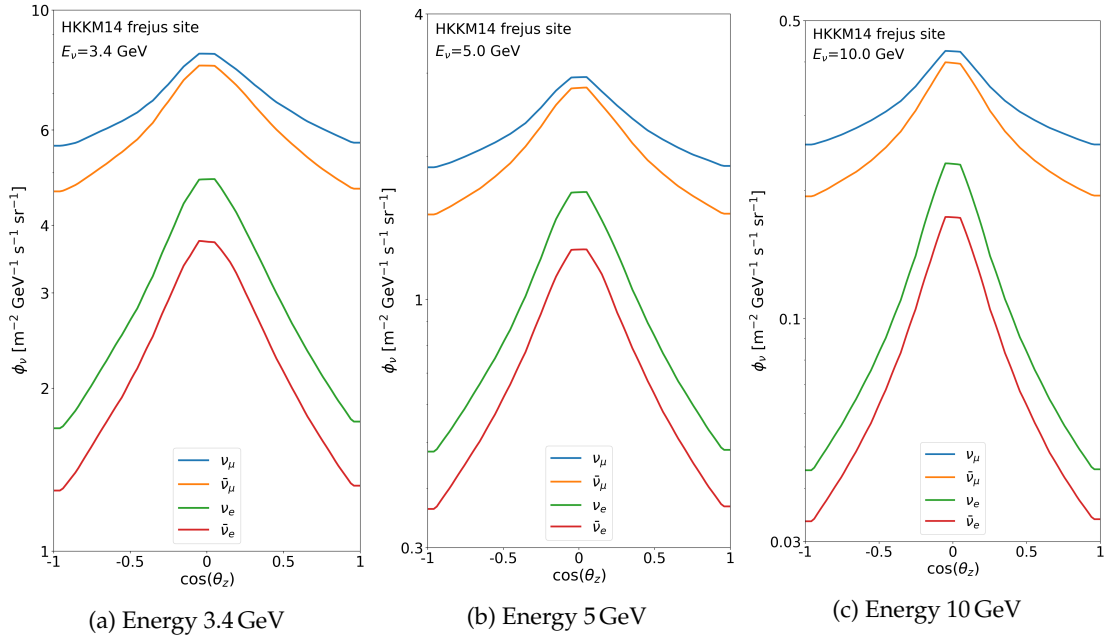
Figure 2.9: Atmospheric neutrino flux dependence of the zenith angle for three neutrino energies, calculated using the HKKM14 model at the Fréjus site. Notice the difference in the scales of the y-axis.

fraction of primary tau neutrinos, but for neutrino energies below $E_\nu \simeq 10$ TeV its contribution to the total flux can be neglected [100].

The atmospheric neutrino flux model used in this dissertation for neutrino rate calculations in the ORCA detector is HKKM14 [101], calculated at the Fréjus site (Modane Underground Laboratory) assuming the solar minimum. The chosen flux table is foreseen to provide an accurate estimation taking into account that the 25th solar cycle has begun a few years ago and the Frejus Road Tunnel is located only about 260 km from the ORCA detector site.

2.3.2 Cherenkov radiation

Cherenkov radiation is emitted when a charged particle travels in a dielectric medium with a speed faster than the speed of light in that medium. This phenomenon is originated by the medium polarisation induced by the charged particle passing through and locally disturbing the electric field. The excited atoms emit photons, which are able to create a wave front due to constructive interference when the polarising particle moves with a velocity $v > c/n$, where n is the refractive index. A scheme of the Cherenkov radiation creation mechanism is shown in Fig. 2.10. As can be seen, the emitted radiation interferes constructively on the cone surface with a characterising opening angle called Cherenkov angle. The Cherenkov angle θ_{Ch} is given by

$$\cos\theta_{Ch} = \frac{1}{\beta n}. \tag{2.3}$$

In seawater (average $n \sim 1.35$) with an ultra-relativistic particle ($\beta \simeq 1$), the angle is $\theta_{Ch} \approx 42°$. In fact, seawater is a dispersive medium, which means that the real index of refraction will vary slightly depending on the wavelength of the light. Moreover, the refractive index might differ with the increasing pressure or change in the temperature. Nevertheless, these second order effects have a marginal impact on
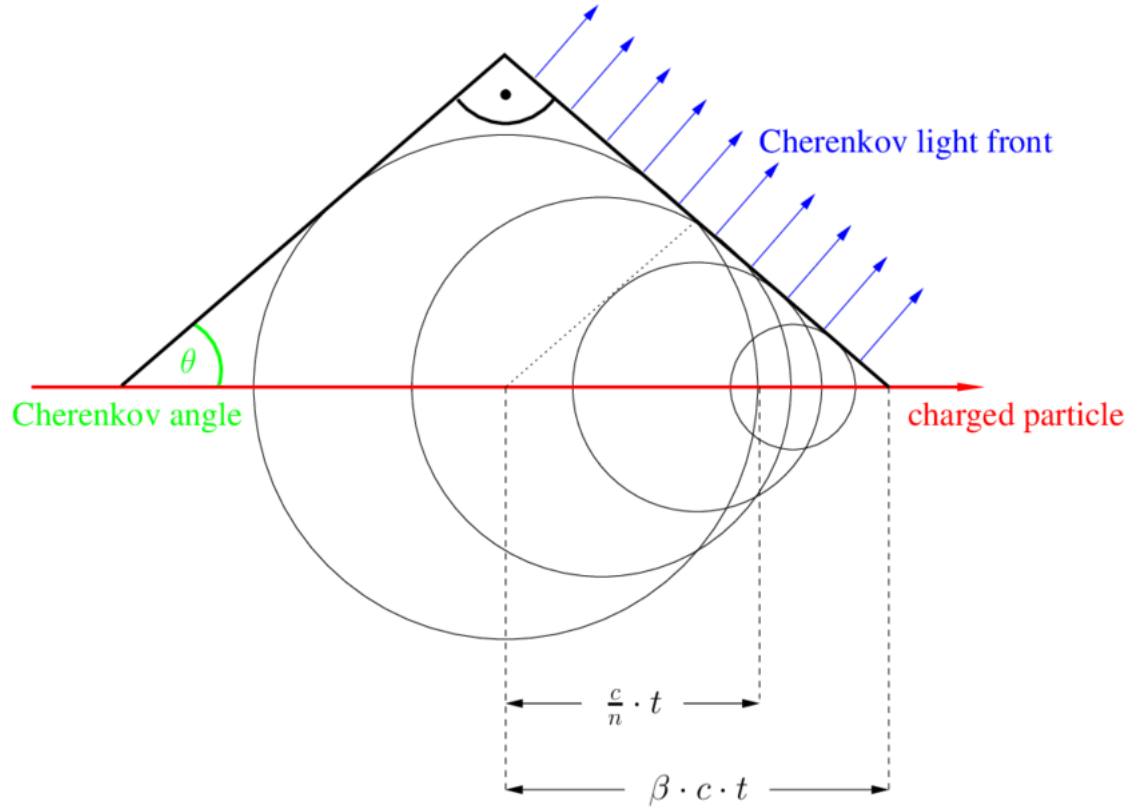
Figure 2.10: Cherenkov radiation mechanism scheme. Taken from [102].

the ORCA measurements when compared with the other water characteristics such as absorption and scattering length. The Cherenkov photons emission spectrum is given by [20]

$$\frac{\mathrm{d}N_\gamma}{\mathrm{d}\lambda\mathrm{d}x} = \frac{\alpha 2\pi}{\lambda^2}\left(1 - \frac{\beta^2}{n^2}\right),\qquad(2.4)$$

where $\alpha \simeq \frac{1}{137}$ denotes the fine-structure constant, λ is the light wavelength and x is the path length along which the Cherenkov photons are emitted. With the assumptions of a constant refractive index $n \approx 1.35$ and an ultra-relativistic particle $\beta \simeq 1$, the formula from Eq 2.4 integrated between 300 nm and 700 nm gives roughly 400 photons/cm. The energy threshold required for a particle to be able to generate Cherenkov radiation is given by

$$E_{th} = \frac{mc^2}{\sqrt{1 - 1/n^2}},\qquad(2.5)$$

where m is the particle mass. For electrons and muons travelling in seawater we get respectively $E_{th}^e \approx 240$ keV and $E_{th}^\mu \approx 53$ MeV.

2.3.3   Water properties and photon propagation

Cherenkov photons propagating in the seawater are absorbed and scattered. Absorption reduces the light intensity and scattering leads to a photon path distortion effectively reducing the information about the primary neutrino direction. Both quantities can be

defined by an exponential distribution

$$I(\lambda_{a,s}) = I_0 e^{-x/l_{a,s}} \tag{2.6}$$

where x is the photon path length, $l_{a,s}$ denotes the absorption length l_a or the scattering length l_s and I_0 can be interpreted as the initial unabsorbed or unscattered light yield. The scattering length depends on the scattering angle θ and the photon wavelength λ via the total scattering probability defined as

$$b(\lambda) = 2\pi \int_0^\pi \sin(\theta)\beta(\lambda,\theta)\mathrm{d}\theta, \tag{2.7}$$

where $\beta(\lambda,\theta)$ is a volume scattering function. In calculations it is usually more convenient to operate with the angular scattering function

$$\hat{\beta} = \frac{\beta(\lambda,\theta)}{b(\lambda)}. \tag{2.8}$$

The benchmark for the light scattering models in seawater comes from the Petzold measurements [103]. The Petzold average particle phase function is often approximated by the Henyey-Greenstein function [104]

$$\hat{\beta}_{HG}(g,\theta) = \frac{1}{4\pi}\frac{1-g^2}{(1+g^2-2g\cos(\theta))^{3/2}}, \tag{2.9}$$

where g is an average $\cos(\theta)$, which for the description of the seawater can be taken from the Petzold data $g = 0.924$. To account for the size variety of the obstacles that photons can potentially scatter off in the seawater, a simplified version of the Kopelevich model is used [105]. The total scattering probability function in the model used in KM3NeT simulations reads

$$b(\lambda) = 1.7 \cdot 10^{-3}\left(\frac{550\,\mathrm{nm}}{\lambda}\right)^{4.3} + 7.5 \cdot 10^{-3}\left(1.34\left(\frac{550\,\mathrm{nm}}{\lambda}\right)^{1.7} + 0.312\left(\frac{550\,\mathrm{nm}}{\lambda}\right)^{0.3}\right),$$
$$\tag{2.10}$$

where the first term corresponds to the scattering in pure seawater and the second and the third terms correspond respectively to the scattering contribution from small and large particles in the Kopelvich model. This approach was found to reproduce quite well the measurements performed at the ANTARES site [106], which is very close to the ORCA location. The scattering length can be directly obtained from Eq 2.10 as

$$l_s = \frac{1}{b(\lambda)}. \tag{2.11}$$

Figure 2.11 shows an overlap of the Cherenkov light emission spectrum from Eq. 2.4 and the wavelength-dependent photon absorption and scattering lengths in the seawater. The interplay between these three quantities illustrates the requirement for the PMT quantum efficiency from Fig. 2.6 as most of the photons to be detected are expected between the wavelengths from 350 nm to 500 nm.

2.3.4 Muon propagation

Muons constitute an especially important experimental signature in the ORCA measurements. They are expected to originate from the following sources:
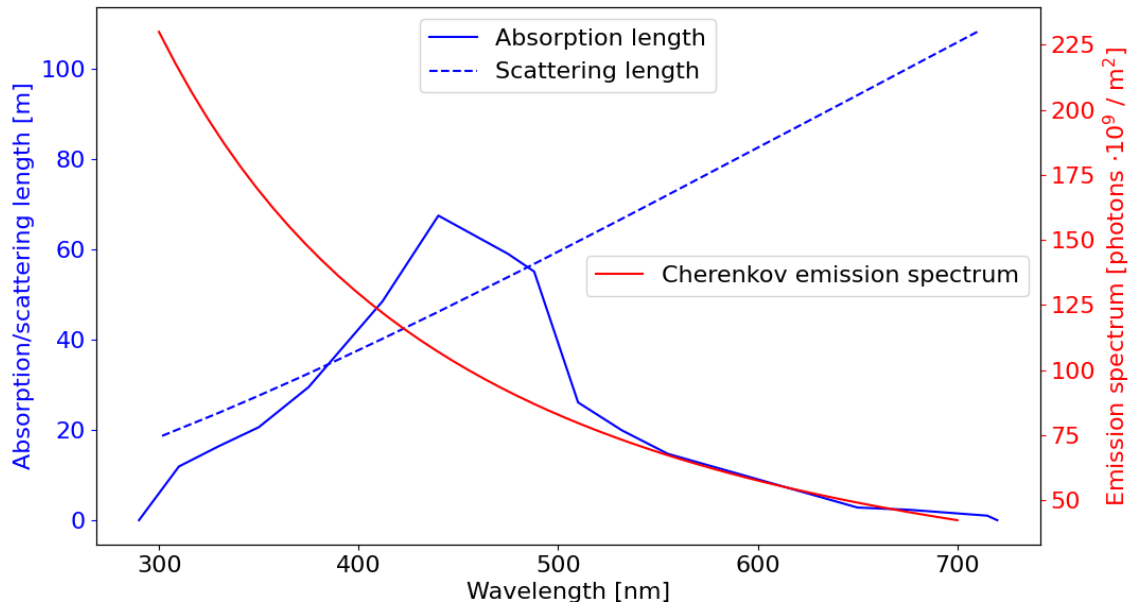
Figure 2.11: The Cherenkov emission spectrum follows Eq 2.4. The scattering length is calculated from Eq. 2.10 and 2.11. The absorption length measurements are based on results presented in [107].

1. $\nu_\mu/\bar{\nu}_\mu$ CC interactions: in this case the presence of a muon allows for the primary neutrino flavour identification,

2. primary cosmic ray showers: even under a layer of water roughly 2500 meters thick, it is still possible for a high energetic atmospheric muon to reach the detector. These events contribute to the background, which has to be efficiently distinguished from the first case. More about the sources of background in ORCA will be said in Section 2.5,

3. $\nu_\tau/\bar{\nu}_\tau$ CC interactions: taus created in such interaction decay into muon and two neutrinos with $\sim$ 17% probability. In the energy regime of ORCA, such events are basically indistinguishable from the first case, because taus decay almost immediately, but the muon originating from such decays would on average carry only about 1/3 of the tau energy.

Cherenkov radiation is the most important physical phenomenon used in ORCA for neutrino detection, but it is responsible only for a very small fraction of the total energy loss of muons travelling in water. Energy loss of particles in matter is generally described by the Bethe-Bloch formula, which applies to energies spanning many orders of magnitude starting from the MeV scale. However, the energy loss of muons with energies in the GeV scale and above can be very accurately expressed by a simplified formula [108]

$$-\frac{\mathrm{d}E}{\mathrm{d}x} = a(E) + b(E)E, \tag{2.12}$$

where $a(E)$ is the ionization term and $b(E)$ incorporates the energy loss due to e^+e^- pair production, bremsstrahlung, and photonuclear effects. In the regime where a and b can be considered constant, the average distance travelled by a muon with an initial energy

of E_0 until reaching the reduced final energy E_f is

$$R(E_0, E_f) \approx - \int_{E_0}^{E_f} \frac{\mathrm{d}E}{a + bE} = \frac{1}{b} \ln \left(\frac{a + bE_0}{a + bE_f} \right). \tag{2.13}$$

The range of a muon with an energy E_0 can be estimated in an iterative process using Eq. 2.13 by choosing an energy step adequate for the desired precision, but always small enough to maintain the assumption of constant a and b within a single iteration.

Figure 2.12 shows the energy loss of muons passing through water. As can be seen, to a very good approximation, we can consider ionization as the only relevant contribution for the muons with energies up to 100 GeV. Muon energy loss in seawater in the
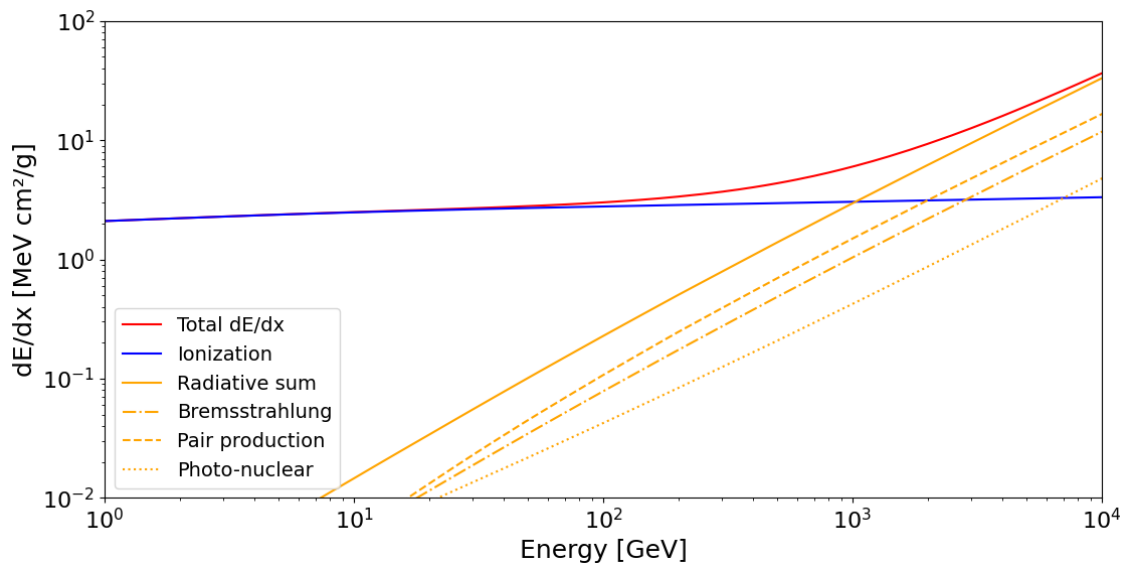
Figure 2.12: Muon stopping power in water [109]. The presented values of the radiative loss do not correspond directly to the b factor in Eq 2.12 due to the energy factor incorporated in the unit.

minimum ionizing particle (MIP) regime is about 0.25 GeV/m. This allows for a simple muon energy estimation based on the reconstructed muon track length. Figure 2.13 shows a comparison of the energy dependent muon range in seawater between the calculations with Eq. 2.12 and the constant minimum ionizing approximation of 0.25 GeV/m. As can be seen, this approach gives a good description for muon energies below ~100 GeV. In the case of the limited size of the ORCA6 configuration, it is rare to observe a muon track which starts and stops inside the detector volume. Therefore, in most situations the muon energy can only be known up to the measured track length. Following this limitation, in the ORCA6 sample used for our analysis, the energy estimation was decided to be based on the measured track length following the simplified relation 0.25 GeV/m.

2.3.5 Electromagnetic and hadronic showers

Electrons created for example in the CC interactions of ν_e or muon decays induce an avalanche of bremsstrahlung photons and electron-positron pairs frequently referred to as electromagnetic shower. A majority of the primary electron energy is deposited within a cylinder defined by the material-characteristic Molière radius transverse to the shower
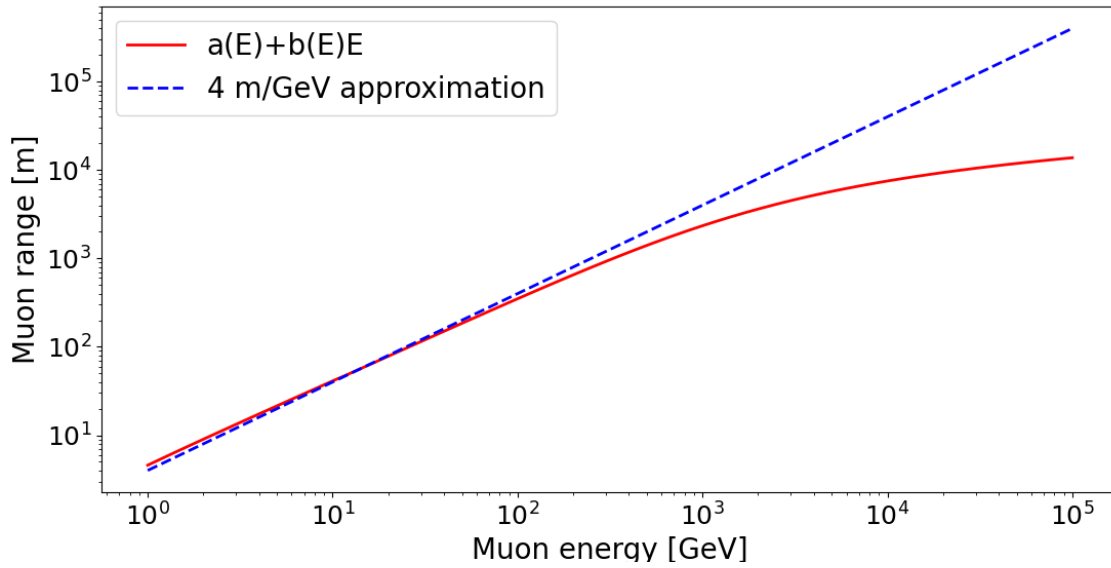
Figure 2.13: Muon range in seawater with an assumed constant density of $1.35\,\text{g/cm}^3$. The
calculations are done assuming continuous-slowing-down-approximation (CSDA)
with a step of $1\,\text{GeV}$.

direction. The longitudinal electromagnetic shower Cherenkov emission probability can
be parameterised as

$$p(x, a, b) = x^{a-1}\frac{e^{-x/b}}{b^a\Gamma(a)},\tag{2.14}$$

where x is the distance from the shower vertex and the parameters $a = 1.85 +$
$0.62\ln(E/\text{GeV})$ and $b = 0.54$ for the seawater [110]. Figure 2.14 shows the results
of Eq. 2.14 for primary electron energies $E_e = \{1, 10, 100, 1000\}$ GeV. Combining this
distribution with the Molière radius value in pure water ($\sim$10 cm) results in very localised
events within the context the ORCA detector size.
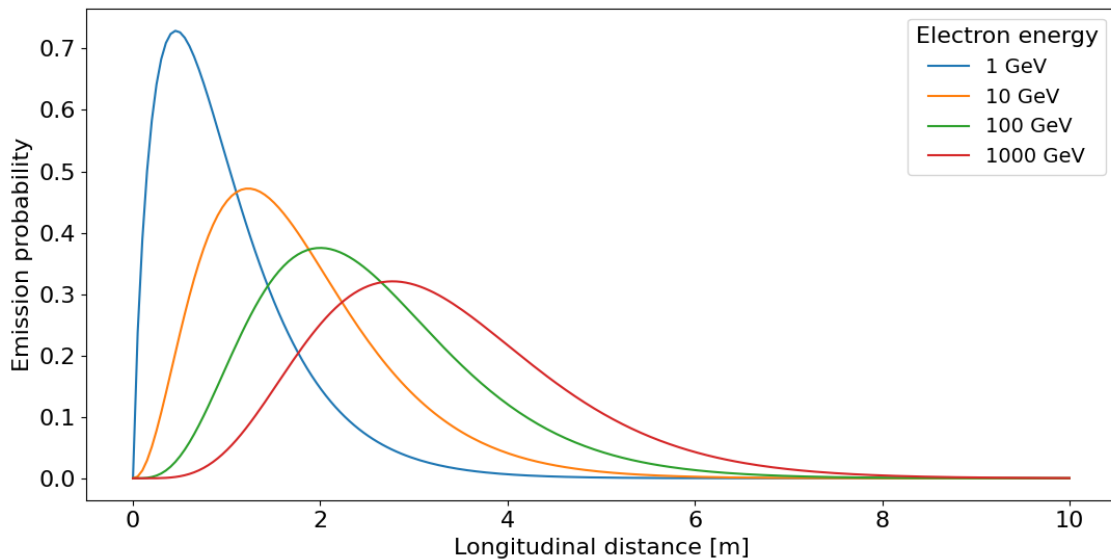
Figure 2.14: Cherenkov photon emission probability distribution in a longitudinal profile of an
electromagnetic shower induced by a primary electron.

Almost all neutrino interactions measured in ORCA also create some form of a hadronic shower by either ejecting a nucleon from the target nucleus or direct scattering off a quark (see Section 1.1.1.3). Generally, ORCA is not capable of resolving the differences between electromagnetic and hadronic showers. Hence, hadronic showers can not really be used separately for the flavour identification. The detailed description of the Cherenkov profile of hadronic showers can be found in refs. [111][112].

2.4 Event signatures

In KM3NeT there are two main event signatures: track-like events and shower-like events (for short *tracks* and *showers*). A visualisation of what the event class topologies would look like in the detector signal is depicted in Fig. 2.15. Track events are induced by a muon crossing the detector, so they are expected to originate either from ν_μ-CC interactions, ν_τ-CC interactions (if the tau decays into a muon) or atmospheric muons reaching the sea bottom. A muon crossing the detector array leaves a trace of DOMs flashing in a volume, which can be approximated by a cylinder around the muon's direction axis. After applying an adequate set of cuts to suppress the atmospheric muon contamination, the track-like signature becomes the main tool for neutrino flavour identification.

On the other hand, shower-like events can be caused by a variety of processes: ν_e-CC, ν_τ-CC and all-flavour NC interactions. In the KM3NeT detectors electromagnetic showers are generally not distinguishable from the hadronic ones. It is important to mention that even ν_μ-CC interactions have a hadronic component next to the outgoing muon. In the case of low energy neutrinos interacting inside the detector, a muon created in ν_μ-CC can quickly decay to an electron eventually leading to a shower-like topology. More details about how the expected event topologies are incorporated into the data-taking procedures are given in Section 2.6.

(a) Track-like event   (b) Shower-like event
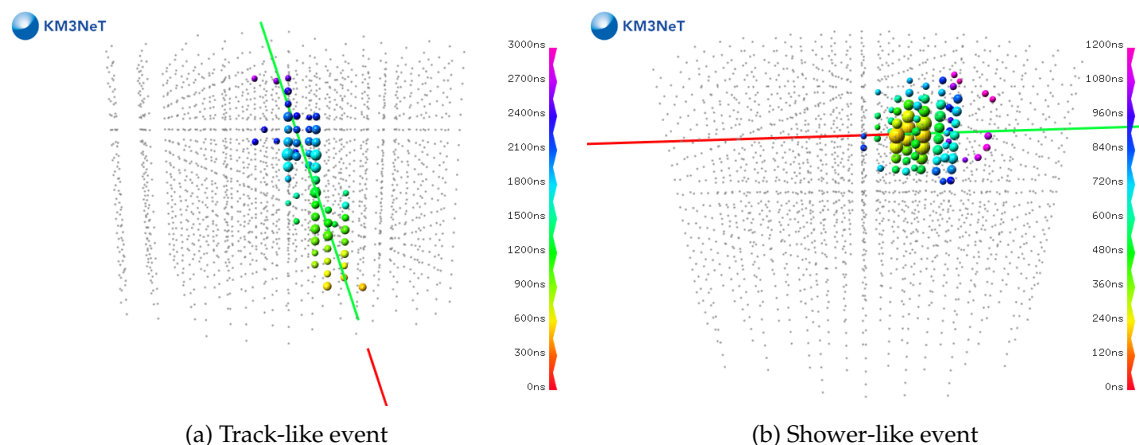
Figure 2.15: Event signatures in KM3NeT. The dots represent an array of DOMs. The colour scale reflects the PMT hit time and the blob size the amount of light. Taken from [83].

Machine learning models are being developed to be used for the event classification in ORCA data as they were successfully used in the past for the Monte Carlo (MC) simulations modelling the response of the full ORCA detector [83, 84]. However, for the results presented in this work, only the manually optimised cuts on the reconstruction quantities were used to extract a neutrino sample. These will be described in details in Chapter 4.

2.5   Sources of background

Generally background events originate from three different sources:

1. electronics internal noise,

2. radioactive isotopes and bioluminescent organisms present in seawater,

3. muons coming from the atmosphere.

2.5.1   Dark current

The PMT components undergo a temperature-dependent spontaneous emission of electrons, which leads to low-frequency background noise in the readout. Moreover, the glass material used for the DOM outer shell contains trace amounts of radioactive isotopes. These processes can be observed even in a perfectly lightless environment and therefore are frequently referred to as dark noise.

2.5.2   Optical noise

A kilogram of seawater contains roughly 400 mg of potassium with a ^{40}K abundance of about 0.012%. This isotope has two main decay channels

$$\beta^- \text{ decay}:$$
$$^{40}\text{K} \rightarrow {}^{40}\text{Cl} + e^- + \bar{\nu}_e \quad (\text{BR} : 89.27\%) \tag{2.15}$$

$$\text{electron capture}:$$
$$e^- + {}^{40}\text{K} \rightarrow {}^{40}\text{Ar} + \nu_e + \gamma \quad (\text{BR} : 10.72\%) \tag{2.16}$$
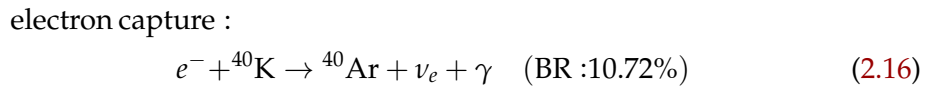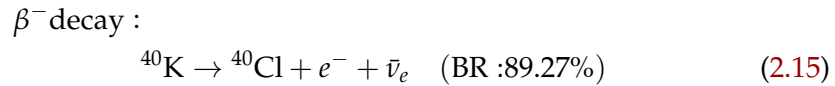
In the case with ^{40}Cl as the final product, the electron is emitted with an average energy of 560.2 keV and the endpoint at 1310.89 keV [113], which by far exceeds the Cherenkov emission threshold for electrons $E^e_{Ch} \approx 240$ keV (see Section 2.3.2). The second process results in the emission of a gamma photon with an energy of 1460.82 keV, which can subsequently lead to pair production or electron ejection via Compton scattering. The aforementioned processes cause a flat noise rate of about $7 - 8$ kHz in each PMT [114]. Because of the random nature of the ^{40}K induced PMT hits, they can be easily filtered by requiring a coincidence of signals in at least two DOMs within a certain time window. More about triggering techniques will be given in Section 2.6.

The other source of background light in the sea abyss is bioluminescence. The visible light can be produced by various marine organisms such as plankton, some fish species or even certain types of bacteria [115]. Due to the environmental adaptation of these life forms, such light is emitted in the region of the spectrum which is the least absorbed by the seawater, mostly blue (around 475 nm). The same criteria are applied to the sensitivity optimisation for the PMTs used in the KM3NeT detectors, so the bioluminescence signal can be very intense. The bacteria-induced light yields a relatively stable, low-rate noise uniformly distributed in space. Bioluminescent emission from bigger organisms is often stimulated by a local variation of water pressure or physical collisions with the detector components. Therefore the bursts of bioluminescence are usually clustered in space and time. Data taking periods with flashes caused by increased bioluminescence are filtered by applying the so-called high-rate veto (HRV) with a typical threshold of 20 kHz [116]. Once the HRV is triggered, the data is discarded until the rates come back below the threshold.

2.5.3 Atmospheric muons

Atmospheric muons are the muons created in extensive air showers stemming from the interactions of primary cosmic rays in the atmosphere. Their enormous abundance is one of the reasons for placing the KM3NeT detectors about 3 km deep underwater — this provides shielding from the overwhelming signal from all the particles produced in the atmosphere. The need for this shielding effect is illustrated in Fig. 2.16, which shows the zenith-dependent flux of the primary atmospheric muons and of the muons originating in neutrino interactions. The comparison between the atmospheric muon fluxes at different depths (in meters of water equivalent) is also shown. As can be seen, the main tool to clean an event sample from the atmospheric muon background is to select only up-going muons.
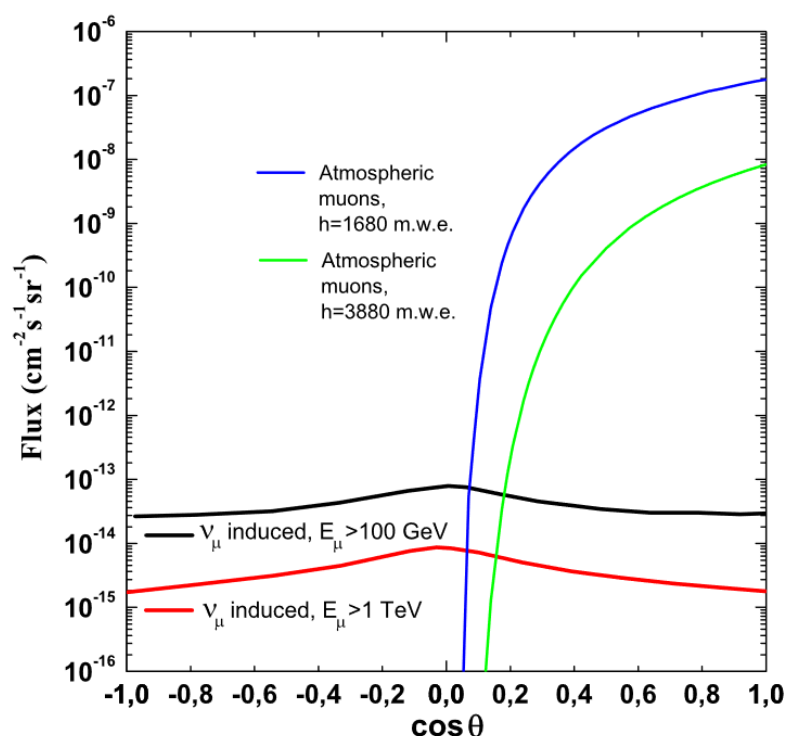
Figure 2.16: Atmospheric muon fluxes compared to the rates of the neutrino-induced muons for different depths and energy thresholds. Atmospheric muon flux rates calculated according to the parametrisation presented in [117]. Taken from [118].

2.6 Data acquisition and triggering

KM3NeT detectors operate on the all-data-to-shore basis, which means that the decision whether a certain sample should be stored or discarded is taken at the on-shore data processing centre. There are different PMT hit levels based on certain type of coincidences and causal relations:

- **L0 hit** (Level zero hit) - single photon PMT hit, which fulfils the criterion of being above 0.3 p.e. (photo-electrons) equivalent signal. Every L0 hit has its associated hit time and the Time-Over-Threshold (ToT) information,

- **L1 hit** - at least 2 L0 hits registered in the same DOM within a given time window (typically 10 ns for ORCA),

- **L2 hit** - an L1 hit with an additional requirement for the hit PMTs angular separation (usually minimum 90°).

Based on the use of the different hit levels, there are several trigger algorithms to suppress the background events described in Section 2.5 and select true neutrino events with high likelihood:

- **3D muon** trigger algorithm - designed to select the track-like events, takes a set of causally related L2 hits on a given number of DOMs inside the volume of a hypothetical cylinder with a predefined radius. To roughly cover the full solid angle, more than 200 hypotheses are tested for the potential track directions corresponding to the cylinder axis. The trigger parameters can be adjusted according to the detector conditions. Their typical values in ORCA are: $3 - 8$ L2 hits, $3 - 4$ DOMs and a ~ 160 m radius.

- **3D shower** trigger algorithm - similar to the 3D muon, but in this case the single hypothesis volume is a sphere of a given radius. A typical value for the sphere radius is about 50 m.

- **MX** trigger algorithm - developed especially to target the low energy events in ORCA. It works in a similar way to the 3D shower trigger, but with a relaxed hit level condition. Only one L2 hit is required and with the remaining hits at the L0 level.

The trigger algorithms are applied on the fly in the on-shore data centre to reduce the data storage. When one of the triggers is fired, all the L0 hits are saved within a snapshot time window of ± 1.3 μs around the occurred trigger time. These hits are then stored for event reconstruction.

2.7   Detector monitoring and calibration

To be able to account for the varying detector conditions and provide proper synchronisation between DOMs, a set of calibration data is being gathered in real-time or during special dedicated runs. To take advantage of the high seawater transparency for blue light combined with a long photon scattering length the PMT photon arrival times have to be measured with nanosecond accuracy. The time calibration is twofold:

- Intra-DOM calibration - photons from ^{40}K decays are used to account for the transit time and detection efficiency spread between PMTs in the same DOM. The fact that a single ^{40}K decay can sometimes produce a coincidence hit in two PMTs is exploited to derive the average time difference between all the combinations of PMT pairs. The bigger the angular separation the less likely it is to observe a coincidence.

- Inter-DOM calibration - performed with the LED nanobeacons (see Section 2.2.2.2) to set the time offsets between adjacent DOMs. The light with a known wavelength of 470 nm is flashed from the LED in a lower DOM to be received by the down-looking PMT of the upper DOM. With the assumption of the light velocity in seawater and known time stamps of the nanobeacon flashes, the time shift between each two DOMs on the same string can derived. The inter-DOM calibration with nanobeacon flashing happens only during calibration-dedicated detector runs. The calibration data from these special runs can also be used to study the potential changes in seawater properties caused for example by seasonal variations.

However, to make the time-synchronised information from consecutive DOMs appropriate for the reconstruction procedure, the DOM positions have to be known with roughly a 10 cm precision (photons travel ~20 cm each nanosecond in water). A sea-floor network of acoustic emitters anchored to a fixed position combined with hydrophones at the basis of each DU and piezo transducers attached inside the bottom hemisphere of each DOM give sufficient information for precise triangulation [119, 120]. A compass chip with an embedded accelerometer installed inside the DOM provide the information about the pitch, yaw and roll of each optical module. All this information together allow for the real-time monitoring of the current detector shape. An independent method of position calibration based on atmospheric muons has also been developed as a complementary approach [121].

3 Detector modelling

Contents

In this chapter we introduce the ORCA detector simulation chain, that mimics the signal expected from data. Most of the procedures described in this chapter are valid regardless of the exact configuration of the ORCA detector, although some details and results apply only to the ORCA6 configuration. When this is the case, it is explicitly indicated. The Monte Carlo (MC) simulation of the response of the detector is a key process to be able to define selection criteria to disentangle signal from background and to estimate the corresponding efficiencies and contamination.

3.1 Simulation chain

The modelling of the ORCA detector is divided in several steps, each of which is taken care of by different simulation packages:

1. Event generation (subsections 3.1.1 and 3.1.2): Neutrinos and atmospheric muons are generated based on interaction models. The detector geometry and the surrounding materials (sea water and Earth's crust) are taken into account.

2. Propagation of secondaries and light generation (subsection 3.1.3): The particles produced in the previous step are propagated and the Cherenkov light that they induce is generated. The sea water properties are taken into account and the PMT hits are assigned based on the generated photon PMT hit probability distributions or a detailed step-by-step tracking process.

3. Triggering (subsection 3.1.4): The data trigger algorithms are applied to the simulated PMT hits taking into account the effects of electronics and other background sources.

From this point onward the simulated data undergo the same processes as those applied to data.

4. Event reconstruction (subsection 3.1.5): The triggered events are processed by the specialised reconstruction algorithms, which assume either a track-like or a shower-like topology.

5. Event selection/Particle identification (subsection 3.1.6): Only those events with a high probability of having a neutrino origin are selected. The probability of the type of event (track or shower-like) can also be estimated. This selection and classification can be done by applying manual cuts on the available reconstructed variables or preferably by using more sophisticated machine learning techniques.

The simulations performed for ORCA6 were done in the so called run-by-run mode (RBR), which takes into account the actual measured detector conditions that vary among the data runs, such as for example the high-rate veto fraction or the malfunctioning PMTs.

No dedicated simulation of the noise events was performed for ORCA6. From previous studies of ORCA4 data and earlier simulations of the full detector it was found that the pure noise events that manage to pass the triggering stage can be easily rejected by a simple cut on the absolute number of hits or the reconstruction likelihood divided by the number of hits. More details will be given in Chapter 4.

3.1.1   Neutrino generation

Neutrino generation is done with gSeaGen [122], which, apart from simulating neutrino interactions, takes also into account the geometry and the environment of an underwater (or under-ice) neutrino telescope. For the underlying physics of neutrino interactions generation, gSeaGen makes use of the GENIE Monte Carlo Neutrino generator [123]. GENIE offers a variety of physics parameters and model features that can be tuned by the user. Three different "volumes" are defined when neutrino event simulations are performed:

- Instrumented volume - it is the volume occupied by the detector instrumentation (see Fig 3.1). The instrumented volume does not play a role directly in gSeaGen simulations, but can be used as an input to automatically define the *can* volume.

- *Can* volume - Cherenkov photons created in the cylinder defined by the *can* volume have a non-negligible chance to be detected by the PMTs in the detector. Typically the size of the can is set to the instrumented volume, approximated by a cylinder, extended by 5 photon attenuation lengths in radius and height. The *can* size can

also be manually set by the user. By default, all the non-muon neutrino interaction products created outside the *can* volume are discarded in the output file. Muons outside the can are propagated from the primary interaction vertex and, if they manage to reach the *can*, they are saved on its surface to be further taken care of by the Cherenkov light propagation software. The relation between the can and the instrumented volume is shown in Fig. 3.1.

- Interaction or generation volume - calculated by gSeagen at runtime, it depends on the simulated neutrino flavour, maximum energy and the weak current type. In the case of ν_e-CC and all-flavour NC interactions, the interaction volume is by default identical to the *can* volume. For events capable of producing muons in the final state, namely ν_μ-CC and ν_τ-CC, the interaction volume is defined by the maximum muon range in sea water and the rock surrounding the detector.
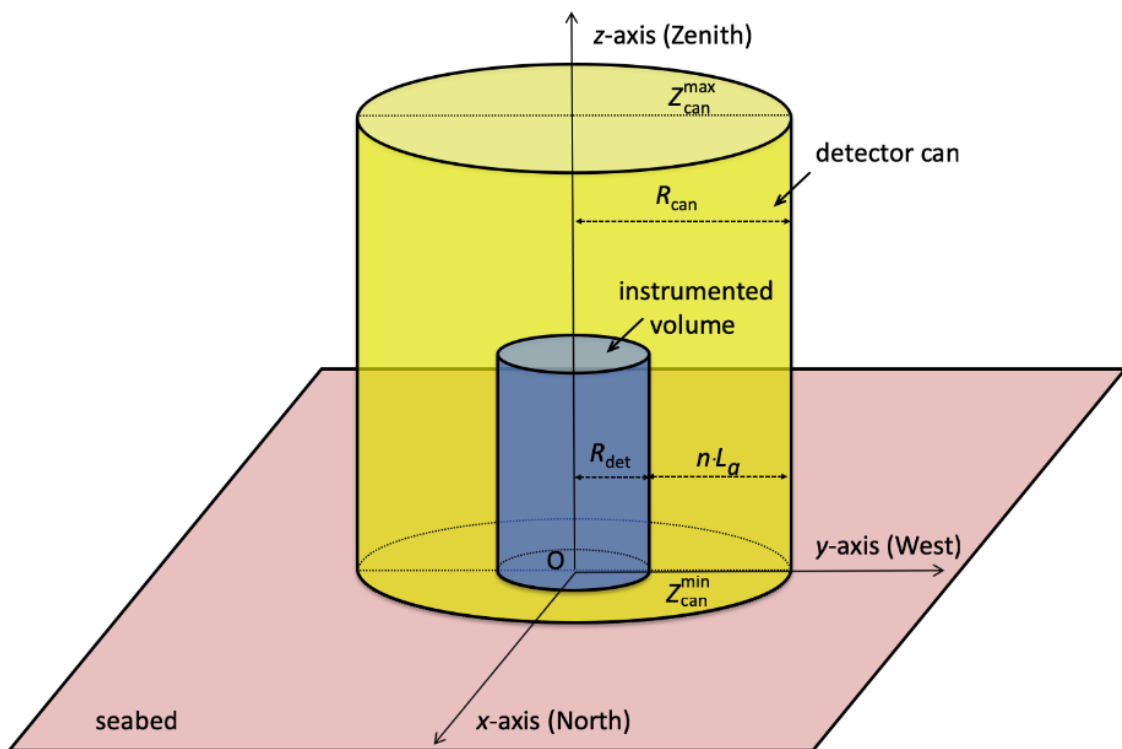
Figure 3.1: The geometrical relation between the instrumented volume and the *can* volume. R_{det} is the radius of the smaller cylinder that contains all the active detector components (see Fig 2.2), L_a is the photon attenuation length and n number of attenuation lengths used to define the detector can (usually five), R_{can} is the *can* radius and Z_{can} denotes the maximum and the minimum z of the *can*; Z_{can}^{max} is taken so as to allow for five attenuation lengths form the upper surface of the detector cylinder. Drawing taken from [122].

All the simulated neutrinos are forced to interact and a generation weight is assigned. The generation weight accounts for the simulated energy spectrum (usually a simple power law), the interaction cross section, the Earth crossing probability, the vertex generation area etc. A detailed description of the generation weight components can be found in [122]. To obtain an event weight

$$w_{evt} = \frac{w_{gen}}{N_{tot}} \cdot \phi(E, \cos(\theta)) \tag{3.1}$$

the generation weight w_{gen} has to be multiplied by a physical flux $\phi(E, \cos(\theta)$ (in the case of ORCA it is the atmospheric neutrino flux) and divided by the total number of simulated events, N_{tot}. The flux depends on the primary neutrino energy, E, and the cosine of the incoming neutrino zenith angle, $\cos\theta$. By default, the simulation livetime, and therefore the generation weights, corresponds to one year in every single simulation run. The division by the total number of simulated events from all the simulated runs combined retains the events-per-year interpretation of the event weight regardless of how many separate runs are generated for the same flavour and in the same energy range. Neutrino flavours and weak currents are simulated separately, so the re-scaling is applied separately to the single flavour sets of simulation runs ν_e-CC, ν_μ-CC and ν_τ-CC and a single flavour (in the case of ORCA6 it is ν_μ) NC interactions. No difference is expected between neutrino flavours in the case of NC interactions, so only one flavour is simulated to reduce the computing time. The separation of flavours during the neutrino generation procedure is due to the following factors:

- interactions which are able to produce muons, namely ν_μ-CC and ν_τ-CC, have a different interaction volume than the ones which do not create muons: ν_e-CC and NC,

- ν_τ-CC have a higher interaction energy threshold due to the relatively high mass of the tau lepton.

3.1.2 Muon generation

Unweighted atmospheric muons are generated with `MUPAGE` [124][125] assuming a parameterised muon flux model. Since the abundance of atmospheric muons is a few orders of magnitude higher than that of atmospheric neutrinos, the muon generation is usually the most computationally expensive part of the ORCA simulation chain. To have a good trade-off between the simulation time and the statistics, muons are generated only for a fraction of the real detector operation time and then each muon event goes into the final event rate prediction weighted with the factor of the run data acquisition time divided by the muon simulation run livetime. This factor for the ORCA6 sample simulation used in this work is about 3. It means that for each run, a third of its livetime is covered by the corresponding muon simulation and every single muon event passing the cuts is an equivalent of ~ 3 muons in the event rate.

3.1.3 Light propagation

The Cherenkov light generation is performed with two different software frameworks `JSirene` and `KM3Sim` [126]. The former is a part of an internal KM3NeT multi-purpose software package called `Jpp` (all the software names starting with "J" appearing in this chapter are submodules of `Jpp`). `JSirene` provides a Cherenkov hit distribution in the detector based on the particle-specific tabulated probability distribution functions of the photon arrival time. `KM3Sim` is a GEANT4 [127] based application performing a detailed step-by-step propagation of all the individual Cherenkov photons created by the particles present in the event generation output. As `JSirene` is much faster than `KM3Sim`, it is typically used for atmospheric muon simulations and high neutrino energies ($E_\nu > 50$ GeV in the MC production for ORCA6 sample used in this work).

3.1.4 Trigger simulation

In order to mimic the behaviour of the data trigger algorithms (see Section 2.6), the output from the light generators is processed by the `JTriggerEfficiencyRBR` application. The

RBR suffix stands for the run-by-run mode. At this level also a random noise of a constant frequency corresponding to various coincidence rates induced by ^{40}K decays is added to the simulated hits before the trigger algorithms come into play.

3.1.5 Event reconstruction

Starting from this stage, the simulation output and the data are treated in exactly the same way. All the triggered events are reconstructed with two separate algorithms optimised for one of the event topologies described in Section 2.4. The track-like hypothesis is tested with the `JGandalf` reconstruction chain. A detailed description of the track reconstruction procedure can be found in [128]. In the case of the first ORCA6 data set, it was decided to use the reconstructed track length as a proxy for the reconstructed energy. The approximation of a minimum ionising particle assumes $0.25\,\text{GeV/m}$ (see Section 2.3.4). This approach provides a simple and robust estimation of the muon energy and does not introduce a significant error given the ORCA6 dimensions and the maximum length of the track crossing the detector cylinder (more information will be given in Section 3.4). Figure 3.2 shows the angular deviation of the reconstructed direction and the reconstructed energy resolutions in the ORCA6 MC sample with the track length used as the reconstructed energy proxy. The angular deviation is defined as $\theta_{dev} = \arccos\left(\vec{d}_{true} \cdot \vec{d}_{reco}\right)$, where $\vec{d}_{true}$ and $\vec{d}_{reco}$ are respectively the true and the reconstructed track direction vectors. As can be seen, the reconstructed energy gets saturated quickly due to the limited size of the detector. The fits are done in the binned

(a) Angular resolution   (b) Energy resolution
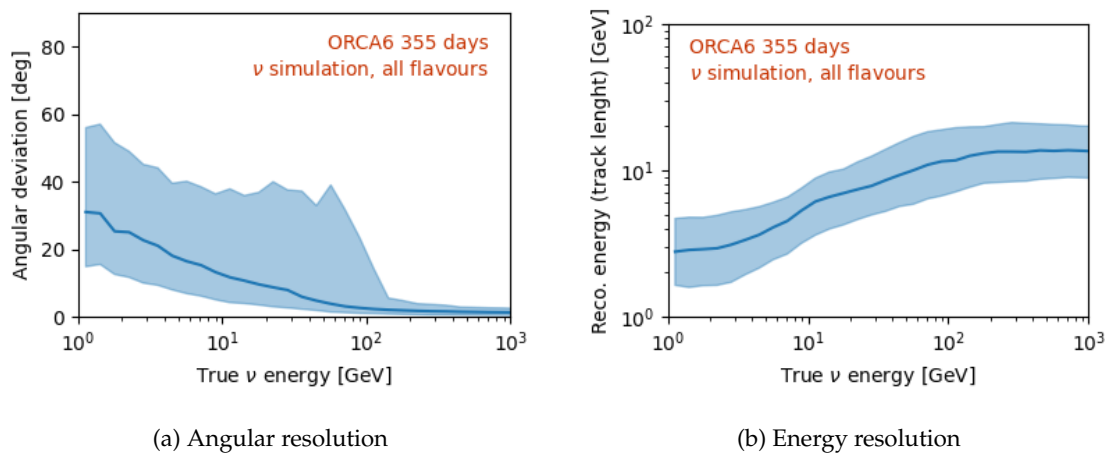
Figure 3.2: Reconstruction resolutions of the ORCA6 event sample used in this work. The large drop in the angular deviation for $E_{true} \geq 150$ GeV is due to the a very limited number of high energy events passing the event selection cuts. More details about the selection are given in Chapter 4 Section 4.2

.

two-dimensional space of the reconstructed energy versus reconstructed cosine zenith, so it is more informative to look into the reconstruction resolutions in bin-by-bin manner. The bin-by-bin energy resolution is depicted in Fig. 3.3. Note that the $\cos\theta$ binning is linear, but the energy binning is logarithmic (or linear in log(energy)). A ratio between the median true energy and the mean reconstructed energy of a given bin was chosen as a metric to evaluate how much the energy is overestimated in the reconstruction. The median is used instead of the mean because the true energy distributions appear to be strongly asymmetric. The true energy distribution width, ΔE_{true}, is calculated as the difference between the 83rd and the 16th percentile. Again this approach deals

with the fact that the true energy distributions are very asymmetric. For example, the distribution of the true energy reconstructed in the bin with boundaries $E_{reco} = [5.01, 6.31]$GeV, $\cos(\theta_{reco}) = [-0.6, -0.7]$ is shown in Fig. 3.4. In Chapter 4, the impact of the reconstruction resolutions in the context of the analysis will be discussed. A similar

(a) $E_{true}^{median} / E_{reco}^{mean}$

(b) ΔE_{true}.
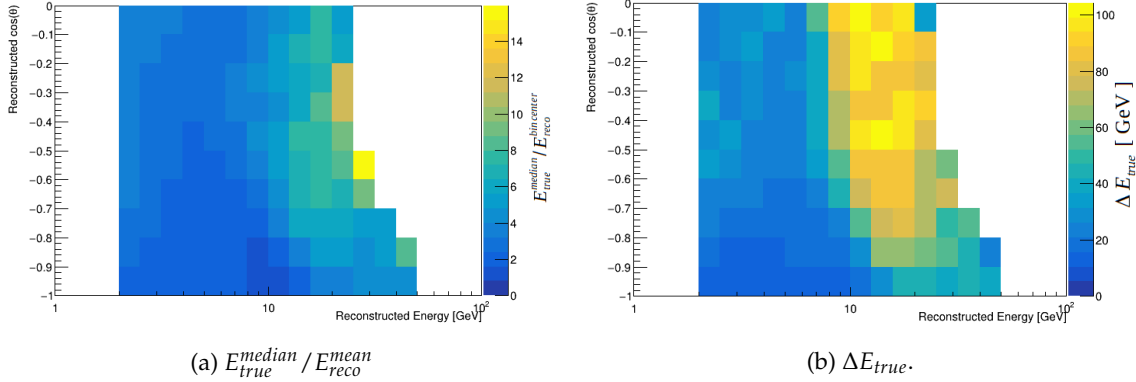
Figure 3.3: Reconstructed energy resolution as a function of the reconstructed energy and the reconstructed $\cos\theta$. Left: Median of the true energy distribution contributing to a single bin in the reconstructed space divided by the average reconstructed energy of that bin (bin centre). All the depicted values are greater than 1 which means that the energy is generally overestimated in each bin. Right: Width of the true energy distribution contributing to a single bin in the reconstructed space, ΔE_{true}.

.
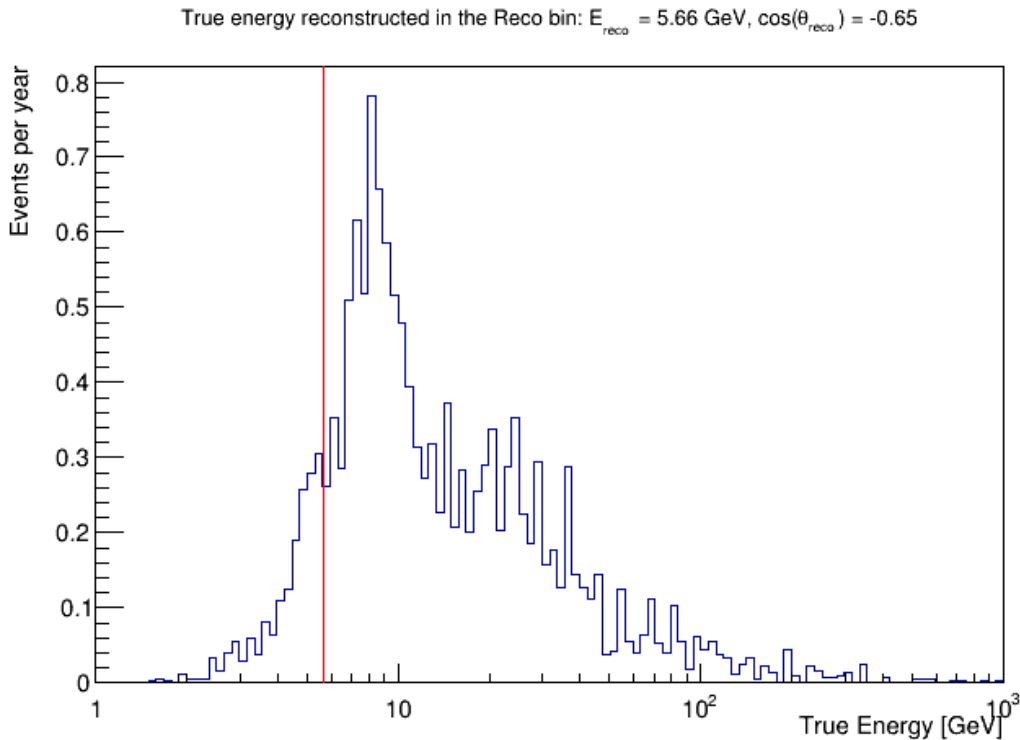
Figure 3.4: The distribution of the true energy reconstructed in the reconstructed bin with boundaries $E_{reco} = [5.01, 6.31]$GeV, $\cos(\theta_{reco}) = [-0.6, -0.7]$. The red line indicates the bin centre $E_{reco} = 5.66$ GeV in the energy dimension, which is also indicated on top.

study of the angular resolution can be done in the 2D reconstructed phase space. Here the resolution is much better and the average $\cos\theta_{true}$ generally aligns very well with the centre of the bin in $\cos\theta_{reco}$. Figure 3.5 shows the standard deviation of the distributions of true $\cos\theta_{true}$ reconstructed in a single bin in the reconstructed space. The $\cos\theta$ angular resolution improves with the energy as expected from the kinematics, but also , for the low energies, exhibits some dependency on the reconstructed value of $\cos\theta$ itself. An example distribution of $\cos\theta_{true}$ reconstructed in a single bin is depicted in Fig. 3.6.
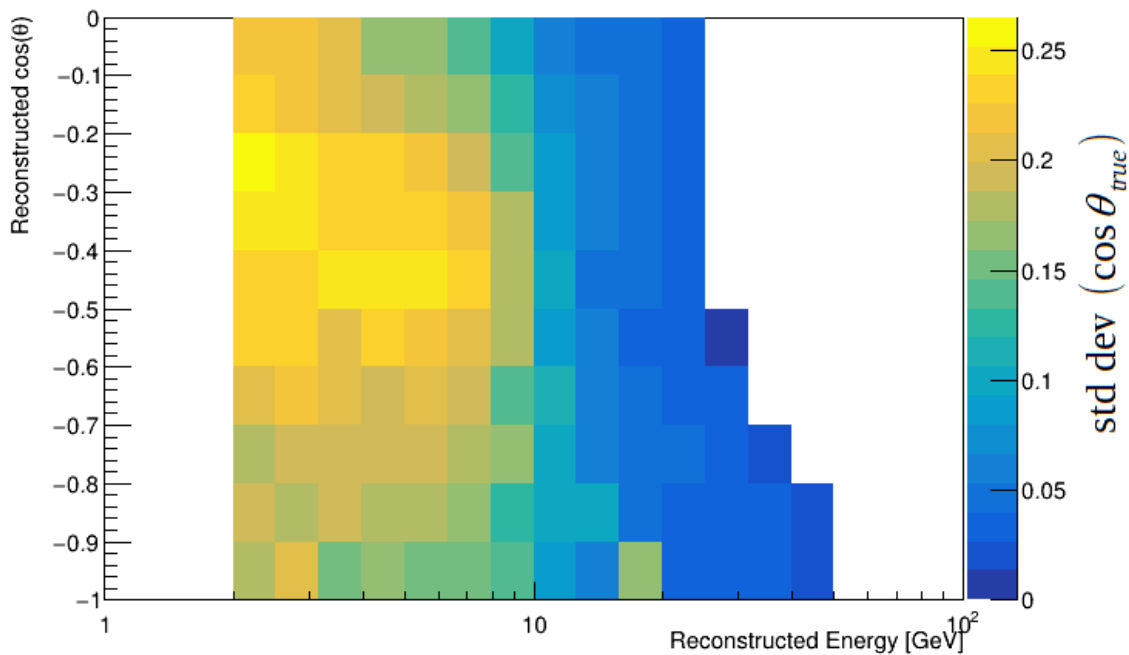
Figure 3.5: Standard deviation of the true $\cos\theta_{true}$ distribution reconstructed in a single bin.

In parallel, the triggered events are also treated with an algorithm assuming a shower-like scenario. The newest shower reconstruction chain in ORCA is called `JShowerFit` and its comprehensive description can be found in [129]. This algorithm was designed to be also applicable to the early stages of ORCA such as ORCA6. However, at the moment the ORCA6 data has not yet been processed with `JShowerFit` waiting for the adequate adjustments. For this reason, the ORCA6 results presented in this thesis are exclusively based on the track reconstruction output from `JGandalf`.

3.1.6 Event selection

After all the events have been reconstructed, it is necessary to select a pure neutrino sample for the oscillation analyses. It was shown in the past that machine learning algorithms provide very promising results in this matter and they are likely to outperform the manual cuts based on an educated guess and visual comparisons. These methods developed for the KM3NeT output are described in [83] and [84]. However, due to the fact that the first ORCA6 data set is lacking the shower reconstruction and that the data/MC agreement was still a topic of investigation, it was decided to simplify the event selection approach to reduce the number of possible sources of discrepancies. Therefore, a set of manual cuts was used, which are described in more detail in Chapter 4.
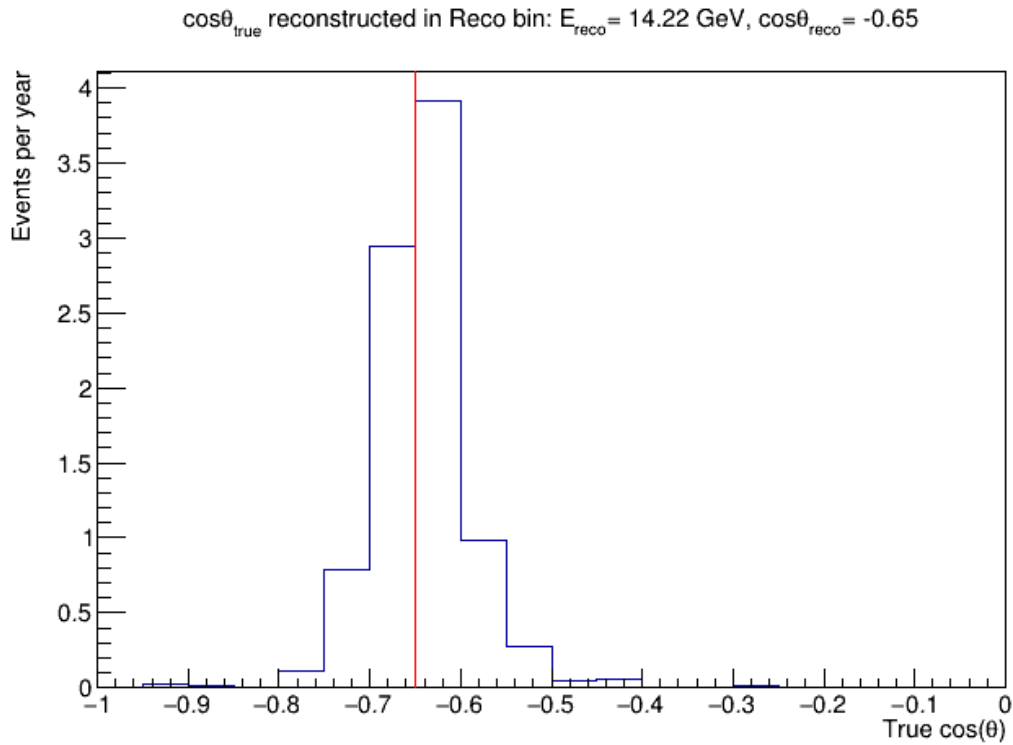
Figure 3.6: The true $\cos\theta_{true}$ distribution reconstructed in the bin with boundaries E_{reco} = [12.58, 15.85] GeV, $\cos\theta_{reco}$ = [−0.7, −0.6]. The red line indicates the bin centre in the reconstructed cosine theta dimension.

3.2 Calculating event rates at the detector

To calculate the expected event rates at the detector, the following ingredients are necessary:

1. oscillation probability,

2. energy and zenith angle dependent neutrino flux,

3. detector response based either on neutrino generation weights (event-by-event approach) or on the reconstruction efficiencies (binned response matrix),

4. in the case that the binned response matrix is used, the effective mass and neutrino interaction cross section have to be calculated externally,

5. the atmospheric muon distribution and

6. the detector exposure.

The physical processes related to the above-mentioned stages are decoupled and therefore they can be separated in the event rate calculation model. The true neutrino rates are calculated based on the combination of the neutrino flux, the oscillation probability and the information about the effective mass and the cross section, which can be computed externally or taken from the `gSeagen` generation weights. For the calculation of event rates at the detector for a given livetime, the MONA software is used. MONA basically adapts RooFit [130] functionalities for the purpose of neutrino oscillation analysis. It also provides a framework allowing for the incorporation of

systematic uncertainties associated with the physical models and detector effects. The systematic uncertainty parameters will be discussed in Section 3.3.

3.2.1 Oscillation calculations

To calculate the neutrino oscillation probabilities for the Earth-crossing neutrino paths an openly available software called `OscProb` [58] is used. To model the Earth's matter profile, the software takes advantage of the 44-layer PREM model [52]. To speed up the event rate calculation procedure, the oscillation probability is cached per interactions channel in a two-dimensional space of neutrino energy versus incoming direction corresponding to the true space binning of the response matrix (see Section 3.2.5). The cached oscillation probability values are averaged over each bin. Example oscillograms calculated with various configurations of `OscProb` can be found in Chapter 1 Section 1.3 and in Appendix A. The Earth's density profile provided by the PREM model used for the simulation is shown in Fig. 3.7. The initial measurements for the PREM model was further confirmed with greater precision in later works [131, 132].

(a) Matter density on an Earth-crossing neutrino path for various incident directions. The $\cos(\theta_z)$ values correspond to the layer boundaries.

(b) PREM model Earth density profile: full 425 layers version vs 44 layer approximation
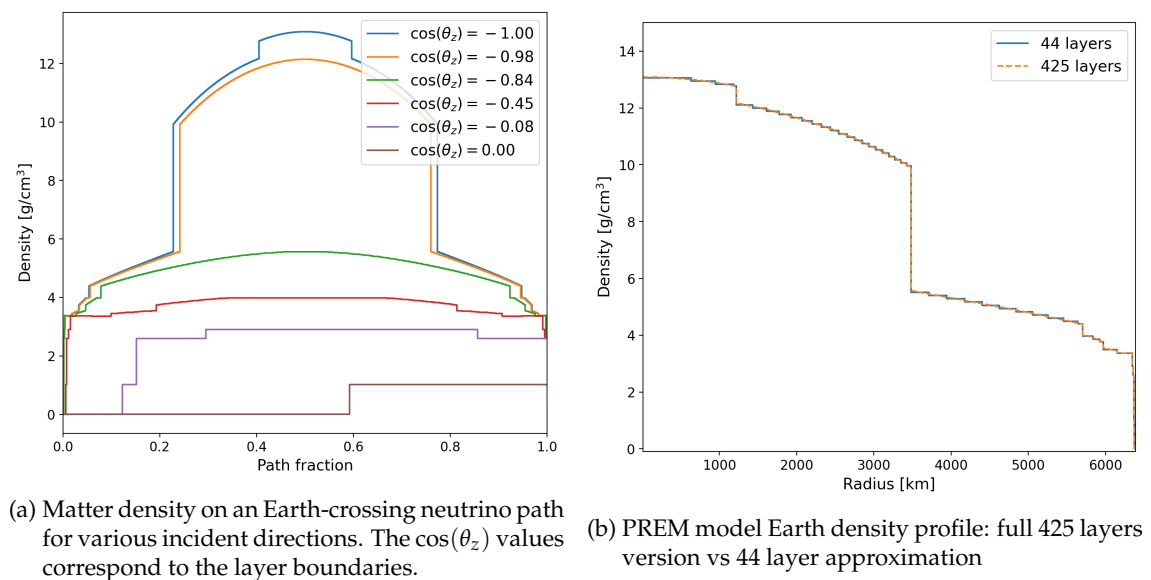
Figure 3.7: Matter density on a neutrino path crossing the Earth as a function of the incident direction (left) and the PREM model Earth density profile (right).

The Earth's chemical composition in terms of the average Z/A ratio (atomic number to mass number) is based on the Geo-chemical Earth Reference Model (GERM)[1] [133]. The GERM tables summarise a set of different models, which might vary in the chemical composition leading to slight variations in the average Z/A. In `OscProb`, the Z/A calculation for the Earth's core [134] and the calculation for the mantle takes advantage of the model described in ref. [135][2]. A comparison between the mantle models is presented in [136]. These details can be especially important for comparing the results on NSIs with other experiments potentially using different assumptions with respect to the Earth's matter composition (PREM model is a widely agreed upon benchmark, but it

---

[1]The GERM tables, which allow for the calculation of the average Z/A in Earth can be found online: https://earthref.org/GERMRD/datamodel/

[2]A full list of 44 Earth layers properties can be found in the `OscProb` repository https://github.com/joaoabcoelho/OscProb/blob/master/PremTables/prem_44layers.txt

only provides the density profile). The most important layers indicating the significant change in the average Z/A are described in Table 3.1.

Layer	approximate density [g/cm^3]	Z/A
Inner Core	13	0.4691
Outer Core	$12 - 10$	0.4691
Lower Mantle	$5.5 - 4.4$	0.4954
Upper Mantle	$4 - 3.4$	0.4954
Crust	$2.9 - 2.6$	0.4956
Ocean	1.02	0.5525
Atmosphere	0.001	0.4991

Table 3.1: Simplified table with Earth layers characteristics used for the oscillation probability calculations in `OscProb`.

Having Z/A fixed, the average *d*-quark or neutron to electron ratio in a given layer can be derived. For example, with the values from Table 3.1, in the core we would have

$$\langle \frac{Z}{A} \rangle = \frac{N_p}{N_p + N_n} = 0.4691, \quad N_p = N_e,$$

$$N_e = 0.4691(N_e + N_n)$$

$$Y_n = \frac{N_n}{N_e} = \frac{1 - 0.4691}{0.4691} = 1.132,$$

$$Y_d = \frac{N_d}{N_e} = 1 + 2Y_n = 3.264,$$

(3.2)

where N_p, N_n and N_e denote the number densities of protons, neutrons and electrons and the $N_p = N_e$ assumption comes from the postulated electric neutrality of the Earth's matter. As can be seen, the value $Y_n = 1.132$ in the core is slightly different from the one circulating in literature: $Y_n = 1.137$ (see again Section 1.2.3). This discrepancy is expected from the differences among Earth's chemical composition models present in the GERM tables.

3.2.2 Oscillated neutrino flux

As it was already mentioned in Section 2.3.1, the atmospheric neutrino flux model for the neutrino oscillation study with ORCA is taken from the azimuth angle averaged tables provided by HKKM14 (Honda group)[3] [101] . The flux table variant is chosen at the Frejus site for the solar minimum and without a mountain over the detector. For better precision, the interpolation between the tabulated points is done after multiplying by a factor of E_ν^3. The original atmospheric neutrino flux is cached in a histogram of true energy versus true $\cos\theta$ with the binning corresponding to the true space of the response matrix. The flux values are evaluated at the centre of each bin. The oscillated flux is then defined as

$$\phi_\alpha^{osc}(E, \cos(\theta)) = P(\nu_e \to \nu_\alpha) \cdot \phi_e(E, \cos(\theta)) + P(\nu_\mu \to \nu_\alpha) \cdot \phi_\mu(E, \cos(\theta)),$$ (3.3)

where $\alpha \in \{e, \mu, \tau\}$ is the neutrino flavour of a given event, $P(\nu_e \to \nu_\alpha)$ and $P(\nu_\mu \to \nu_\alpha)$ are the transition probabilities and $\phi_e(E, \cos(\theta))$ and $\phi_\mu(E, \cos(\theta))$ are the unoscillated neutrino fluxes of ν_e and ν_μ respectively. The corresponding formula for anti-neutrinos

---

[3]The tables are publicly available online: https://www.icrr.u-tokyo.ac.jp/~mhonda/nflx2014/index.html

can be directly derived from Eq. 3.3. As it was discussed in Section 2.3.1, tau neutrinos are not present in the atmospheric neutrino flux and they emerge through the tau appearance oscillation channels $P(\nu_e \rightarrow \nu_\tau)$ and $P(\nu_\mu \rightarrow \nu_\tau)$. Figure 3.8 shows an example of how the unoscillated atmospheric neutrino flux convoluted with the oscillation probabilities gets transformed into the physical muon neutrino oscillated flux expected at the detector (the NuFIT 5.1 NO oscillation parameters values were used).

3.2.3 Effective mass

The effective mass is a detector characteristic commonly used for neutrino telescopes and is analogous to the detector acceptance in high energy physics experiments. The effective mass

$$M_{eff}^{\alpha} = \frac{N_{sel}}{N_{gen}} V_{gen} \, \rho, \tag{3.4}$$

is defined for each simulated neutrino flavour, α, and interaction type (CC, NC) as the ratio between the number of selected events, N_{sel}, and the number of generated events, N_{gen}, within a given neutrino generation volume, V_{gen}, multiplied by the interaction medium density, ρ (sea water in our case). When the generation weights are used, the information about the interaction cross section and the effective volume is already included. This approach spares the necessity for the external calculation of the effective mass and can be considered as more accurate. In general, the effective mass depends on the event selection criteria. In the ORCA6 analysis the effective mass is not used in the event rate calculation and the detector response is based directly on the gSeagen generation weights.

3.2.4 Interaction cross section

When the effective mass is used together with detection efficiencies, the interaction cross section has to be calculated externally. In this case, the neutrino-water molecule cross section averaged per nucleon is used as an approximation (see Fig. 1.5). Within the energy spectrum observable in the KM3NeT detectors, neutrinos interact directly with the nucleons confined in the water target (see Section 1.1.1.3). The interactions with electrons are neglected due to their subdominant contribution (see Section 1.1.1.1). This approach is not used for the ORCA6 based analysis as the cross sections are embedded in the neutrino generations weights provided by gSeagen (see Section 3.2.5). The details about the external cross section calculation can be found in [32, 137].

3.2.5 Detector response

Once the simulation is completed and the high level reconstructed variables, such as the reconstructed energy and the zenith angle, are obtained, a detector response parameterization can be created to estimate the detector resolution in different phase space regions. The mapping of the true characteristics of the primary neutrino, namely the true energy, E_{true}, and the true cosine zenith angle $\cos\theta_{true}$, to the observable phase space spanned by the reconstructed energy, E_{reco}, and the reconstructed cosine zenith $\cos\theta_{reco}$ provides resolution functions for a given event selection. An additional dimension appears when more than one event class is used, typically when events are classified as tracks and showers. This is not the case for the ORCA6 analysis of this dissertation.
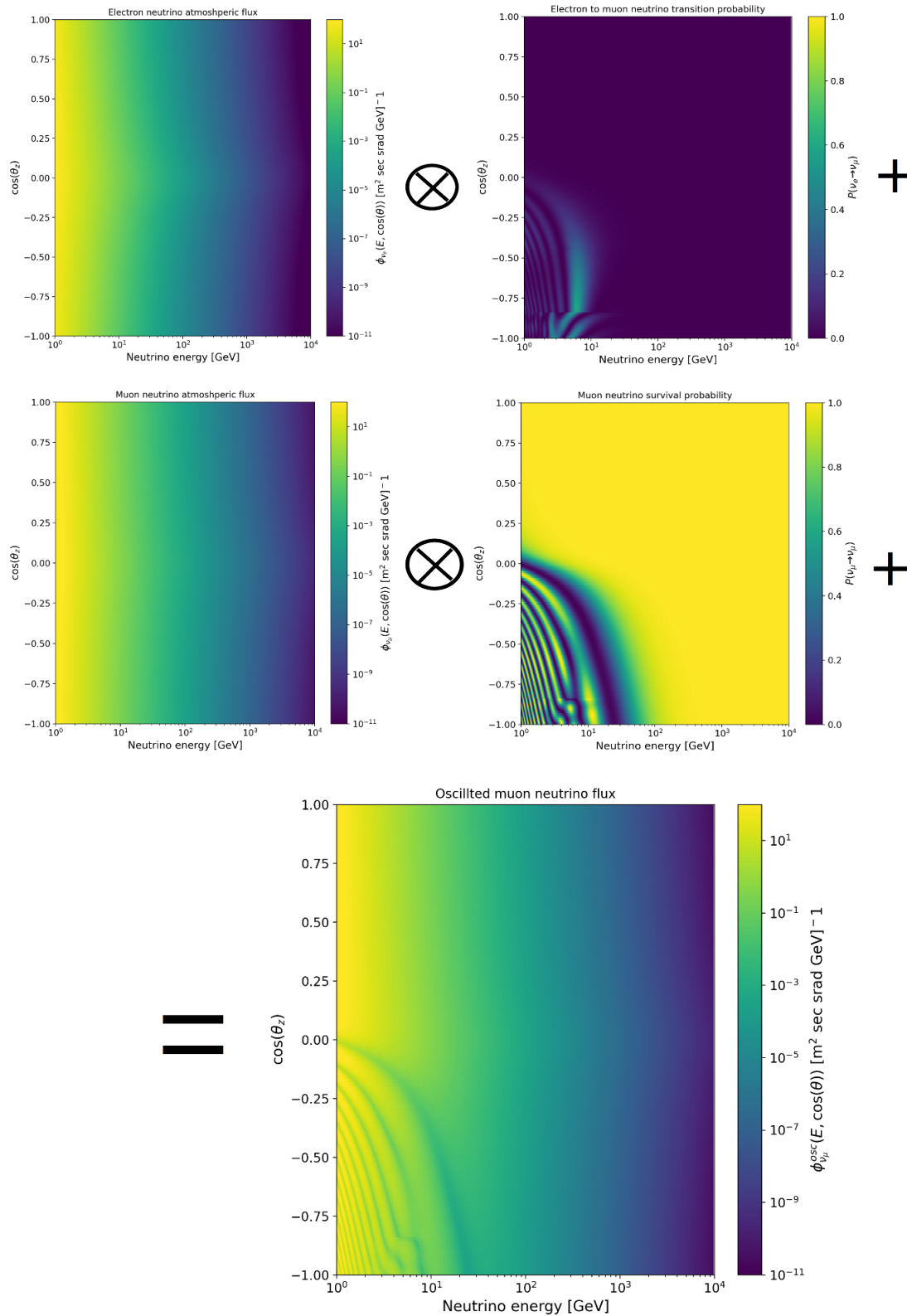
Figure 3.8: Oscillated atmospheric ν_μ flux distribution (bottom center) obtained as the sum of the unoscillated primary fluxes ϕ_{ν_μ} and ϕ_{ν_e} (left upper corner) multiplied by the corresponding oscillation probabilities: the appearance channel $P(\nu_e \rightarrow \nu_\mu)$ and the survival probability $P(\nu_\mu \rightarrow \nu_\mu)$ (right upper corner).
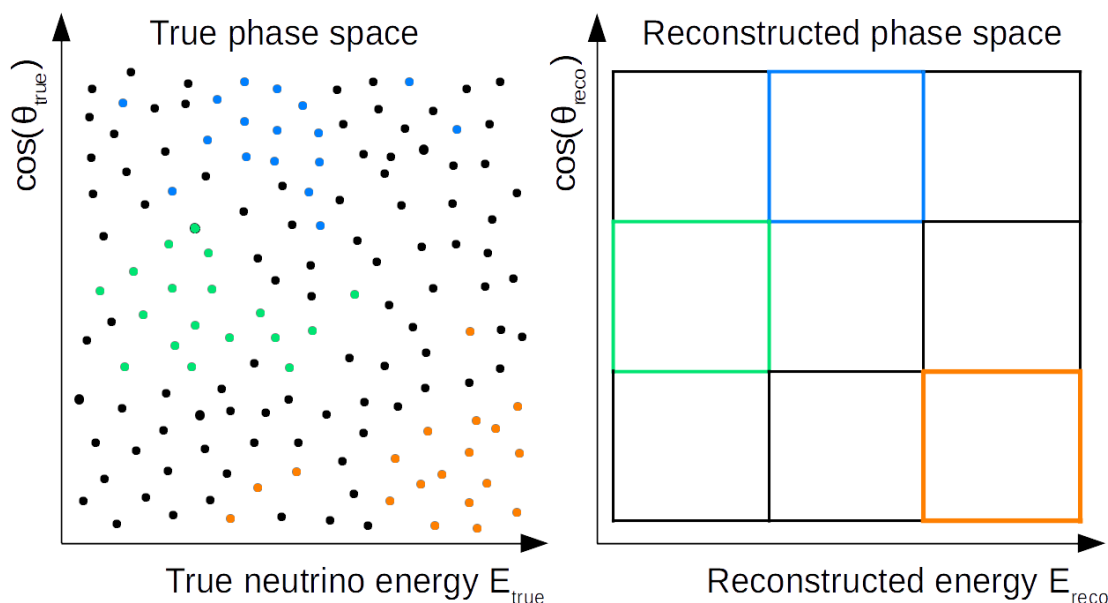
Figure 3.9: A schematic representation of the event-by-event detector response. The colours represent single MC events (on the left) being reconstructed in a given bin (on the right) in the observable phase space. What is not portrayed in the picture is that in reality the distribution of events and their weights reflect the generation flux, which in the gSeagen simulation for ORCA6 follows a power law $E^{-2.5}$. It means that high energy events are sparser, but their individual weights are larger (see Section 3.1.1). A single event contributes only to one bin in the reconstructed space.

The most straightforward approach to estimate the detector response is the event-by-event method, which loops over all the single MC true events contributing to a given bin defined in the reconstructed space. A schematic view of the event-by-event approach is depicted in Fig. 3.9. At the event rate calculation stage, the generation weight of each event is multiplied by the detector exposure and the oscillated flux calculated exactly at the true value of the primary neutrino energy and the incoming direction (equivalent to the oscillation baseline). The event-by-event approach is precise, but also rather slow, so in the ORCA study it is generally used only as a cross-check for the faster binned approach. One of the possible disadvantages of using directly the generation weights is that no systematic uncertainty farther than a simple normalisation can be applied to the cross section model. In MONA, the event-by-event detector response is implemented with a significant simplification to speed up the calculation process. The oscillation probability and the flux are not calculated precisely at the value of the primary neutrino characteristics, but they are stored in tables (more in Sections 3.2.2 and 3.2.1). Even though the true event weights are not binned in this approach, the true space binning has still to be defined to specify the caching granularity.

An alternative, fully binned approach is expressed in the form of a multi-dimensional matrix frequently referred to as response matrix or smearing matrix [138]. In the case of ORCA6, it has 8 dimensions related to the neutrino flavour and the interaction type: ν_e-CC, ν_μ-CC, ν_τ-CC, ν-NC and the corresponding anti-neutrino channels. The response matrix elements

$$R_j^i = N_{sel}^j / N_{gen}^i \qquad (3.5)$$
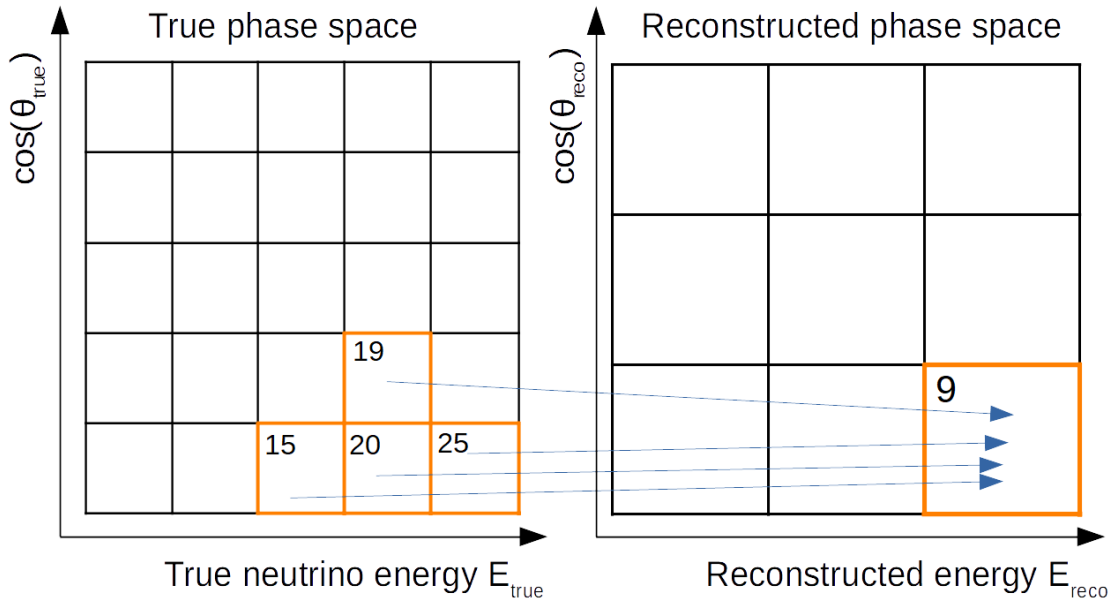
Figure 3.10: A schematic representation of a binned response matrix. The arrows correspond to the matrix elements described by Eq. 3.5. If the true and the reconstructed bins are uniquely labelled as depicted in the figure, the arrows represent the matrix elements R_9^{15}, R_9^{19}, R_9^{20} and R_9^{25}. One true bin normally contributes to multiple reco bins, the one-to-one correspondence appears only if $R_j^i = 1$.

are defined as the fraction of the events generated within a given true bin i reconstructed in a given bin j in the reconstructed space. The matrix elements R_j^i can also be interpreted as a conditional probability

$$R_j^i = P(\text{reco bin } j | \text{true bin } i) \tag{3.6}$$

of finding an event in the bin j in the reconstructed space if it falls in bin i in the true space. A schematic picture of how the binned response matrix works is shown in Fig. 3.10. The choice of the binning is arbitrary, but it is usually driven by the available distribution and abundance of MC events and the detector reconstruction resolutions. The finer the true space binning, the more precise the model predictions can get, but if some of the bins are not sufficiently populated, the MC statistics uncertainty becomes an important source of error. The discussion on this issue is continued in Appendix A.2. Once the response matrix elements are calculated from a given MC sample, the reconstructed rates become

$$n_r^j = \sum_i \sum_{\alpha \in e,\mu,\tau} \sum_{CC/NC} R_j^i \times \phi_{\nu_\alpha}^{osc}(E_i, \cos(\theta_i)) \times \sigma_{\nu_\alpha}(E_i) \times M_{i,eff}^\alpha(E_i, \cos(\theta_i)) \times T, \tag{3.7}$$

where the sum goes over all the true bins and T is the detector exposure time.

With respect to the full event-by-event approach, the speed-up for the binned approach can be seen in the number of iterations. For example, in the case of the ORCA6 event selection, a single template calculation with an event-by-event response would require a loop over true events with ~ 250000 iterations (see Section 4.2). In the case of the binned response used for the ORCA6 analysis in Chapter 4 (30x20 bins in the reconstructed space and 120x40 bins in the true space), the maximum number of iterations reaches $30 \times 20 \times 120 \times 40 \times 8 \approx 2.3 \cdot 10^7$. Nevertheless, since the response matrix is sparse, omitting the matrix elements equal to 0 ends up with $\sim 1.4 \cdot 10^5$ iterations - on average, 228 true

bins contribute to a single reco bin. Improving the reconstruction resolutions and the track/shower classification could reduce this number. Since the oscillation probability and the flux are cached in the same way in both approaches, the expected improvement in calculation speed is of the order of ~ 2.

The MONA software also offers a third method, which can be seen as an intermediate stage between the event-by-event approach and the binned response matrix. Instead of efficiency weights, the true space histogram gets filled directly with the gSeagen event generation weights. In this case, the response matrix elements contain the fraction of the sum of all the generation weights falling into a given true bin. The event rates are obtained as

$$n_r^j = \sum_i \sum_{\alpha \in e, \mu, \tau} \sum_{CC/NC} w_i^j \times \phi_{\nu_\alpha}^{osc}(E_i, \cos(\theta_i)) \times T, \tag{3.8}$$

where the sum goes over the true bins and the interaction channels. The weights w_i^j, which appear in Eq. 3.8 are already divided by the total number of events simulated in each channel (see Section 3.1.1). In this way, the exposure time factor, T, is given in years. This version of the response matrix is used for the analysis in Chapter 4. A few examples of true bin contributions to a single reconstructed bin are shown in Figs 3.11, 3.12, 3.13 and 3.14. The interaction channels are merged into a single output to show the general reconstruction resolution of a given bin. A few features of the detector resolution can be observed:

- the angular resolution increases with the reconstructed energy,

- the reconstructed energy saturates (the explanation of this phenomenon is given in Section 3.4),

- the overall resolution below $E_{reco} \approx 10$ GeV is generally bad.

Instead of histogrammig, other tools like for example Kernel Density Estimators can also be used to obtain the detector resolution functions [139]. In ORCA oscillation analyses, the alternatives were not yet explored as so far the methods described in this section provide a good computing time/precision trade-off.
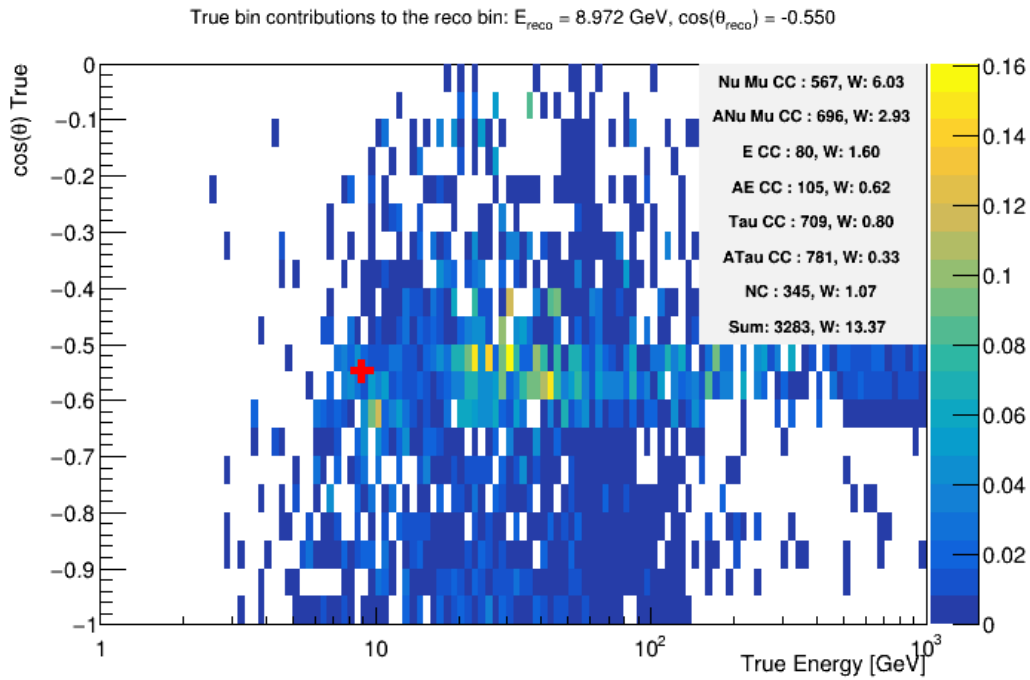
Figure 3.11: True space bins contributions to single reco bin $E_{reco} = [7.94, 10]$ GeV, $\cos(\theta_{reco}) = [-0.6, -0.5]$, whose centre is indicated by the red cross and in the histogram title. The table in the right upper corner shows the number of MC events for each interaction channel and the summed event weights indicated as "W". The weights correspond to NuFIT 5.1 NO best-fit parameters.
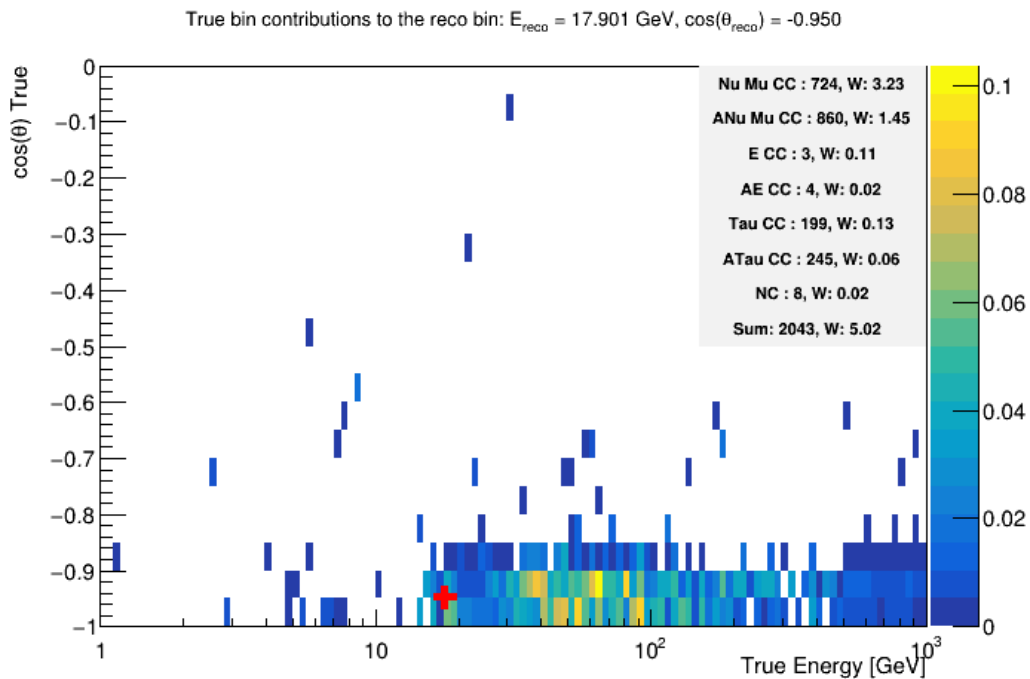
Figure 3.12: True space bins contributions to single reco bin $E_{reco} = [15.85, 19.95]$ GeV, $\cos(\theta_{reco}) = [-1.0, -0.9]$, whose centre is indicated by the red cross and in the histogram title. The table in the right upper corner shows the number of MC events for each interaction channel and the summed event weights indicated as "W". The weights correspond to NuFIT 5.1 NO best-fit parameters.
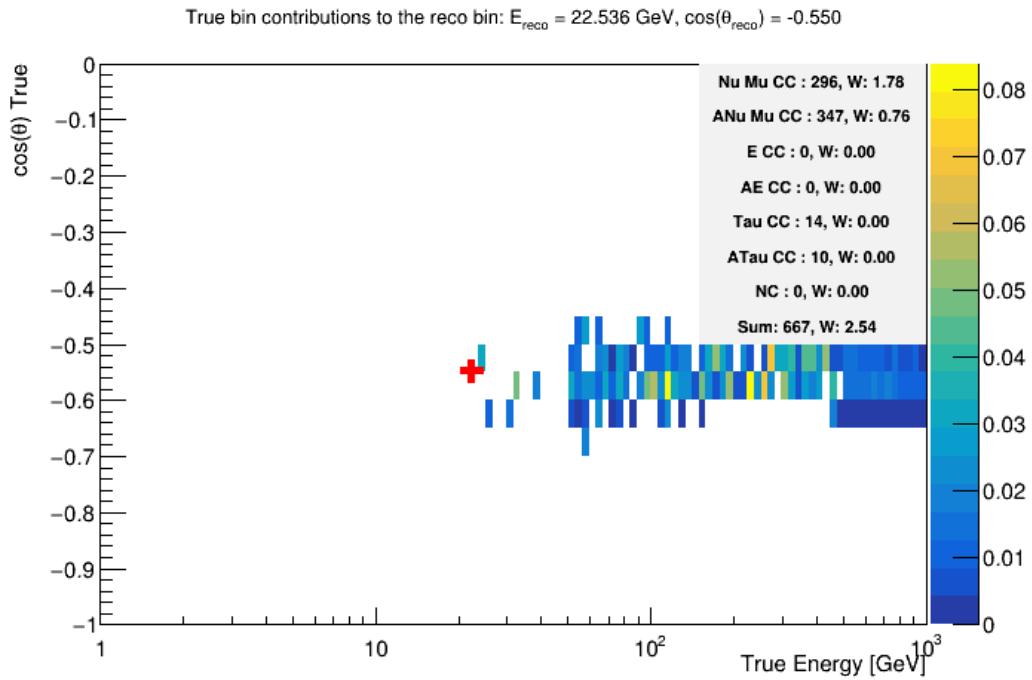
Figure 3.13: True space bins contributions to single reco bin $E_{reco} = [19.95, 25.11]$ GeV, $\cos(\theta_{reco}) = [-0.6, -0.5]$, whose centre is indicated by the red cross and in the histogram title. The table in the right upper corner shows the number of MC events for each interaction channel and the summed event weights indicated as "W". The weights correspond to NuFIT 5.1 NO best-fit parameters.
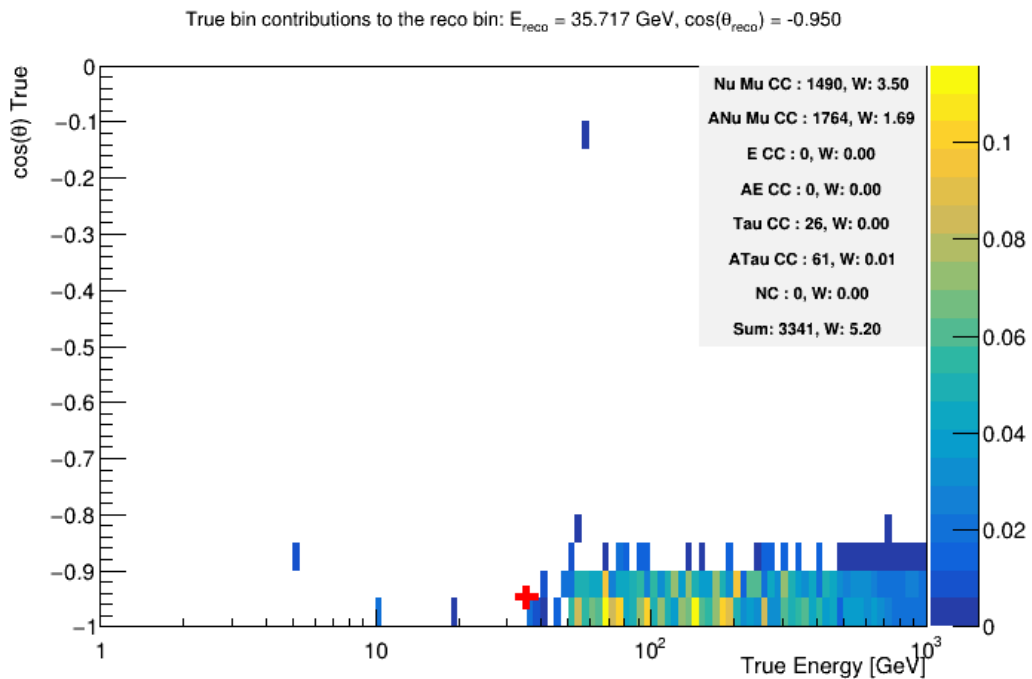
Figure 3.14: True space bins contributions to single reco bin $E_{reco} = [31.62, 39.81]$ GeV, $\cos(\theta_{reco}) = [-1.0, -0.9]$, whose centre is indicated by the red cross and in the histogram title. The table in the right upper corner shows the number of MC events for each interaction channel and the summed event weights indicated as "W". The weights correspond to NuFIT 5.1 NO best-fit parameters.

3.3   Systematic uncertainties

The analysis software incorporates parameters which are designed to account for the systematic uncertainties of the models used for the event rate calculation. When fitting for a given parameter of interest these systematic uncertainty parameters (systematics for short) are treated as nuisance parameters in the statistical model. For example, the systematics associated with the neutrino flux might account for the seasonal variations and the intrinsic uncertainties related to the primary cosmic ray spectrum and composition. In this section, all the systematics affecting the event rate predictions are briefly described.

3.3.1   Flux shape

A parameter referred to as the *flux energy tilt* $\Delta\gamma$ is used to account for the uncertainty in the atmospheric neutrino flux spectral index γ so that the effect of changing the standard flux to a new flux

$$\phi(E, \cos(\theta)) \rightarrow \phi(E, \cos(\theta)) \times E^{\Delta\gamma}. \tag{3.9}$$

is studied. The atmospheric neutrino flux generally follows a power law $\phi \propto E_\nu^{-\gamma}$ with γ varying depending on the neutrino incoming direction ($\cos(\theta)$), the flavour and the neutrino or anti-neutrino nature. For example, for the ν_μ flux in the energy region $1\,\text{GeV} < E_\nu < 10\,\text{TeV}$, the spectral index varies between $\gamma \approx 2.7$ and $\gamma \approx 3.5$. Figure 3.15 shows the ν_μ flux dependence on $\log(E_\nu)$ together with a linear fit, which gives an idea of the typical energy-dependent values of γ for muon neutrinos for vertically up-going directions, $\cos(\theta) = -1$. In principle, more than one flux energy tilt parameter could be needed to cover the wide energy spectrum under study, but we have not considered that scenario for simplicity. The implementation ensures that with the change of $\Delta\gamma$, the
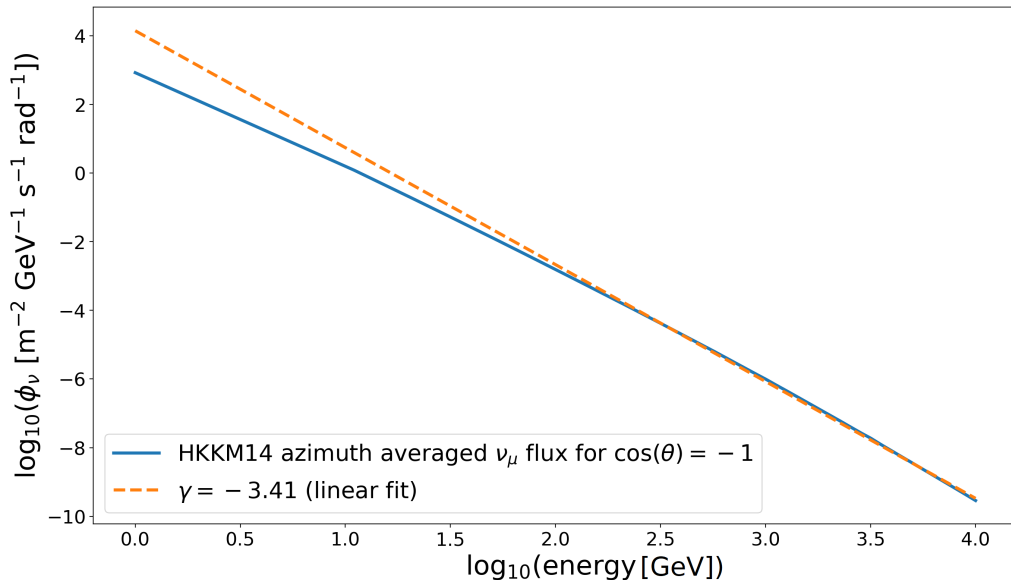
Figure 3.15: Unoscillated muon neutrino atmospheric flux as a function of the neutrino energy plotted in a log-log scale. A linear fit is added to help visualise a typical spectral index value.

overall normalisation of the flux is not affected, but only the flux density gets moved to lower energies ($\Delta\gamma > 0$) or higher energies ($\Delta\gamma < 0$). Figure 3.16 shows how the

initial ν_μ flux changes when a ± 0.2 change is applied in $\Delta\gamma$. An energy independent and fixed $\Delta\gamma$ effectively leads to a relative shift of the spectral index, which increases with the neutrino energy. Even though the global normalisation of the flux is not changed by
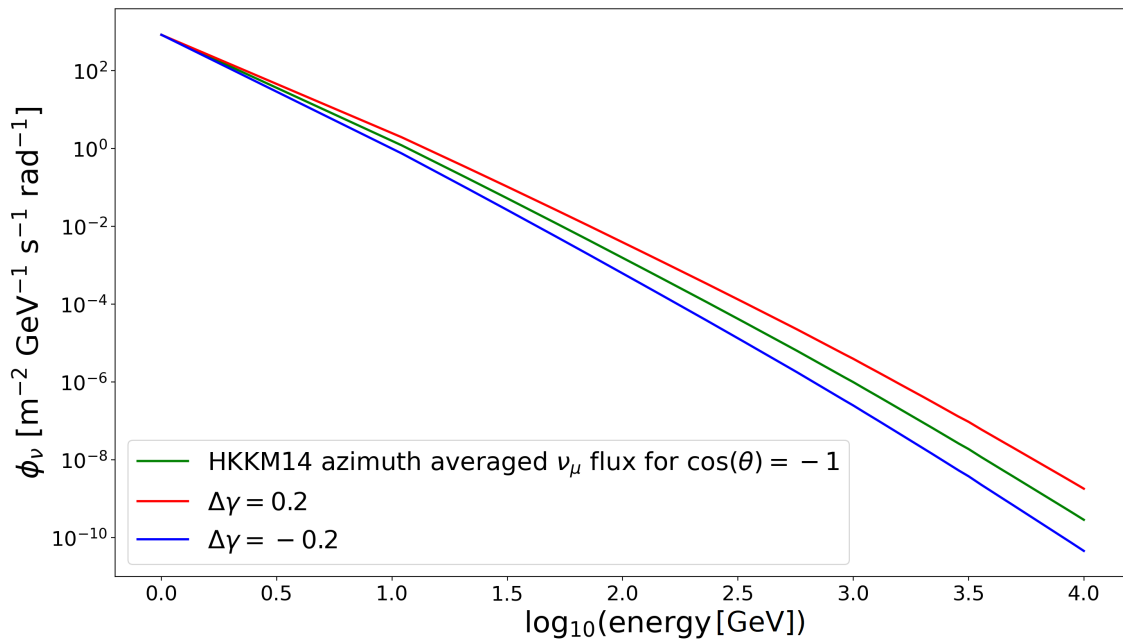
Figure 3.16: Impact of a change ± 0.2 in the flux energy tilt, $\Delta\gamma$ on the unoscillated atmospheric muon neutrino flux as a function of the neutrino energy.

the $\Delta\gamma$ parameter, a non-zero value would effectively change the normalisation of the flux within a certain energy window - for example from 100 to 1000 GeV. Therefore, the normalisation of the distribution used for the analysis might be modified, because the fit range choice does not usually span over the full simulation energy range. The fit range is defined in the reconstructed space, so the level of correlation between $\Delta\gamma$ and the overall normalisation of the event rate distribution depends on the energy resolution. In fact, in MONA, the fit range is forbidden to cover the whole detector response reconstructed phase space, because there has to be some room left for the potential event migration induced by the energy scale systematic (see Section 3.3.6).

Another systematic uncertainty parameter related to the flux shape that is incorporated into the model is the so-called *cosine zenith tilt* Δd, which affects the ratio between the up-going and the down-going events

$$\phi(E, \cos(\theta)) \rightarrow \phi(E, \cos(\theta)) \times (1 + \Delta d \cos(\theta)). \tag{3.10}$$

The effect of a non-zero Δd is depicted in Fig. 3.17: negative values of Δd move the flux towards the up-going directions effectively introducing a positive ν_{up}/ν_{down} skew. A positive Δd has an opposite effect. Due to the fact that the neutrino oscillation analyses are based on up-going events only, the Δd might also be correlated with the overall normalisation, as it was mentioned before for the case of $\Delta\gamma$. However, here the effect is expected to be less significant as Δd can be constrained thanks to the very good angular resolution of the detector in the high energy regime (see Fig. 3.2).
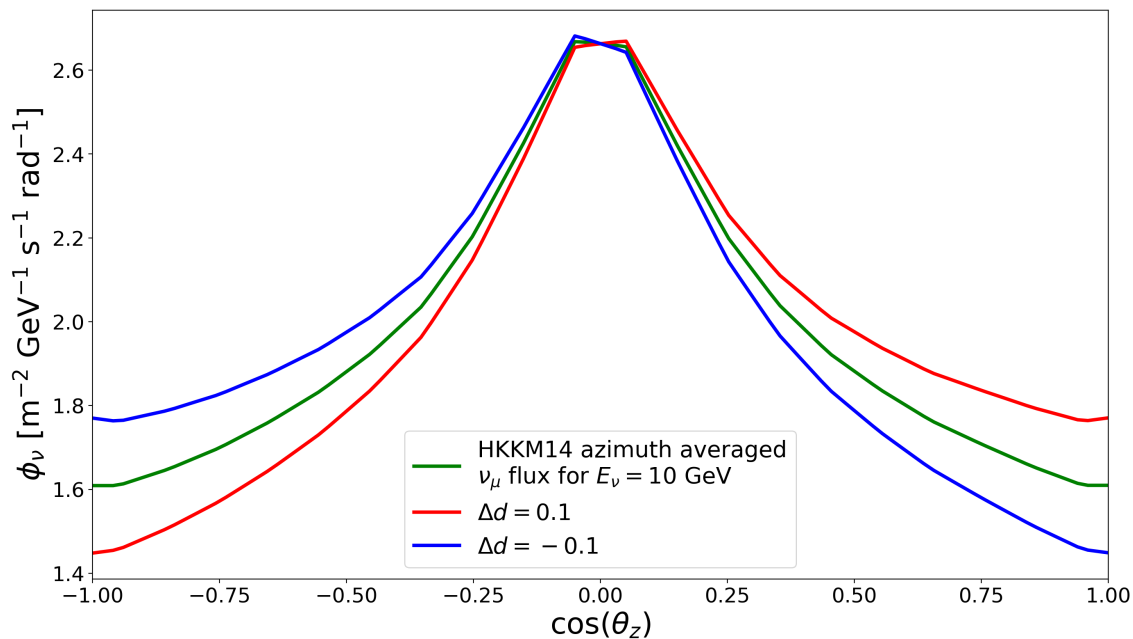
Figure 3.17: Impact of a change in $\pm - .1$ in Δd on the unoscillated atmospheric muon neutrino flux as a function of the cosine of the neutrino zenith angle.

When the flux shape systematics are applied, the overall normalisation of the flux is conserved by applying a re-scaling factor of

$$n_{tilt} = \frac{\sum_i \phi_\nu(E_i, \cos(\theta)_i)}{\sum_i \phi_\nu(E_i, \cos(\theta)_i) \times E^{\Delta\gamma}(1 + \Delta d \cos(\theta))}, \qquad \nu \in \{\nu_e, \nu_\mu, \bar{\nu}_e, \bar{\nu}_\mu\} \qquad (3.11)$$

separately for all the atmospheric flux contributions: $\nu_e, \nu_\mu, \bar{\nu}_e, \bar{\nu}_\mu$. The sum goes over all the entries i in the two-dimensional E_ν versus $\cos(\theta)$ cached flux table. The uncertainty of the flux normalisation is accounted for with a separate parameter described in Section 3.3.4.

3.3.2 Flavour ratios

Three skews are used to account for the uncertainties in the atmospheric neutrino flux ratios:

- $1 + \zeta_{\mu e} = \phi_{\nu_\mu}/\phi_{\nu_e}$,

- $1 + \zeta_{\mu\bar{\mu}} = \phi_{\nu_\mu}/\phi_{\bar{\nu}_\mu}$,

- $1 + \zeta_{e\bar{e}} = \phi_{\nu_e}/\phi_{\bar{\nu}_e}$.

The flux skew parameters are incorporated in the flux calculation by the following formulas:

$$n_{e\bar{e}} = \frac{\phi_{\nu_e} + \phi_{\bar{\nu}_e}}{\phi_{\nu_e}(1 + \zeta_{e\bar{e}}) + \phi_{\bar{\nu}_e}}, \qquad (3.12)$$

$$\phi_{\nu_e}^{\zeta_{e\bar{e}}} = \phi_{\nu_e}(1 + \zeta_{e\bar{e}})n_{e\bar{e}}, \qquad (3.13)$$

$$\phi_{\bar{\nu}_e}^{\zeta_{e\bar{e}}} = \phi_{\bar{\nu}_e} n_{e\bar{e}} \qquad (3.14)$$

where $\phi^{\zeta_{e\bar{e}}}$ is the flux modified by the skew parameter $\zeta_{e\bar{e}}$. An analogous formula is used for the $\phi_{\nu_\mu}/\phi_{\bar{\nu}_\mu}$ flux ratio. In this way the integral of the summed neutrino and

antineutrino flux is conserved

$$\phi_{\nu_e}^{\zeta_{e\bar{e}}} + \phi_{\bar{\nu}_e}^{\zeta_{e\bar{e}}} = \phi_{\nu_e} + \phi_{\bar{\nu}_e}, \tag{3.15}$$

$$\phi_{\nu_\mu}^{\zeta_{\mu\bar{\mu}}} + \phi_{\bar{\nu}_\mu}^{\zeta_{\mu\bar{\mu}}} = \phi_{\nu_\mu} + \phi_{\bar{\nu}_\mu}. \tag{3.16}$$

A similar logic applies to the $\zeta_{\mu e}$ parameter, but in this case the initial flux would already be skewed by the particle-antiparticle ratio asymmetry:

$$n_{\mu e} = \frac{\phi_{\nu_e}^{\zeta_{e\bar{e}}} + \phi_{\bar{\nu}_e}^{\zeta_{e\bar{e}}} + \phi_{\nu_\mu}^{\zeta_{\mu\bar{\mu}}} + \phi_{\bar{\nu}_\mu}^{\zeta_{\mu\bar{\mu}}}}{(\phi_{\nu_\mu}^{\zeta_{\mu\bar{\mu}}} + \phi_{\bar{\nu}_\mu}^{\zeta_{\mu\bar{\mu}}})(1 + \zeta_{\mu e} + \phi_{\nu_e}^{\zeta_{e\bar{e}}} + \phi_{\bar{\nu}_e}^{\zeta_{e\bar{e}}})}, \tag{3.17}$$

$$\phi_{\nu_\mu}^{\zeta_{\mu e}} = \phi_\mu^{\zeta_{\mu\bar{\mu}}}(1 + \zeta_{\mu e})n_{\mu e}, \tag{3.18}$$

$$\phi_{\nu\bar{\mu}}^{\zeta_{\mu e}} = \phi_{\nu\bar{\mu}}^{\zeta_{\mu\bar{\mu}}}(1 + \zeta_{\mu e})n_{\mu e}, \tag{3.19}$$

$$\phi_{\nu_e}^{\zeta_{\mu e}} = \phi_{\nu_e}^{\zeta_{\mu\bar{\mu}}}n_{\mu e}, \tag{3.20}$$

$$\phi_{\bar{\nu}_e}^{\zeta_{\mu e}} = \phi_{\nu\bar{e}}^{\zeta_{\mu\bar{\mu}}}n_{\mu e} \tag{3.21}$$

The above formulas ensure that the skew systematics do not affect the total normalisation of the flux.

3.3.3 Cross-section normalisation

Among all the neutrino cross-section measurements, two have the weakest constraints: σ_{NC} and $\sigma_{CC}^{\nu_\tau}$. Therefore, two normalisation factors are included in the model $n_{\sigma_{NC}}$ and $n_{\sigma_{CC}^{\nu_\tau}}$, which effectively multiply the event rates calculated for ν-NC and ν_τ-CC interactions.

3.3.4 Overall normalisation

A global normalisation factor, n_{tot}, which multiplies the whole reconstructed space histogram, is included in the model to account for a variety of effects such as the flux normalisation, cross section etc. In principle, this parameter should be easily constrained by the measurement of neutrino events in the phase space region where the oscillation effects are not present, but in the presence of NSI, especially $\epsilon_{\mu\tau}$, this assumption might not hold anymore.

3.3.5 Muon normalisation

The distribution of muons passing the event selection enters into each event count template as a constant background unaffected by any of the model parameters. An additional normalisation factor n_μ^{atm} is then assigned to scale all the muon events equally to mitigate the effect of a high statistical uncertainty in the muon count prediction caused by a small number of muon events passing the selection cuts.

3.3.6 Energy scale

The energy scale systematic is designed to account for the uncertainty in the energy estimate stemming from the uncertainties in the quantum efficiency of the PMTs and the seawater properties such as the absorption length. The current implementation in MONA operates in the reconstructed space by shifting the reconstructed energy bin

edges by a constant factor $1 + E_{scale}$, so that the shifted bin boundaries become

$$E^i_{min} \rightarrow E^i_{min} \times (1 + E_{scale}), \tag{3.22}$$

$$E^i_{max} \rightarrow E^i_{max} \times (1 + E_{scale}), \tag{3.23}$$

where i denotes the bin number. The energy bins are equally distributed in logarithmic scale, so their widths are not conserved after the linear shift of their edges, but this effect is rather small. To avoid a full re-calculation of the detector response, the shifted bin boundaries only determine the event density contributions from the original bins which overlap with the boundaries of the shifted bin. Figure 3.18 shows the graphical representation of the shift induced by the energy scale systematic and how the contributions from the original bins to the shifted bin are weighted. The event density from bin 1 contributes to the shifted bin with weight w_1 = (*w1* width / bin 1 width) and analogously the event density from bin 2 contributes with the weight w_2 = (*w2* width / bin 2 width). In other words, the weights denote what fraction of the original bin is contained within the overlapping region. One detail is important to mention: MONA
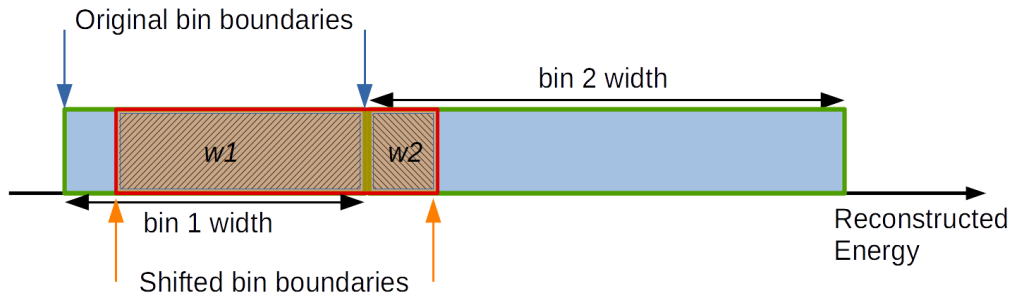
Figure 3.18: A schematic view of the energy scale parameter impact on a reconstructed energy bin. The binning in energy is usually equally spaced in $\log(\text{energy})$.

probability density functions operate on event densities, which are transformed to event rates at the level of the PDF normalisation re-calculation. At the level of the event rate calculation, to conserve the total integral, the event densities contributing from the original bins to the shifted bins have to be multiplied by their corresponding original bin widths.

This approach to the energy scale uncertainty works better with the energy estimate based mainly on the absolute number of detected hits. It is not well suited for the energy reconstruction based on the track length, because the track reconstruction relies more on the photon arrival time compared to a hypothesised cone emerging from the Cherenkov emission. Moreover, in a limited size detector like ORCA6, the full containment of a track is rarely guaranteed – the deposited muon energy is usually only partial and therefore the linear relation between the true and the reconstructed energy is hard to achieve.

3.4   Template generation - the event count ingredients combined

Having all the stages properly modelled, a set of parameters including:

- neutrino oscillation parameters $\theta_{12}, \theta_{13}, \theta_{23}, \Delta m^2_{21}, \Delta m^2_{31}$ and δ_{CP} extended by

- NSI parameters $\epsilon_{\alpha\beta}$ with $\alpha, \beta \in \{e, \mu, \tau\}$,

- flux systematics $\Delta\gamma, \Delta d, \zeta_{e\bar{e}}, \zeta_{\mu\bar{\mu}}, \zeta_{\mu e}$,

- cross section systematics $n_{\sigma_{CC}^{\nu\tau}}$ and $n_{\sigma_{NC}}$,

- overall normalisation n_{tot},

- muon normalisation n_{atm}^{μ},

- detector energy scale E_{scale}

creates a MC event distribution (further referred to as a template) representing a model prediction or a statistical hypothesis, which can be compared to the data or other templates. More about hypothesis testing will be given in Chapter 4. The reconstructed event count is defined as

$$n_{reco}^{j}(E_{reco}^{j}, \cos\left(\theta_{reco}^{j}\right), E_{scale}) = \sum_{i} \sum_{\alpha \in \{e,\mu,\tau\}} \sum_{\nu,\bar{\nu}} \sum_{CC/NC} w_{i}^{j} \times$$

$$n_{tilt}(\Delta\gamma, \Delta d) \cdot [P(\nu_e \to \nu_\alpha)(\text{std osc}, \epsilon_{NSI}) \cdot \phi_e^{\zeta_{\mu e}}(E_{true}^i, \cos\left(\theta_{true}^i\right), \zeta_{\mu e}, \zeta_{e\bar{e}}, \zeta_{\mu\bar{\mu}}, \Delta\gamma, \Delta d) +$$

$$P(\nu_\mu \to \nu_\alpha)(\text{std osc}, \epsilon_{NSI}) \cdot \phi_\mu^{\zeta_{\mu e}}(E_{true}^i, \cos\left(\theta_{true}^i\right), \zeta_{\mu e}, \zeta_{e\bar{e}}, \zeta_{\mu\bar{\mu}}, \Delta\gamma, \Delta d)]$$

$$\times n_{tot} \times \delta_{\alpha\tau} n_{\sigma_{CC}^{\nu\tau}} \times \delta_{xx,NC} n_{\sigma_{NC}} + n_{atm}^{\mu} \cdot N_{atm,j}^{\mu},$$

$$(3.24)$$

where

- the reconstructed bin j has its centre at $\{E_{reco}^{j}, \cos\left(\theta_{reco}^{j}\right)\}$, potentially modified by the E_{scale} systematic uncertainty parameter,

- the first sum goes over all the true bins i contributing to bin j,

- the other sums go over the interaction channel dimension of the response matrix: ν_e-CC, $\bar{\nu}_e$-CC, ν_μ-CC, $\bar{\nu}_\mu$-CC, ν_τ-CC, $\bar{\nu}_\tau$-CC, ν-NC and $\bar{\nu}$-NC,

- std osc = $\{\theta_{12}, \theta_{13}, \theta_{23}, \Delta m_{21}^2, \Delta m_{31}^2, \delta_{CP}\}$ denotes the standard oscillation parameters,

- ϵ_{NSI} denotes all the non-zero NSI parameters used in the oscillation model,

- $\delta_{\alpha\tau}$ and $\delta_{(N/C)C,NC}$ are Kronecker deltas isolating the tau neutrino flavour or the NC interactions (keep in mind that the single flavour which was used for the NC simulation was ν_μ, so the deltas do not introduce extra terms)

- $N_{atm,j}^{\mu}$ represents the number of atmopsheric muons found in the reconstructed bin j.

Examples of event distributions of ORCA6 MC sample weighted for 355 days of detector exposure are shown in Fig. 3.19. The irregular, non-rectangular shape is caused by the choice of the energy estimator - track length using the 0.25 GeV/m relation. The zenith-dependent maximum track length roughly follows

$$l_{max}(\cos(\theta)) = \begin{cases} \frac{d}{\sqrt{(1-\cos^2(\theta))}}, \text{for } \cos(\theta) \in [-0.958, 0] \\ \frac{h}{-\cos(\theta)}, \text{for } \cos(\theta) \in [-1.0, -0.958] \end{cases} \quad (3.25)$$

where $d = 58.6$ m is the approximated instrumented volume cylinder diameter and $h = 189.8$ m is its height. The limiting angle θ_{lim} corresponding to $\cos(\theta_{lim}) \approx -0.958$ determines the global maximum muon path length inside the cylinder $\hat{l}_{max}(-0.958) \approx 198.1$ m. For directions below $\cos(\theta_{lim})$, it is the height, which is constant in the maximum path calculation. Above $\cos(\theta_{lim})$, it is the diameter. Figure 3.20 shows the scheme of the instrumented volume cylinder with the Eq. 3.25 related definitions. In reality, the

(a) Normal Ordering NuFIT 5.1.

(b) Normal Ordering NuFIT 5.1 $+ \epsilon_{\mu\tau} = 0.02$.
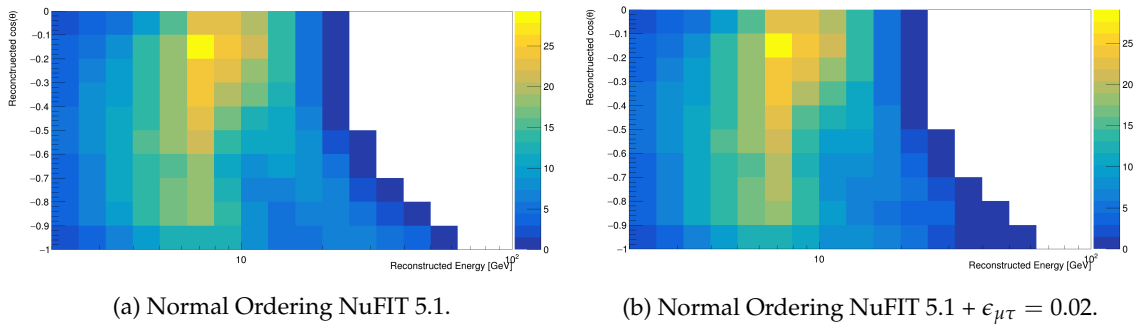
Figure 3.19: Example of templates with event rate predictions for an ORCA6 selected sample. All the systematic uncertainty parameters are fixed at their nominal values. The oscillation parameters are set according to the neutrino mass ordering, the oscillation parameters given by NuFIT 5.1 and the indicated NSI parameter.
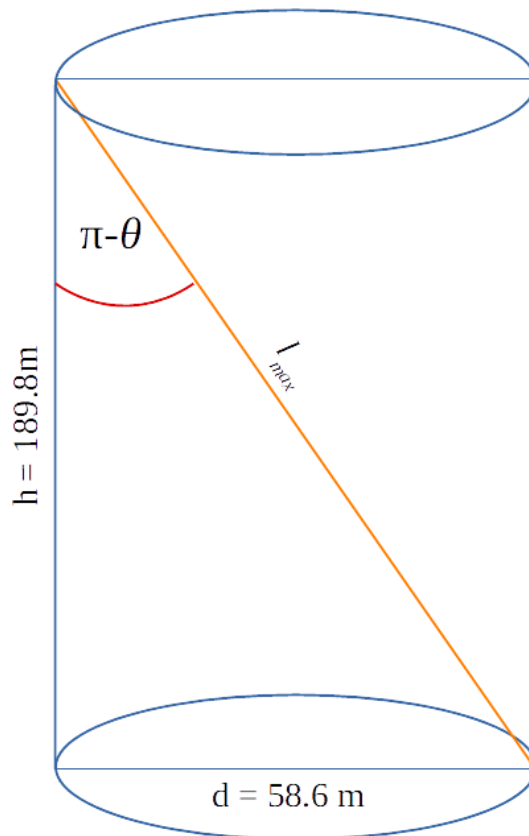
Figure 3.20: The dimensions of a cylinder approximating the instrumented volume of ORCA6. The relation between the cylinder base and the positions of the ORCA6 DUs can be seen in Fig. 2.3. The angle definition corresponds to the convention used in KM3NeT: for up-going events $\cos(\theta) = -1 \rightarrow \theta = \pi$; for horizontal events $\cos(\theta) = 0 \rightarrow \theta = 0$. The presented case corresponds to the limiting case, which determines the shift in the l_{max} definition in Eq. 3.25.

geometry has to be extended by the distance to the first photon emission point, which can lay outside the approximated cylinder. This is especially important for horizontal tracks, where the maximum measured length is roughly equal to the diameter of the approximated cylinder. The actual maximum track length, which was reconstructed in the ORCA6 MC event sample is 202.1 m. Transforming Eq. 3.25 with the relation

$E_{reco}^{max} = l_{max}/4 \text{ m} \cdot \text{GeV}$, we get

$$E_{reco}^{max}(\cos(\theta_{reco})) = \frac{d}{4\sqrt{(1 - \cos^2(\theta))}}, \tag{3.26}$$

$$\cos(\theta_{reco}) = -\sqrt{1 - \left(\frac{r/2}{E_{reco}}\right)^2}, \tag{3.27}$$

where $r = d/2$ is the cylinder radius. The function in Eq. 3.27 on top of an ORCA6 event distribution is shown in Fig. 3.21.
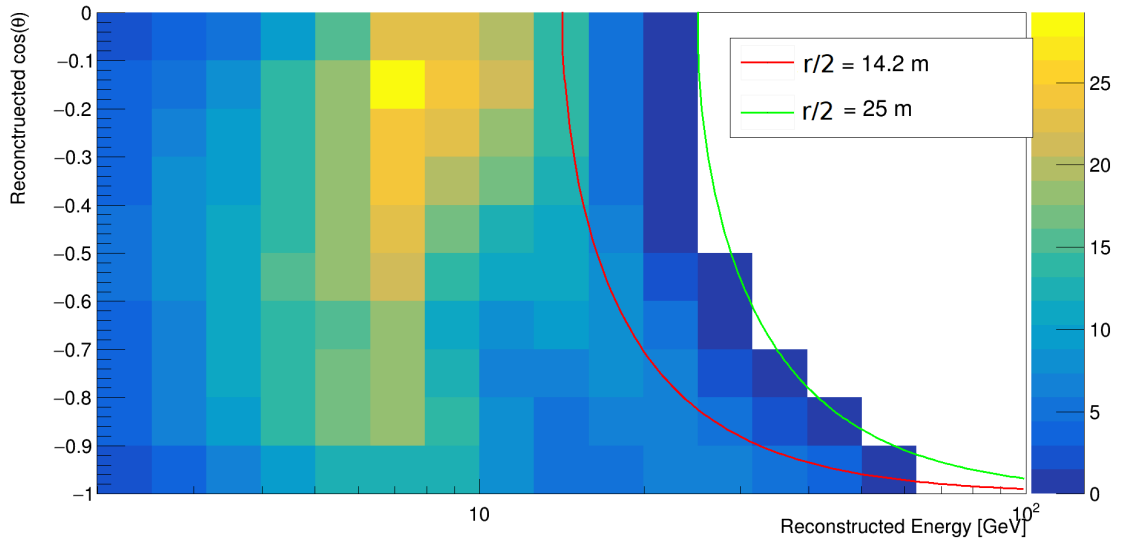
Figure 3.21: An ORCA6 event distribution using the NuFIT 5.1 NO oscillation parameter set. The lines indicate the maximum possible reconstructed energy calculated with the formula in Eq. 3.27 assuming different values of the instrumented volume cylinder radius. The red line corresponds to the ORCA6 DUs smallest enclosing circle shown in Figs 2.3 and 3.20, while the green line is adjusted for the first photon emission distance (see text for details).

4 Neutrino Non-Standard Interactions measurement with ORCA6

Contents

This chapter presents the first results on neutrino non-standard interactions obtained with ORCA6 data. First, in Section 4.1, the tested NSI models are introduced. The run and the event selection developed to extract a pure neutrino sample are described in Section 4.2. The statistical methods used to perform the analysis and verify the results can be found in Section 4.3. The treatment of the systematic uncertainty parameters and the evaluation of their impact on the tested models appears in Section 4.6. The final results are presented in Section 4.7 and then partially verified with a more strict statistical treatment in Section 4.9 and a variation in the Earth matter model (Section 4.8). Finally, the results are compared with other measurements and discussed for conclusions and future prospects.

4.1   The NSI analysis approach

Neutrino non-standard interactions with their 9 effective parameters (3 real diagonal terms, 3 moduli and 3 complex phases) provide many possible combinations, which in principle represent different models. Looking into one isolated NSI parameter at a time probes a very specific subset of idealised NSI models which neglect possible correlations and synergies between the NSI parameters. However, this approach was adopted before by other experiments as it can already provide a useful insight in the area of the NSI research. Considering the limited resolution of the early stage detector, the following scenarios were chosen to be tested with the ORCA6 data:

1. one NSI parameter at a time assuming its real nature ($\delta_{\alpha\beta} = 0$): $\{\epsilon_{\mu\tau}, \epsilon_{e\tau}, \epsilon_{e\mu}, \epsilon_{\tau\tau} - \epsilon_{\mu\mu}\}$,

2. the off-diagonal, flavour-violating parameters profiled over the corresponding complex phase treated as a nuisance parameter (in these cases $\delta_{CP} = 0$ is set to avoid any possible interference with the NSI complex phases),

3. two-dimensional scans in the space of a non-diagonal parameter versus its corresponding complex phase.

As explained before in Section 1.2.3, in our models, NSIs are assumed to couple to d quarks only. The $\epsilon_{ee} - \epsilon_{\mu\mu}$ parameter is not considered in the analysis, because, without a sample optimised for selecting electron neutrinos, no sensitivity in ORCA is expected. This kind of selection can be achieved only with a shower reconstruction, which is not yet available for ORCA6.

4.2   Event sample

In this analysis we follow the run and event sample used for the standard oscillation analysis [137], so that our results can be compared straight away to those obtained in that analysis. The ORCA6 data taking period which is taken into account in the analysis spans between January 2020 and March 2021.

4.2.1   Run selection

In KM3NeT, a run is defined as a 6-hour data taking period. To ensure the proper quality of the data taking conditions, data runs have to fulfil some quality criteria. To be considered for the event selection, runs had to first pass the so-called "Silver" criteria:

- The detector configuration must be set to "physics" mode (some runs are dedicated for calibration),

- The runs must have at least one hour of livetime,

- The trigger rate must be above $0\,\text{Hz}$ (i.e. data was actually taken) and below $1\,\text{kHz}$ (exclude temporary problems with the triggering procedure).

Out of the total data taking period of 402.1 days, the processed runs passing the quality conditions add up to 354.6 days (1545 runs) of detector exposure. Figure 4.1 shows the available detector exposure at the different selection levels evolving with the data taking time together with the high-rate veto fraction and the average trigger rate. As can be seen, 88% of the total number of data runs were processed and passed the run selection. Most of the peaks at the PMT rates (correlating with the HRV rates) correspond to the drops

in the trigger rates as expected (see Chapter 2). Some jumps in the HRV rates which do not cause the trigger rate to drop are most likely induced by very localised background flashes possibly happening at the edge of the detector.
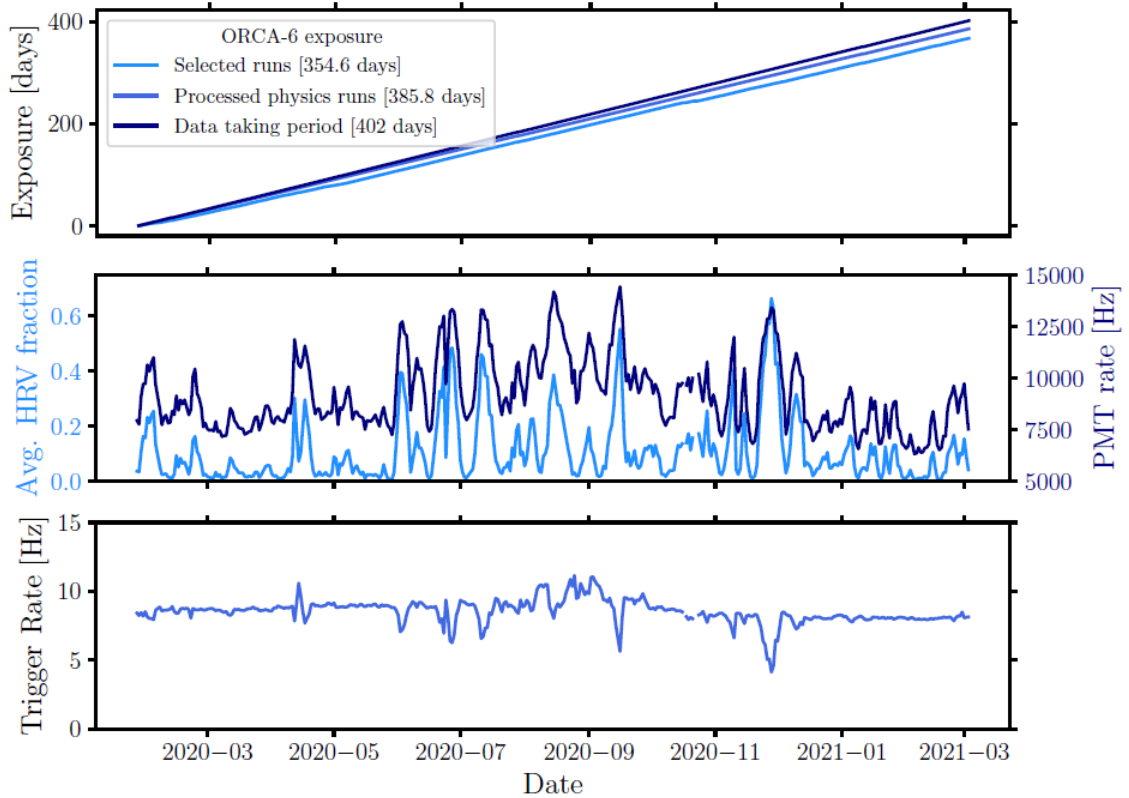
Figure 4.1: Top: Exposure (cumulative livetime) of the detector for three run processing levels. Middle: The daily average PMT rate on top of the average high-rate veto fraction as a function of the detector operation date (center). Both quantities averaged per day. The one day average trigger rate (bottom). Taken from ref. [137].

4.2.2 Event selection criteria

In a raw data sample the vast majority of the measured events come from atmospheric muons and optical background. In order to study oscillations, it is essential to select neutrino events from the data. Here, the neutrino selection is based on a set of manual cuts applied both to low and high level variables extracted from the trigger information and the reconstruction output. Due to the fact that only the track reconstruction was applied to the data sample used in this analysis (see Section 2.4), the selection cuts presented in this section are mainly targeting muon neutrinos identified by a track induced by the secondary muon (track-like events).

The criteria applied to select a proper neutrino event sample (the "selection cuts", for short) are described in Table 4.1. The definitions of the cut variables are:

1. ℓ – log(likelihood) of the best solution from the track reconstruction algorithm,

2. Max ToT – Maximum time over threshold among the triggered hits present in the event,

3. N_{early}^{trig} – early triggered hits; the hits whose difference between the hit time in data, t_{hit}, and the hit time expected from the reconstruction hypothesis ,t_{exp}, is smaller than 10 ns:

$$t_{hit} - t_{exp} < 10 \text{ ns}$$

4. N_{DOM}^{Ch} – number of DOMs fulfilling the Cherenkov condition of having at least one hit passing the following constraints:

   - the distance of closest approach between the hit PMT and the line representing the track hypothesis is smaller than 100 m,

   - the photon arrival direction, calculated assuming the Cherenkov angle and the reconstructed track, faces the front side of the PMT,

   - the absolute time difference between the measured hit time t_{hit} and the hit time expected from the reconstruction hypothesis t_{exp} is smaller than 10 ns

$$|t_{hit} - t_{exp}| < 10 \text{ ns}$$

   .

5. ℓ/n_{hits} – log(likelihood) divided by the total number of hits used in the reconstruction,

6. $\ell^{up} - \ell^{down}$ – the difference between the best up-going and the best down-going solutions in the track reconstruction,

7. r_{vertex} – the reconstructed vertex radial position,

8. $\langle z_{hits}^{trig} \rangle$ – the mean z of the trigger hits using the PMT coordinates,

9. z_{vertex} - the reconstructed vertex z position.

The target of the cuts can be divided into the following general classes:

- Anti-background – these basic cuts are meant to completely discard the optical noise and most of the atmospheric muons coming from above the detector (see Section 2.5.3).

- Reconstruction (Reco) quality – this set of cuts ensures that the information provided by the reconstruction algorithm is plausible and represents a clear track.

- Track quality – a higher-level set of cuts targeting the misreconstructed atmospheric muons. The reconstructed tracks are expected to be unambiguously up-going with a strict requirement for the up-going solution preference. The cut relating the likelihood with the reconstructed vertex position avoids muons arriving at the direction with $\theta_z \approx \pm\theta_{Ch}$ roughly equal to the Cherenkov angle. If such a muon passes far from the detector centre, its signal will be seen as a horizontal wall of light making a reasonable direction reconstruction impossible.

- Containment – generally, the farther the particles pass from the detector barycenter the more unreliable the track reconstruction becomes. Moreover, the set of cuts was aimed mainly for the standard oscillation analysis, where the signal is expected in the energy region roughly between 10 GeV and 30 GeV. Therefore, there is no loss of signal in the exclusion of the tracks with vertices far from the detector centre.

These classes are meant to give the reader an idea of the main goal of the cuts, however they are interconnected and typically cannot be used separately.

The number of MC events passing the cuts split by the interaction channel together with the summed weights are shown in Table 4.2. The NuFIT 5.1 NO parameters have been used and the numbers correspond to a livetime of 354.6 days. The total number of events passing the cuts in the data was 1237. A more detailed description of the impact of every single selection cut on the data and the MC sample together with a closer look on how the changing data-taking conditions are incorporated into the simulation can be found in ref. [137]. For the NuFIT 5.1 oscillation parameters, the flavour composition expected at

Purpose	Cut variable and value
Anti-background	$\ell > 40$
	Max ToT $< 250\,\text{ns}$
	$\cos(\theta_{reco}) < 0$
Reco quality	$N_{early}^{trig} < 6$
	$N_{DOM}^{Ch} \geq 8$
Track quality	$\ell / n_{hits} > 2$
	$\ell^{up} - \ell^{down} > 40$
	$\ell > (r_{vertex} - 30) \times 5.6 + 60$
Containment	$r_{vertex} < 60\,\text{m}$
	$\langle z_{hits}^{trig} \rangle > 55\,\text{m}$
	$\langle z_{hits}^{trig} \rangle > z_{vertex}$

Table 4.1: Selection criteria (cuts) of the ORCA6 event selection. For the definitions of the cut variables see text.

the detector for an Asimov data set (a pseudo data set created at the expectation values of the model parameters [140]) is the following:

- ν_μ CC – 70% (out of which 24% belongs to $\bar{\nu}_\mu$, this gives $\nu_\mu / \bar{\nu}_\mu$ ratio of about 2),

- ν_e CC – 16.5%,

- ν_τ CC – 5.5%,

Interaction channel	Number of MC events	Number of reconstructed events weighted for NuFIT 5.1 NO
ν_μ CC	56197	570.2
$\bar{\nu}_\mu$ CC	69556	300.5
ν_e CC	9362	149
$\bar{\nu}_e$ CC	12242	56.4
ν_τ CC	35376	48.3
$\bar{\nu}_\tau$ CC	38738	19.4
NC	25907	67.8
atmospheric muons	10	33.58
total events	247388	1245

Table 4.2: Monte Carlo simulated events in ORCA6, weights correspond to 354.6 days of livetime.

- NC all flavours – 5%,

- atmospheric muons – 2.7%.

Notice that the total adds up to 99.7% because of rounding. Figure 4.2 shows the distribution of the data and the MC samples split by interaction channels as a function of the reconstructed energy for 354.6 days exposure of ORCA6 with the event selection defined in Table 4.2. Above 10 GeV muon neutrinos become the only relevant neutrino flavour. The data/MC agreement appears to be very good and already indicates the presence of neutrino oscillations as the oscillation parameters in the MC prediction are set to NuFIT 5.1 NO. Figure 4.3 shows the ORCA6 data and MC samples divided into neutrino and atmospheric muon contributions as a function of the reconstructed $\cos(\theta)$. The distributions are depicted either only for the first cut (pure-noise-cut) in Table 4.1 (empty boxes) or the full set of neutrino selection cuts (filled boxes). As can be seen in both plots, the MC/data agreement is very good.

4.2.3   Muon background in the analysis

The atmospheric muon contamination contributes to the event rate predictions at the detector as a constant background distribution scaled with the livetime and added on top of the oscillated neutrino signal. The integral of the muon distribution is controlled in the fit by the overall normalisation and the separate muon normalisation, which in this configuration defines the ratio between the total yield of muons and neutrinos in the model. The event selection described in Section 4.2 was optimised for high neutrino purity, so it deliberately provides a very aggressive rejection of atmospheric muon events. The problem with this approach is that the statistics available in the MC sample (only 10 MC events passing the cuts) is insufficient to reliably evaluate the shape of the distribution of the atmospheric muons passing the selection cuts. As it was mentioned in Section 3.1.2, muon generation is the most computationally expensive part of the KM3NeT simulation chain. Therefore, simply generating more statistics is typically not feasible. The problem is approached with the distribution smearing using kernel algorithm using the ROOT function `TH2::Smooth()` with the default options[1]. The distribution of the muon events passing the cuts weighted for the 354.6 days of detector exposure is shown in Fig. 4.4. The smoothed muon distribution is shown in Fig. 4.5. Notice that the total number of muons is conserved.

---

[1]for details see https://root.cern.ch/doc/master/classTH2.html
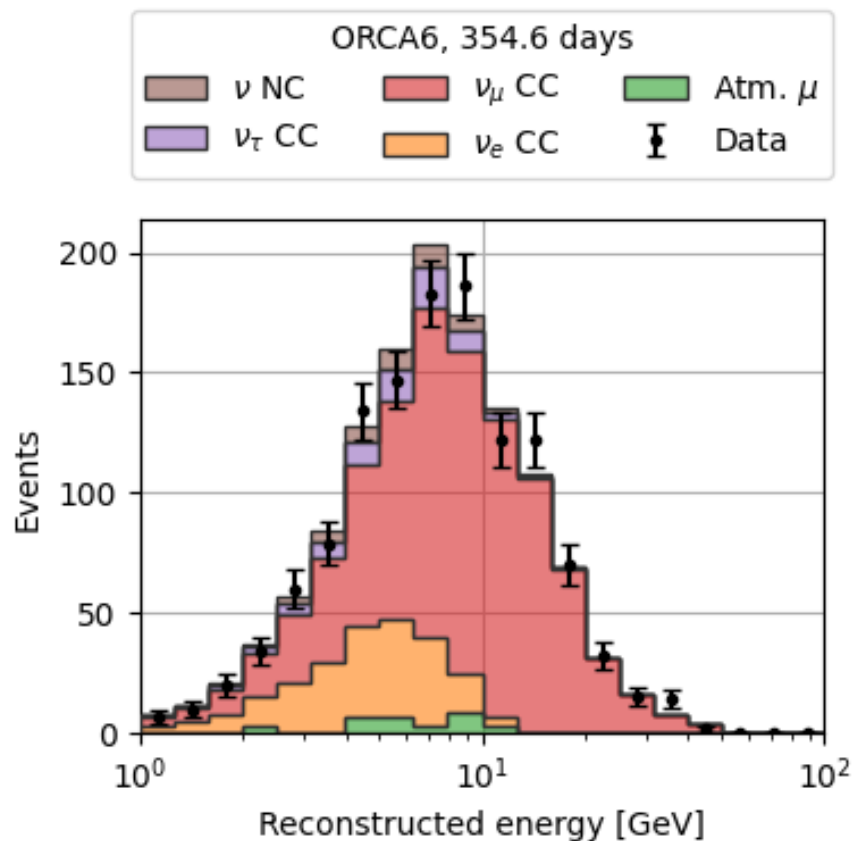
Figure 4.2: Distribution of the number of events as a function of reconstructed energy split by interaction channel for 354.6 days of ORCA 6 livetime. For the MC predictions, the NuFIT 5.1 NO parameters were used.

4.3 Analysis method

This section describes the statistical tools used in the analysis to obtain the results presented in Section 4.7. The distinct methods are aimed at the following objectives:

- parameter estimation,
- confidence interval estimation,
- *goodness of fit* evaluation,
- verification of the Wilks' theorem approximation.

4.3.1 Parameter estimation

Parameter estimation is based on the maximum likelihood method. Likelihood $L(\overline{\omega}) = P(\overline{x}|\overline{\omega})$ denotes the conditional probability of the measured data $\overline{x}$ given the set of parameters in the model $\overline{\omega} = \{\omega_1, \omega_2, ..., \omega_n, \}$. Maximising the likelihood for a given data set gives the maximum likelihood estimates (MLEs) of the parameters. To simplify the calculations and improve numerical stability, it is often convenient to minimise the negative log-likelihood instead, taking advantage of the monotonicity of the logarithm function. In such a case, the maximum likelihood estimators are found with the set of
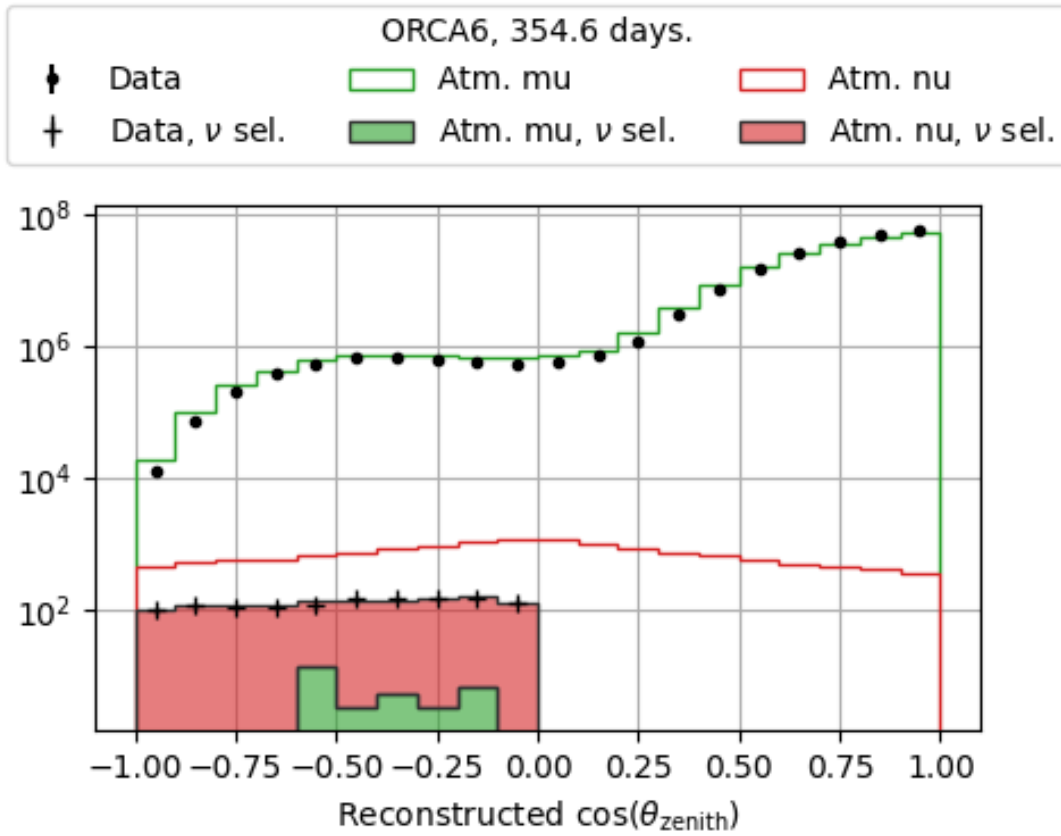
Figure 4.3: Distribution of the number of events as a function of reconstructed cosine zenith divided into neutrino and atmospheric muon contributions for 354.6 days of ORCA 6 livetime. For the MC predictions, the NuFIT 5.1 NO parameters were used.
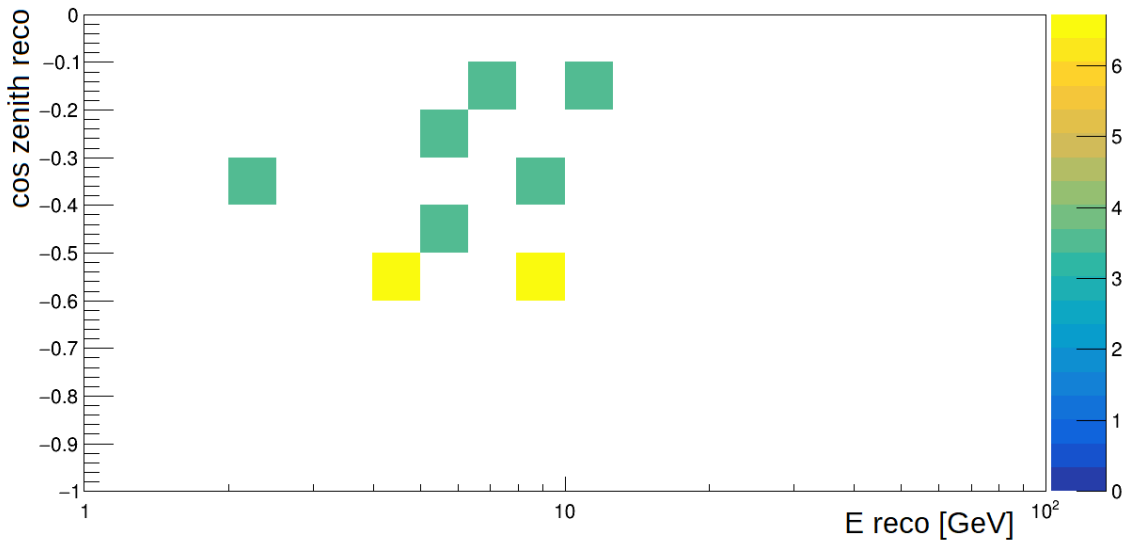
Figure 4.4: Muon events passing the ORCA6 event selection cuts before the distribution smearing.

equations:

$$-\frac{\partial \ln(L)}{\partial \omega_i} = 0, \quad i = 1, 2, ..., n. \tag{4.1}$$
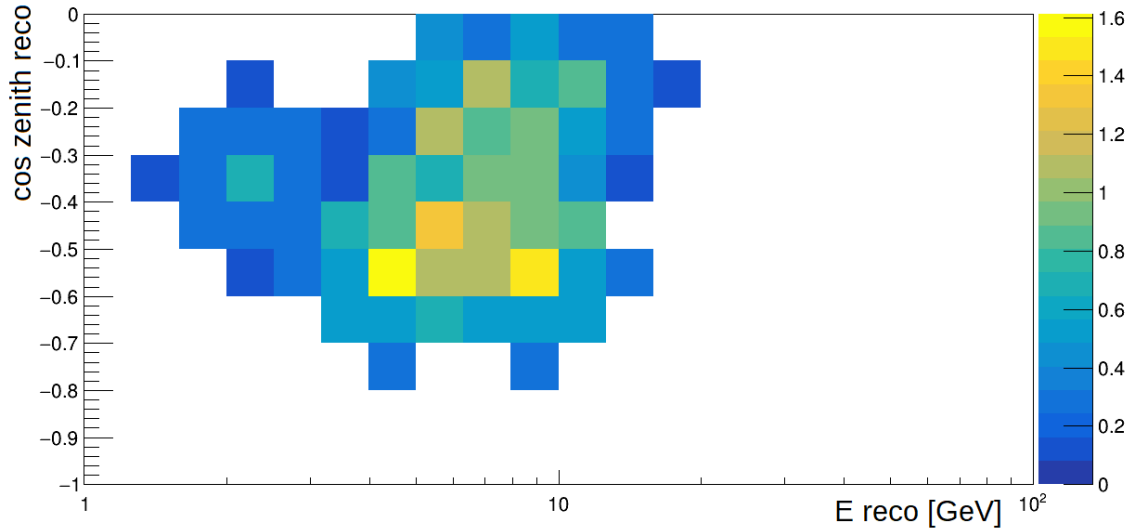
Figure 4.5: The smeared MC distribution of the atmospheric muons contributing to 354.6 days in ORCA6 event selection. The smearing was done with the ROOT `TH2::Smooth()` function using the default kernel.

Since in our case the data is histogrammed, a binned likelihood is used in the analysis. Each measured bin content N_i is treated as an independent Poisson distributed variable with an expectation value of μ_i so that the total likelihood function can be written as

$$L = \prod_i^{n_{reco}} \text{Pois}(N_i | \mu_i(\overline{\omega})), \tag{4.2}$$

where the expectation values for the bin contents μ_i depend on the model parameters $\overline{\omega}$. The parameters of the model used in this analysis are summed up in Section 3.4. The total number of events also follows a Poisson distribution with the expectation value $\mu_{tot} = \sum \mu_i$. The Poisson probability distribution is defined as

$$\text{Pois}(k|\mu) = \frac{\mu^k e^{-\mu}}{k!}, \tag{4.3}$$

where k is the measured number of events and μ is the parameter denoting the expectation value and the variance at the same time. The standard deviation is therefore equal to $\sqrt{\mu}$.

4.3.2 Goodness of fit

Once the $-\ln(L)$ minimisation is done and the maximum likelihood estimates of the model parameters are established, it is necessary to estimate *goodness of fit*, which is essentially a way to evaluate if a given hypothesis is consistent with the data. In other words, goodness of fit should quantify the probability of getting a result at least as extreme as the measured data under the assumption that the hypothesis being tested (maximum likelihood fit in this case) is true. This probability is frequently referred to as the p-value. To evaluate goodness of fit of the best-fit hypothesis, we choose a commonly used Chi-square goodness of fit method, which evaluates the p-value using χ^2 statistic with the corresponding number of degrees of freedom. Any test statistic asymptotically approaching the χ^2 distribution can be used for this test [141]. The -2log-likelihood ratio

is used in our case [142]:

$$-2\ln\left(\frac{L(\hat{\mu})}{L(N)}\right) = 2\sum_i^{n_{reco}}\left(\hat{\mu}_i(\overline{\omega}) - N_i + N_i\ln\frac{N_i}{\hat{\mu}_i(\overline{\omega})}\right) \tag{4.4}$$

where $\hat{\mu}_i$ is the MLE of the expected number of events in bin i and N_i is the measured number of events in this bin. For Poisson distributed measurements, the test statistic in Eq. 4.4 is believed to approach the χ^2 distribution faster than the Pearson's Chi-squared [20]. In the case of a histogram and the binned likelihood in Eq. 4.2, there are $B - p$ degrees of freedom, where B is the number of bins and p is the number of fitted parameters.

However, a problem with the definition of the number of degrees of freedom may emerge if the fitted model has a non-linear dependence on any of the model parameters or in the case when the parameters are constrained with priors [143]. Even for linear models, the number of degrees of freedom can still vary between $B - 1$ and $B - p$. Therefore, as a cross-check for the Poisson Chi-square goodness of fit evaluation, the Kolmogorov-Smirnov (KS) test is used [144, 145]. In its original version, the KS test can only be applied to verify if a data set can be described by a continuous distribution [146]. However, in an approximate way, the test can also be used with two discrete distributions, like histograms. In this case, it is tested if the two histograms come from the same distribution, but the advantage is that no distribution shape has to be assumed like it is done in the Chi-square test. The method compares the normalised cumulative distributions of the two histograms (in our case the data and the best-fit MC prediction) and takes the maximum distance between them as a metric for the p-value evaluation. The implementation for the case of two-dimensional histograms is described in ref. [147]. As can be read there:

- "As long as the bin width is small compared with any significant physical effect (for example the experimental resolution) then the binning cannot have an important effect" and

- "The effect of binning (if any) is always to make the value of PROB slightly too big" (here PROB refers to the p-value).

Since in the ORCA6 response matrix (see Section 3.2.5) the bins are much smaller than the expected resolution (see Section 3.1.5), the use of KS test seems to be a good choice for a more conservative cross-check for the Chi-square goodness of fit.

4.3.3   Hypothesis testing and confidence intervals

If the goodness of fit test does not imply a rejection of the best-fit hypothesis, it is desired to know how the likelihood of other hypotheses corresponding to different values of the parameters of interest (PoIs) compare to the best-fit scenario. To achieve this, a test statistic of the -2log-likelihood ratio is used [140]:

$$t_\omega = -2\ln\frac{L(\omega_0|\overline{x})}{L(\hat{\omega}|\overline{x})}, \tag{4.5}$$

where in the denominator the parameters of the model are set to their MLEs, $\hat{\omega}$, and the parameter values in the numerator, ω_0, correspond to the tested hypothesis. For simplicity, the vector notation is omitted as the method described here applies regardless of the number of parameters. By construction, t_ω is restricted to be positive and the higher values mean worse agreement of the tested hypothesis with the data, as far as the

tested hypothesis ω_0 is a nested hypothesis meaning that it represents a special case of the full model ω and one or more parameters in ω_0 are fixed to the hypothesised value. In other words, the parameter space of the ω_0 hypothesis is a subspace of the ω hypothesis. The p-value, p_ω, for given values of the tested parameters ω_0 and the observed data set can be obtained with the integral

$$p_\omega = \int_{t_{\omega_0}^{obs}}^{\infty} f(t_\omega | \omega_0) dt_\omega. \tag{4.6}$$

According to Wilks' theorem [148], assuming that the ω_0 hypothesis is true and certain regularity conditions are met, the t_ω test statistic in the large sample limit follows the χ^2 distribution with the degrees of freedom equal to the difference between the number of free parameters fitted in $L(\hat{\omega})$ and $L(\omega_0)$. The maximum likelihood solution $L(\hat{\omega})$ by definition fits for all the parameters $\overline{\omega}$ and, for the aforementioned approximation to apply, the ω_0 hypothesis has to be nested.

Having a measurement of the parameter of interest (PoI) represented as the best-fit point estimate, usually the goal of the experiment is also to state the statistical precision of the performed measurement. In the frequentist statistics, to which we restrict our analysis, this goal is achieved following the Neyman construction [149] for confidence intervals. The confidence interval of a desired confidence level (CL) is interpreted as an interval in the parameter of interest, which should contain the true value CL percent of the times if the experiment is to be repeated. Sometimes this probability, frequently called coverage probability or just coverage, is not exactly equal to the confidence level targeted in the procedure of the confidence interval construction. In such a case, one would say that the interval undercovers (the real coverage is lower than the claimed confidence level) or overcovers (coverage can actually be higher than the claimed confidence level). A confidence interval can be created using the test statistic in Eq. 4.5 [150]. First, the formula complementary to Eq. 4.6

$$1 - p_\omega = \int_0^{t_{\omega_0}^{crit}} f(t_\omega | \omega_0) dt_\omega \tag{4.7}$$

has to be solved for $t_{\omega_0}^{crit}$ to obtain the test statistic critical value corresponding to the probability $1 - p_\omega$ equal to the chosen confidence level. Then, the observed values of $t_{\omega_0}^{obs}$ for a wide range of ω_0 hypotheses have to be compared to the corresponding $t_{\omega_0}^{crit}$. The values of ω_0 which are included in the confidence interval fulfil the condition

$$t_{\omega_0}^{obs} \leq t_{\omega_0}^{crit}. \tag{4.8}$$

With the Wilks' theorem approximation, the critical value t_ω^{crit} in Eq. 4.7 is given by the inverse function of the χ^2 cumulative distribution function for the adequate number of degrees of freedom. The subscript in ω_0 is omitted, because, if the approximation holds in the whole parameter space, $f(t_\omega | \omega_0)$ has the same distribution for all the values of ω_0.

In reality, the conditions for Wilks' theorem to apply are not always fulfilled. When this happens, the χ^2 approximation of the t_ω distribution will no longer hold. However, the discrepancy from the χ^2 distribution does not always have to be drastic. If there is a reason to believe that the deviation from the χ^2 shape is significant, the exact shape of the t_ω distribution can be obtained with MC simulations so that Eq. 4.6 can still be used in the confidence interval evaluation. More about this issue in the context of the results obtained in this work will be given in Sections 4.5.2 and 4.9.

4.3.3.1   Profile likelihood ratio and nuisance parameters treatment

The parameters which are present in the model, but are not of intrinsic interest in a given analysis are referred to as nuisance parameters. They often represent systematic uncertainty parameters (see Section 3.3) which are introduced to reduce bias and improve the model accuracy. However, the presence of the nuisance parameters usually increases the statistical uncertainty of the parameters of interest due to possible correlations. This effect can be reduced by constraining the nuisance parameters with external measurements.

Suppose we divide the likelihood parameter set $\overline{\omega} = \{\epsilon, \eta\}$ into the parameters of interest, ϵ, and the nuisance parameters, η. Then, for a certain hypothesised value of ϵ_0, the rigorous frequentist approach allows the rejection of ϵ_0 during the confidence interval construction only if it is excluded for all the possible values of η. The resulting interval will then be conservative meaning that it covers the true value of the parameter of interest with the probability equal to or greater than the nominal CL. However, the dependence of the test statistic in Eq. 4.5 on the nuisance parameters can be approximately lifted with the use of the profile likelihood ratio defined as

$$\frac{L(\epsilon_0, \hat{\hat{\eta}})}{L(\hat{\epsilon}, \hat{\eta})}, \tag{4.9}$$

where $\hat{\hat{\eta}}$ denotes the profiled values of η which minimise the negative log-likelihood for a given value of ϵ_0. $\hat{\epsilon}$ and $\hat{\eta}$ are the MLEs of the parameters of interest and the nuisance parameters respectively. The confidence interval created with the profile likelihood ratio will have the proper coverage only in the case when the nuisance parameters true values are equal to the profiled values. In other cases, the exact coverage is not guaranteed [20].

4.4   The fitting procedure

For each of the tested NSI models, a profile likelihood scan is performed before the search for the global minimum (best-fit point). Profile likelihood scan minimises the negative profile likelihood from the numerator in Eq. 4.9 at the set of points on a predefined grid in the parameter(s) of interest. The profile likelihood values are then linearly interpolated between the grid points to create a profile likelihood curve which defines the final output of a single profile likelihood scan. To turn this curve into a representation of -2log-likelihood ratio test statistic, the -2 profile likelihood value evaluated at the global best-fit point has to be subtracted. The fits are performed with the `MINUIT` [151] minimizer provided by the `ROOT` [152, 153] software framework through the `RooFit` [130] interface within the MONA package. To assure the fit convergence and prevent the fitter from getting stuck at local minima, the following procedure was developed:

1. Perform a profile likelihood scan for the parameter of interest on a given set of points.

2. If any of the fits shows a lack of convergence, change the `MINUIT` strategy to 0 (do not run `Hesse` algorithm under any circumstances) and repeat step 1. In this case the desired EDM (estimated distance to the minimum) is set to $0.5 \cdot 10^{-3}$ instead of the default $1 \cdot 10^{-3}$.

3. Once a fully converged profile likelihood scan is obtained, perform the global minimum search with the parameter of interest free in the fit. The starting values for all the model parameters should be taken from the minimum likelihood point of

the profile likelihood scan. In this way, it is ensured that the global minimum search can only improve with respect to the lowest negative log-likelihood value from the profile likelihood scan. Having a fixed starting point for the model parameters in the search for the global minimum involves the risk of having the fitter getting stuck in a local minimum. However, this strategy has certain advantages even though it might provide less precise results. The discussion on this issue is continued in Sections 4.5.2 and 4.9.

4. Perform the profile likelihood scans on all the nuisance parameters to obtain the asymmetric 1σ errors which might diverge from the parabolic approximation of the Hessian matrix. This is equivalent to the use of the MINOS algorithm with MINUIT.

All the fits are done with profiling over the mass ordering with the Δm^2_{31} starting values at the NuFIT 5.1 NO set and the IO set. The ambiguity in the octant of θ_{23} is accounted for with two starting values of $\sin^2(\theta_{23})_{init} = \{0.4, 0.6\}$. It means that for each fitted hypothesis, four starting points are tested in the case of the real NSI models. In the case of the complex NSI models, additional starting values are added in $\delta^{init}_{\alpha\beta} = \{0, \pi/2, \pi, 3\pi/2\}$ resulting in a total of 16 starting points for each fit.

The grid points for the profile likelihood scans of all the tested NSI models are the following:

- real $\epsilon_{\mu\tau}$: 41 points linearly distributed from -0.02 to 0.02 with the step of 0.001,

- real $\epsilon_{\tau\tau} - \epsilon_{\mu\mu}$: 41 points linearly distributed from -0.04 to 0.04 with a step of 0.002,

- real $\epsilon_{e\tau}$: 51 points linearly distributed from -0.2 to 0.2 with a step of 0.008

- real $\epsilon_{e\mu}$: 36 points linearly distributed from -0.1 to 0.1 with a step of 0.00625,

- complex $\epsilon_{\mu\tau}$: 21 points in $|\epsilon_{\mu\tau}|$ linearly distributed from 0 to 0.02 and 41 points with a step of 0.01 in $\delta_{\mu\tau}$ from 0 to 360° with a step of 9°,

- complex $\epsilon_{e\tau}$: 21 points in $|\epsilon_{e\tau}|$ linearly distributed from 0 and 0.2 with a step of 0.01 and 41 points in $\delta_{e\tau}$ from 0 to 360° with a step of 9°,

- complex $\epsilon_{e\mu}$: 21 points in $|\epsilon_{e\mu}|$ linearly distributed from 0 and 0.1 with a step of 0.005 and 41 points in $\delta_{e\mu}$ from 0 to 360° with a step of 9°.

The densities of the points for the sampling grids were chosen to provide a reliable linear interpolation in the profile likelihood scans.

4.5 Pseudo experiments

Pseudo experiments are artificial data sets generated with the MC model introducing some level of randomisation. In the simplest approach, the bin contents of the reconstructed event rates for a given set of the model parameters are randomised with Poisson distributions, which take the nominal bin contents as their expectation values. In a more complex approach aimed at mimicking the authentic possible data taking conditions, before the Poisson randomisation, the input values of the systematics are varied within their prior distributions (for details see Section 4.6). In our analysis, pseudo experiments are used for two purposes:

1. to estimate the sensitivity of ORCA6 for the NSI parameters which are about to be measured and

2. to check the Wilks' theorem applicability and derive the actual test statistic critical values corresponding to 68% ($\sim 1\sigma$) and 90% confidence level.

Sensitivity can be defined by the confidence interval created with a pseudo data set where the sought after signal is not present. For example, the sensitivity at 90% CL pins down the minimum true values of the parameter of interest which would have to be realised in nature for the given experiment to allow detection at 90% CL. In the case of our analysis, the background or the no-signal hypothesis is represented by a pseudo data generated with the NuFIT 5.1 NO oscillation parameters, all the systematics set at their nominal value and the NSI parameters fixed at zero.

4.5.1   Pseudo experiments for sensitivity estimation

To estimate the statistical spread of the ORCA6 sensitivity to the NSI parameters, the following procedure was used:

1. set the standard oscillation parameters to their global best-fit values from the NuFIT 5.1 NO set and the systematics to their nominal values — this represents the no-signal hypothesis,

2. create an Asimov data set with all the bin contents equal to their Poisson expectation values.

3. fluctuate the bin contents treating them as Poisson-distributed.

4. perform a profile likelihood scan for a given NSI parameter of interest (only one-at-a-time) on a grid defined in Section 4.4,

5. repeat the procedure many times to get sufficient statistics, which generally depends on the desired confidence level.

With the above procedure, 1000 pseudo experiments were scanned for each real NSI model separately (see Section 4.1). Only the simple statistical fluctuation between the pseudo experiments is used here, because the statistics is expected to be the main source of error in our analysis (see Section 4.6) and implementing a full nuisance parameter randomisation is a computationally difficult challenge (the discussion on this issue will appear in Section 4.5.2). The procedure ends up with 1000 profile likelihood scans, which are used to derive 1000 sensitivity confidence intervals. These intervals create a distribution which is used to illustrate the sensitivity bands — two sided regions containing a given percentage of the sensitivity interval distribution, we choose 68% and 90%.

The pseudo experiment study for the sensitivity estimation was done only for the real NSI scenarios described in Section 4.1. Taking into account the theoretical model, the ORCA6 detector resolution and the event selection, no sensitivity to the complex phases is expected in the analysis and therefore they are not really treated with the same caution as the moduli. From the practical point of view, the model with a complex phase included requires many more fits varying the starting values of the complex phase to account for the potential local minima (see Section 4.4). This becomes computationally very expensive. Therefore the sensitivity bands for the complex NSI models are omitted.

4.5.2   Feldman-Cousins approach

The procedure of generating pseudo experiments to derive the true -2log-likelihood ratio test statistic distribution defined in Eq. 4.5 is often referred to as the Feldman and Couins

(FC) approach [154, 155] defined in ref. [150]. The FC approach verifies if the Wilks'
theorem approximation holds in a given analysis. Wilks' theorem is only applicable
under a set of certain conditions [156]. For our analysis, the important ones are:

- The true values of the parameters cannot lie close to their limits defined in the
  model. From the statistical point of view, this ensures a more general condition
  that the parameter estimators have to be Gaussian with the mean falling at the true
  value.

- The sample limit has to be sufficiently large (in our case, the Gaussian
  approximation of the Poisson distribution should be applicable).

- The tested hypothesis has to be nested. In our case, this is realised with the profile
  likelihood construction. Testing both mass orderings as the starting values does not
  break the nestedness condition, because technically each fit probes the full allowed
  parameter space in Δm^2_{31} (positive and negative).

- The model has to be correct — it is capable of providing an unbiased fit.

The FC approach describes the general idea, but the implementation depends on
the specific analysis and the simulation model. To check if the distribution of the
-2log-likelihood ratio test statistic really follows the χ^2 distribution, the following
procedure is proposed:

1. Create a pseudo data set with the parameter of interest fixed at the hypothesised
   value ϵ_0 and the nuisance parameters randomised within their Gaussian prior
   distributions. For the unconstrained normalisation factors the following Gaussian
   distributions are assigned for the randomisation $n_{tot} \in \mathcal{N}(1, 0.25)$, $n^{\mu}_{atm} \in \mathcal{N}(1, 1)$.
   The overall normalisation distribution width incorporates in a conservative
   manner the sum of the statistical uncertainty, the flux normalisation uncertainty
   and other potentially unaccounted effects. For the unconstrained standard
   oscillation parameters, the following uniform intervals were used instead: $\Delta m^2_{31} \in$
   $[-3.5, -1.5] \cup [1.5, 3.5] \cdot 10^{-3}$, $\sin^2(\theta_{23}) \in [0.3, 0.7]$. The standard oscillation
   parameters are not randomised according to their current uncertainties from the
   NuFIT global fit used as a general point of reference in this thesis. The wider
   intervals are taken for the randomisation to account for the limited sensitivity of
   ORCA6.

2. In the pseudo experiment generated with the randomised nuisance parameters,
   fluctuate the bin contents according to the bin-by-bin Poisson distributions.

3. Fit the model to the generated pseudo data set with two scenarios: with the PoI
   fixed at ϵ_0 value and with PoI free. This gives two values of the likelihood: $L(\epsilon_0, \hat{\hat{\eta}})$
   and $L(\hat{\epsilon}, \hat{\eta})$

4. Calculate the profile likelihood ratio test statistic by taking the
   $-2\ln\left(L(\epsilon_0, \hat{\hat{\eta}})/L(\hat{\epsilon}, \hat{\eta})\right)$.

5. Repeat the procedure a number of times to obtain sufficient statistics depending on
   the desired confidence level.

6. Histogram the values calculated in step 4 to obtain the real distribution of the test
   statistic t_{ϵ_0}.

The distribution of the test statistic with a sufficient number of trials enables the
estimation of the exact critical value corresponding to a desired confidence level, in our

case 90%. The example of $\epsilon_{\mu\tau}$ is chosen to test the proposed procedure, because ORCA6 is more sensitive to this particular NSI parameter. The results will be shown in Section 4.9. The complex scenario is not included to simplify and speed up the fits. Nevertheless, the following study can be applied to any model analysed in this work, including the complex flavour-violating NSI parameters.

The described procedure has to be applied to a number of points in the parameter space of the PoI to ensure a reliable interpolation (not necessarily all the points used for the profile likelihood scan). We assume that for a single parameter in the fit and 90% CL, 1000 pseudo experiments should provide a sufficient estimate of the test statistic critical value. The uncertainty of this estimate is then calculated using the bootstrapping method described in Section 4.5.2.1. In the full model used for testing a real NSI parameter, there are 13 parameters, so, without taking into account correlations, the necessary number of pseudo experiments could reach a prohibitive number. However, profiling of the likelihood accounts for the correlations between the parameters and approximately eliminates the dependence of the -2log-likelihood ratio test statistic on the nuisance parameters. Therefore, the number of 1000 experiments is believed to be sufficient for the critical value calculation at 90% CL, if all the most impactful systematics are included in the pseudo data fit.

In terms of the fit configuration for the third step in the proposed procedure, for the final critical values to be applicable in the analysis, the procedure should follow exactly the same approach as the data fit (see Section 4.4). However, it is not computationally feasible to perform a full profile likelihood scan for every single pseudo data set. To give the reader an idea, for an extreme pseudo data set the fit to a single point can take up to 30 hours, on average $\sim$20 hours. A full likelihood scan comprises 41 points. For 1000 pseudo experiments this gives 820 000 hours of computing time. A regular user account on the IN2P3 cluster used by the KM3NeT collaboration is allowed to run in parallel $\sim$2000 jobs. This means that the test statistic critical value estimation for a single point would require roughly 17 days of uninterrupted computing with the full use of the computing resources. For a reliable interpolation, at least 10 points are needed to cover the probed parameter space of one parameter of interest. This gives $\sim$170 days assuming that the jobs on the cluster will run continuously without any interruptions and errors, which in reality is almost never achieved.

Finding the true global minimum of the likelihood is a non-trivial computational problem. In a model which incorporates many parameters and the majority of them are, to some extent, correlated, there is always the question of how to choose the starting values to properly scan the parameter space. This problem is usually sorted out using the prior knowledge on the physical meaning of the model parameters and the degeneracies that should be expected among them from the theory (see for example Section 1.2.3). For example, in our case we always take into account both mass orderings and both θ_{23} octants in the fit starting points to account for the yet non-conclusive results of the global fits. To make the procedure described in this section computationally accessible, the starting value of $\epsilon_{\mu\tau}$ in all the fits is set to only one point of $\epsilon_{\mu\tau}^{init} = 0$. For the obtained test statistic distributions to apply, the data has to be treated in the same way. Therefore the procedure of the search for the global minimum described in 4.4 is changed for the results presented in Section 4.9 — the starting value of the free $\epsilon_{\mu\tau}$ is always set to $\epsilon_{\mu\tau}^{init} = 0$ and all the nuisance parameters start at their nominal values. If the negative log-likelihood value from the global minimum search with the starting point at $\epsilon_{\mu\tau}^{init} = 0$ turns out to be higher than any of the values from the fits in the profile likelihood scan, then the minimum from the scan is chosen as the best-fit point in the analysis. Strictly speaking, this procedure

ends up with a custom test statistic, which is based on the -2log-likelihood ratio, but with a different condition for the maximum likelihood estimation. The discussion is continued in Section 4.9, where the results of this FC-like procedure are presented.

4.5.2.1 Bootstrapping

Running pseudo experiments can be very computationally expensive and generally the higher the desired quantile order (confidence level), the more experiments are needed to generate a reliable shape of the distribution tail. Bootstrapping is a method which enables the estimation of the standard deviation of the critical values obtained from the test statistic distributions generated with the procedure described in Section 4.5.2. With this method, a tool is provided to assess if the number of the generated experiments was sufficient or the distributions are too sparse.

With a data set with N entries (in our case a set of 1000 or 2000 pseudo experiments for a given value of $\epsilon_{\mu\tau}$) generated from the random variable X (in our case -2log-likelihood ratio calculated from each experiment), the concept of bootstrapping is to evaluate a given statistical property (in our case the critical value of the -2log-likelihood ratio test statistic) from a statistic $q(X)$ by randomly drawing new data sets of the same size N, re-sampled with replacement from the original data set [157]. In each of the re-sampled data sets a significant number of the original events will appear more than once, since all the re-sampled sets have the same size as the original data set. From every re-sampled set, the 68th and the 90th percentiles (in other words, the critical values) are derived and gathered into a distribution from which the average value and the standard deviation can be calculated.

To give an example, Figure 4.6 shows a histogram of 1000 random numbers generated from the χ^2 distribution with 1 degree of freedom. The red line indicates the 90th percentile of the generated distribution equal to 2.62 (lower than the analytical 2.701). To
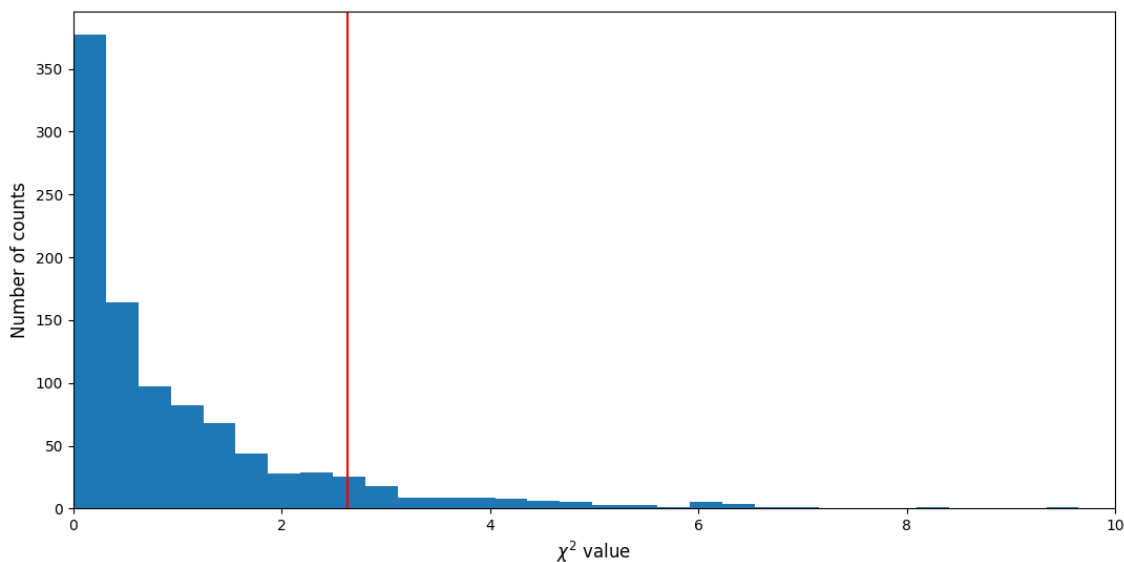
Figure 4.6: A histogram of 1000 values randomly generated from the χ^2 distribution with 1 degree of freedom. The red line indicates the 90th percentile of the equal to 2.62.

calculate the standard deviation of this estimate of the percentile, we use bootstrapping by re-sampling with replacement a number of times the original sample depicted in Fig. 4.6, in this case 20000. From each of these re-sampled data sets, a 90th percentile can be

evaluated. This gives a distribution of the percentile, which is shown in Fig. 4.7 in the form of a histogram. Now, the standard deviation can be obtained and in this example case it turns out to be equal to 0.11.
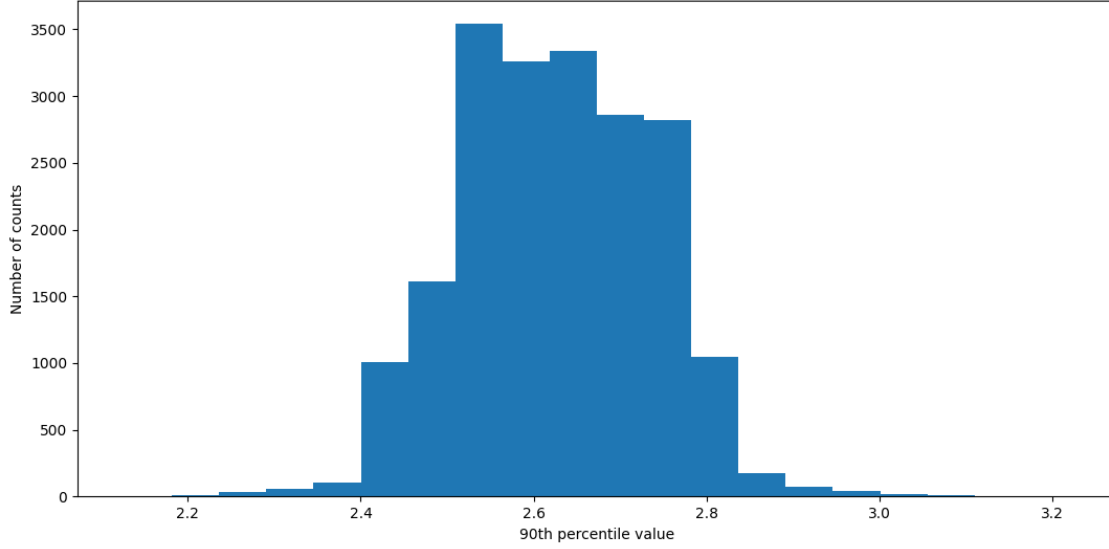
Figure 4.7: The distribution of 90th percentiles evaluated from boostrapping the random data set shown in Fig. 4.6.

4.6   Systematics

All the systematic uncertainty parameters described in Section 3.3 are included in the model as nuisance parameters. Two standard oscillation parameters are also added to the set of the nuisance parameters: Δm_{31}^2 and $\sin^2(\theta_{23})$. The choice of these particular parameters is driven by the design of the ORCA detector, which is optimised for the atmospheric oscillation study. Therefore, the parameters Δm_{31}^2 and $\sin^2(\theta_{23})$ which govern the atmospheric neutrino oscillations are expected to interfere with the NSI measurements.

In our analysis, the prior knowledge about the systematics is incorporated in the likelihood using Gaussian *penalty terms* or external constraints (sometimes also referred to as priors), which multiply the binned likelihood in Eq. 4.2 resulting in the modified likelihood form:

$$L(\mu(\epsilon, \eta^C, \eta^{UC})|\overline{N}) = \prod_i^{n_{reco}} \frac{\mu_i^{N_i} e^{-\mu_i}}{N_i!} \prod_k^{\eta^C} \frac{1}{\sigma_{\eta_k}\sqrt{2\pi}} \exp\left\{-\frac{(\eta_k - \eta_k^0)^2}{2\sigma_{\eta_k}^2}\right\}, \qquad (4.10)$$

$$\ln(L) = \sum_i^{n_{reco}} \left(N_i \ln(\mu_i) - \mu_i\right) - \sum_k^{\eta^C} \frac{(\eta_k - \eta_k^0)^2}{2\sigma_{\eta_k}^2} + \text{const}, \qquad (4.11)$$

where η^C are the constrained nuisance parameters and η^{UC} are the unconstrained ones. In Eq. 4.11, all the ingredients which do not depend on μ are omitted as they are irrelevant for the minimisation and hypothesis testing. The Gaussian distribution parameters of the external constraints used in the analysis are shown in Table 4.3. The uncertainties of the flux ratios and the cosine zenith tilt, which can also be interpreted as ν_{up}/ν_{down} skew, are derived from ref. [158], which summarises the topic of the uncertainties in the

	Nuisance parameter	Penalty term
Constrained	Energy scale E_{scale}	$\mathcal{N}(0, 0.1)$
	Flux energy tilt $\Delta\gamma$	$\mathcal{N}(0, 0.3)$
	Flux cosine zenith tilt Δd	$\mathcal{N}(0, 0.07)$
	Flux $\nu_\mu/\bar{\nu}_\mu$ skew	$\mathcal{N}(0, 0.1)$
	Flux $\nu_e/\bar{\nu}_e$ skew	$\mathcal{N}(0, 0.1)$
	Flux ν_μ/ν_e skew	$\mathcal{N}(0, 0.03)$
	NC cross section normalisation $n_{\sigma_{NC}}$	$\mathcal{N}(1, 0.1)$
	ν_τ-CC cross section normalisation $n_{\sigma_{CC}^{\nu_\tau}}$	$\mathcal{N}(1, 0.2)$
Unconstrained	Δm^2_{31}	–
	$\sin^2(\theta_{23})$	–
	Overall normalisation n_{tot}	–
	Muon normalisation n_μ^{atm}	–

Table 4.3: Penalty term functions for the nuisance parameters constrained in the model used for the analysis. $\mathcal{N}(\bar{x}, \sigma)$ stands for the normal distribution with mean $\bar{x}$ and standard deviation σ. The parameter symbols correspond to the descriptions in Section 3.3.

atmospheric neutrino flux models. As can be read in this article, the uncertainties of the flux ratios generally grow with increasing neutrino energy and the values used in the analysis can be roughly considered as average. In the case of the ν_{up}/ν_{down} ratio, the prior width is taken to be the most conservative value quoted in [158] which applies to sub-GeV neutrinos and decreases with neutrino energy to become negligible already at around $\sim 3\,$GeV.

The uncertainty of the flux energy tilt of the spectral index is chosen to be approximately 10% assuming an average spectral index $\gamma \sim 3$. Percentage-wise, the actual uncertainty will depend on the energy, the neutrino type and the incident direction (see Section 3.3.1). The problem of such choice is, similarly to the case of the other flux systematics used in our model, that the overall flux uncertainty grows with the energy [159], but so as the spectral index itself. Therefore, a single $\Delta\gamma$ parameter with a constant prior is not able to properly reflect the flux uncertainty. However, our choice of the prior for the spectral index tilt turns out to be rather conservative compared to the analyses performed by DeepCore [160, 81], which use the same atmospheric neutrino flux model. The Gaussian prior width equal to 0.1, used in the aforementioned works, is claimed to be derived from the uncertainties of the primary cosmic ray spectrum measurement from ref. [159]. It makes sense when we take into account the very strong correlation between the primary cosmic ray flux normalisation and its spectral index quoted in the same article. Since we keep the overall normalisation unconstrained in the fit, it might be the case that our estimation of $\Delta\gamma$ prior width is too wide.

The cross section normalisation prior widths come from ref. [28] for $n_{\sigma_{CC}^{\nu_\tau}}$ and from ref. [29] for $n_{\sigma_{NC}}$.

In the case of the energy scale systematic, the prior width is wider compared to the

study on seawater properties and the PMT efficiencies within the context of muon energy reconstruction in KM3NeT [111, 83]. This is due to the fact that the energy scale for the early stages of the ORCA detector has not been studied in detail yet. Therefore, a conservative approach is taken.

The overall normalisation is not constrained to account for relatively low statistics and the sources of error which might be missing/unidentified in the model. It is expected to be strongly correlated with the flux spectral index energy tilt as it is claimed in ref. [159] and briefly discussed in Section 3.3.1. The separate normalisation factor of the atmospheric muon distribution is left free in the fit taking into account the very low number of muon events passing the cuts. Moreover, the actual atmospheric muon flux is a topic of investigation and the MUPAGE model used in the KM3NeT simulation chain (see Section 3.1.2) has an average error of $\sim$13% [161]. The treatment of the atmospheric muon events in the analysis is described in detail in Section 4.2.3.

Some known systematic uncertainty sources are not accounted for in the model. One example, already briefly discussed in Section 3.2.1, is the Earth chemical composition and the Earth's density. Nevertheless, the uncertainties in these quantities are not expected to impact the relatively low-precision measurements with ORCA6. The use of an alternative Earth model and its impact on the NSI analysis will be presented in Section 4.8. The other yet unexplored potential source of systematic uncertainty are the interaction models incorporated in the neutrino generation. The commonly used neutrino event generators differ in the approach to the modelling of certain types of interactions and in principle their neutrino cross sections output can vary. Aside from the dedicated normalisation factors for NC and ν_τ-CC interactions, the cross section uncertainty is to some extent accounted for in the overall normalisation. However, the cross section models might differ in shape as well and this would require a more advanced approach to be accounted for in the MC event rate calculation. Currently, the effort is being taken in the KM3NeT collaboration to implement an alternative neutrino generator, GiBUU [162], to evaluate a possible impact on the oscillation analysis stemming from using different cross section models [163].

4.6.1   Evaluating the impact of the systematics on the parameter of interest

The impact on the estimation of the parameter of interest from a single nuisance parameter can be calculated with the following procedure:

1. Shift the nuisance parameter by its uncertainty value and fix it at the shifted value.

2. Fit for all the other parameters including the parameter of interest.

3. Read the fitted value of the parameter of interest $\epsilon_{\alpha\beta}^{shift}$.

In principle, the approach described above, frequently referred to as the one-parameter-at-a-time method, facilitates the calculation of the systematic error on the measured parameter. Here it is used rather to evaluate the importance of a given systematic in the analysis model. The procedure is applied separately using the pre-fit uncertainty and the post-fit uncertainty. The pre-fit uncertainties, $\Delta\theta$, represent the width of the Gaussian priors assigned to the externally constrained parameters. The parameters which are free in the fit do not have the pre-fit uncertainty by definition. The post-fit uncertainties, $\Delta\hat{\theta}$, are obtained as the width of the interval between values fulfilling the condition -2log-likelihood ratio = 1 in the profile likelihood scan of each of the nuisance parameters.

An illustrative example of the procedure is presented in Fig. 4.8. It provides information about the systematics and their impact on the estimation of $\epsilon_{\mu\tau}$ with the observed data. The black dots and the black lines should be read with the upper x-scale. The dots represent the statistical pulls of the systematics constrained in the likelihood function; the parameters which are unconstrained in the fit do not have the pulls defined, so for them the dots are fixed at zero. The horizontal black lines show how the data constrained the given nuisance parameter compared to the assumed priors. Both coloured boxes, the empty one and the filled one, are drawn with the lower x-scale. The values of $\epsilon_{\mu\tau}^{shift}$ are obtained with the procedure indicated at the beginning of this section. $\epsilon_{\mu\tau}^{BF}$ and $\sigma_{\epsilon_{\mu\tau}}$ represent the best-fit value and the error of the parameter of interest $\epsilon_{\mu\tau}$. The error, $\sigma_{\epsilon_{\mu\tau}}$, is customarily calculated as the width of the 68% CL confidence interval divided by two. The values indicated by the boxes and described by the lower x-axis are designed to show the relative shift in the best-fit value of the parameter of interest caused by a single nuisance parameters if its true value is at $\pm 1\sigma$ confidence limit. The reason why the absolute values of $\epsilon_{\mu\tau}^{shift}$ and $\epsilon_{\mu\tau}^{BF}$ are taken is that the results are expected to be approximately symmetric around zero and the sign depends on the locally fitted mass ordering to which the experiment has no sensitivity. If the modulus is not used, a misleading effect appears: a change just in the $\epsilon_{\mu\tau}^{shift}$ sign would lead to a false large post/pre fit impact. The only exception is Δm_{31}^2 where the actual signed values are used instead of the absolute values (it is not indicated in the plot). Further in the text, the type of the plot shown in Fig. 4.8 is referred to as the "rank plot". This type of plot was inspired by the approach found in ref. [164].
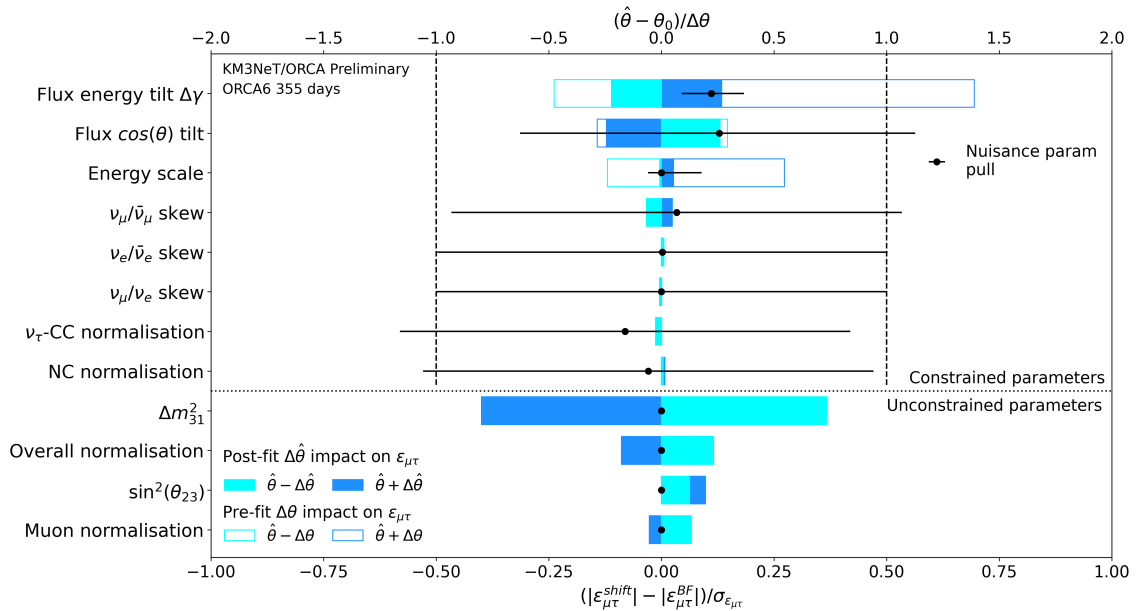
Figure 4.8: Rank plot for the real $\epsilon_{\mu\tau}$ model. See text for explanation.

An alternative approach is to look how the sensitivity to the parameter of interest worsens when the systematics are added to the model stacked one by one. This method helps to investigate the synergistic effect of these systematic uncertainties, which start to have an impact on the analysis only when they are combined. The outcomes of applying this procedure for $\epsilon_{\mu\tau}$, $\epsilon_{\tau\tau} - \epsilon_{\mu\mu}$, $\epsilon_{e\tau}$ and $\epsilon_{e\mu}$ are shown in Fig. 4.9. As can be seen, for all the models, at least within the 90% CL median sensitivity, the statistics is the dominating source of uncertainty. Among the flavour-violating parameters, the complex

phase is expected to be important in the analysis only in the case of $\epsilon_{\mu\tau}$. The diagonal parameter $\epsilon_{\tau\tau} - \epsilon_{\mu\mu}$ is mostly impacted by the systematics affecting the normalisation. The general trend shows that the most important nuisance parameters in all the analyses (in various orders depending on the particular epsilon) are: Δm_{31}^2, $\sin^2(\theta_{23})$, the overall normalisation, the energy scale, the flux energy tilt and the cosine zenith tilt. Adding the flux skews and the cross section normalisation factors has a negligible effect on the sensitivities.

4.7 Results

All the presented ORCA6 results are obtained with a livetime of 354.6 days, which corresponds to the selected data runs of ORCA6 data taking period between January 2020 and March 2021 (see Section 4.2). The reconstructed energy proxy is based on the reconstructed track length and the 0.25 GeV/m approximation (see Section 2.3.4). The atmospheric oscillation parameters Δm_{31}^2 and $\sin^2(\theta_{23})$ are treated as unconstrained nuisance parameters in the NSI fits. All the fits are performed profiling over the mass ordering and $\sin^2(\theta_{23})$ octant. The details about the fitting procedure can be found in Section 4.4. In the search for the maximum likelihood estimates, the likelihood in Eq. 4.11 is used with the external constraints from Table 4.3. The confidence intervals presented in this section are based on the profile likelihood ratio

$$-2\ln\frac{L(\epsilon,\hat{\hat{\eta}})}{L(\hat{\epsilon},\hat{\eta})} = 2\sum_{i}^{n_{reco}}\left(\mu(\epsilon,\hat{\hat{\eta}}) - \mu(\hat{\epsilon},\hat{\eta}) + N_i\ln\frac{\mu(\hat{\epsilon},\hat{\eta})}{\mu(\epsilon,\hat{\hat{\eta}})}\right) + \sum_{k}^{\eta^C}\frac{\hat{\eta}_k^2 - \hat{\hat{\eta}}_k^2 + \eta_k^0(\hat{\hat{\eta}}_k - \hat{\eta}_k)}{2\sigma_{\eta_k}^2},$$

(4.12)

which incorporates the statistical methods and the symbols introduced in Sections 4.3 and 4.6. A negative Δm_{31}^2 in the best-fit result means that the best fit was found for the IO starting point. In the tables with the best-fit parameter values that will be shown in the following sections, for each of the tested models, the quoted errors are calculated as 1σ (68%) confidence intervals evaluated with the procedure described in Section 4.3.3 by treating each model parameter separately, one by one, as the parameter of interest.

Figure 4.10 shows the measured event rates in the 2D reconstructed phase space. For comparison, Fig. 4.11 shows the event rate prediction in the 2D reconstructed space generated with the parameter values from the best-fit point of the real $\epsilon_{\mu\tau}$ model. As they show very small differences with respect to Fig. 4.11, the event rate histograms for all the best-fit points of the other tested NSI models are moved to Appendix A.3.

4.7.1 Real NSI scenario

In this section the results on the real (non-complex) NSI are presented.

$\epsilon_{\mu\tau}$ measurement

Here the results on $\epsilon_{\mu\tau}$ assuming it to be real are presented. The best-fit values of the model parameters are shown in Table 4.4. The observed profile likelihood scan on top of the sensitivity bands is portrayed in Fig. 4.12. The observed 90% CL confidence interval is

$$-8.7 \times 10^{-3} \leq \epsilon_{\mu\tau} \leq 9.0 \times 10^{-3}.$$

(4.13)

Figure 4.13 illustrates the measured data on top of the reconstructed event distributions generated with the best-fit parameter set and the same set with $\epsilon_{\mu\tau}$ shifted to the
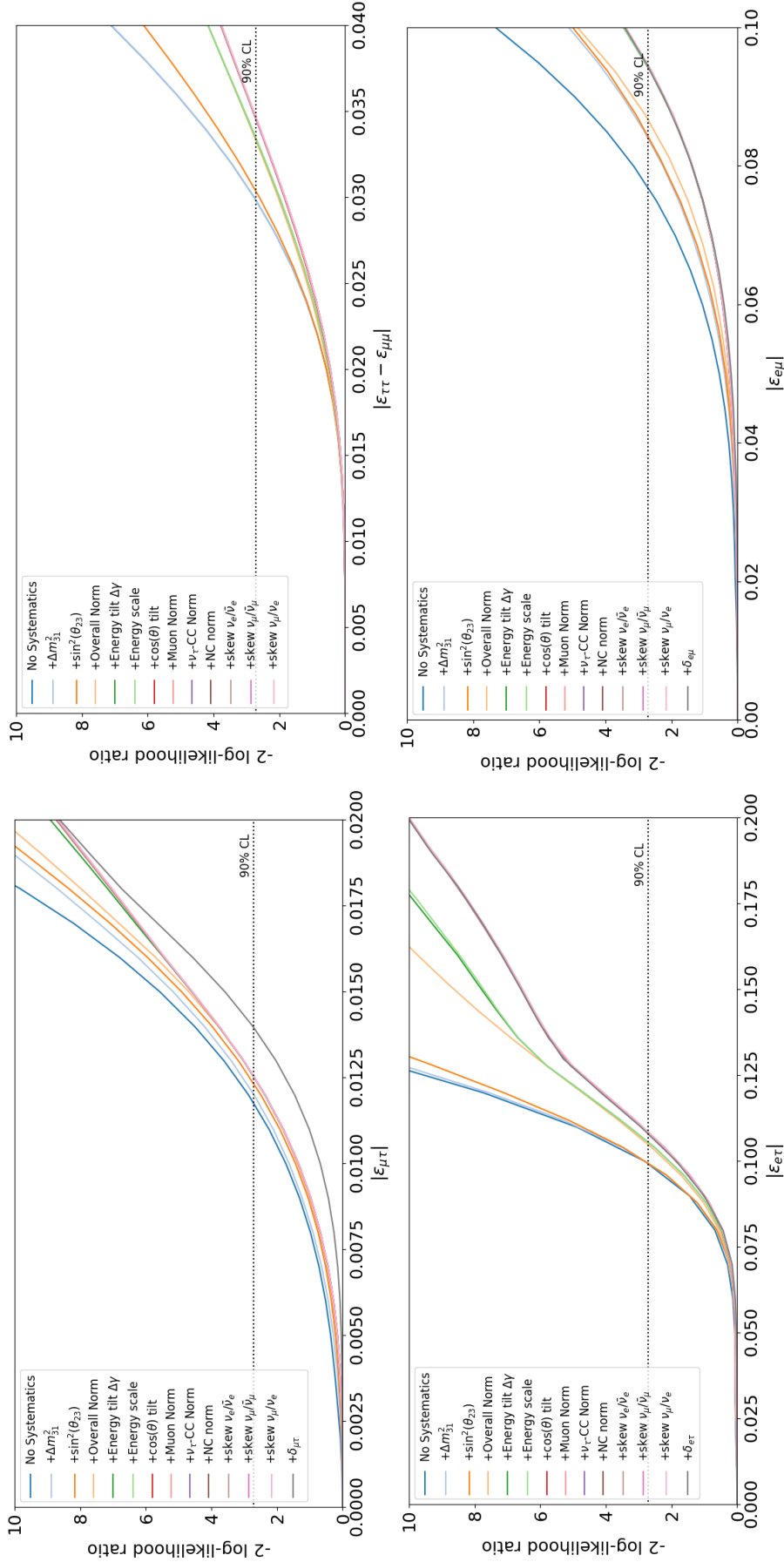
Figure 4.9: Effect of systematics (listed in Tab. 4.3), when fitted incrementally, on the sensitivity to $\epsilon_{\mu\tau}$ (top left), $\epsilon_{\tau\tau} - \epsilon_{\mu\mu}$ (top right), $\epsilon_{e\tau}$ (bottom left) and $\epsilon_{e\mu}$ (bottom right) at ORCA6 for NO assumption and 355 days of livetime. The "No Systematics" curve corresponds to the statistical-only sensitivity. Each colour coded curve corresponds to the effect of that particular systematic plus (+) the ones appearing on top of it being fitted simultaneously. The systematics are added cumulatively in the sequence as they appear in the legend. The final sensitivity can be read from the widest curve, which refers to the case of inclusion of all the systematic uncertainties accounted in this study throughout this thesis. On the x-axis the plot shows the absolute value of $\epsilon_{\alpha\beta}$, which in fact takes the lower -2log-likelihood ratio value between the two opposite signs of $\epsilon_{\alpha\beta}$. In this way, a slight sign asymmetry is taken into account by always presenting the more conservative value. In the case of the last curve where the complex phase $\delta_{\alpha\beta}$ is added to the fit, the $|\epsilon_{\alpha\beta}|$ in the x-axis means the complex modulus.
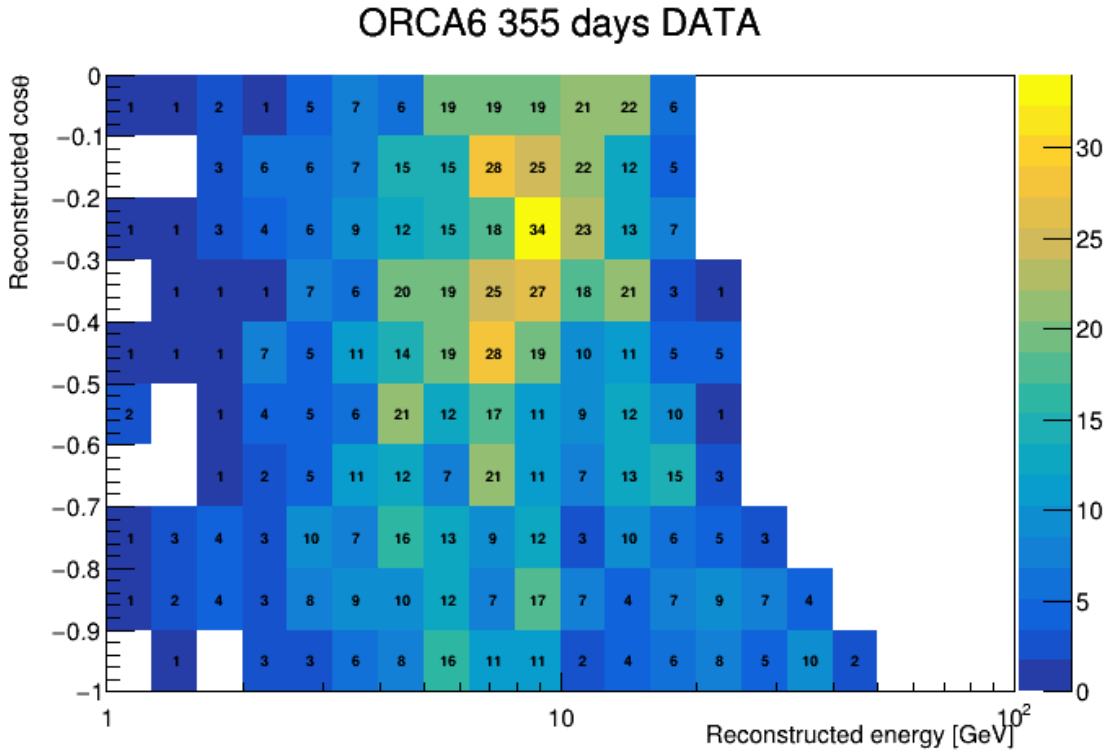
Figure 4.10: The distribution of data events in 355 days of ORCA6 event selection depicted in the two-dimensional space of reconstructed energy versus reconstructed cosine zenith.

positive confidence limit. The bins in two-dimensional reconstructed space are grouped into four reconstructed energy slices and projected onto the reconstructed cosine zenith dimension. As can be seen, the sensitivity of ORCA6 to $\epsilon_{\mu\tau}$ comes mostly from the events reconstructed above ~ 15 GeV and below $\cos\theta < -0.8$. For a better illustration, in Fig. 4.14 the event rate difference together with the bin-by-bin Poisson Chi-square between the two above mentioned hypotheses (Eq. 4.4) are depicted in the full two-dimensional phase space of the fit. The combined effect of the oscillation probability modification induced by $\epsilon_{\mu\tau}$ in the high neutrino energy and the energy reconstruction saturation can be observed. A very broad spectrum of high energy neutrinos with $E_\nu > \sim 100$ GeV end up in a few up-going reconstructed energy bins. The lack of energy resolution and the incapability to distinguish between neutrinos and anti-neutrinos do not strongly affect the sensitivity to $\epsilon_{\mu\tau}$ because in a wide range of neutrinos carrying the energy above 100 GeV only a deficit of events is expected regardless of whether it is a neutrino or anti-neutrino (see Sections 1.2.4.1 and 1.3). Therefore, there is no destructive interference which often appears if a bad detector resolution causes the event rate integration over a region of fast oscillations (excess and deficit fall into a single bin in the reconstructed space).

There is one bin which in principle should make visible in the ORCA6 detector also the $\epsilon_{\mu\tau}$-induced shift of the first oscillation resonance. It is the lowest reconstructed energy bin among the most prominent bins in the Chi-square plot in Fig. 4.14 – its boundaries are $E_{reco} \in [20, 25)$ GeV, $\cos(\theta_{reco}) \in [-1, -0.9)$. Figure 4.15 shows the energy resolution of this bin. Figure 4.16 shows the two-dimensional resolution and the true neutrino flavour composition expected in the bin in the standard oscillation scenario. Due to the expected asymmetry $\nu_\mu/\bar{\nu}_\mu \simeq 2$, the resonance position shift should be observable as the opposite effect on ν_μ and $\bar{\nu}_\mu$ will not be cancelled out completely (see Section 1.2.4.1).
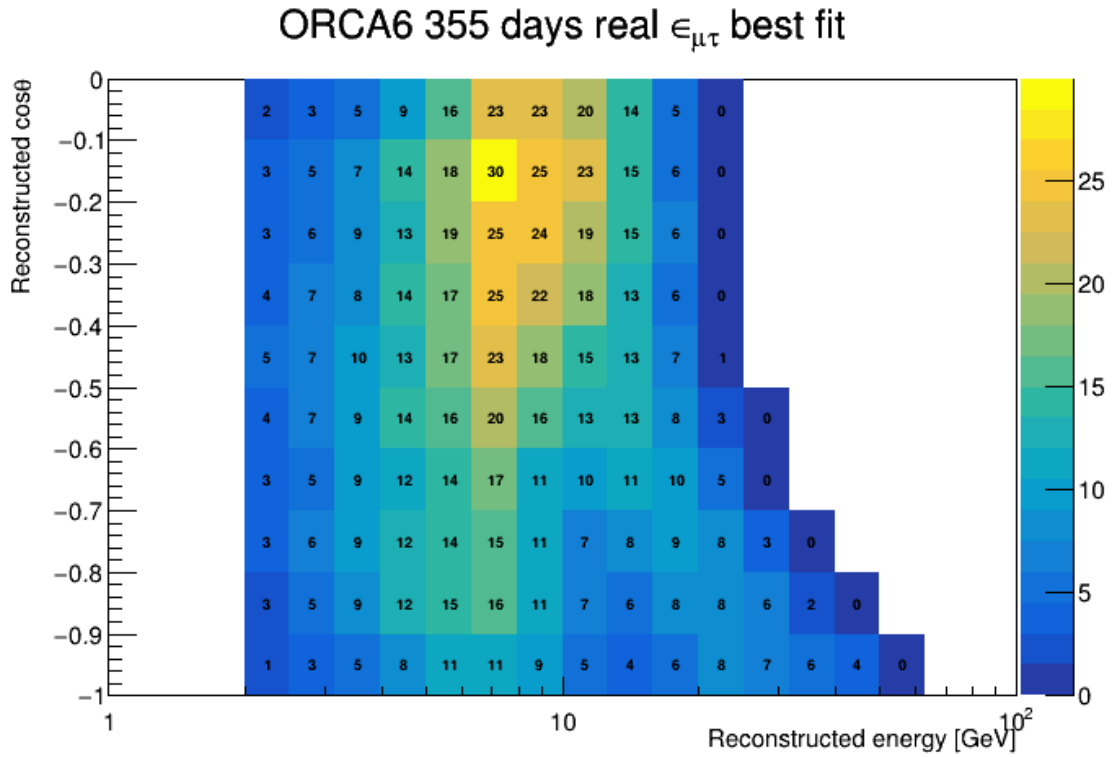
Figure 4.11: The event rates from the MC prediction of the best-fit point of the real $\epsilon_{\mu\tau}$ NSI model in 355 days of ORCA6 event selection depicted in the two-dimensional space of reconstructed energy versus reconstructed cosine zenith.
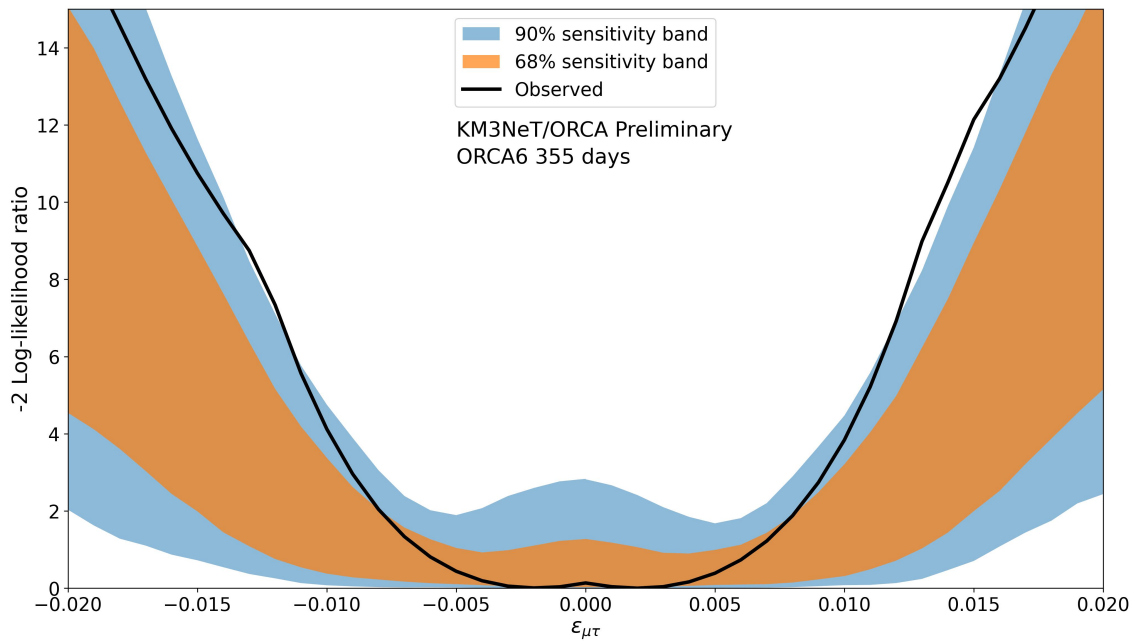
Figure 4.12: The observed profile likelihood scan for the measurement of $\epsilon_{\mu\tau}$ with 355 days of ORCA6 (see Section 4.4 for explanation). The central 68% and 90% confidence regions of the experimental sensitivity are shown as shaded bands. See Section 4.5.1 for details.

Parameter	Fitted value
$\epsilon_{\mu\tau}$	$0.002^{+0.005}_{-0.009}$
$sin^2(\theta_{23})$	$0.51^{+0.10}_{-0.11}$
$\Delta m^2_{31}[eV^2]$	$(1.92^{+0.25}_{-0.23}) \cdot 10^{-3}$
Overall Normalisation	$0.80^{+0.12}_{-0.10}$
Muon Normalisation	2.0 ± 1.5
Flux: Spectral index tilt	0.07 ± 0.04
Flux: $\cos(\theta)$ tilt	0.02 ± 0.06
Flux: $\nu_\mu/\bar{\nu}_\mu$ skew	0.0 ± 0.1
Flux: $\nu_e/\bar{\nu}_e$ skew	0.0 ± 0.1
Flux: ν_μ/ν_e skew	0.00 ± 0.03
Cross-section: NC norm	1.0 ± 0.1
Cross-section: tau norm	1.0 ± 0.2
Detector: Energy scale	$0.000^{+0.018}_{-0.006}$
χ^2	108.8
Degrees of freedom	108
Chi2-square p-value	0.46
Kolmogorov-Smirnov p-value	0.35

Table 4.4: Best-fit values from the ORCA6 data fit to the $\epsilon_{\mu\tau}$ real NSI model.

The rank plot prepared for the $\epsilon_{\mu\tau}$ analysis is shown in Fig. 4.8 (the example from Section 4.6). The data constrains the energy scale and the spectral index flux energy tilt much better than the assumed priors. This is expected from the discussion about the choice of prior widths present in Section 4.6. The most important systematic appears to be Δm^2_{31}. This was also predicted from the incremental study of the systematics shown in Fig 4.9. With Δm^2_{31} fixed, the fitter does not have a way to compensate for the shift in the resonance position (see Section 1.2.4.1), so the sensitivity to $\epsilon_{\mu\tau}$ can emerge also in the lower reconstructed energy region as it was discussed before (see Fig 4.14). The relatively high importance of the flux shape systematics can also be derived from the impact of $\epsilon_{\mu\tau}$ on neutrino oscillations in matter (see Section 1.3). The expected difference in the oscillation probability which contributes to the ORCA6 sensitivity for $\epsilon_{\mu\tau}$ is localised in a narrow region of the phase space of neutrino energy versus direction; mostly in the high neutrino energy regime with $E_\nu > 100$ GeV and only for the very up-going directions of $\cos(\theta) < -0.84$ (the incident directions crossing the Earth's core).

$\epsilon_{\tau\tau} - \epsilon_{\mu\mu}$ measurement

Here, the results on $\epsilon_{\tau\tau} - \epsilon_{\mu\mu}$ are presented in the same manner as the results on $\epsilon_{\mu\tau}$ from the previous section. The MLE values of the model parameters are shown in Table 4.5. The observed profile likelihood scan is depicted on top of the ORCA6 sensitivity bands
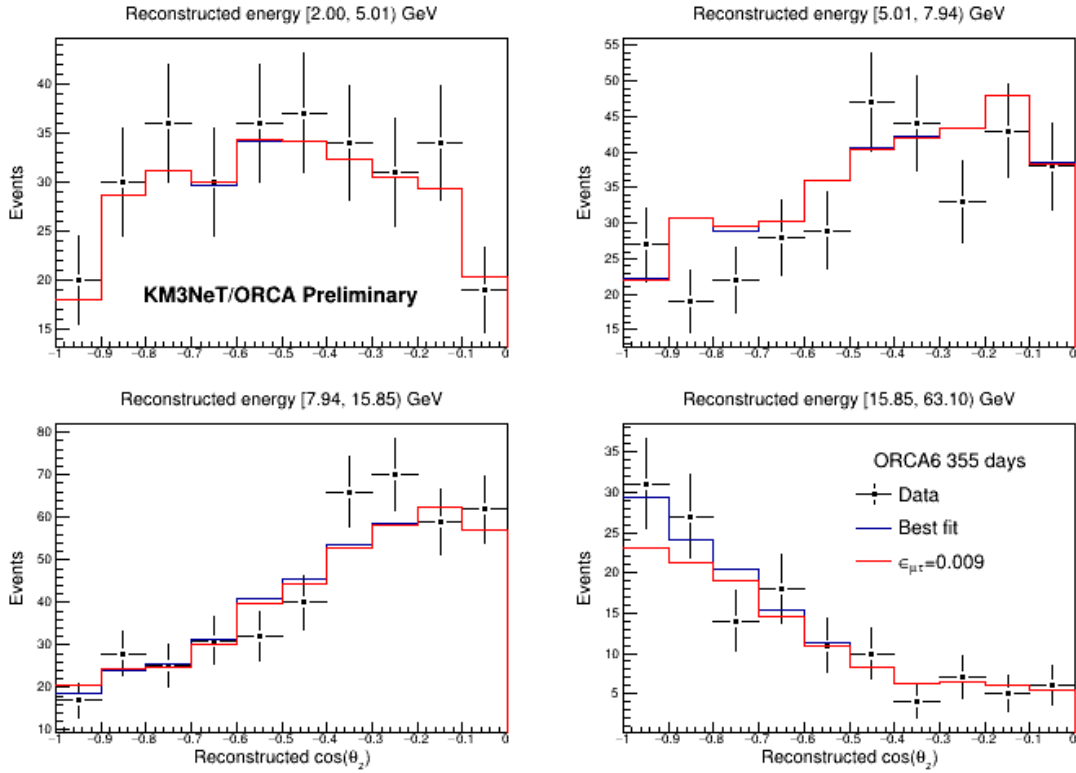
Figure 4.13: Histograms of observed events as a function of $\cos(\theta_{reco})$ for different slices in the reconstructed energy (indicated at the top of each panel), together with the MC expectation under the real $\epsilon_{\mu\tau}$ fit outcome (see Table 4.4) labelled as "Best fit" and the $\epsilon_{\mu\tau} = 0.009$ shifted to its 90% confidence limit.
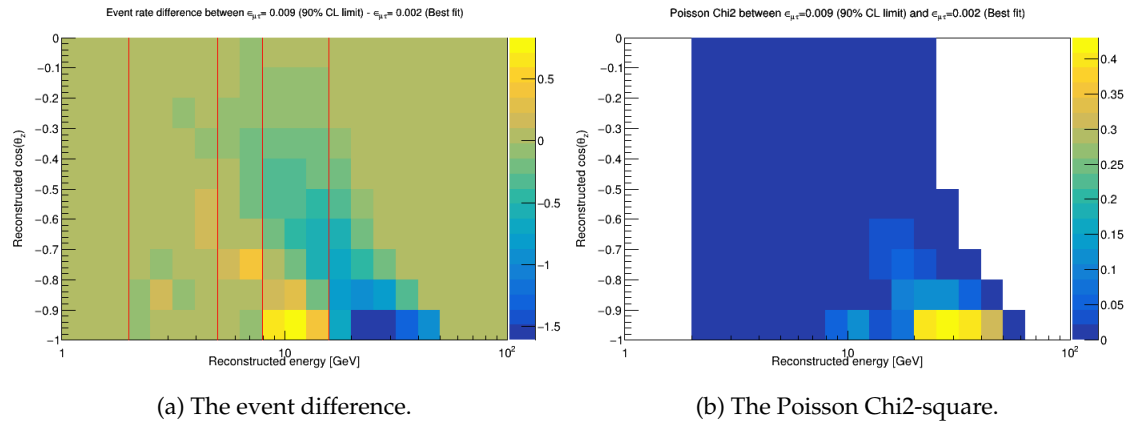
(a) The event difference.

(b) The Poisson Chi2-square.

Figure 4.14: The Poisson Chi-square calculated with Eq. 4.4 (right) and the event rate difference (left) between the 90% CL limit value of $\epsilon_{\mu\tau} = 0.009$ and the best-fit value $\epsilon_{\mu\tau} = 0.002$. All the nuisance parameters are set to their MLEs. The red lines in the left plot indicate the boundaries for the energy slices shown in Fig. 4.18.

in Fig. 4.17. The observed 90% CL confidence interval is

$$-0.021 \leq \epsilon_{\tau\tau} - \epsilon_{\mu\mu} \leq 0.021. \tag{4.14}$$

Figure 4.18 illustrates the measured data on top of the reconstructed event distributions generated with the best-fit parameter set and the same set with $\epsilon_{\tau\tau} - \epsilon_{\mu\mu}$ shifted to the positive confidence limit. The bins in two-dimensional reconstructed space are grouped into four reconstructed energy slices and projected onto the reconstructed cosine
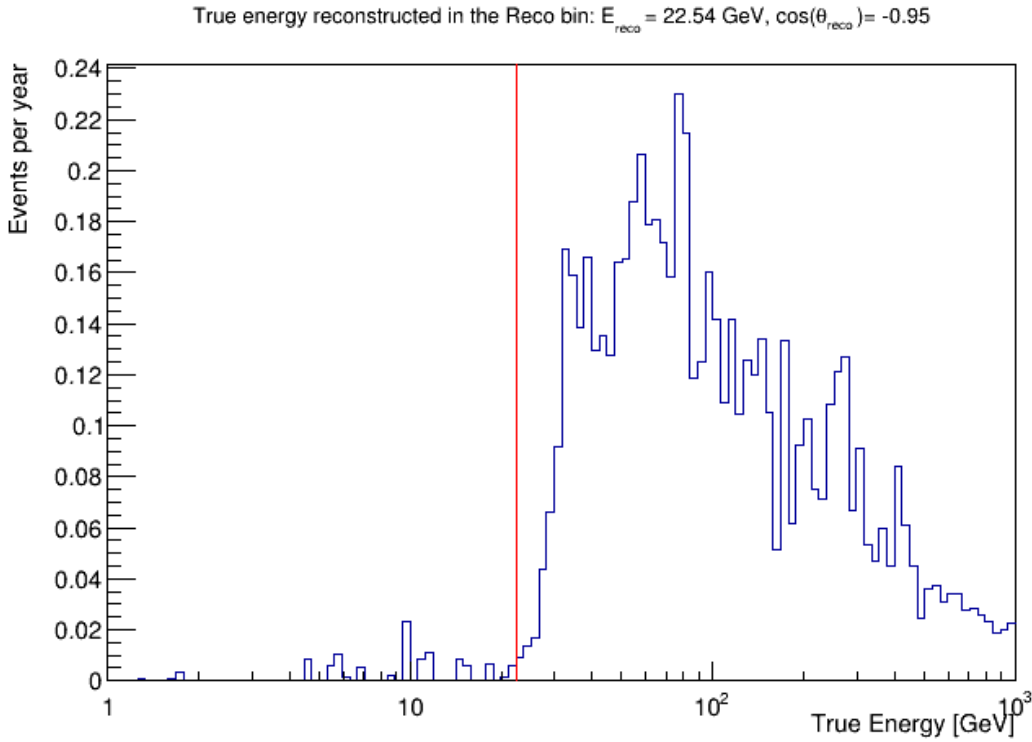
Figure 4.15: The distribution of the true energy reconstructed in the reconstructed bin $E_{reco} \in [20, 25)$, $\cos(\theta_{reco}) \in [-1, -0.9)$. The red line indicates the bin centre in the energy dimension. The weights correspond to NuFIT 5.1 NO best-fit parameters.

zenith dimension. The sensitivity of ORCA6 to $\epsilon_{\tau\tau} - \epsilon_{\mu\mu}$ comes mostly from the events reconstructed between $\sim$8 GeV and $\sim$15 GeV and below $\cos\theta < -0.9$. For a better illustration, in Fig. 4.19 the event rate difference together with the bin-by-bin Poisson Chi-square between the two above mentioned hypotheses (Eq. 4.4) are depicted in the full two-dimensional phase space of the fit. As it was expected from the theoretical discussion in Section 1.2.4.2 and the oscillograms in Section 1.3, the difference in the oscillation probability induced by the $\epsilon_{\tau\tau} - \epsilon_{\mu\mu}$ parameter is located very closely to the first oscillation resonance in the $\cos\theta = -1$ direction where the most matter is present on the neutrino path.

Figure 4.20 shows the "rank plot" for the $\epsilon_{\tau\tau} - \epsilon_{\mu\mu}$ measurement (for the explanation see Section 4.6). As can be seen, the best-fit value of $\epsilon_{\tau\tau} - \epsilon_{\mu\mu}$ is practically independent of the systematics when applied separately. The only nuisance parameter which stands out with its impact on the analysis is $\sin^2(\theta_{23})$ and this motion is fully in agreement with the theoretical discussion in Section 1.2.4.2. In the ν_μ disappearance channel, the most prominent modification in the oscillation pattern induced by $\epsilon_{\tau\tau} - \epsilon_{\mu\mu}$ is the reduction of the first minimum amplitude which in the standard case is governed by the $\sin^2(\theta_{23})$ value. The important detail is that this reduction effect acts similarly on neutrinos and anti-neutrinos and therefore interferes constructively in the flux containing both neutrino charges (see Section 1.2.4.2).

$\epsilon_{e\tau}$ measurement

Here, the results on $\epsilon_{e\tau}$ assuming it to be real are presented. The best-fit values of the model parameters are shown in Table 4.6. The observed profile likelihood curve on top of
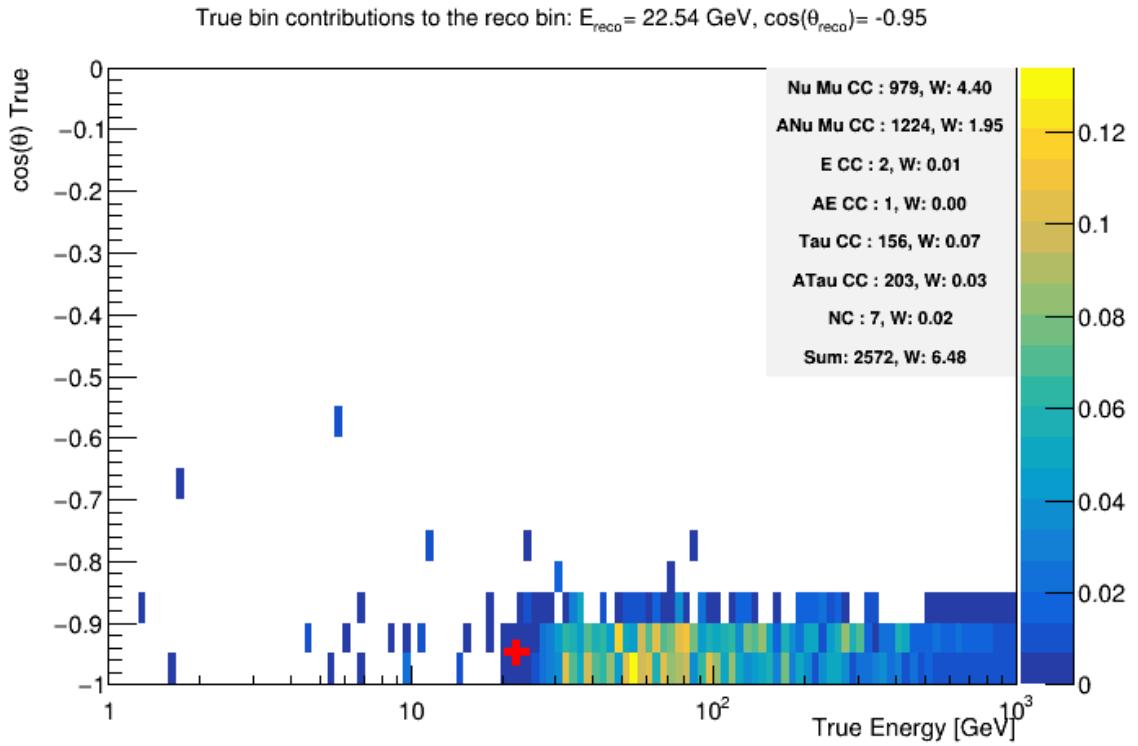
Figure 4.16: True bins contribution to a single reco bin $E_{reco} \in [20, 25)$, $\cos(\theta_{reco}) \in [-1, -0.9]$, whose centre is indicated by the red cross. The table in the plot shows the number of MC events for each interaction channel and the summed event weights indicated as "W". The weights correspond to NuFIT 5.1 NO best-fit parameters.
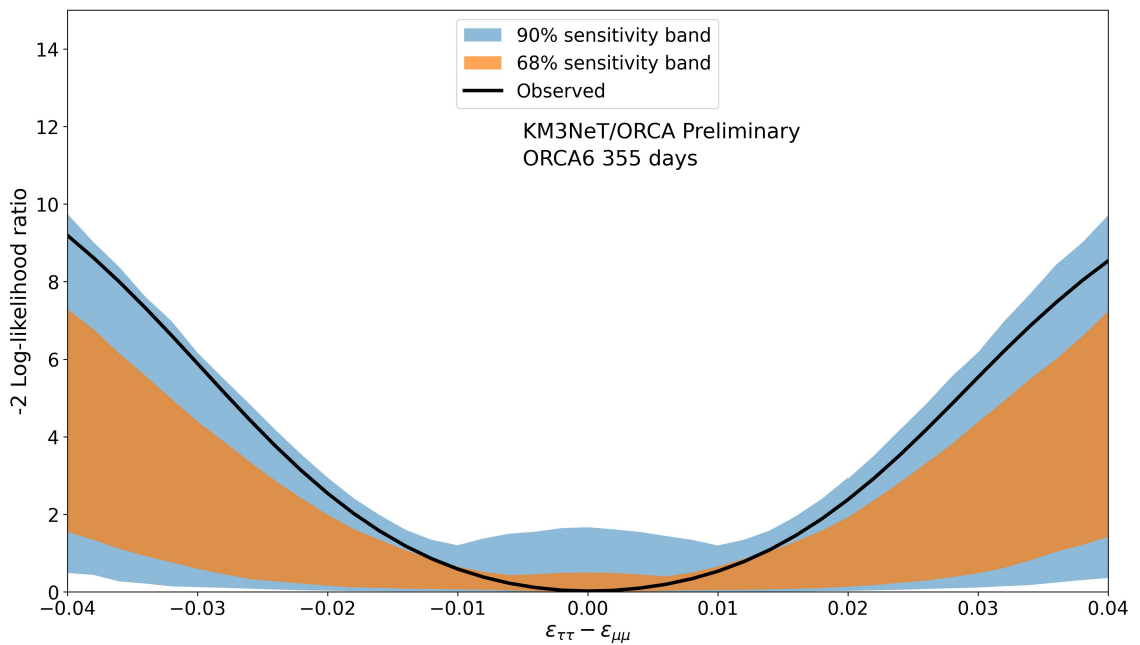
Figure 4.17: The observed profile likelihood scan for the measurement of $\epsilon_{\tau\tau} - \epsilon_{\mu\mu}$ with 355 days of ORCA6 (see Section 4.4 for explanation). The central 68% and 90% confidence regions of the experimental sensitivity are shown as shaded bands. See Section 4.5.1 for details.

Parameter	Fitted value
$\epsilon_{\tau\tau} - \epsilon_{\mu\mu}$	0.00 ± 0.01
$sin^2(\theta_{23})$	0.50 ± 0.11
$\Delta m^2_{31} [\text{eV}^2]$	$(-1.86^{+0.19}_{-0.21}) \cdot 10^{-3}$
Overall Normalisation	0.81 ± 0.11
Muon Normalisation	$2.0^{+1.7}_{-1.4}$
Flux: Spectral index tilt	0.06 ± 0.04
Flux: $\cos(\theta)$ tilt	0.02 ± 0.06
Flux: $\nu_\mu / \bar{\nu}_\mu$ skew	0.0 ± 0.1
Flux: $\nu_e / \bar{\nu}_e$ skew	0.0 ± 0.1
Flux: ν_μ / ν_e skew	0.00 ± 0.03
Cross-section: NC norm	1.0 ± 0.1
Cross-section: tau norm	1.0 ± 0.2
Detector: Energy scale	$0.000^{+0.017}_{-0.006}$
χ^2	108.9
Degrees of freedom	108
Chi-square p-value	0.46
Kolmogorov-Smirnov p-value	0.34

Table 4.5: Best-fit values from the ORCA6 data fit for the $\epsilon_{\tau\tau} - \epsilon_{\mu\mu}$ NSI model.

the sensitivity bands is portrayed in Fig. 4.21. The observed 90% CL confidence interval is

$$-0.080 \leq \epsilon_{e\tau} \leq 0.081. \tag{4.15}$$

Figure 4.22 illustrates the measured data on top of the reconstructed event distributions generated with the best-fit parameter set and the same set with $\epsilon_{e\tau}$ shifted to the positive confidence limit. The bins in the two-dimensional reconstructed space are grouped into four reconstructed energy slices and projected onto the reconstructed cosine zenith dimension. The sensitivity to $\epsilon_{e\tau}$ emerges from the same bins as in the case of $\epsilon_{\tau\tau} - \epsilon_{\mu\mu}$. However, the oscillation probability in the case of $\epsilon_{e\tau}$ is affected in a wider region and here a small shift in the position of the oscillation minimum is expected (see the oscillograms in Section 1.3). For a better illustration, in Fig. 4.23 the event rate difference together with the bin-by-bin Poisson Chi-square between the two above mentioned hypotheses (Eq. 4.4) are depicted in the full two-dimensional phase space of the fit. As can be seen again, the sensitivity to $\epsilon_{e\tau}$ is expected from the same reconstructed bins as in the case of $\epsilon_{\tau\tau} - \epsilon_{\mu\mu}$. These bins are known to have the best resolution in the whole ORCA6 detector response (see Section 3.1.5). The energy resolution of the bin with the boundaries $E_{reco} \in [10, 12.6)$ GeV, $\cos(\theta_{reco}) \in [-1, -0.9]$, is shown in Fig. 4.24. This bin, together with the neighbouring ones, gives ORCA6 the capability to observe the shift in the oscillation phase induced by $\epsilon_{e\tau}$.
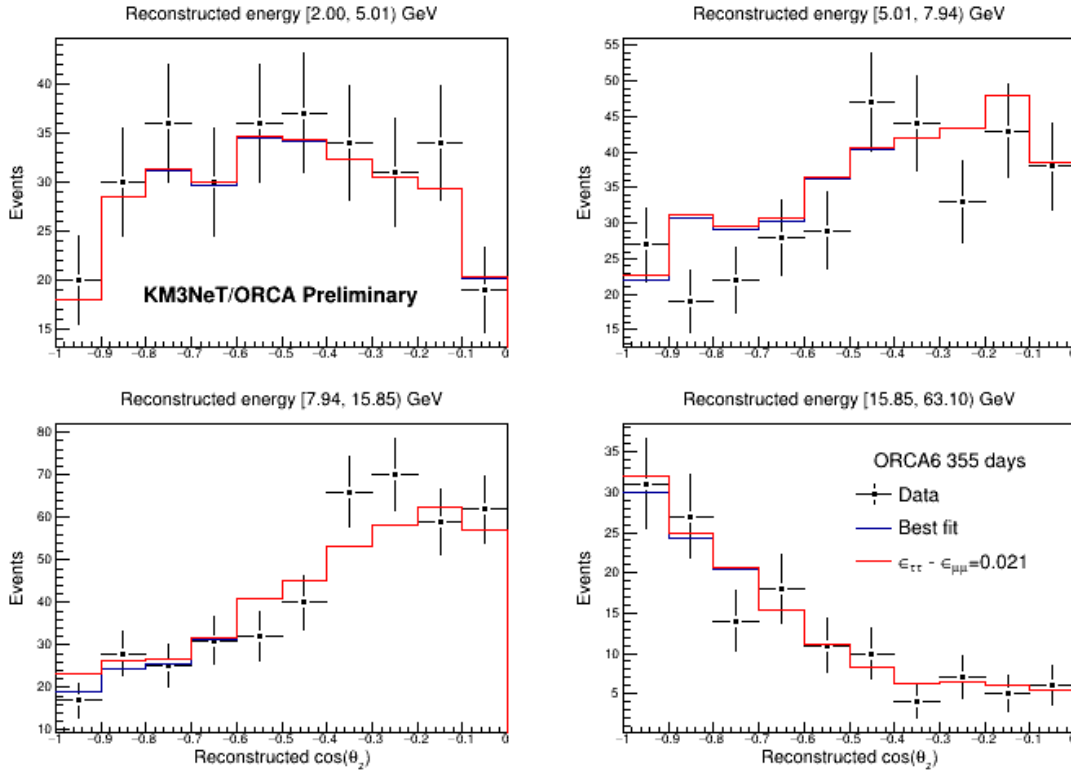
Figure 4.18: Histograms of observed events as a function of $\cos(\theta_{reco})$ for different slices in the reconstructed energy (indicated at the top of each panel), together with the MC expectation under the $\epsilon_{\tau\tau} - \epsilon_{\mu\mu}$ fit outcome (see Table 4.5) labelled as "Best fit" and the $\epsilon_{\tau\tau} - \epsilon_{\mu\mu} = 0.021$ shifted to its 90% confidence limit.
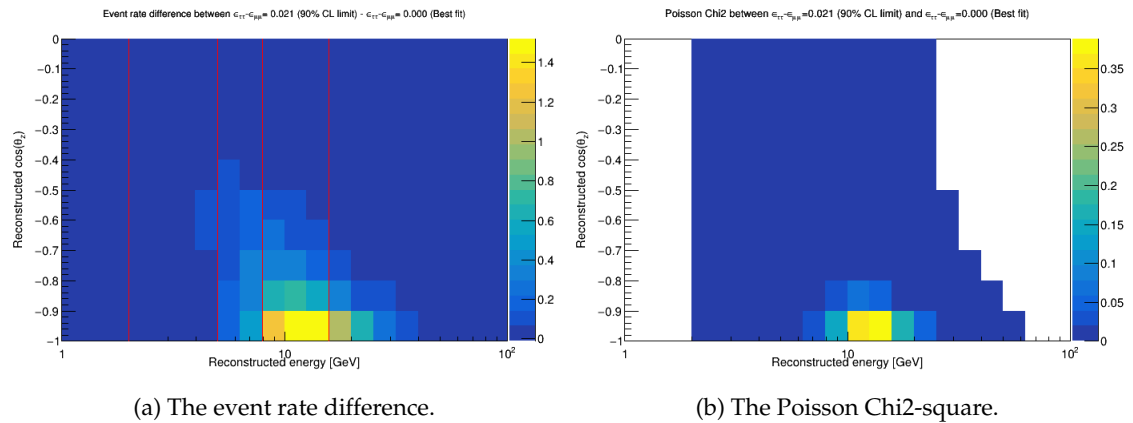
(a) The event rate difference.   (b) The Poisson Chi2-square.

Figure 4.19: The Poisson Chi-square calculated with Eq. 4.4 (right) and the event rate difference (left) between the 90% CL limit value of $\epsilon_{\tau\tau} - \epsilon_{\mu\mu} = 0.021$ and the best-fit value $\epsilon_{\tau\tau} - \epsilon_{\mu\mu} = 0.000$. All the nuisance parameters are set to their MLEs. The red lines in the left plot indicate the boundaries for the energy slices shown in Fig. 4.18.

Figure 4.25 shows the "rank plot" for the $\epsilon_{e\tau}$ measurement (for the explanation see Section 4.6). Similarly to the case of $\epsilon_{\mu\tau}$, Δm^2_{31} stands out with its impact on the analysis. This is expected from the fact that some of the sensitivity to $\epsilon_{e\tau}$ comes from the phase shift in the ν_μ disappearance oscillation channel. However, the supposedly very significant shift from the negative post-fit impact of Δm^2_{31} is caused by the change of the sign of the $\epsilon_{e\tau}$ best-fit point (in the case of Δm^2_{31}, the lower x-axis does use moduli, see Section 4.6.1).
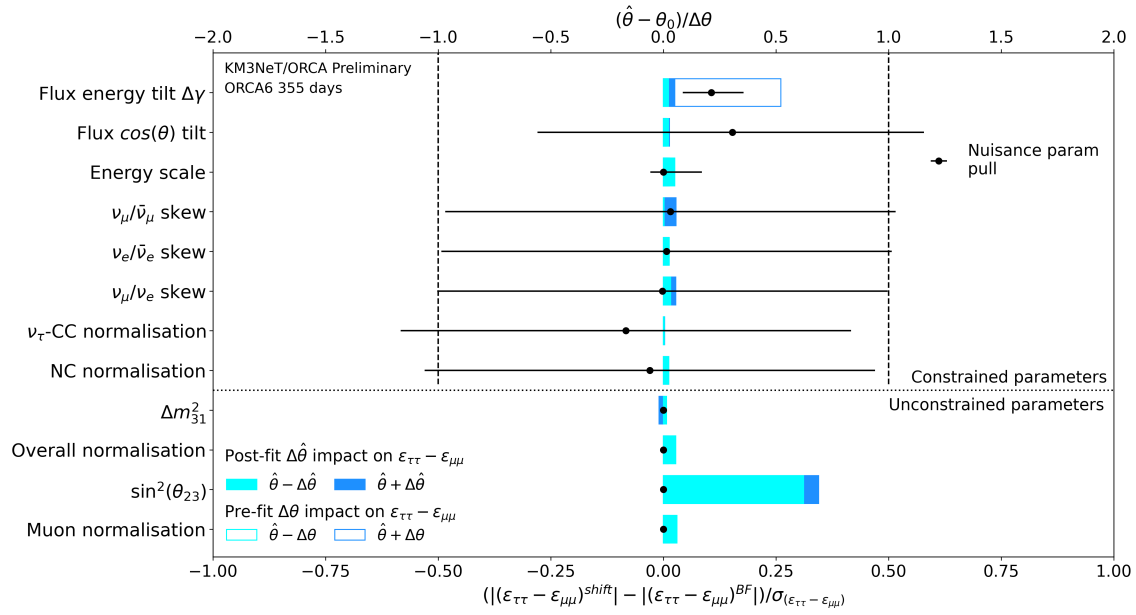
Figure 4.20: Rank plot for the real $\epsilon_{\tau\tau} - \epsilon_{\mu\mu}$ model. See Section 4.6 for explanation.

Parameter	Fitted value
$\epsilon_{e\tau}$	$0.02^{+0.05}_{-0.08}$
$sin^2(\theta_{23})$	$0.50^{+0.10}_{-0.11}$
$\Delta m^2_{31} [\text{eV}^2]$	$(-1.86^{+0.25}_{-0.23}) \cdot 10^{-3}$
Overall Normalisation	$0.81^{+0.12}_{-0.10}$
Muon Normalisation	2.0 ± 1.5
Flux: Spectral index tilt	0.06 ± 0.04
Flux: $\cos(\theta)$ tilt	0.02 ± 0.06
Flux: $\nu_\mu/\bar{\nu}_\mu$ skew	0.0 ± 0.1
Flux: $\nu_e/\bar{\nu}_e$ skew	0.0 ± 0.1
Flux: ν_μ/ν_e skew	0.00 ± 0.03
Cross-section: NC norm	1.0 ± 0.1
Cross-section: tau norm	1.0 ± 0.2
Detector: Energy scale	$0.000^{+0.018}_{-0.006}$
χ^2	108.9
Degrees of freedom	108
Chi-square p-value	0.46
Kolmogorov-Smirnov p-value	0.34

Table 4.6: Best-fit values from the ORCA6 data fit to the $\epsilon_{e\tau}$ real NSI model.
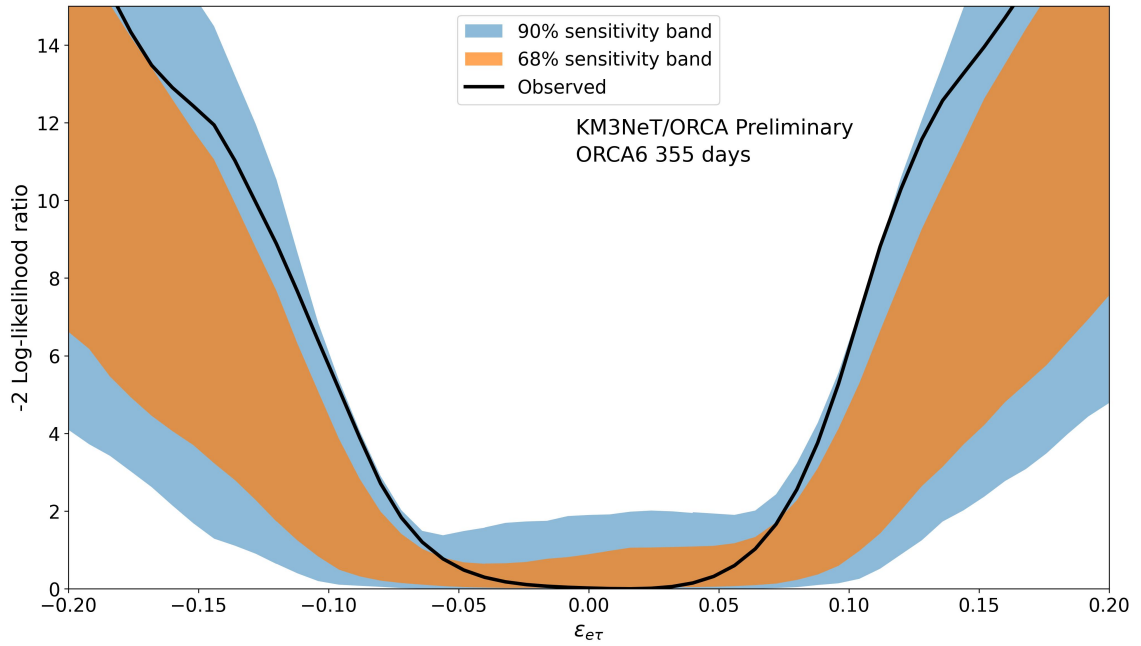
Figure 4.21: The observed profile likelihood scan for the measurement of $\epsilon_{e\tau}$ with 355 days of ORCA6 (see Section 4.4 for explanation). The central 68% and 90% confidence regions of the experimental sensitivity are shown as shaded bands. See Section 4.5.1 for details.
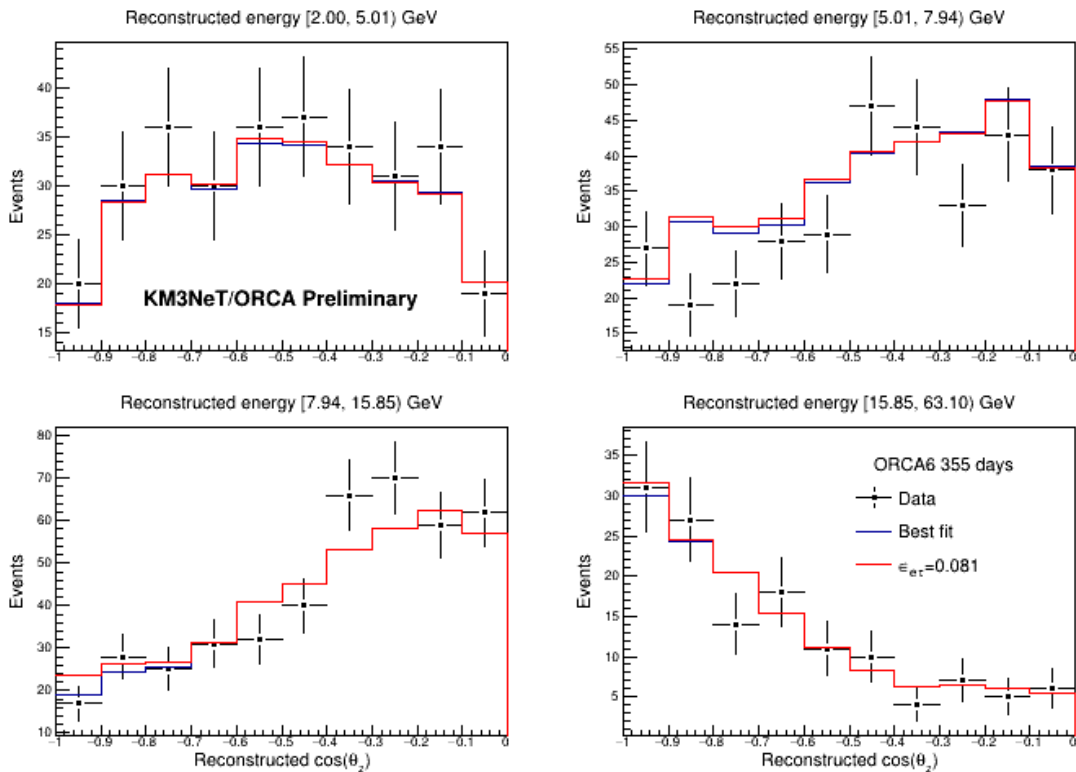
Figure 4.22: Histograms of observed events as a function of $\cos(\theta_{reco})$ for different slices in the reconstructed energy (indicated at the top of each panel), together with the MC expectation under the real $\epsilon_{e\tau}$ fit outcome (see Table 4.6) labelled as "Best fit" and the $\epsilon_{e\tau} = 0.081$ shifted to its confidence limit.

(a) The event difference.   (b) The Poisson Chi-square.
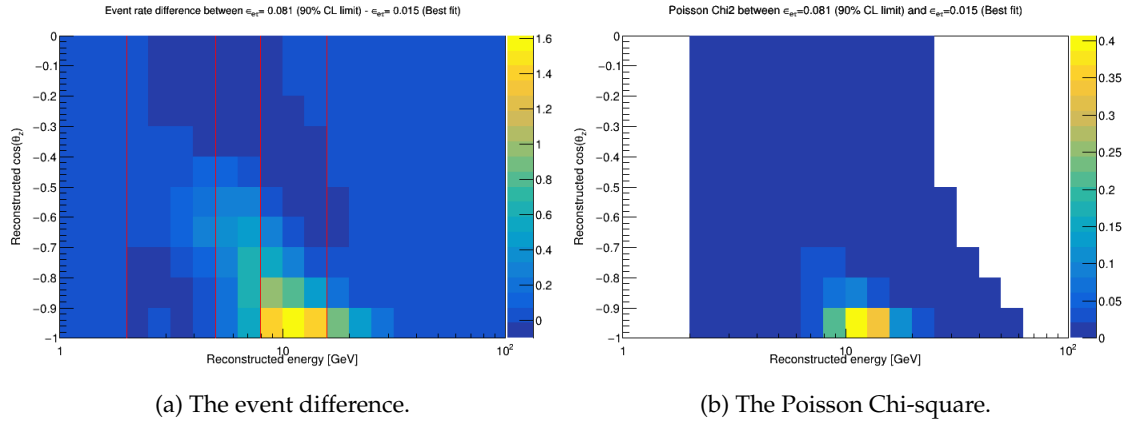
Figure 4.23: The Poisson Chi-square calculated with Eq. 4.4 (right) and the event rate difference (left) between the 90% CL limit value of $\epsilon_{e\tau} = 0.081$ and the best-fit value $\epsilon_{e\tau} = 0.015$. All the nuisance parameters are set to their MLEs. The red lines in the left plot indicate the boundaries for the energy slices shown in Fig. 4.22.
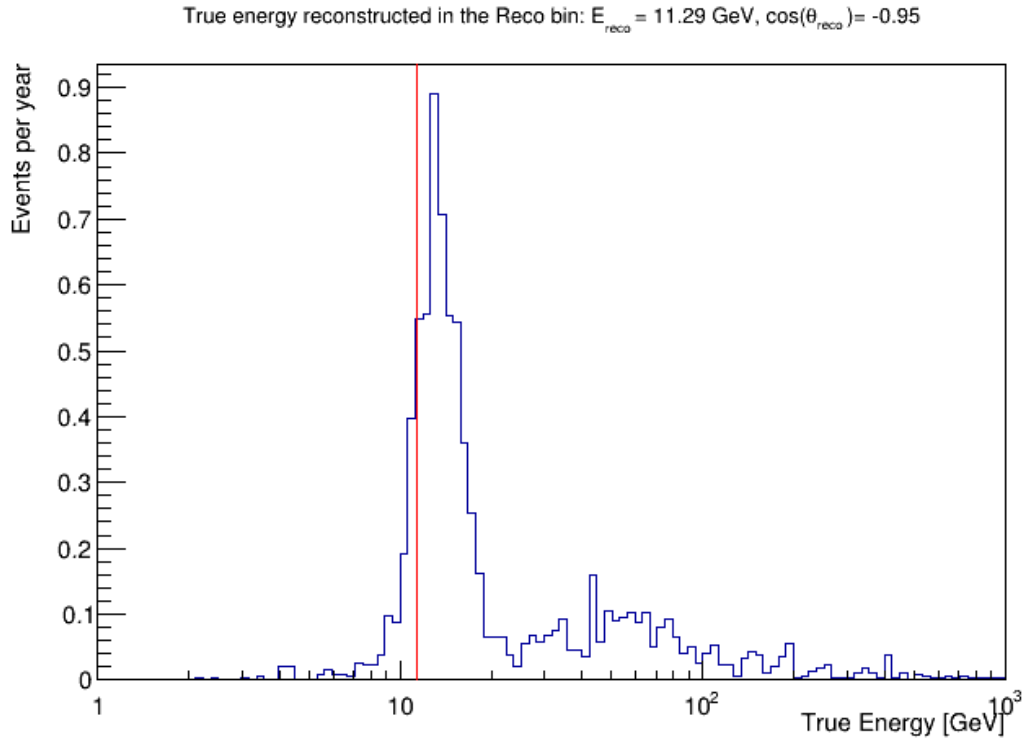
Figure 4.24: The distribution of the true energy reconstructed in the bin $E_{reco} \in [10, 12.6)$ GeV, $\cos(\theta_{reco}) \in [-1, -0.9]$. The red line indicates the bin centre in the energy dimension. The weights correspond to NuFIT 5.1 NO best-fit parameters.

Since the likelihood landscape is very flat around $\epsilon_{e\tau} = 0$, this Δm^2_{31}-induced shift should not be seen as extraordinarily important. The $\nu_\mu / \bar{\nu}_\mu$ skew of the flux is more prominent as the effect of $\epsilon_{e\tau}$ on the ν_μ and $\bar{\nu}_\mu$ survival probabilities is not symmetric around the sign of NSI as it is the case of $\epsilon_{\mu\tau}$. The likelihood landscape is relatively flat around the best-fit point, so the effects of the other systematics can be interpreted as fluctuations.
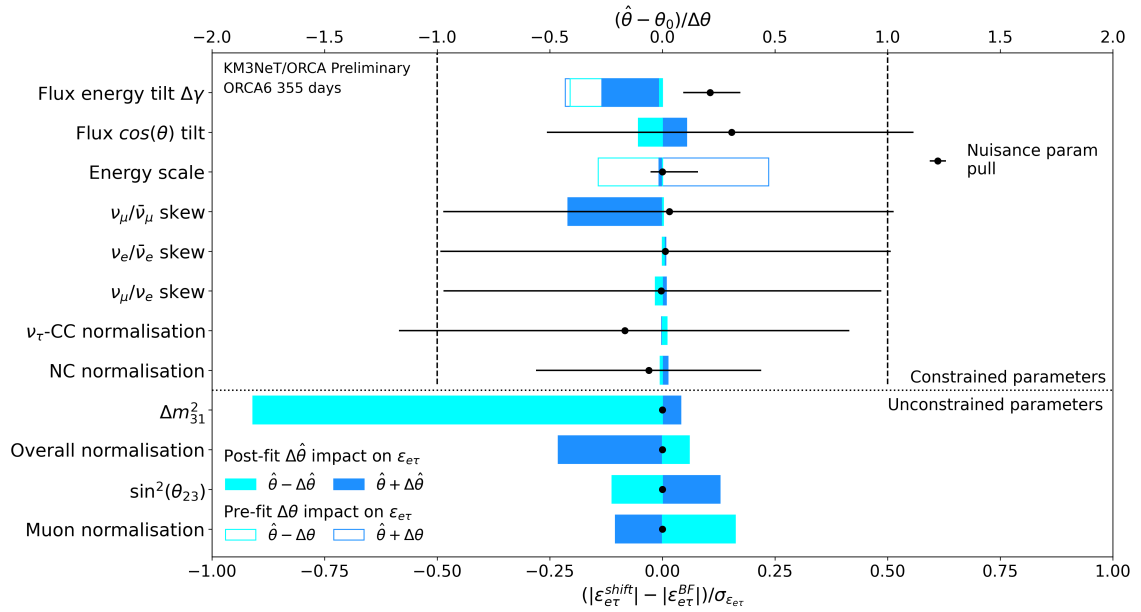
Figure 4.25: The "rank plot" which provides information about the systematics and their impact on the estimation of $\epsilon_{e\tau}$ with the observed data. See Section 4.6.1 for explanation.

$\epsilon_{e\mu}$ measurement

Here, the results on $\epsilon_{e\mu}$ assuming it to be real are presented. The best-fit values of the model parameters are shown in Table 4.7. The observed profile likelihood scan on top of the sensitivity bands is portrayed in Fig. 4.26. The observed 90% CL confidence interval is:

$$-0.069 \leq \epsilon_{e\mu} \leq 0.069. \tag{4.16}$$

Figure 4.27 illustrates the measured data on top of the reconstructed event distributions generated with the best-fit parameter set and the same set with $\epsilon_{e\mu}$ shifted to the positive confidence limit. The bins in the two-dimensional reconstructed space are grouped into four reconstructed energy slices and projected onto the reconstructed cosine zenith dimension. The sensitivity is expected either from the more horizontal events of $-0.5 < \cos(\theta_{reco}) < -0.2$ in the lower reconstructed energy $E_{reco} < 15$ GeV or higher reconstructed energy $E_{reco} > 15$ GeV and more up-going directions of $-0.9 < \cos(\theta_{reco}) < -0.7$. For a better illustration, in Fig. 4.28 the event rate difference together with the bin-by-bin Poisson Chi-square between the two above mentioned hypotheses (Eq. 4.4) are depicted in the full two-dimensional phase space of the fit. The Chi-square map shows what was expected from the oscillograms presented in Section 1.3. The sensitivity comes from the bins looking into very high neutrino energies in the directions of broad landscapes of event deficit. The discontinuity in the cosine zenith dimension is also predicted by the theory. Figure 4.29 shows the "rank plot" for the $\epsilon_{e\mu}$ measurement (for the explanation see Section 4.6). The spectral index energy tilt outreaches the presented lower x-axis scale (it goes up to $\sim$4) in terms of the pre-fit impact on the $\epsilon_{e\mu}$ best-fit point. This behaviour is expected from the wide range of true neutrino energy contributing to the $\epsilon_{e\mu}$ (see the ORCA6 bin-by-bin energy resolution in Section 3.1.5 and the oscillograms in Section 1.3). Nevertheless, this is not problematic since the flux energy tilt is constrained by the data to the level that it does not induce an extraordinary shift anymore. The other systematics do not manifest a very significant

Parameter	Fitted value
$\epsilon_{e\mu}$	$0.01^{+0.06}_{-0.04}$
$sin^2(\theta_{23})$	$0.51^{+0.10}_{-0.11}$
$\Delta m^2_{31}[\text{eV}^2]$	$(1.98^{+0.25}_{-0.23}) \cdot 10^{-3}$
Overall Normalisation	$0.81^{+0.12}_{-0.10}$
Muon Normalisation	2.0 ± 1.5
Flux: Spectral index tilt	0.07 ± 0.04
Flux: $\cos(\theta)$ tilt	0.02 ± 0.06
Flux: $\nu_\mu/\bar{\nu}_\mu$ skew	0.0 ± 0.1
Flux: $\nu_e/\bar{\nu}_e$ skew	0.0 ± 0.1
Flux: ν_μ/ν_e skew	0.00 ± 0.03
Cross-section: NC norm	1.0 ± 0.1
Cross-section: tau norm	1.0 ± 0.2
Detector: Energy scale	$0.000^{+0.018}_{-0.006}$
χ^2	108.8
Degrees of freedom	108
Chi-square p-value	0.46
Kolmogorov-Smirnov p-value	0.33

Table 4.7: Best-fit values from the ORCA6 data fit to the $\epsilon_{e\tau}$ real NSI model.

impact and the general trend from the study of the incremental effect of the systematics is followed (see Section 4.6.1).

4.7.2   Complex NSI scenario

In this section, the results on the models with complex flavour-violating NSI parameters are presented.

$|\epsilon_{\mu\tau}|$ and $\delta_{\mu\tau}$ measurement

Here, the results on the $|\epsilon_{\mu\tau}|$ and $\delta_{\mu\tau}$ are presented. The best-fit values of the model parameters are shown in Table 4.8. The observed 90% CL contour in the 2D parameter space of $|\epsilon_{\mu\tau}|$ versus $\delta_{\mu\tau}$ is shown in Fig. 4.30 together with the 1D profiled likelihood scans. The observed 90% CL limits are:

$$|\epsilon_{\mu\tau}| \leq 0.011, \tag{4.17}$$
$$0° \leq \delta_{\mu\tau} \leq 360°. \tag{4.18}$$

Figure 4.31 illustrates the measured data on top of the reconstructed event distributions generated with the best-fit parameter set and the same set with $|\epsilon_{\mu\tau}|$ shifted to the
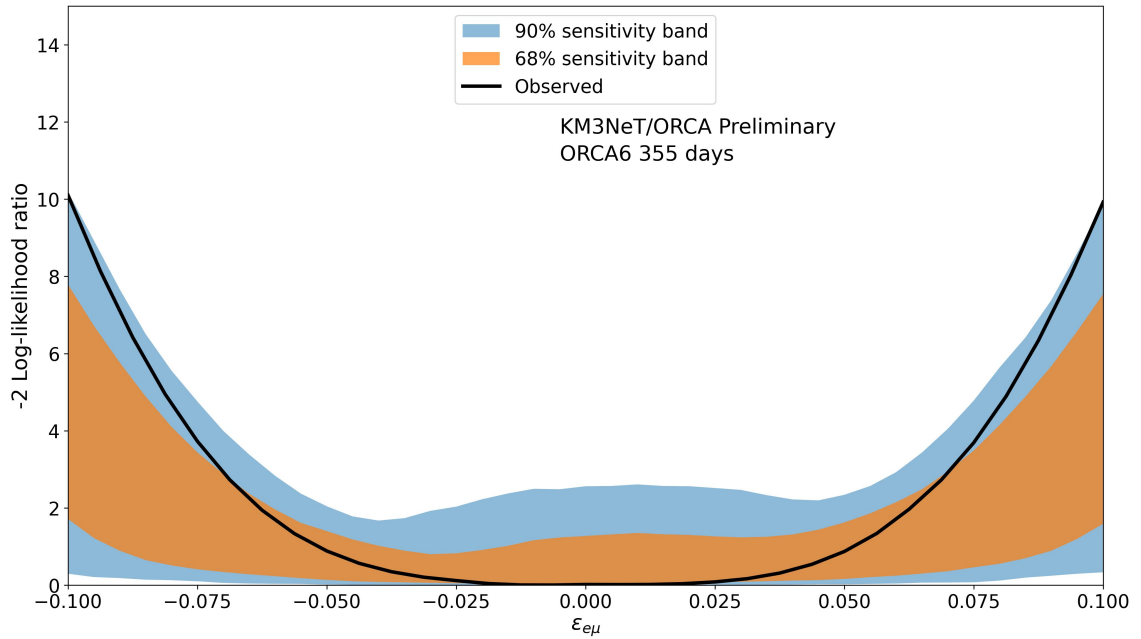
Figure 4.26: The observed profile likelihood scan for the measurement of $\epsilon_{e\mu}$ with 355 days of ORCA6 (see Section 4.4 for explanation). The central 68% and 90% confidence regions of the experimental sensitivity are shown as shaded bands. See Section 4.5.1 for details.
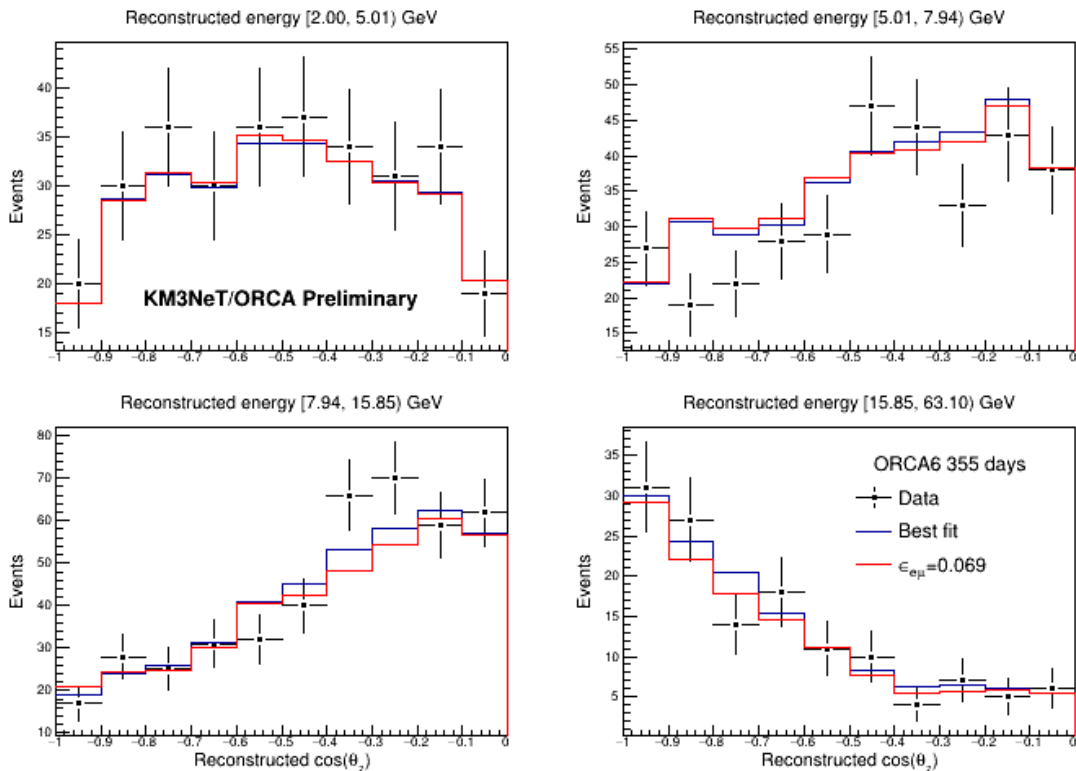
Figure 4.27: Histograms of observed events as a function of $\cos(\theta_{reco})$ for different slices in the reconstructed energy (indicated at the top of each panel), together with the MC expectation under the real $\epsilon_{e\mu}$ fit outcome (see Table 4.7) labelled as "Best fit" and the $\epsilon_{e\mu} = 0.069$ shifted to its 90% confidence limit.

(a) The event rate difference.

(b) The Poisson Chi-square.
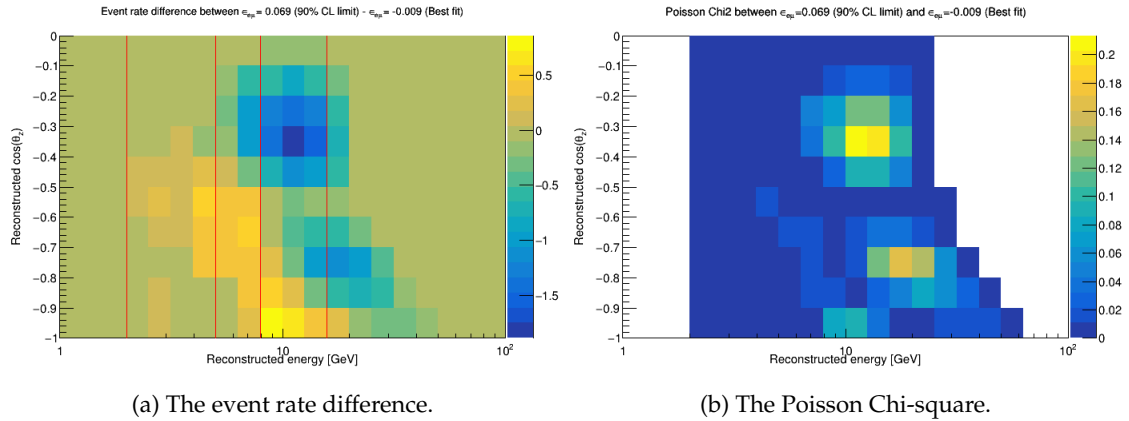
Figure 4.28: The Poisson Chi-square calculated with Eq. 4.4 (right) and the event rate difference (left) between the 90% CL limit value of $\epsilon_{e\mu} = 0.069$ and the best-fit value $\epsilon_{e\mu} = 0.009$. All the nuisance parameters are set to their MLEs. The red lines in the left plot indicate the boundaries for the energy slices shown in Fig. 4.27.
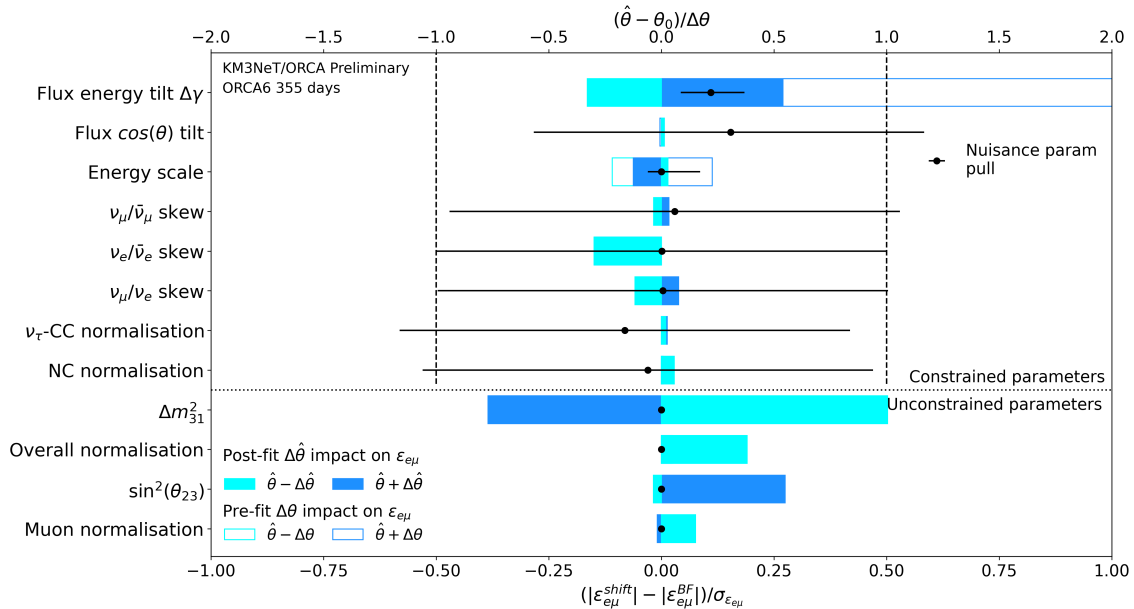
Figure 4.29: The "rank plot" which provides information about the systematics and their individual impact on the estimation of $\epsilon_{e\mu}$ with the observed data. See Section 4.6.1 for explanation

confidence limit. The bins in two-dimensional reconstructed space are grouped into four reconstructed energy slices and projected onto the reconstructed cosine zenith dimension. As can be seen, the special bin from Figs. 4.15 and 4.16 discussed with the results on the real $\epsilon_{\mu\tau}$ is not prominent in the Chi-square map anymore, because the shift in the oscillation resonance is not visible due to the presence of $\delta_{\mu\tau}$. This observation is in agreement with the theoretical predictions from Sections 1.2.4.3 and 1.3, where the impact of the complex phase is expected to diminish the difference between the NSI model and the standard oscillations in the neutrino energies below ~ 80 GeV (the region where the linear terms in $\epsilon_{\mu\tau}$ dominate).

Figure 4.33 shows the "rank plot" for the complex $\epsilon_{\mu\tau}$ measurement (for the explanation see Section 4.6). The complex phase $\delta_{\mu\tau}$ is added to the plot as one of the nuisance

Parameter	Fitted value
$|\epsilon_{\mu\tau}|$	$0.0025^{+0.0059}_{-0.0025}$
$\delta_{\mu\tau}[°]$	37^{+323}_{-37}
$sin^2(\theta_{23})$	$0.51^{+0.10}_{-0.12}$
$\Delta m^2_{31}[eV^2]$	$(1.92^{+0.25}_{-0.23}) \cdot 10^{-3}$
Overall Normalisation	0.80 ± 0.11
Muon Normalisation	$2.0^{+1.7}_{-1.5}$
Flux: Spectral index tilt	0.07 ± 0.04
Flux: $\cos(\theta)$ tilt	0.02 ± 0.06
Flux: $\nu_\mu/\bar{\nu}_\mu$ skew	0.0 ± 0.1
Flux: $\nu_e/\bar{\nu}_e$ skew	0.0 ± 0.1
Flux: ν_μ/ν_e skew	0.00 ± 0.03
Cross-section: NC norm	1.0 ± 0.1
Cross-section: tau norm	1.0 ± 0.2
Detector: Energy scale	$0.000^{+0.018}_{-0.006}$
χ^2	108.8
Degrees of freedom	108
Chi-square p-value	0.46
Kolmogorov-Smirnov p-value	0.35

Table 4.8: Best-fit values from ORCA6 data fit to the $\epsilon_{\mu\tau}$ complex NSI model.

parameters. The post-fit shift values correspond to the limiting cases of $\delta_{\mu\tau} = \{\pi/2, \pi\}$ in the approximate formula in Eq. 1.68. None of the systematics show an especially significant impact on the best-fit point. The 1σ intervals on the constrained nuisance parameters derived from the data have exactly the same relation to the prior widths as in the real $\epsilon_{\mu\tau}$ analysis case. This appears to be the case in all the tested complex NSI models (see the subsequent sections).

$|\epsilon_{e\tau}|$ and $\delta_{e\tau}$ measurement

Here, the results on the $|\epsilon_{e\tau}|$ and $\delta_{e\tau}$ are presented. The best-fit values of the model parameters are shown in Table 4.8. The observed 90% CL contour in the 2D parameter space of $|\epsilon_{e\tau}|$ versus $\delta_{e\tau}$ is shown in Fig. 4.34 together with the one-dimensional profiled likelihood scans. The observed 90% CL limits are:

$$|\epsilon_{e\tau}| \leq 0.082, \tag{4.19}$$
$$0° \leq \delta_{e\tau} \leq 360°. \tag{4.20}$$

As expected, no sensitivity to $\delta_{e\tau}$ from ORCA6 was obtained. Overall, the results on the complex $\epsilon_{e\tau}$ are very similar to the results on the real $\epsilon_{e\tau}$.
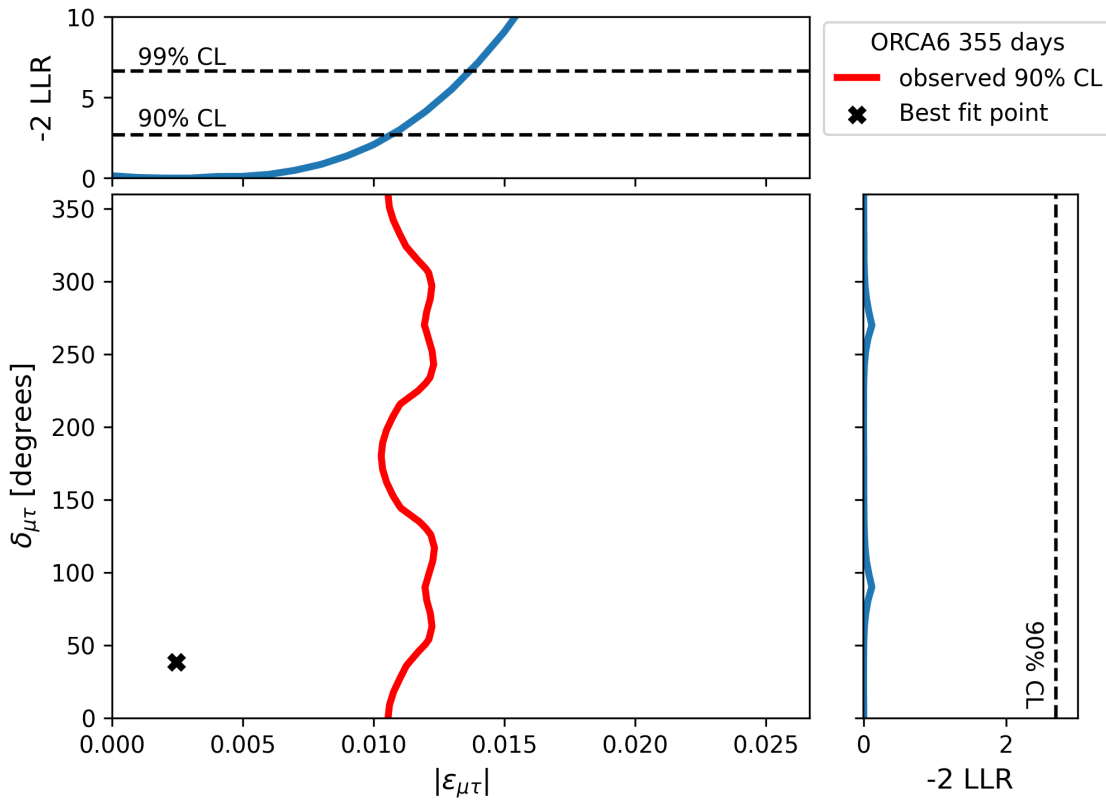
Figure 4.30: Observed 90% confidence regions in the magnitude $\epsilon_{\mu\tau}$ and $\delta_{\mu\tau}$ phase together with the projected one-dimensional -2log-likelihood ratio profile. The best fit point is indicated by the cross.

Figure 4.35 illustrates the measured data on top of the reconstructed event distributions generated with the best-fit parameter set and the same set with $|\epsilon_{e\mu}|$ shifted to the quoted confidence limit. The bins in the two-dimensional reconstructed space are grouped into four reconstructed energy slices and projected onto the reconstructed cosine zenith dimension. Figure 4.36 shows the event rate difference together with the bin-by-bin Poisson Chi-square (Eq. 4.4) between the two above mentioned hypotheses, depicted in the full two-dimensional phase space of the fit. The sensitivity seems to be slightly shifted to the higher reconstructed energy with respect to the real model. Figure 4.33 shows the "rank plot" for the complex $\epsilon_{\mu\tau}$ measurement (see Section 4.6 for explanation). At first glance, it might seem that the individual impact of the systematics has changed significantly compared to Fig. 4.25, but the difference between moduli in the lower x-axis of both plots in practice does not have the same meaning. Overall, no systematic significantly affects the best-fit value.

$|\epsilon_{e\mu}|$ and $\delta_{e\mu}$ measurement

Here the results on the $|\epsilon_{e\mu}|$ and $\delta_{e\mu}$ are presented. The best-fit values of the model parameters are shown in Table 4.8. The observed 90% CL contour in 2D parameter space of $|\epsilon_{e\mu}|$ and $\delta_{e\mu}$ is shown in Fig. 4.34 together with the 1D profiled likelihood scans. The observed one-dimensional 90% CL limits are:

$$|\epsilon_{e\mu}| \leq 0.068, \tag{4.21}$$
$$0° \leq \delta_{e\mu} \leq 360°. \tag{4.22}$$
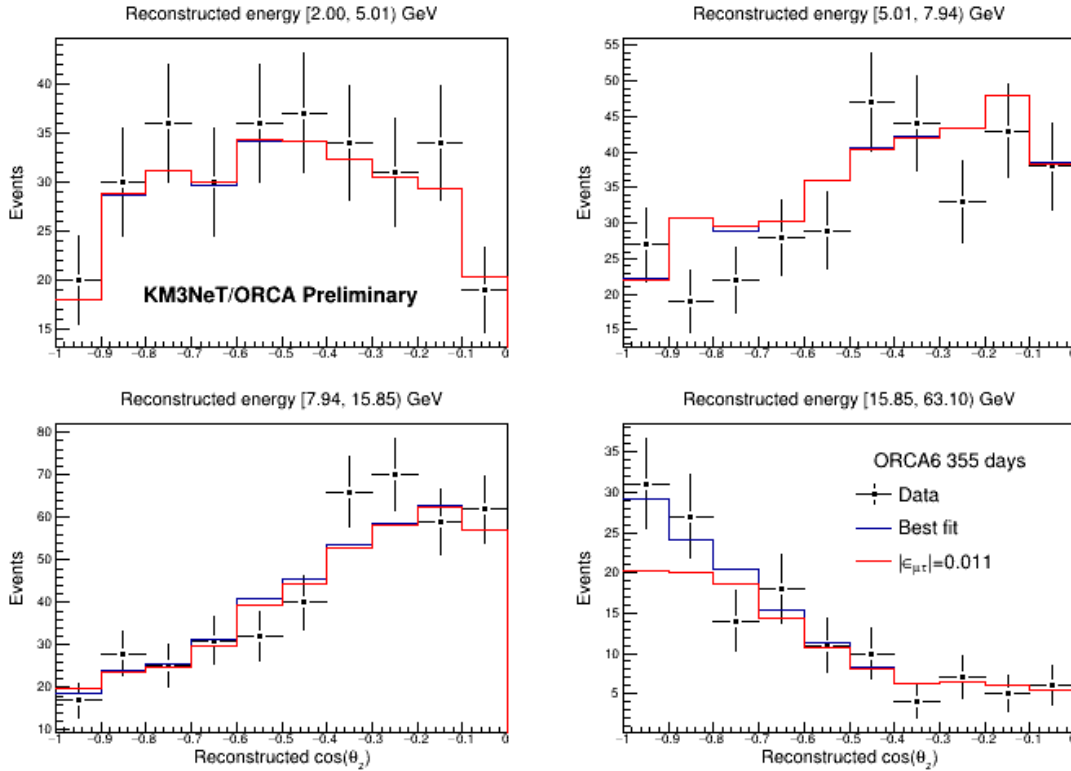
Figure 4.31: Histograms of observed events as a function of $\cos(\theta_{reco})$ for different slices in the reconstructed energy (indicated at the top of each panel), together with the MC expectation under the complex $\epsilon_{\mu\tau}$ fit outcome (see Table 4.8) labelled as "Best fit" and the $|\epsilon_{\mu\tau}| = 0.011$ shifted to its confidence limit.

(a) Event rate difference   (b) Poisson Chi-square
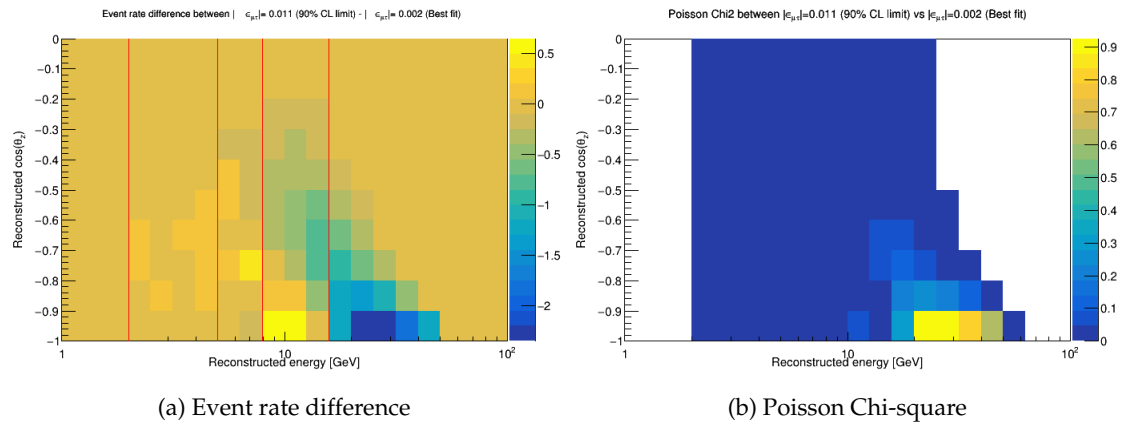
Figure 4.32: The Poisson Chi-square calculated with Eq. 4.4 (right) and the event rate difference (left) between the 90% CL limit value of $|\epsilon_{\mu\tau}| = 0.011$ and the best-fit value $|\epsilon_{\mu\tau}| = 0.0025$. All the nuisance parameters are set to their MLEs. The red lines in the left plot indicate the boundaries for the energy slices shown in Fig. 4.31.

As expected, no sensitivity to $\delta_{e\mu}$ from ORCA6 was observed. The results on the complex $\epsilon_{e\mu}$ are similar to the results on the real $\epsilon_{e\mu}$. The complex model fits a different hierarchy, but the best-fit value of the complex phase is close to 180 degrees so the real part is negative and therefore has the same sign as in the case of the real $\epsilon_{e\mu}$ results.

Figure 4.39 illustrates the measured data on top of the reconstructed event distributions generated with the best-fit parameter set and the same set with $|\epsilon_{e\mu}|$ shifted to the
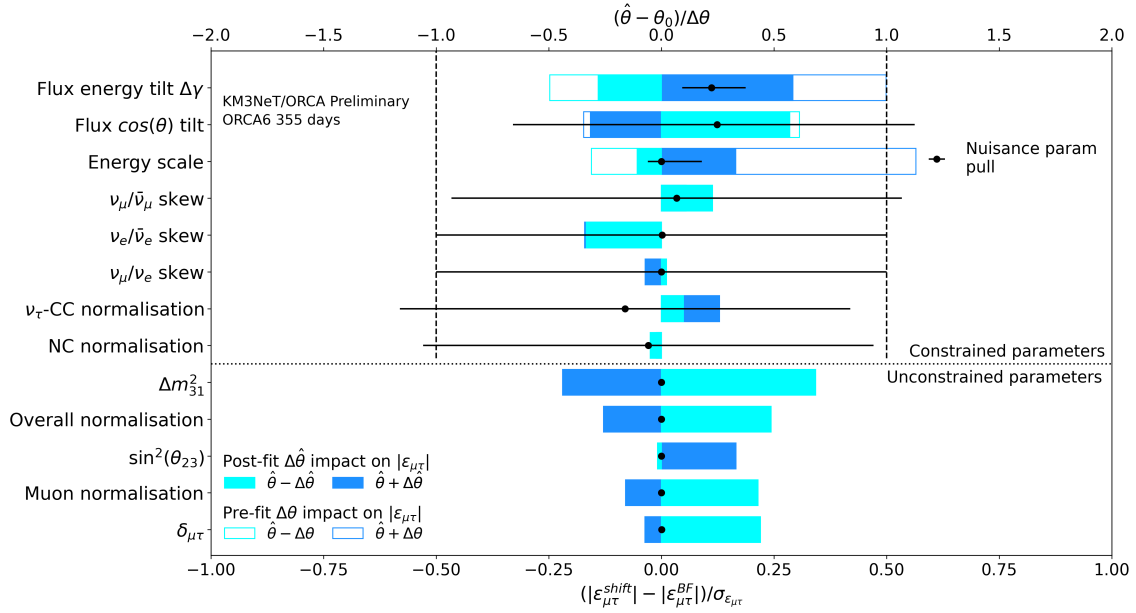
Figure 4.33: The "rank plot" which provides information about the systematics and their individual impact on the estimation of the $|\epsilon_{\mu\tau}|$ with the observed data. See Section 4.6.1 for explanation
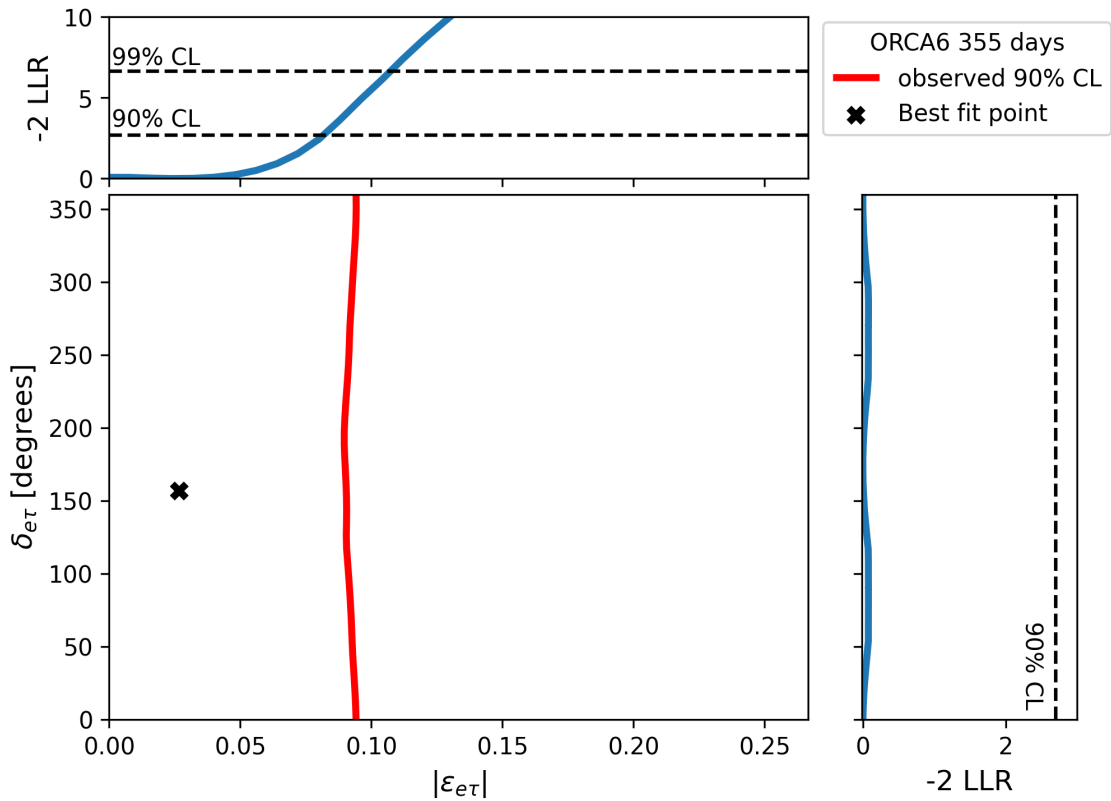
Figure 4.34: Observed 90% confidence regions in the magnitude $\epsilon_{e\tau}$ and $\delta_{e\tau}$ phase together with the projected one-dimensional -2log-likelihood ratio profile. The best fit point is indicated by the cross.

observed confidence limit. The bins in the two-dimensional reconstructed space are

Parameter	Fitted value
$\lvert\epsilon_{e\tau}\rvert$	$0.027^{+0.038}_{-0.027}$
$\delta_{e\tau}[^\circ]$	157^{+203}_{-157}
$sin^2(\theta_{23})$	$0.50^{+0.10}_{-0.11}$
$\Delta m^2_{31}[\text{eV}^2]$	$(-1.90^{+0.25}_{-0.23})\cdot 10^{-3}$
Overall Normalisation	$0.81^{+0.12}_{-0.10}$
Muon Normalisation	2.0 ± 1.5
Flux: Spectral index tilt	0.07 ± 0.04
Flux: $\cos(\theta)$ tilt	0.02 ± 0.06
Flux: $\nu_\mu/\bar{\nu}_\mu$ skew	0.0 ± 0.1
Flux: $\nu_e/\bar{\nu}_e$ skew	0.0 ± 0.1
Flux: ν_μ/ν_e skew	0.00 ± 0.03
Cross-section: NC norm	1.0 ± 0.1
Cross-section: tau norm	1.0 ± 0.2
Detector: Energy scale	$0.000^{+0.018}_{-0.006}$
χ^2	108.8
Degrees of freedom	108
Chi-square p-value	0.461
Kolmogorov-Smirnov p-value	0.336

Table 4.9: Best-fit values from ORCA6 data fit to the $\epsilon_{e\tau}$ complex NSI model.

grouped into four reconstructed energy slices and projected onto the reconstructed cosine zenith dimension. Figure 4.40 shows the event rate difference together with the bin-by-bin Poisson Chi-square between the two above mentioned hypotheses (Eq. 4.4) are depicted in the full two-dimensional phase space of the fit. There is no significant difference in the source of the sensitivity with respect to the real model.

Figure 4.41 shows the "rank plot" for the complex $\epsilon_{\mu\tau}$ measurement (see Section 4.6 for explanation). Once again, the difference with respect to the rank plot of the real model in Fig. 4.29 is mostly ostensible due to the difference in the interpretation of the lower x-axis. After being constrained by the data, none of the presented systematics manifests a statistically significant impact on the analysis, when applied individually.

4.8 Impact of the Earth composition model

Figure 4.42 shows the ORCA6 355 days results for the real $\epsilon_{\mu\tau}$ with the assumption of NSI coupling to electrons or u-quarks, both re-scaled to match the d-quark coupling strength. The original result from Section 4.7.1 is shown for comparison. The re-scaling factors are
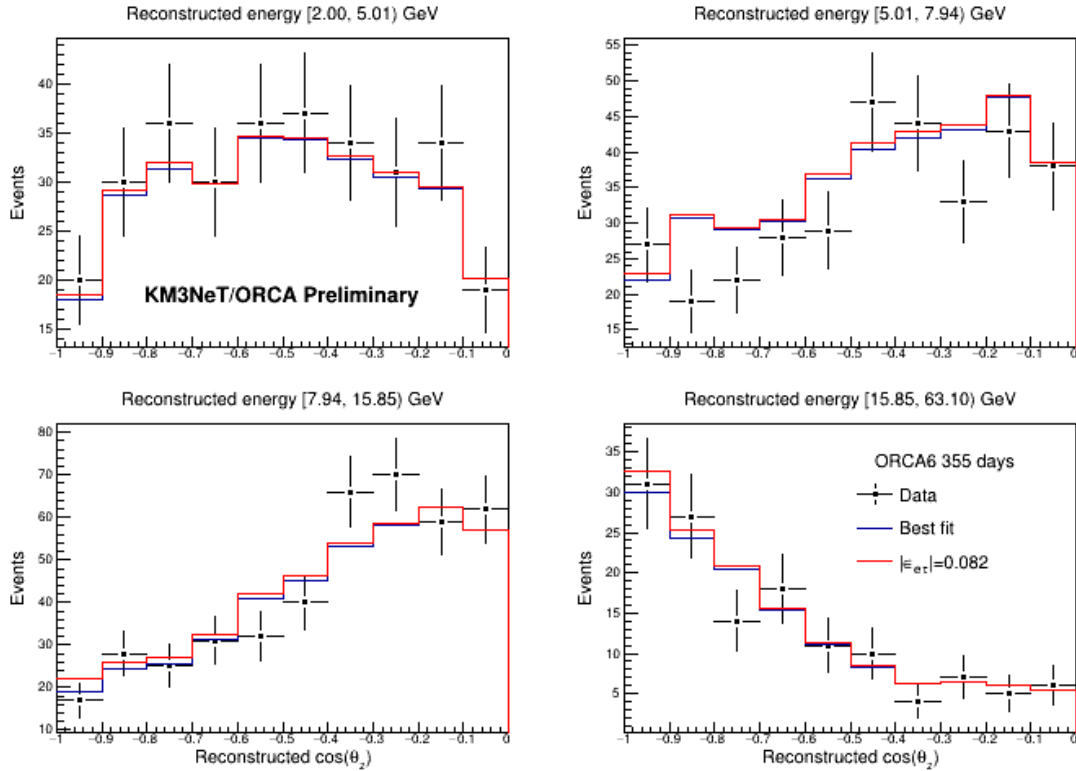
Figure 4.35: Histograms of observed events as a function of $\cos(\theta_{reco})$ for different slices in the reconstructed energy (indicated at the top of each panel), together with the MC expectation under the complex $\epsilon_{e\tau}$ fit outcome (see Table 4.9) labelled as "Best fit" and the $|\epsilon_{e\tau}| = 0.082$ shifted to its confidence limit.
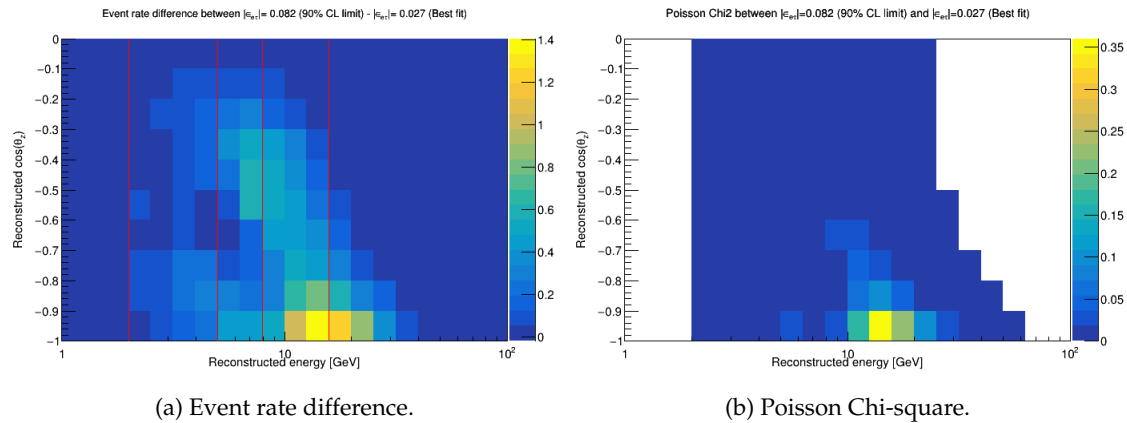
(a) Event rate difference.

(b) Poisson Chi-square.

Figure 4.36: The Poisson Chi-square calculated with Eq. 4.4 (right) and the event rate difference (left) between the 90% CL limit value of $|\epsilon_{e\tau}| = 0.027$ and the best-fit value $|\epsilon_{e\tau}| = 0.082$. All the nuisance parameters are set to their MLEs. The red lines in the left plot indicate the boundaries for the energy slices shown in Fig. 4.35.

the mass-weighted average ratios

$$\langle Y_d \rangle = \langle \frac{N_d}{N_e} \rangle = 3.11 \tag{4.23}$$

$$\langle Y_u \rangle = \langle \frac{N_u}{N_e} \rangle = 3.055 \tag{4.24}$$

$$\langle Y_d \rangle / \langle Y_u \rangle = \langle N_d \rangle / \langle N_u \rangle = 1.018 \tag{4.25}$$
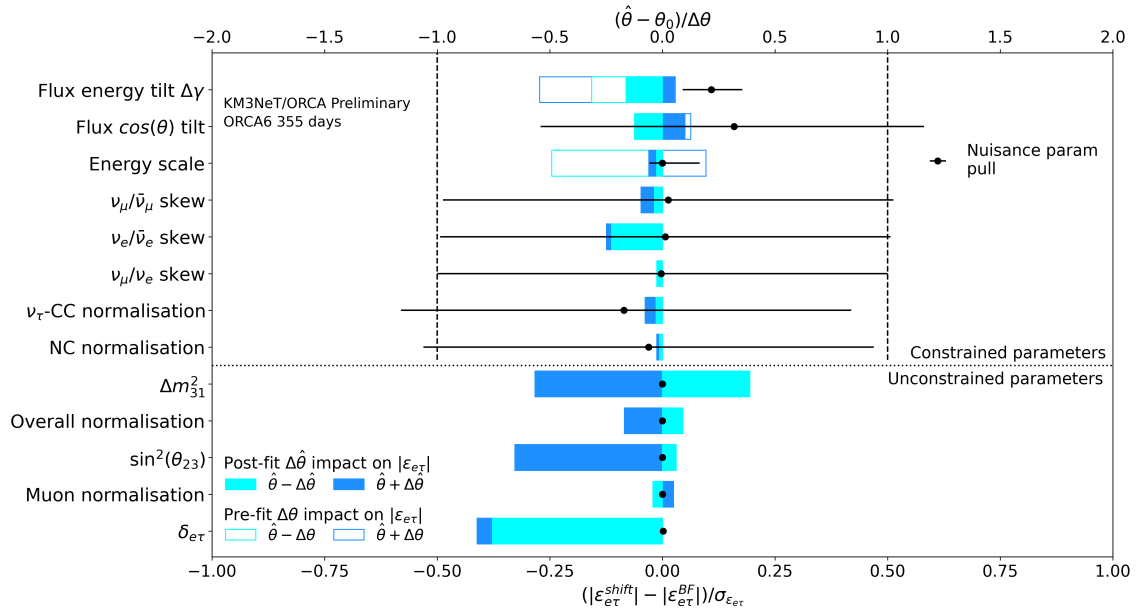
Figure 4.37: The "rank plot" which provides information about the systematics and their individual impact on the estimation of the $|\epsilon_{e\tau}|$ with the observed data. See Section 4.6.1 for explanation.
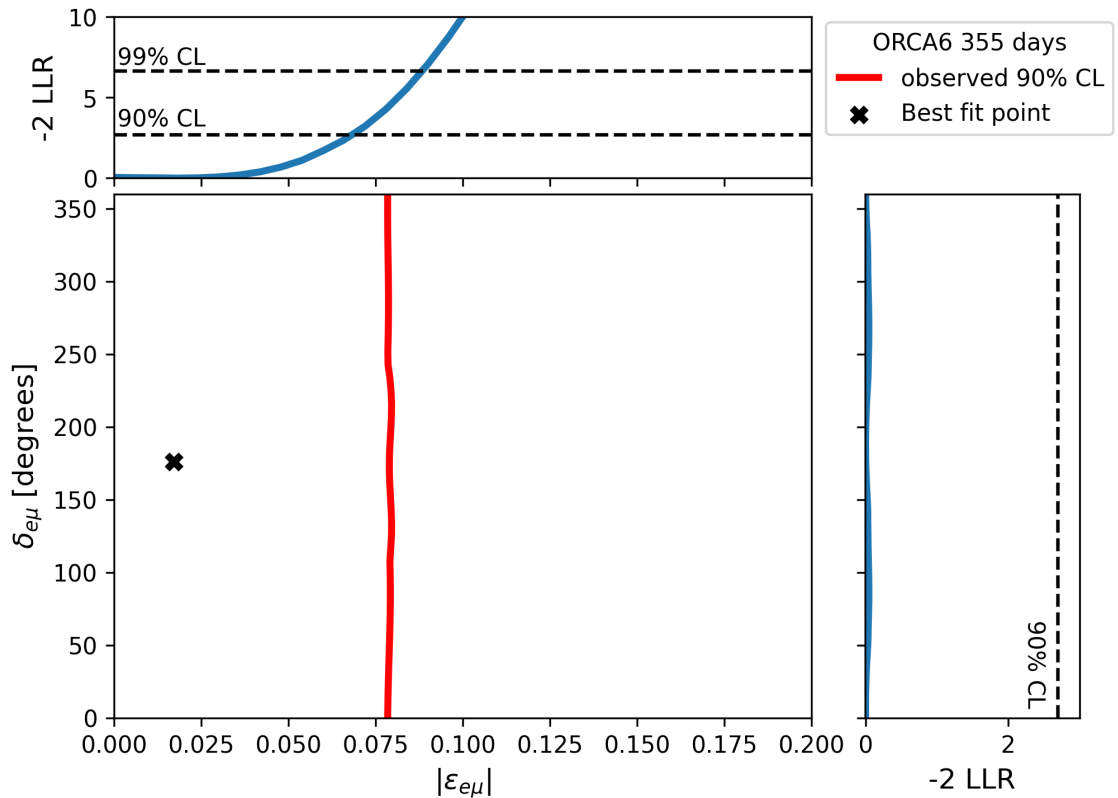
Figure 4.38: Observed 90% confidence regions in the magnitude $\epsilon_{\mu\tau}$ and $\delta_{\mu\tau}$ phase together with the projected one-dimensional -2log-likelihood ratio profile. The best fit point is indicated by the cross.

calculated with the formula in Eq. 3.2 assuming the Earth's core mass of $1.94 \cdot 10^{24}$ kg [165] and the Earth's mantle mass of $4.01 \cdot 10^{24}$ kg [166]. The other layers mentioned

Parameter	Fitted value
$|\epsilon_{e\mu}|$	$0.017^{+0.035}_{-0.017}$
$\delta_{e\mu}[°]$	176^{+184}_{-176}
$sin^2(\theta_{23})$	$0.51^{+0.10}_{-0.12}$
$\Delta m^2_{31}[eV^2]$	$(-1.88^{+0.25}_{-0.23}) \cdot 10^{-3}$
Overall Normalisation	0.81 ± 0.11
Muon Normalisation	2.0 ± 1.5
Flux: Spectral index tilt	0.07 ± 0.04
Flux: $\cos(\theta)$ tilt	0.02 ± 0.06
Flux: $\nu_\mu/\bar{\nu}_\mu$ skew	0.0 ± 0.1
Flux: $\nu_e/\bar{\nu}_e$ skew	0.0 ± 0.1
Flux: ν_μ/ν_e skew	0.00 ± 0.03
Cross-section: NC norm	1.0 ± 0.1
Cross-section: tau norm	1.0 ± 0.2
Detector: Energy scale	$0.000^{+0.018}_{-0.006}$
χ^2	108.8
Degrees of freedom	108
Chi-square p-value	0.46
Kolmogorov-Smirnov p-value	0.33

Table 4.10: Best-fit values from ORCA6 data fit to the $\epsilon_{e\mu}$ complex NSI model.

in Table 3.1 are neglected, but their mass contribution to the Earth model used in our analysis is less than 1%. As can be seen, the re-scaling approach gives a very good approximation for the evaluation of the limits for the individual NSI fermion couplings which are different from the ones used in the oscillation calculation model. A different approach is sometimes explored where one parameter governs the NSI coupling strength to u-quarks and d-quarks at the same time [78, 79]. This is motivated by the possible degeneracy between the current best-fit standard neutrino oscillation parameter values (see Section 1.2.5) and the presence of NSIs combined with different values of the standard oscillation parameters. This scenario is however already widely excluded in the global fits and usually not considered by experimental collaborations.

Figure 4.43 shows the difference in the $\epsilon_{\mu\tau}$ ORCA6 result stemming from using two different Earth matter models. The compared models are the default one used in OscProb and the one used by IceCube collaboration in nuSQuIDS [167] oscillation probability calculation software[2]. The observed difference is negligible. The exercise from Eq. 4.23

---

[2]The nuSQuIDS Earth model file from the public repository was adapted to the OscProb input format: https://github.com/arguelles/nuSQuIDS/blob/master/data/astro/EARTH_MODEL_PREM.dat
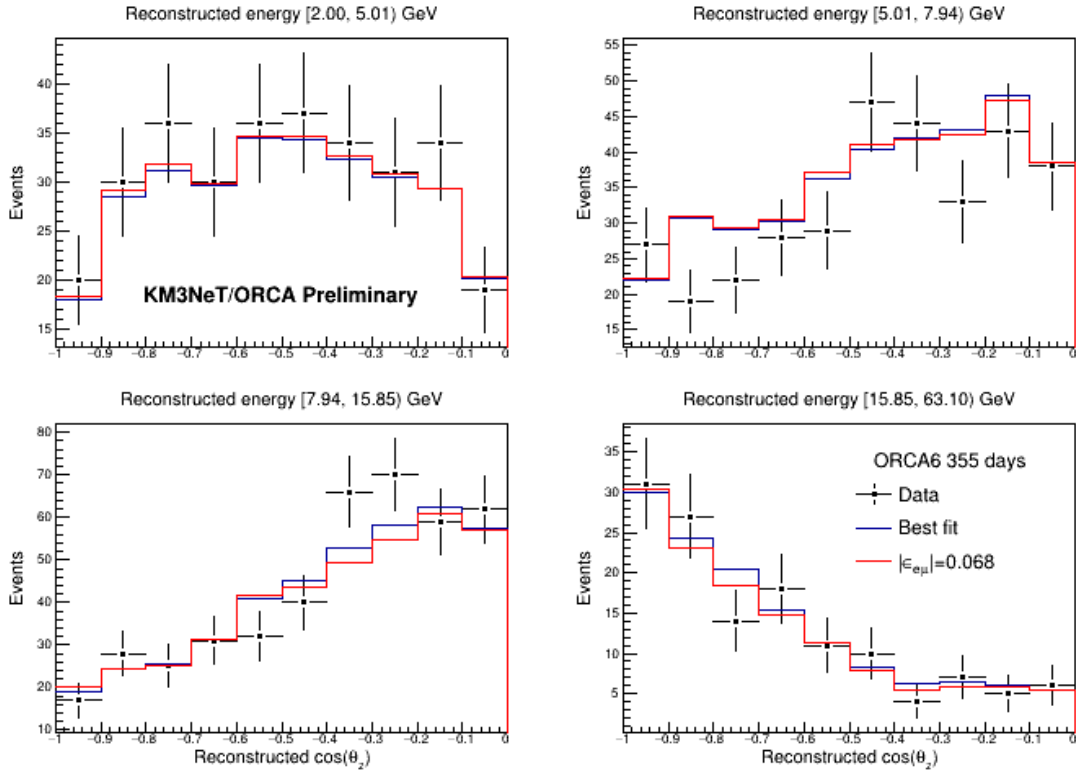
Figure 4.39: Histograms of observed events as a function of $\cos(\theta_{reco})$ for different slices in the reconstructed energy (indicated at the top of each panel), together with the MC expectation under the complex $\epsilon_{e\mu}$ fit outcome (see Table 4.10) labelled as "Best fit" and the $|\epsilon_{e\mu}| = 0.068$ shifted to its confidence limit.

(a) Event rate difference.

(b) Poisson Chi-square.
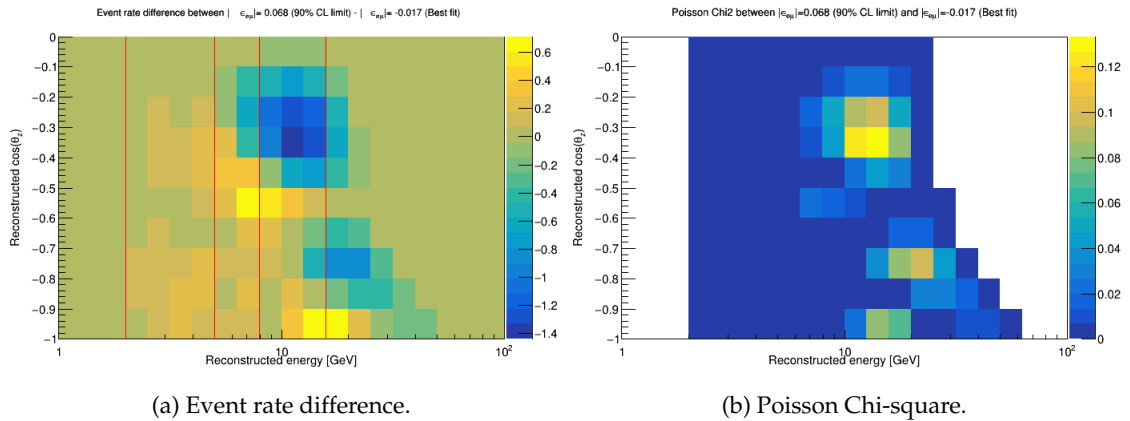
Figure 4.40: The Poisson Chi-square calculated with Eq. 4.4 (right) and the event rate difference (left) between the 90% CL limit value of $|\epsilon_{\mu\tau}| = 0.011$ and the best-fit value $|\epsilon_{\mu\tau}| = 0.0025$. All the nuisance parameters are set to their MLEs. The red lines in the left plot indicate the boundaries for the energy slices shown in Fig. 4.39.

applied to the nuSQuIDS model results in $\langle Y_d \rangle = 3.21$. This factor is used in Section 4.10 for the re-scaling whenever the results from DeepCore [81] are presented.
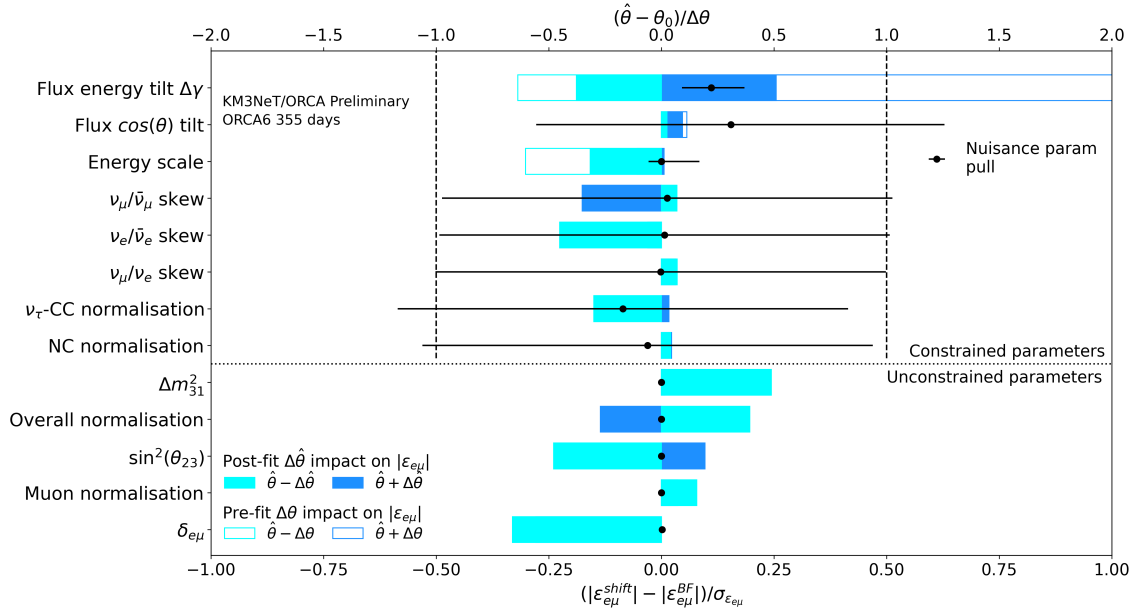
Figure 4.41: The "rank plot" which provides information about the systematics and their individual impact on the estimation of the $|\epsilon_{e\mu}|$ with the observed data. See Section 4.6.1 for explanation.
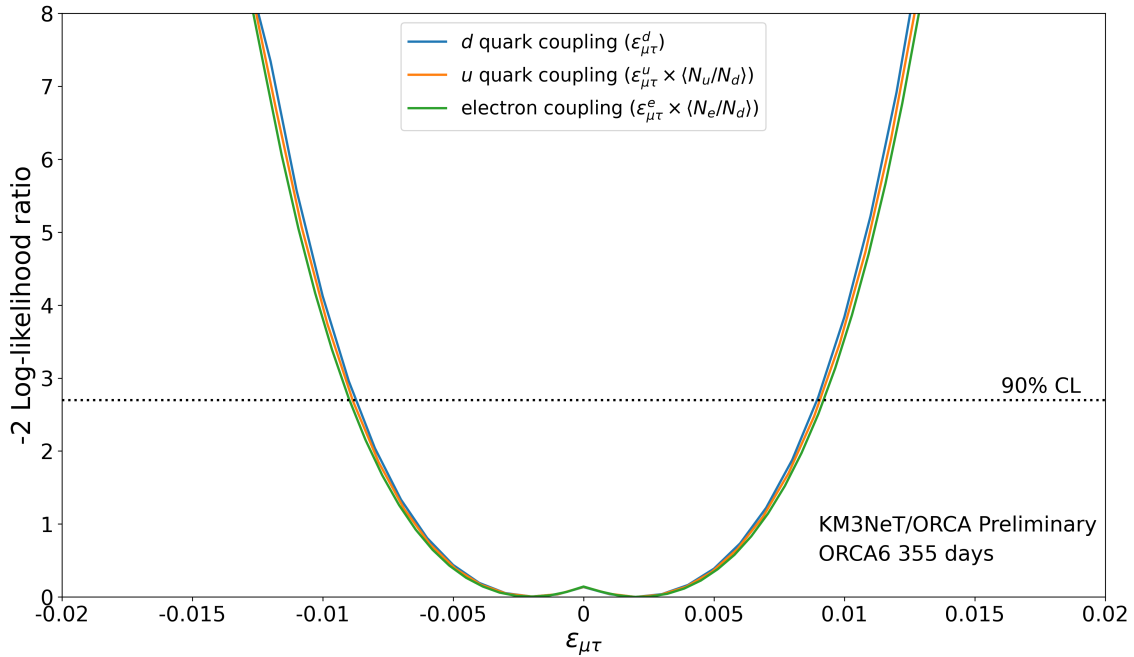
Figure 4.42: The comparison between NSI couplings to different fermions re-scaled with a single factor to match the d-quark coupling results. See text for details.

4.9   Deviations from Wilks' theorem

In this section, the procedure introduced in Section 4.5.2 is applied to the real $\epsilon_{\mu\tau}$ analysis. Figure 4.44 shows the result of the procedure described in Section 4.5.2 where all the systematics are randomised during the pseudo data generation, but only the following are fitted: Δm_{31}^2, $\sin^2(\theta_{23})$, the overall normalisation, the flux spectral index energy tilt, the flux cosine zenith tilt and the energy scale. This subset of the nuisance parameters was
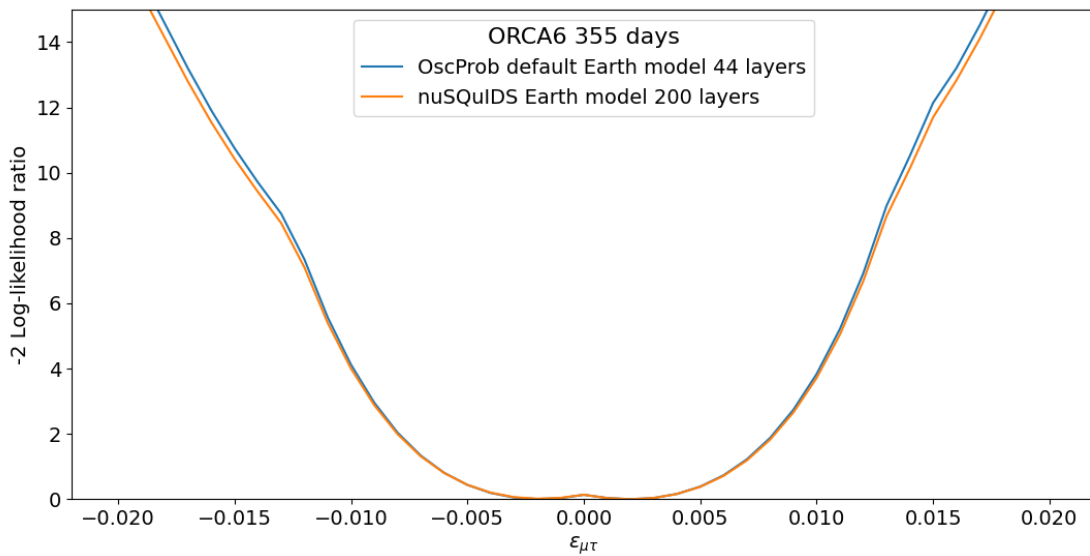
Figure 4.43: The ORCA6 measurement of $\epsilon_{\mu\tau}$ obtained with two different Earth matter models.

identified as the most important for the analysis (see Section 4.6.1). The profile likelihood curve indicated as "Observed" was obtained by fitting only the above-mentioned subset of systematics (the difference from the full model is very small). For each point shown in the plot, an ensemble of 2000 pseudo data sets were created and fitted. The 90% CL confidence interval obtained with the FC procedure and the subset of the most important systematics is:

$$-0.94 \times 10^{-2} \leq \epsilon_{\mu\tau} \leq 1.0 \times 10^{-2} \tag{4.26}$$

The limits obtained are in good agreement with those using Wilks' theorem, reinforcing the soundness of the analysis of Section 4.7. The result provides good evidence that the measured limits quoted in Section 4.7 can be considered reliable within the scope of the goals set for the analysis. As it was mentioned already in Section 4.5.2, the test statistic is not exactly the -2log-likelihood ratio from the original Feldman and Cousins method. The main difference is that it can reach negative values, which by construction are not allowed in the likelihood ratio in Eq. 4.5. There, by definition, the denominator is taken as the negative log-likelihood minimum with respect to all the parameters used in the model. As it was mentioned before in Section 4.5.2, the goal of finding such minimum is not always easy to achieve with numerical methods.

The presence of these negative outcomes in the distribution is the main reason behind the fact that the obtained critical values close to $\epsilon_{\mu\tau} = 0$ are found below the exact χ^2 critical values. In principle, the distribution of our test statistic will not follow the χ^2 distribution even if all the conditions for Wilks' theorem are met. The important feature of the obtained result is that, if the data is treated with exactly the same procedure as the pseudo experiments, the confidence limits should obey the critical values found in the process.

Figure 4.45 shows the outcome of our FC-like approach with all the systematics included in the fit and the pseudo data generation. Due to the high computational cost, only four points around the expected 90% CL confidence limits were calculated. As can be seen, the profile likelihood curve goes exactly through the critical value point found at $\epsilon_{\mu\tau} = -0.009$. The upper limit is obtained from the intersection of the interpolated line
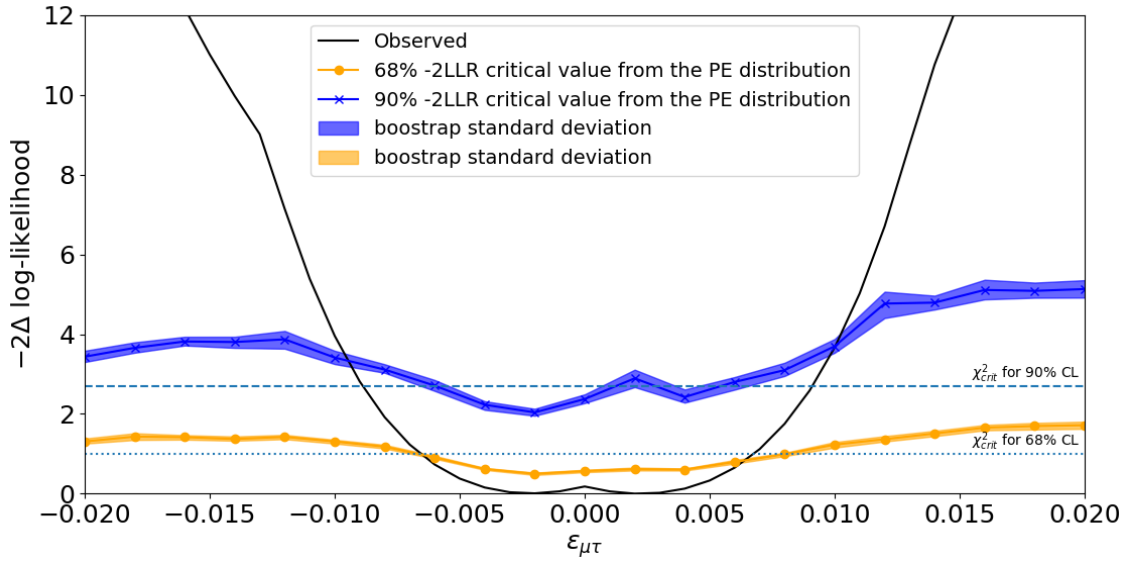
Figure 4.44: The critical values of the likelihood ratio test statistic distribution for different values of $\epsilon_{\mu\tau}$. The values between the points are interpolated linearly. Here, the randomisation of all the systematics is included in the pseudo experiment generation, but only the following subset is fitted for: Δm_{31}^2, $\sin^2(\theta_{23})$, overall normalisation n_{tot}, flux energy tilt $\Delta\gamma$, flux cosine zenith tilt Δd and the energy scale E_{scale}.

with the profile likelihood curve. The obtained 90% CL confidence interval is:

$$-0.9 \times 10^{-2} < \epsilon_{\mu\tau} < 1.0 \times 10^{-2}. \tag{4.27}$$

Following the procedure described in Section 4.5.2, the global fit search was done with the starting point of all the nuisance parameters set to their nominal values and $\epsilon_{\mu\tau} = 0$ (to be precise, 4 starting points accounting for both mass orderings and θ_{23} octant; see Section 4.4). The negative log-likelihood value from this search turned out to be higher than the local minimum from the profile likelihood scan found at $\epsilon_{\mu\tau} = 0.002$. This local minimum point however provides exactly the same best-fit parameter values as the global minimum obtained with the procedure described in Section 4.4. Therefore, the observed curve in Fig. 4.45 and the one in Fig. 4.12 are the same and the limits can be directly compared with those quoted in Section 4.7.

Figure 4.46 shows the distribution of the -2log-likelihood ratio for the pseudo experiment ensemble with the assumed true $\epsilon_{\mu\tau} = -0.009$ together with the analytical χ^2 function for one degree of freedom. It is not very clear that the critical value of the experimental distribution for the 90th percentile is actually higher than the exact value for χ^2, especially taking into account that some values are negative and they should pull all the quantiles towards lower values. This is however the effect of binning, which is hard to adjust with only 1000 entries. It is more informative to look at the cumulative distributions, shown in Fig. 4.47, as they are not very sensitive to the choice of binning. As can be seen, the cumulative -2log-likelihood ratio distribution calculated from the pseudo experiments reaches 90% slightly farther than the analytical χ^2 cumulative distribution. Nevertheless, the difference is not significant, which is reflected in the standard deviation band in Fig. 4.45.
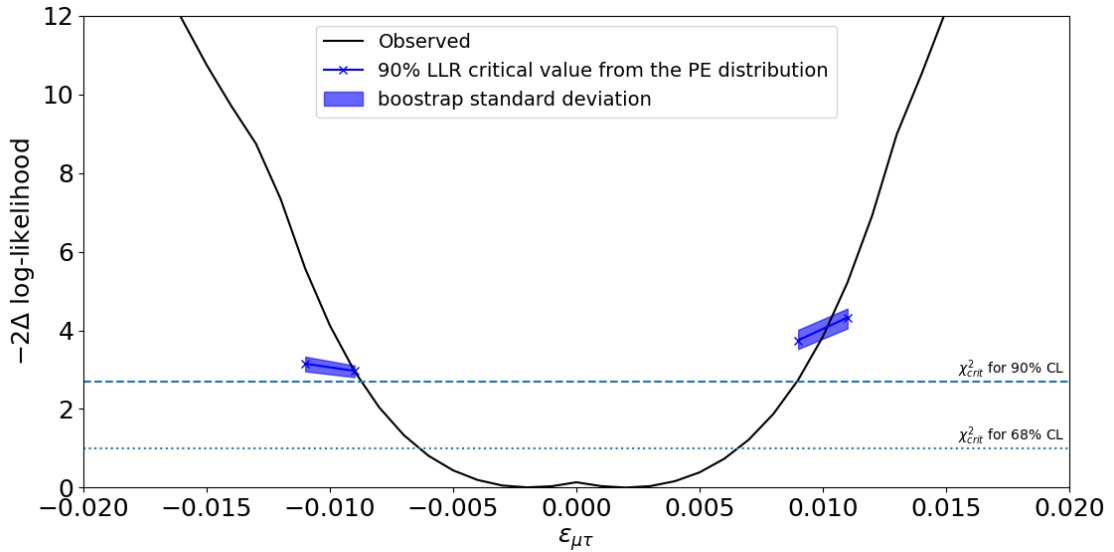
Figure 4.45: The critical values of the likelihood ratio test statistic distribution for different values of $\epsilon_{\mu\tau}$. The values between the points are interpolated linearly. All the systematics are included in the pseudo experiment generation and in the fits.
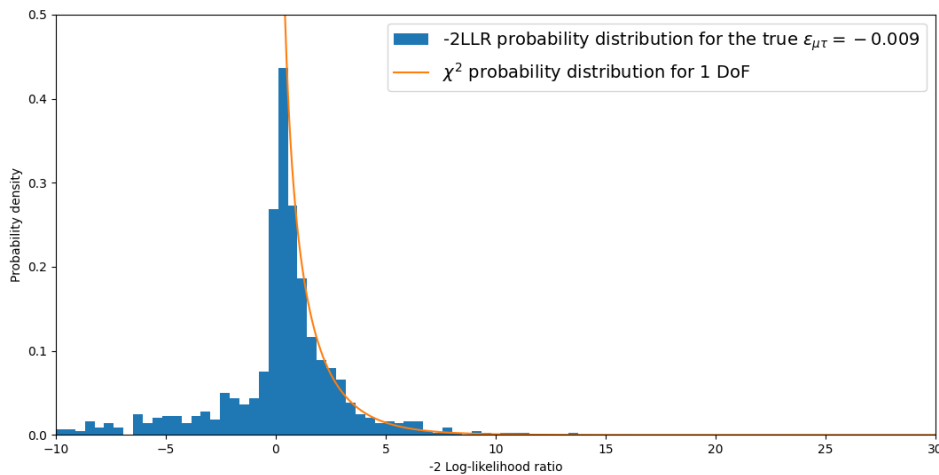
Figure 4.46: The -2log-likelihood ratio (-2LLR) distribution obtained from the FC-like procedure described in Section 4.5.2 with the assumption of a true $\epsilon_{\mu\tau} = -0.009$. All the systematics are randomised and fitted. The analytical curve of the χ^2 distribution for 1 degree of freedom (DoF) is shown for comparison.

4.10 Comparison with other experiments

Figure 4.48 shows our result for real $\epsilon_{\mu\tau}$ compared to the current world's best limits from other experiments. Even with the corrections to the Wilks' theorem approximation discussed in Section 4.9, the limits obtained with ORCA6 are only roughly 2.5 times worse.

Figures 4.49, 4.50, 4.51 and 4.52 show the comparisons between ORCA6 limits and DeepCore results for $|\epsilon_{\mu\tau}|$, $\epsilon_{\tau\tau} - \epsilon_{\mu\mu}$, $|\epsilon_{e\tau}|$ and $|\epsilon_{e\mu}|$, respectively. The likelihood is profiled over the corresponding phase. The DeepCore results do not profile over the
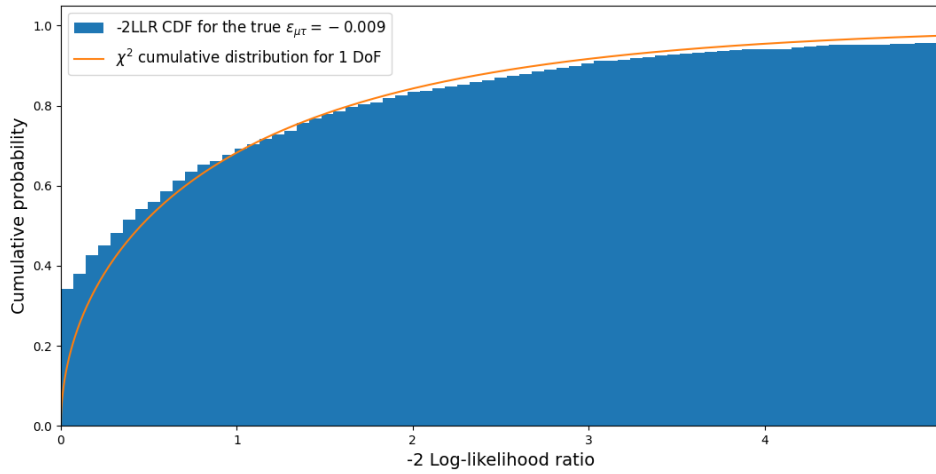
Figure 4.47: The cumulative distribution (CDF) of the -2log-likelihood ratio (-2LLR) distribution
            obtained from the FC-like procedure described in Section 4.5.2 with the assumption
            of a true $\epsilon_{\mu\tau} = -0.009$. The analytical cumulative distribution of the χ^2 function for
            1 degree of freedom (DoF) is shown for comparison.
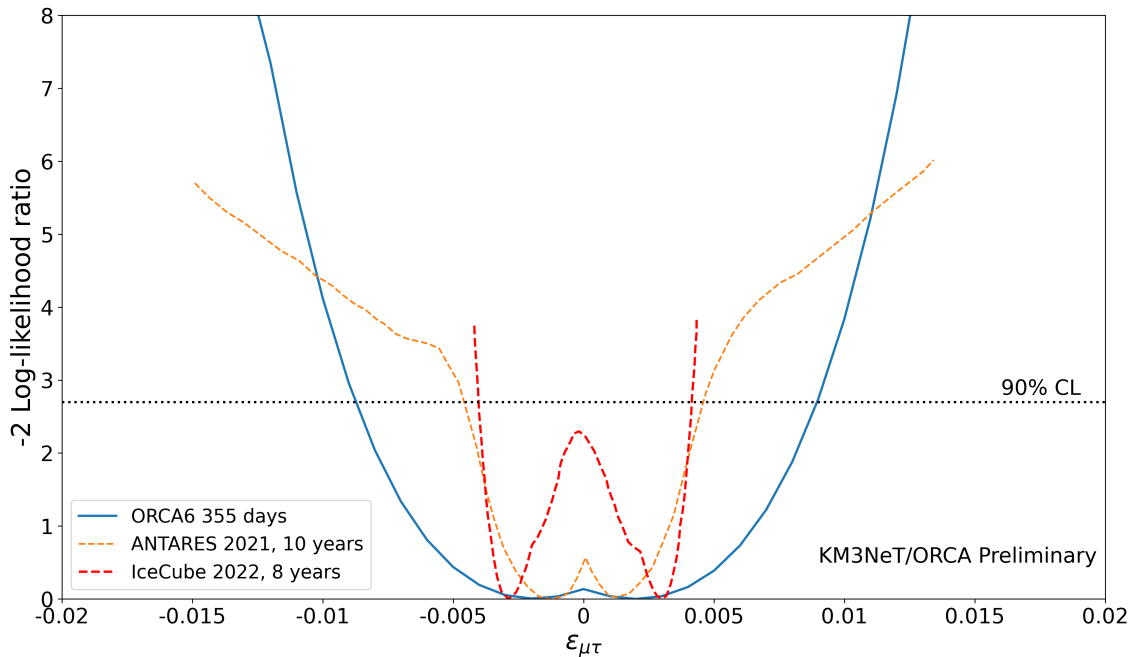
Figure 4.48: ORCA6 real $\epsilon_{\mu\tau}$ measurement compared to the results from ANTARES [77] and
            IceCube [51]. Originally these experiments present separate limits for NO and IO, so
            a combined curve is plotted, which represents the more conservative case for a given
            $\epsilon_{\mu\tau}$ sign. This way of drawing the external results is done to mimic the profiling over
            the NMO performed for ORCA6.

mass ordering, but the depicted curves assume NO. The limits at 90% CL measured
with ORCA6 compared to the DeepCore results appear to be on average ∼2 times
less stringent. Looking at a higher confidence level within the Wilks' approximation,
the discrepancy increases in favour of DeepCore for all the measured parameters with
the exception of the $\epsilon_{\mu\tau}$ case where the discrepancy remains approximately constant.

However, it is likely that comparing the results at a confidence level higher than 90% does not make much sense as ORCA6 does not yet provide sufficient statistics.
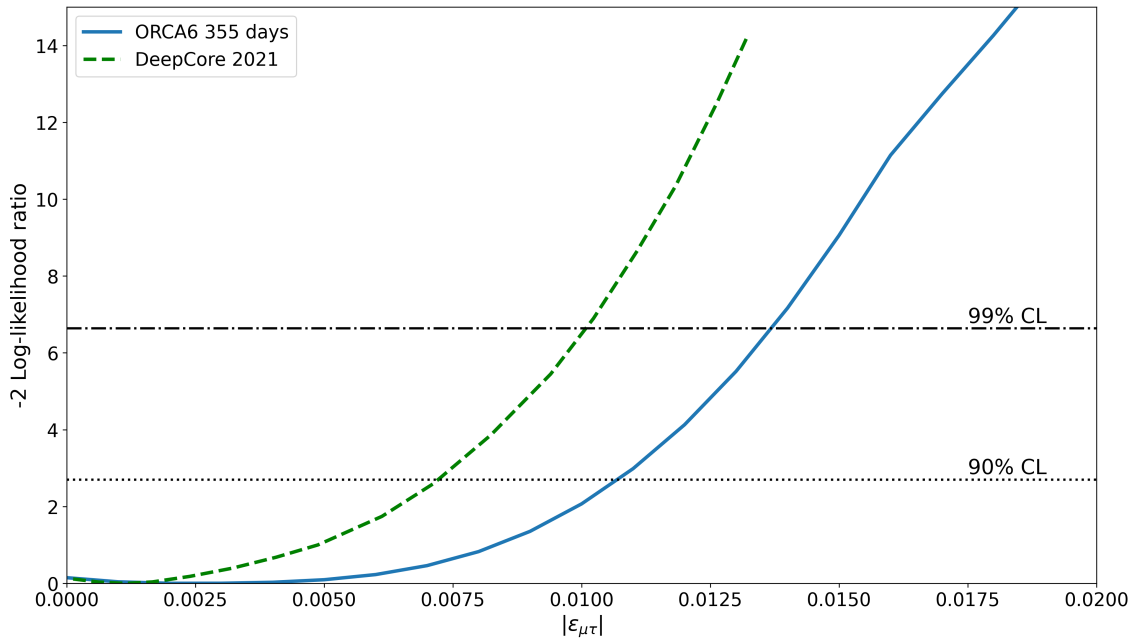
Figure 4.49: ORCA6 complex $|\epsilon_{\mu\tau}|$ measurement compared to the results from DeepCore [81]. The DeepCore results are divided by 3.21 to account for the assumption of NSIs coupling to d-quarks only (see Section 4.8).
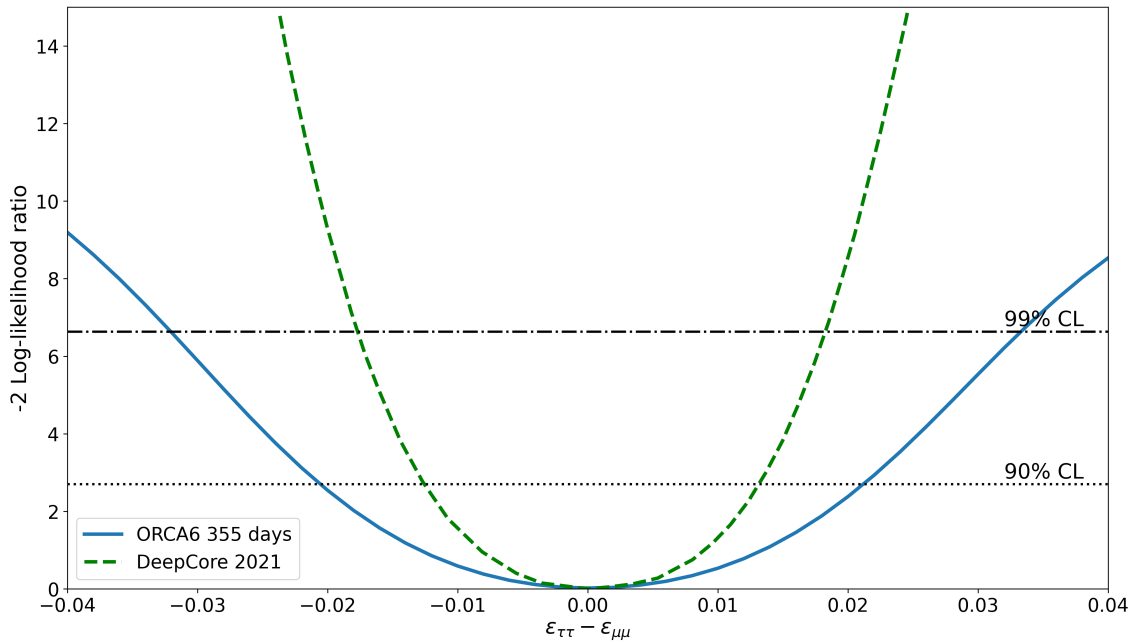
Figure 4.50: ORCA6 $\epsilon_{\tau\tau} - \epsilon_{\mu\mu}$ measurement compared to the results from DeepCore [81]. The DeepCore results are divided by 3.21 to account for the assumption of NSIs coupling to d-quarks only (see Section 4.8).
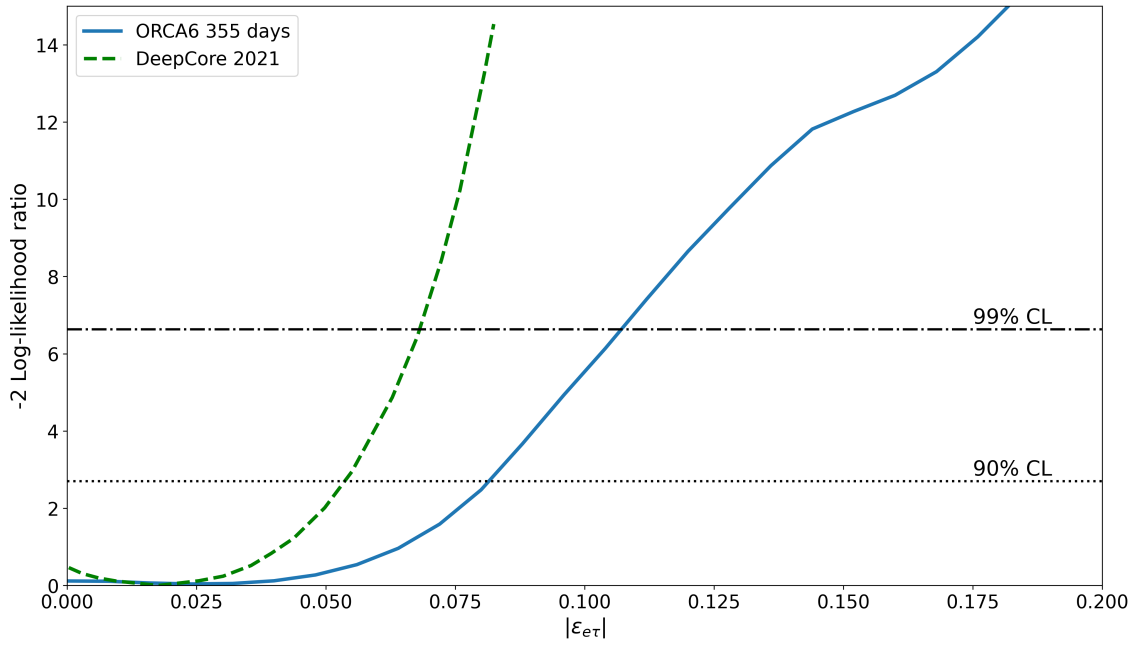
Figure 4.51: ORCA6 complex $|\epsilon_{e\tau}|$ measurement compared to the results from DeepCore [81]. The DeepCore results are divided by 3.21 to account for the assumption of NSIs coupling to d-quarks only (see Section 4.8).
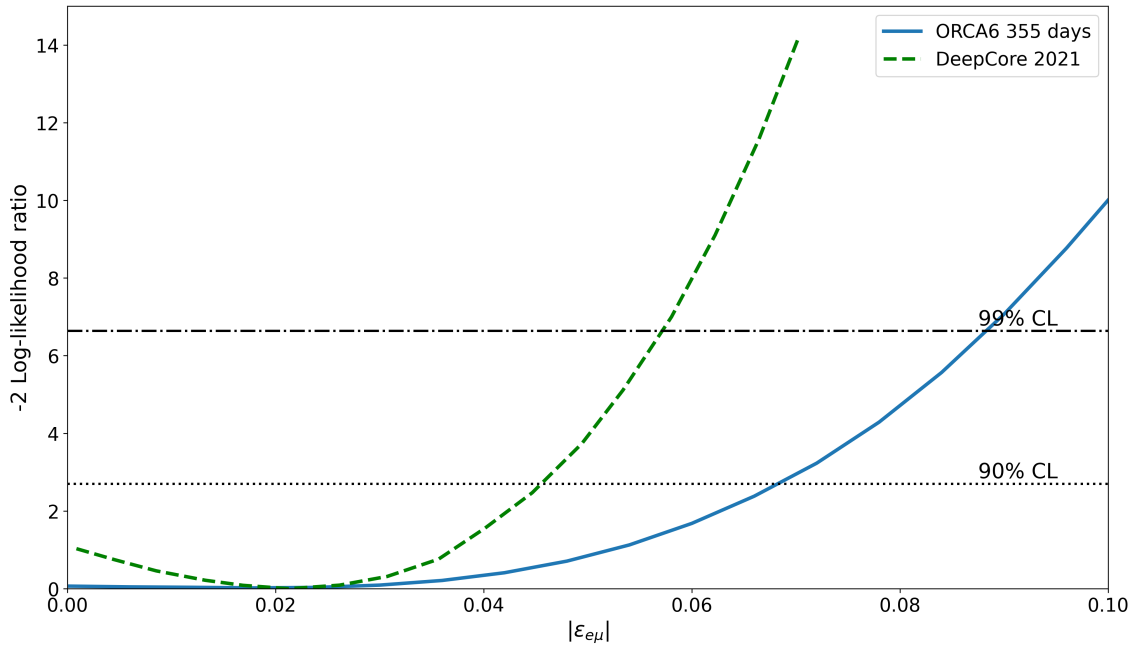
Figure 4.52: ORCA6 complex $|\epsilon_{e\mu}|$ measurement compared to the results from DeepCore [81]. The DeepCore results are divided by 3.21 to account for the assumption of NSIs coupling to d-quarks only (see Section 4.8).

Taking into account that ORCA6 comprises only six out of the final 115 planned DUs and the event sample includes slightly less than a year of data taking, the obtained results give a very positive impression about the reach of the full ORCA in future NSI studies.

4.11 Conclusions and discussion

No hint of NSIs was found in the data. The measured event distribution can be explained with the standard oscillations, as it could be expected from the known limits to NSIs obtained by other experiments and the sensitivities of ORCA6. The best-fit values of all the nuisance parameters and their confidence intervals are found to be almost exactly the same for all the tested NSI models and very similar to the ones from the ORCA6 standard oscillation analysis presented in ref. [137]. None of the nuisance parameters exhibits a significant statistical pull — generally the priors for the nuisance parameters described well the measured data. However, the data constrains the energy scale and the flux energy tilt parameters much better than the assumed priors. This is somewhat expected from the discussion on the prior widths presented in Section 4.6.

All the data fits exhibit a very good Chi-square goodness of fit, which however does not agree very well with the outcomes of the generally more sensitive Kolmogorov-Smirnov test. This should not be worrying as the two methods are different in principle and the p-value is expected to undergo statistical fluctuations. All the fits have almost exactly the same values of the goodness of fit evaluations because essentially they represent the same distribution with no NSIs present (see the best-fit event distributions in Appendix A.3). Nevertheless, the result hints that there might be an issue with the definition of degrees of freedom. Aside from the possible model-specific problems briefly introduced in Section 4.3.2, the choice of the reconstructed energy proxy results in certain limitations of the phase space which effectively might be different in data and in MC predictions (see Section 3.4). Even if in our model the degrees of freedom are well described by the commonly used difference between the number of bins and the number of parameters, the question remains which bins should be counted in. When looking at the data distribution and an example best-fit prediction in Figs. 4.10 and 4.11, it can be seen that some of the bordering bins have a prediction rounded to 0 (in fact these predictions are of the order of 0.01) and all of the corresponding bins in data are empty. From a statistical point of view, these bins are not problematic in the Poisson Chi-squared calculation, but it has to be taken into account that the reconstruction can be biased and in reality the data events cannot be found in these problematic bins. In such a case, the real number of degrees of freedom (in a perfectly linear model case) could vary between 100 and 108.

As can be seen in the profile likelihood scans of the real NSI models, the observed curves systematically tend to fall into the region of better sensitivity in the sensitivity bands. It is hard to believe that this behaviour can be explained by the effect of the same statistical fluctuations affecting all the measurements, because generally the sensitivity to different NSI parameters comes from various phase space regions. What is interesting to notice is that a similar behaviour (to smaller extent) was also observed in the last result on NSIs from DeepCore [81]. There, the behaviour is not very drastic and may still be originating from a pure statistical fluctuation. Nonetheless, the result presented in Section 4.9 provides a possible explanation — the critical values of the actual profile likelihood ratio test statistic used in the analyses detours from the asymptotic χ^2 approximation towards higher values when the hypothesised value of a given ϵ drifts away from zero. Therefore, the observed profile likelihood scans give the impression that they outperform the median sensitivity, but in fact it just reflects the increasing critical value of the test statistic distribution. To make sure, it would require the sensitivity bands to be prepared with the randomisation of systematics, but this approach needs large computational resources (see Section 4.5.2).

An important conclusion which can be drawn from the study presented in Section 4.9 is

that the area of the MC generation of the test statistic distribution has to be investigated further before more measurements with ORCA data are performed. Applying a full range profile likelihood scan to each and every pseudo experiment would increase the overall precision of the results, but, as it was discussed in Section 4.5.2, this method would definitely require fit software optimisation. The issue will become especially important once the sensitivity of ORCA to NSIs outperforms the current world's best limits.

An interesting aspect of all the recent result on $\epsilon_{\mu\tau}$ (including our result) shows that generally $\epsilon_{\mu\tau} = 0$ is more disfavoured than the opposite sign of the best-fit value. This could give a false impression that there is some indication of NSIs and all that is needed to observe it is more more statistics or better constraints on the systematics. However, it is important to notice that the likelihood shape disfavouring $\epsilon_{\mu\tau} = 0$ is the most prominent in the ANTARES and IceCube results which are basically exclusively based on the high energy region where the muon neutrino disappearance shows an asymptotic behaviour induced by the $\epsilon_{\mu\tau}$ parameter. Therefore, the slightest deficit of events leads to a preference in a non-zero $\epsilon_{\mu\tau}$ value. The normalisation and the energy slope of the atmospheric neutrino flux are less constrained for the high neutrino energies. For the future analyses it would be good to prepare a more sophisticated approach to the flux spectral index systematic which could properly account for the floating uncertainty.

Ideally, in the future one would like to test the full NSI model where all the NSI parameters are free in the fit. This approach would be computationally expensive with the currently used software and most likely not worth the effort with the early stages of the ORCA detector. The detector resolutions and the limited statistics would not be able to sufficiently decouple the simultaneous effects of a few NSI parameters at the same time. Nevertheless, the growing detector size and the future inclusion of the shower reconstruction can shed a light on multi-parameter NSI models and push future NSI results of ORCA towards the competitive region.

Summary

Neutrinos with all their peculiarities are currently one of the most pursued topics in particle physics research. Several of the characteristics of these elusive particles remain a mystery until this very day, even though neutrinos were postulated in 1930 and detected for the first time in 1956. Neutrinos interact only via the weak interaction and therefore measuring them with a reasonable statistics requires a specific approach involving huge detector volumes.

Over the last few decades, many experiments contributed to provide a strong evidence of the existence of neutrino oscillations. The research on this topic culminated in the Nobel prize awarded in 2015. The observation of the transition between neutrino flavour states along the travelled distance was an ultimate proof that neutrinos are in fact massive particles. Moreover, further investigation showed that the number of non-degenerate neutrino mass states is at least two. Within the scope of the Standard Model, which is the established state-of-the-art theory of fundamental interactions, neutrinos are not allowed to have mass. The majority of the postulated theoretical extensions of the Standard Model, aimed at the inclusion of neutrino masses, require the existence of a new type of interactions which has not yet been observed. From the phenomenological point of view, these interactions can be gathered under the concept of Neutrino Non-Standard Interactions (NSIs) which would affect neutrino oscillations on a sub-leading level. In an analogy to the weak interactions, there are two types of NSIs: Charged Current (CC) and Neutral Current (NC). Since the neutrino oscillation experiments are not sensitive to CC NSI, in our work we focus exclusively on NC NSI, which are frequently referred to as matter NSI. The study of non-standard interactions of neutrinos with matter fermions is envisaged from this phenomenological point of view, since their existence provides a probe of the nature of new physics beyond the Standard Model.

The KM3NeT/ORCA project is a next-generation neutrino telescope aimed at measuring the atmospheric neutrino oscillations. One of its scientific objectives is the search for beyond standard model phenomena, which can manifest themselves in the modification of the neutrino oscillation patterns. Neutrino non-standard interactions are one of the phenomena within the above definition. The early stage of the ORCA detector, called ORCA6, comprises only six out of the planned 115 detection units, but it has already proved to be capable of observing neutrino oscillations [137]. The data sample used for the measurement of the standard neutrino oscillation parameters is exploited in this work for the search of NSIs with the focus on the $\mu - \tau$ sector.

Neutrino oscillations with NSIs

NSIs introduce a modification to the equation of motion for neutrinos travelling through matter. This modification, in the form of a perturbation term to the Hamiltonian,

is parameterised by a 3x3 matrix with 9 parameters: 3 complex flavour-violating, off-diagonal terms characterised by a modulus and a corresponding phase and 3 flavour non-universal, real diagonal terms. Actually, in analogy to the neutrino masses, in the case of the diagonal parameters, only the difference between them can be observed in neutrino oscillation experiments, which makes the total number of measurable NSI parameters with the ORCA detector reduced to 8. The impact of NSIs on neutrino oscillations in matter depends on the particular parameter, oscillation channel and the amount of matter present on the neutrino path. In the Earth's matter, the effect of NSIs is the most prominent for neutrino directions crossing the core as its high density amplifies the overall influence of matter on neutrino propagation. The most important oscillation channel measured in ORCA is the muon neutrino disappearance, which for neutrino energies above 20 GeV happens almost exclusively in favour of the appearance of tau neutrinos. Therefore, the most important NSI parameters for the NSI research with ORCA are $\epsilon_{\mu\tau}$ and $\epsilon_{\tau\tau} - \epsilon_{\mu\mu}$ (the so-called $\mu - \tau$ sector).

In general, the flavour-violating NSI parameters $\epsilon_{\mu\tau}$, $\epsilon_{e\tau}$ and $\epsilon_{e\mu}$ can carry a corresponding complex phase, which under certain conditions would affect the influence of NSI on neutrino oscillations. However, in the $\nu_\mu/\bar{\nu}_\mu$ disappearance channel, only the sensitivity to $\epsilon_{\mu\tau}$ is foreseen to be affected by its corresponding phase $\delta_{\mu\tau}$.

Objectives

The thesis is aimed at testing the hypothesis of the existence of Neutrino Non-Standard Interactions manifesting themselves as sub-leading effects in the atmospheric neutrino oscillation patterns observed in ORCA6 data. Considering the limitations of the early stage of the ORCA detector, the goal of the analysis is not to compete with the other experiments in the field, but rather to create a proof of concept of ORCA capabilities in the beyond Standard Model physics searches. Therefore, the objectives of this dissertation are as follows:

- Study the phenomenological consequences of different configurations of the NSI parameters potentially realised in nature.

- Investigate the detector resolution in various regions of the reconstructed phase space in the context of the signal expected from NSIs.

- Identify the impact of the systematic uncertainties and the possible complex nature of the flavour-violating NSI parameters.

- Measure (or set limits to) the parameters $\epsilon_{\mu\tau}$, $\epsilon_{e\tau}$, $\epsilon_{e\mu}$ and $\epsilon_{\tau\tau} - \epsilon_{\mu\mu}$ paying special attention to the $\mu - \tau$,

- Develop a statistically robust procedure, which supports the claimed results. Numerous systematic uncertainty parameters of different nature combined with low statistics of the ORCA6 event sample are potentially problematic in the scope of the widely used Wilk's approximation.

- Compare the obtained results with the world-leading measurements and elaborate on the differences between the Earth models commonly used in the field of the NSI study.

Methodology

Before neutrino oscillations can be studied with statistical models, the data has to be first recorded, reconstructed and selected for a pure neutrino sample. On the other hand, a reliable Monte Carlo simulation model is necessary to provide the reconstructed event rate predictions which can be directly compared to the data. These predictions should represent the hypotheses of different values of the NSI parameters which are targeted in the analysis.

The analysis model has to account for the systematic uncertainties stemming from the uncertainties in the modelling of physics and the detector-specific effects which can possibly affect the data. These uncertainties are included in the analysis in the form of parameters, later referred to as systematics, which can be varied by the fitter software. These parameters reflect the precision of the current state of knowledge about atmospheric neutrino flux, atmospheric muon flux, neutrino interaction cross sections, absorption of light in seawater and quantum efficiency of the photomultipliers.

The statistical inference is based on the frequentist approach with the use of maximum likelihood estimation and the log-likelihood ratio test statistic. For the verification of the χ^2 approximation provided by Wilks' theorem, a procedure involving pseudo data generation was developed to derive the exact shape of the test statistic for one example case of the analysed models.

The ORCA6 detector

As it was already mentioned, the ORCA6 detector is an early stage of the KM3NeT/ORCA project. It is located in the Mediterranean Sea at a depth of 2450 m, about 40 km south from the French city of Toulon. It consists of six vertical strings anchored at the sea bottom with an average horizontal distance of about 20 m. Along each string, there are 18 Digital Optical Modules (DOMs) located with an average vertical separation of $\sim$9 m.

The detection principle in ORCA is based on the Cherenkov effect leading to the emission of light by the charged particles passing through the seawater inside or in the vicinity of the detector volume. These particles can originate from the interactions of neutrinos, which cannot be observed directly due to their lack of electric charge. However, there is a plethora of background sources which are able to mimic the signal expected from the interacting neutrino or cover it with background. At the data taking stage, these sources are tackled with the trigger algorithms and certain data monitoring systems ensuring that only the stable and reliable data taking conditions are accepted.

The device responsible for the Cherenkov light detection is the Digital Optical Module, which essentially is a pressure resistant sphere equipped with 31 photomultipliers (PMTs) arranged to monitor the full solid angle around it. The PMT model is chosen to maximise the quantum efficiency for the photon wavelengths between 350 and 500 nm where the Cherenkov emission is high and at the same time the wavelength-dependent seawater transparency is the most favourable.

The study of neutrino oscillations with ORCA makes use of neutrinos produced in the Earth's atmosphere. The atmospheric neutrino flux emerges mostly from the decay chains of pions and kaons created in the interactions of the primary cosmic rays. Tau neutrinos are basically absent in the primary atmospheric neutrino flux, but they can be seen in the detector thanks to oscillations. For the neutrino energies above 10 GeV, where

most of the signal in ORCA6 is expected, muon neutrinos are much more abundant than electron neutrinos and the ratio of neutrinos to anti-neutrinos stays close to one.

Neutrinos cannot be separated from anti-neutrinos in a neutrino telescope like ORCA. For certain NSI parameters, the effects on the oscillations are opposite for neutrinos and anti-neutrinos and therefore could be partially cancelled out (notice that in the atmospheric neutrino flux the $\nu/\bar{\nu}$ ratio is close to one for a broad spectrum of neutrino energy). However, the overall impact can still be observed thanks to the cross section asymmetry $\sigma_\nu/\sigma_{\bar{\nu}} \simeq 2$ in the ordinary matter. The above-mentioned problem is especially important for the flavour-violating parameter $\epsilon_{\mu\tau}$, because its effects are observable mainly through the muon neutrino disappearance channel which decouples from the electron flavour state for neutrino energy $E_\nu > 20$ GeV. It means that the effect of the standard matter potential does not interfere much with the potential impact of $\epsilon_{\mu\tau}$ and the degeneracy between the $\epsilon_{\mu\tau}$ sign and the neutrino lepton charge is almost exact. Nevertheless, the cancellation is expected only in the phase space region where the NSI effects are dominated by the linear terms of the given parameter. For the high energies $E_\nu > 80$ GeV, the $\epsilon_{\mu\tau}$ effect converge for neutrino and anti-neutrinos to a stable deficit of events with respect to standard oscillations. In the muon disappearance channel, the destructive interference between the NSI effects on ν $\bar{\nu}$ is not prominent for the flavour-violating NSI parameter not involving the muon flavour, $\epsilon_{e\tau}$, and the non-universal $\epsilon_{\tau\tau} - \epsilon_{\mu\mu}$.

Event reconstruction and detector resolution

In ORCA, two general event categories are normally distinguished: track-like events and shower-like events; tracks and showers in brief. Tracks are induced by ν_μ-CC events, atmospheric muons and ν_τ-CC interactions with the tau lepton decaying into a muon. Showers can generally emerge from all types of neutrino interactions, because even the ν_μ-CCs have a hadronic component. Nevertheless, the majority of shower-like events are expected from ν_e-CC and all flavour NC interactions. Track and showers differ significantly by their topology: showers give a more isotropic and localised signal while tracks leave a trace of flashing DOMs in the whole detector along the path of the muon. After applying an adequate set of cuts to suppress the atmospheric muon contamination, the track-like signature becomes the main tool for muon neutrino flavour identification. To the ORCA6 data sample used in this dissertation, only the track reconstruction was applied, being the reconstructed energy evaluated directly from the reconstructed track length. The length is translated into the energy with the simple relation 0.25 GeV/m which corresponds to the minimum ionising particle regime of a muon. This approach does not introduce a significant error in the muon energy range up to $\sim$100 GeV. However, the geometrical constraints of the ORCA6 size, allowing the longest observable track of about 200 meters, cause a strong saturation of the reconstructed energy. Atmospheric neutrinos in a wide range of energies above 80 GeV are reconstructed in only a few bins in the reconstructed energy space, which by the construction of the reconstructed energy proxy is restricted to E_{reco} $\sim$50 GeV. At the same time, the direction reconstruction is very good; the distributions of the true cosine zenith reconstructed in a given bin in the reconstructed space are usually aligned at the bin centre with Gaussian-like shapes. As expected from the kinematics, the direction reconstruction resolution improves with the increasing neutrino energy and also, in the lower energies, shows a mild dependence on the true direction itself.

Event rate calculation with the Monte Carlo methods

The data is binned in two-dimensional phase space of the reconstructed energy versus the reconstructed cosine zenith. The analysis model has to be able to generate predictions in a similar manner based on the values of the model parameters which can be manipulated by the fitter software. The Monte Carlo event rate predictions are generated using the staged approach which decouples the calculation of the neutrino flux, the neutrino oscillation probability and the detector resolution factor, which includes the cross section and the detector acceptance. To evaluate the detector resolution in the form of a response matrix, first it is necessary to simulate neutrinos and atmospheric muons interacting at the detector site, which subsequently are treated with the same trigger and reconstruction algorithms normally applied to the data.

The event count prediction at the detector level is calculated with the following formula:

$$
n^j_{reco}(E^j_{reco}, \cos\left(\theta^j_{reco}\right), E_{scale}) = \sum_i \sum_{\alpha \in \{e,\mu,\tau\}} \sum_{\nu,\bar{\nu}} \sum_{CC/NC} w^j_i \times
$$

$$
n_{tilt}(\Delta\gamma, \Delta d) \cdot [P(\nu_e \to \nu_\alpha)(\text{std osc}, \epsilon_{NSI}) \cdot \phi^{\zeta_{\mu e}}_e(E^i_{true}, \cos\left(\theta^i_{true}\right), \zeta_{\mu e}, \zeta_{e\bar{e}}, \zeta_{\mu\bar{\mu}}, \Delta\gamma, \Delta d)+
$$

$$
P(\nu_\mu \to \nu_\alpha)(\text{std osc}, \epsilon_{NSI}) \cdot \phi^{\zeta_{\mu e}}_\mu(E^i_{true}, \cos\left(\theta^i_{true}\right), \zeta_{\mu e}, \zeta_{e\bar{e}}, \zeta_{\mu\bar{\mu}}, \Delta\gamma, \Delta d)]
$$

$$
\times n_{tot} \times \delta_{\alpha\tau} n_{\sigma^{\nu\tau}_{CC}} \times \delta_{xx,NC} n_{\sigma_{NC}} + n^\mu_{atm} \cdot N^\mu_{atm,j} \, ,
$$

$$
(28)
$$

where

- the reconstructed bin j has its centre at $\{E^j_{reco}, \cos\left(\theta^j_{reco}\right)\}$, potentially modified by the E_{scale} systematic uncertainty parameter,

- the first sum goes over all the true bins i contributing to bin j,

- the other sums go over the interaction channel dimension of the response matrix: ν_e-CC, $\bar{\nu}_e$-CC, ν_μ-CC, $\bar{\nu}_\mu$-CC, ν_τ-CC, $\bar{\nu}_\tau$-CC, ν-NC and $\bar{\nu}$-NC,

- std osc = $\{\theta_{12}, \theta_{13}, \theta_{23}, \Delta m^2_{21}, \Delta m^2_{31}, \delta_{CP}\}$ denotes the standard oscillation parameters,

- ϵ_{NSI} denotes all the non-zero NSI parameters used in the oscillation model,

- $\delta_{\alpha\tau}$ and $\delta_{(N/C)C,NC}$ are Kronecker deltas isolating the tau neutrino flavour or the NC interactions (keep in mind that the single flavour which was used for the NC simulation was ν_μ, so the deltas do not introduce extra terms)

- $N^\mu_{atm,j}$ represents the number of atmospheric muons found in the reconstructed bin j.

A MC event rate prediction, also referred to as a template, represents a single hypothesis for given values of the model parameters, which are:

- neutrino oscillation parameters $\theta_{12}, \theta_{13}, \theta_{23}, \Delta m^2_{21}, \Delta m^2_{31}$ and δ_{CP} extended by

- NSI parameters $\epsilon_{\alpha\beta}$ with $\alpha, \beta \in \{e, \mu, \tau\}$,

- flux systematics: flux energy tilt $\Delta\gamma$, flux cosine zenith tilt Δd, $\nu_e/\bar{\nu}_e$ skew $\zeta_{e\bar{e}}$, $\nu_\mu/\bar{\nu}_\mu$ skew $\zeta_{\mu\bar{\mu}}$, ν_μ/ν_e skew $\zeta_{\mu e}$,

- cross section normalisation factors $n_{\sigma^{\nu\tau}_{CC}}$ and $n_{\sigma_{NC}}$,

- overall normalisation n_{tot},

- atmospheric muon normalisation n_{atm}^{μ},

- detector energy scale E_{scale}

Among the parameters of the model, only one or two NSI parameters at a time are of the intrinsic interest to our analysis. However, the remaining parameters, frequently referred to as nuisance parameters, are usually correlated with the parameters of interest. The nuisance parameters are normally designed to account for the systematic uncertainties and improve the accuracy of the model, so excluding them could introduce a bias in the measurement. To achieve an approximate independence of the likelihood from these nuisance parameters, a profile likelihood is used.

Model fitting and statistical methods

Fits are performed with the MINUIT [151] minimizer provided by the ROOT [153] software framework. All the fits are done with profiling over the mass ordering with the Δm_{31}^2 starting values taken from the NuFIT 5.0 [73] standard neutrino oscillation parameter values. The ambiguity in the octant of θ_{23} is accounted for with two starting values of $\sin^2(\theta_{23})_{init} = \{0.4, 0.6\}$. It means that for each fitted hypothesis, four starting points are tested in the case of the real NSI models. All the other standard oscillation parameters are fixed at their best-fit values from NuFIT and not included in the fits. In the case of the complex NSI models, additional starting values are added in $\delta_{\alpha\beta}^{init} = \{0, \pi/2, \pi, 3\pi/2\}$ resulting in the total of 16 starting points for each fit.

The statistical analysis is exclusively based on the frequentist approach. For the parameter estimation we use the maximum likelihood method. To evaluate the *goodness of fit*, the Chi-square goodness of fit approach is exploited assuming the asymptotic behaviour of the Poisson Chi-squared, which essentially is the log-likelihood ratio calculated with the binned Poisson likelihood assuming the data bin contents as the alternative hypothesis. The chi-square approach is cross-checked with the Kolmogorov-Smirnov test. Some of the systematic uncertainty parameters are constrained in the model with Gaussian penalty terms, which reflect the prior knowledge from external measurements and theoretical studies. The final form of the negative log-likelihood function used for fitting the NSI models to the data is

$$-\ln\left(L(\overline{\mu}|\overline{N})\right) = \sum_{i}^{n_{reco}} (\mu_i - N_i \ln(\mu_i)) + \sum_{k}^{\eta^C} \frac{(\eta_k - \eta_k^0)^2}{2\sigma_{\eta_k}^2} + \text{const}, \qquad (29)$$

where $\overline{N}$ is the vector of bin contents in data, $\overline{\mu}$ is the vector of the corresponding bin-wise expectation values of the Poisson distributions predicted by the model and η^C are the constrained nuisance parameters among all the nuisance parameters η. The sum runs over the bins in the two-dimensional reconstructed space in the reconstructed energy versus the reconstructed cosine zenith. The values of $\overline{\mu}$ are in general functions of the parameters of interest, ϵ, and the nuisance parameters, η. The constant terms which do not depend on μ are omitted as they are irrelevant for the negative log-likelihood minimisation and hypothesis testing. The confidence interval construction is based on the profile likelihood ratio test statistic

$$-2\ln\frac{L(\epsilon_0, \hat{\hat{\eta}}|\overline{N})}{L(\hat{\epsilon}, \hat{\eta}|\overline{N})}, \qquad (30)$$

where $\hat{\hat{\eta}}$ denotes the profiled values of η which minimise the negative log-likelihood for a given value of ϵ_0. $\hat{\epsilon}$ and $\hat{\eta}$ are the maximum likelihood estimates of the parameters

of interest and the nuisance parameters respectively. The ordering principle follows the Feldman and Cousins approach [150] and the χ^2 approximation of the test statistic in Eq. 30 is used, provided by Wilks' theorem.

Results

There are several factors that lead our analysis to focus on the NSI in the $\mu - \tau$ sector:

- Only the track reconstruction output is available so far for the ORCA6 sample,

- The ORCA6 detector resolution is not reliable below the reconstructed energy of 10 GeV,

- Even above 10 GeV, the energy reconstruction quickly becomes saturated due to the energy reconstruction method based on the reconstructed track length. Thanks to the phenomenology of matter NSI with $\mu - \tau$ flavour violating term, this saturation does not significantly deteriorate the sensitivity to the $\epsilon_{\mu\tau}$ parameter,

- The atmospheric neutrino flux above a neutrino energy of 10 GeV and in the up-going directions with $\cos\theta_z < -0.84$, where the matter effects are the most prominent, is suppressed for electron neutrinos.

The results of our analysis are compatible with the non observation of neutrino Non-Standard Interactions. The obtained confidence limits with a statistical significance at the 90% confidence level for all the tested NSI models are summarised in Table 11.

NSI Couplings	90% CL allowed regions
Real NSI	
$\epsilon_{\mu\tau}$	$[-0.0087, 0.0090]$
$\epsilon_{\tau\tau} - \epsilon_{\mu\mu}$	$[-0.021, 0.021]$
$\epsilon_{e\tau}$	$[-0.080, 0.081]$
$\epsilon_{e\mu}$	$[-0.069, 0.069]$
Complex flavour-violating NSI	
$|\epsilon_{\mu\tau}|$	≤ 0.011
$\delta_{\mu\tau}$	$[0, 2\pi]$
$|\epsilon_{e\tau}|$	≤ 0.082
$\delta_{e\tau}$	$[0, 2\pi]$
$|\epsilon_{e\mu}|$	≤ 0.068
$\delta_{e\mu}$	$[0, 2\pi]$

Table 11: Summary of the measured limits on the NSI couplings with 355 days of ORCA6 data. The top section contains those couplings which are assumed to be real. The bottom section presents measurements where the possible complex nature of the flavour-violating NSI parameters is accounted for. NSI are assumed to couple to the d-quark only. For complex NSI parameters, the limits on the moduli, $|\epsilon_{\alpha\beta}|$, are obtained by profiling over the corresponding phase $\delta_{\alpha\beta}$.

It was found that the data puts better constraints on some of the nuisance parameters than it was assumed with their Gaussian priors. None of the measurements introduced a significant statistical pull in any of the nuisance parameters — all of the maximum likelihood estimates remained well within the assumed prior distributions.

The flavour-violating NSI models were also extended with the introduction of their corresponding complex phases. It was found that the possible complex nature of the

NSI parameters has an impact only on the $\epsilon_{\mu\tau}$ measurement, as it was expected from theory. The maximum likelihood estimates of the nuisance parameters in the fits to the complex NSI models had almost exactly the same values as in the real case.

The results claimed in Table 11 were obtained with the assumption of the Wilks' theorem approximation that the profile log-likelihood ratio used in the confidence interval construction converges to the χ^2 distribution. However, the actual shape of the profile log-likelihood ratio can be derived with pseudo experiments and the procedure which in literature is frequently referred to as the Feldman and Cousins approach. Nevertheless this is a computationally expensive procedure so it was applied only to the real $\epsilon_{\mu\tau}$ parameter, to which ORCA6 was expected to be the most sensitive. The new exact confidence interval at 90% confidence level was obtained:

$$-0.009 \leq \epsilon_{\mu\tau} \leq 0.010. \tag{31}$$

The procedure was applied only to one example parameter, because there were no significant reasons to believe that the Wilks' approximation should not hold in any of the tested NSI models. The main idea was to develop a procedure which cross checks the Wilks' theorem assumption and can be applied to the future analyses with ORCA, when the sensitivity will reach the current world's best limits. In this way, ORCA measurements will be able to be compared to the results from other experiments in a reliable way.

An issue that usually does not get a lot of attention in the NSI research with atmospheric neutrinos was investigated: the Earth's matter model. Regarding the density profile of the Earth layers, the Preliminary Earth Model (PREM) [52] is widely used as its accuracy of a few percent, verified with subsequent works [131, 132], does not introduce a significant source of systematic uncertainty. A not well known characteristic of the Earth's matter is its chemical composition. The current models do not converge to a stable result. The difference in the chemical composition affects the relative number densities of electrons, u-quarks and d-quarks, which are important especially when the limits obtained for a single fermion are re-scaled for comparison. By re-running the analysis with an alternative Earth model adapted from the repository of the publicly available nuSQUiDS neutrino oscillation calculation software [167] and comparing the outcome to the results obtained with the OscProb [58] default model, it was found that the difference was negligible. The models were first verified to be different in the chemical composition.

The limits obtained were compared to the most recent results from other experiments, namely ANTARES [77], IceCube [51] and DeepCore [81]. It was found that ORCA6 was able to set the limits only 2 to 3 times worse than the current world's best results. Taking into account that the selected neutrino sample corresponds to only 355 days of data taking, the results of this work provide a strong proof of concept for the future NSI studies with the ORCA detector.

Conclusions

The NSIs were not observed and all the fitted models are consistent with each other and with the standard oscillation scenario. Nevertheless, the limits obtained in this thesis provide a very strong evidence that non-standard interactions of neutrinos can and should be studied with the incomplete, early stages of the KM3NeT/ORCA detector. Despite the very limited energy reconstruction resolution, ORCA6 was able to provide results on the measured NSI parameters only a factor of 2 to 3 worse than the current

world's best limits. Even though the detector construction advanced quickly in the last year and there are many components ready to be deployed in the near future, it is not easy to predict when the final stage of the ORCA detector will be ready. Nevertheless, a big advantage of the KM3NeT project is that the detectors can gather data with the number of detection lines already installed regardless of the status of the full construction. Several improvements in the reconstruction and event selection are being developed based on the experience gathered with the first ORCA6 data set. The current stage of the detector with seven additional detection units will most likely be able to push future ORCA NSI results towards the competitive region.

Outlook

A dedicated event selection could improve the sensitivity to the $\epsilon_{\mu\tau}$ and $\epsilon_{e\mu}$ parameters. They embody a special case where the sensitivity would benefit significantly from the increased statistics of the high energy muon neutrinos with $E_\nu > 100$ GeV. Normally, these events are not targeted in the event selection for ORCA as the standard oscillations and most of the beyond standard model phenomena, which can be probed with atmospheric neutrinos, focus on the energies at the GeV scale. On the other hand, an improved energy resolution in the low energy phase space region can be used to derive better constraints for the complex phase. In the case of the diagonal, non-universal $\epsilon_{\tau\tau} - \epsilon_{\mu\mu}$ NSI term, most of the future improvement is expected from the increase of the statistics with extended detector exposure. The modification in the oscillation amplitude seems to be already well measurable.

There is a great potential for the improvement in measurements of the NSI parameters involving electron flavour. This improvement would come from the addition of shower samples, which is foreseen to give access to electron neutrino oscillation channels, such as ν_μ to ν_e appearance. Also, with a working shower reconstruction some potential for the $\epsilon_{ee} - \epsilon_{\mu\mu}$ might appear. This possibility, however, has to be investigated further.

The prediction for the distribution of the atmospheric muons passing a set of selection cuts which is optimised for neutrino purity should be improved. Nevertheless, the muon generation is the most computationally expensive part of the KM3NeT simulation chain. One of the ideas investigated in the past for the sensitivity study of the full ORCA detector was first to relax the cuts to obtain a more abundant and widely spread atmospheric muon distribution and then re-normalise it to the number of the muon events present in the original, strict neutrino event selection. The task should become easier to achieve with the future use of the event classifiers based on machine learning algorithms.

Resumen

Los neutrinos y todas sus peculiaridades son actualmente uno de los temas más estudiados en física de partículas. Muchas de las características de estas escurridizas partículas siguen siendo un misterio hasta el día de hoy, a pesar de que los neutrinos fueron postulados en 1930 y detectados por primera vez en 1956. Los neutrinos interactúan solo a través de interacciones débiles y, por lo tanto, observarlos con estadísticas razonables requiere un enfoque específico que involucra detectores de volumen enorme.

En las últimas décadas, muchos experimentos han contribuido a proporcionar una clara evidencia de la existencia de oscilaciones de neutrinos. Las investigaciones sobre este tema culminaron en el Premio Nobel otorgado en 2015.

La observación de la transición entre los estados de sabor de los neutrinos al propagarse fue una prueba definitiva de que los neutrinos son partículas con masa. Además, estudios posteriores mostraron que el número de estados de masa de neutrinos no degenerados es al menos dos. Dentro del Modelo Estándar, que es la teoría establecida de las interacciones fundamentales, no se contempla que los neutrinos tengan masa. La mayoría de las extensiones teóricas postuladas del Modelo Estándar dirigidas a la inclusión de masas de neutrinos requieren la existencia de un nuevo tipo de interacciones que aún no se ha observado. Desde el punto de vista fenomenológico, estas interacciones se pueden agrupar bajo el concepto de interacciones no estándar de neutrinos (INE o NSIs por sus siglas en inglés) que afectarían la oscilación de neutrinos a un nivel secundario. En analogía con las interacciones débiles, hay dos tipos de INE: de Corriente Cargada (CC) y de Corriente Neutra (NC). Dado que los experimentos de oscilación de neutrinos no son sensibles a las INE de CC, en nuestro trabajo nos centramos exclusivamente en INE de NC, que con frecuencia se denominan INE de la materia. El estudio de interacciones no estándar de neutrinos con fermiones de materia se concibe desde este punto de vista fenomenológico, ya que su existencia proporciona una manera de investigar la naturaleza de la nueva física más allá del Modelo Estándar.

El proyecto KM3NeT/ORCA es un telescopio de neutrinos de próxima generación destinado a medir las oscilaciones de los neutrinos atmosféricos. Uno de sus objetivos científicos es la búsqueda de fenómenos más allá del Modelo Estándar, que pueden manifestarse en la modificación de los patrones de oscilación de neutrinos. Las interacciones no estándar de neutrinos son uno de los fenómenos dentro de la definición anterior. La primera etapa del detector ORCA, llamada ORCA6, comprende solo seis de las 115 unidades de detección planificadas, pero ha demostrado ser capaz de observar oscilaciones de neutrinos [137]. En este trabajo se ha usado la muestra de datos utilizada para la medición de los parámetros estándar de oscilación de neutrinos para la búsqueda de INE con el foco en el sector $\mu - \tau$.

Oscilaciones de neutrinos con INE

Las INE introducen una modificación en la ecuación de movimiento de los neutrinos que viajan a través de la materia. Esta modificación, en forma de término de perturbación del hamiltoniano, está parametrizada por una matriz 3x3 con 9 parámetros: 3 términos complejos fuera de la diagonal que violan la conservación de sabor, caracterizados por un módulo y una fase compleja correspondiente, y 3 términos diagonales de no universalidad de sabor. Efectivamente, de forma análoga a las masas de los neutrinos, en el caso de los parámetros diagonales, en los experimentos de oscilación de neutrinos solo se puede observar la diferencia entre ellos, lo que hace que el número total de parámetros INE medibles con el detector ORCA se reduzca a 8. El impacto de las INE en las oscilaciones de neutrinos en la materia depende del parámetro particular, el canal de oscilación y la cantidad de materia presente en la trayectoria de los neutrinos. En la materia de la Tierra, el efecto de las INE es más prominente para las direcciones de neutrinos que cruzan el núcleo, ya que su alta densidad amplifica la influencia general de la materia en la propagación de neutrinos. El canal de oscilación más importante medido en ORCA es la desaparición de neutrinos muónicos, que para energías de neutrinos superiores a 20 GeV ocurre casi exclusivamente en favor de la aparición de neutrinos tau. Por lo tanto, los parámetros INE más importantes para la investigación de INE con ORCA son $\epsilon_{\mu\tau}$ y $\epsilon_{\tau\tau} - \epsilon_{\mu\mu}$ (el llamado sector $\mu - \tau$).

En general, los parámetros INE que violan el sabor $\epsilon_{\mu\tau}$, $\epsilon_{e\tau}$ y $\epsilon_{e\mu}$ pueden llevar una fase compleja, que bajo ciertas condiciones afectaría la influencia de las INE en las oscilaciones de neutrinos. Sin embargo, en el canal de desaparición de $\nu_\mu/\bar{\nu}_\mu$, se prevé que la sensibilidad a $\epsilon_{\mu\tau}$ se vea afectada solo por su fase correspondiente $\delta_{\mu\tau}$.

Objetivos

La tesis tiene como objetivo probar la hipótesis de la existencia de interacciones no estándar de neutrinos manifestada como efectos secundarios en los patrones de oscilación de neutrinos atmosféricos observados en los datos de ORCA6. Teniendo en cuenta la limitación de la etapa inicial del detector ORCA, el objetivo del análisis no es competir con los otros experimentos en el campo, sino crear una prueba de concepto de las capacidades de ORCA en las búsquedas por física más allá del Modelo Estándar. Por lo tanto, los objetivos de esta tesis doctoral son los siguientes:

- Estudiar las consecuencias fenomenológicas de diferentes configuraciones de los parámetros INE que potencialmente ocurran en la naturaleza.

- Investigar la resolución del detector en varias regiones del espacio de fase reconstruido en el contexto de la señal esperada de las INE.

- Identificar el impacto de las incertidumbres sistemáticas y la posible naturaleza compleja de los parámetros INE que violan el sabor.

- Medir (o establecer límites en) los parámetros $\epsilon_{\mu\tau}$, $\epsilon_{e\tau}$, $\epsilon_{e\mu}$ y $\epsilon_{\tau\tau} - \epsilon_{\mu\mu}$ prestando especial atención al sector $\mu - \tau$,

- Desarrollar un procedimiento estadísticamente sólido que respalde los resultados obtenidos. Numerosos parámetros de incertidumbres sistemáticas de diferente naturaleza combinados con la estadística baja de la muestra de eventos ORCA6 son potencialmente problemáticos para la ampliamente utilizada aproximación de Wilks.

- Comparar los resultados obtenidos con las mediciones líderes en el mundo y estudiar las diferencias entre los modelos de la Tierra comúnmente utilizados en el campo del estudio de INE.

Metodología

Antes de que las oscilaciones de neutrinos puedan estudiarse con modelos estadísticos, los datos primero deben medirse, reconstruirse y seleccionarse para obtener una muestra pura de neutrinos. Por otro lado, es necesario un modelo de simulación de Monte Carlo fiable para proporcionar las predicciones de las tasas de eventos reconstruidos que se pueden comparar directamente con los datos. Estas predicciones deben representar las hipótesis de diferentes valores de los parámetros INE que son el objetivo del análisis.

El modelo de análisis tiene que tener en cuenta las incertidumbres sistemáticas derivadas de las incertidumbres en el modelado de la física y los efectos específicos del detector que posiblemente puedan afectar a los datos. Estas incertidumbres se incluyen en el análisis en forma de parámetros, en adelante denominados sistemáticos, que pueden ser modificados por el software de ajuste. Estos parámetros reflejan la precisión del estado actual del conocimiento sobre el flujo de neutrinos atmosféricos, el flujo de muones atmosféricos, las secciones eficaces de interacción de neutrinos, la absorción de luz en el agua de mar y la eficiencia cuántica de los fotomultiplicadores.

La inferencia estadística se basa en el enfoque frecuentista con el uso de la estimación de máxima verosimilitud y el test estadístico del logaritmo del cociente de verosimilitud. Para la verificación de la aproximación χ^2 proporcionada por el teorema de Wilks, se desarrolló un procedimiento que involucra la generación de pseudodatos para derivar la forma exacta del test estadístico para un caso de ejemplo de los modelos analizados.

El detector ORCA6

Como ya se ha mencionado, el detector ORCA6 es una etapa temprana del proyecto KM3NeT/ORCA. Se encuentra en el mar Mediterráneo a una profundidad de 2450 m, a unos 40 km al sur de la ciudad francesa de Tolón. Consiste en seis líneas verticales ancladas en el fondo del mar con una distancia horizontal promedio de alrededor de 20 m. A lo largo de cada línea hay 18 módulos ópticos digitales (DOMs) ubicados con una separación vertical promedio de ∼9 m.

El principio de detección en ORCA se basa en el efecto Cherenkov que da lugar a la emisión de luz por las partículas cargadas que pasan a través del agua del mar dentro o cerca del volumen del detector. Estas partículas pueden tener su origen en las interacciones de los neutrinos, que no pueden observarse directamente debido a su falta de carga eléctrica. Sin embargo, hay varias fuentes de fondo que pueden imitar la señal esperada de los neutrinos que interactúan o enmascararla completamente con ruido de fondo. En la etapa de toma de datos, estas fuentes se abordan con los algoritmos de trigger y ciertos sistemas de monitoreo de datos que garantizan que solo se aceptan las condiciones de toma de datos estables y confiables.

El dispositivo responsable de la detección de luz Cherenkov es el módulo óptico digital, que esencialmente es una esfera resistente a la presión equipada con 31 fotomultiplicadores (PMTs) dispuestos para monitorear el ángulo sólido completo a su alrededor. El modelo de PMT se elige para maximizar la eficiencia cuántica para las longitudes de onda de los fotones entre 350 y 500 nm, donde la emisión de Cherenkov es

alta y, al mismo tiempo, las propiedades del agua de mar dependientes de la longitud de onda son las más favorables.

El estudio de las oscilaciones de neutrinos con ORCA hace uso de los neutrinos producidos en la atmósfera terrestre, cuyo flujo surge principalmente de las cadenas de desintegración de piones y kaones creadas en las interacciones de los rayos cósmicos primarios. Prácticamente no hay neutrinos tau en el flujo de neutrinos atmosféricos primarios, pero pueden verse en el detector gracias a las oscilaciones. Para las energías de los neutrinos por encima de $10\,\text{GeV}$, donde se espera la mayor parte de la señal en ORCA6, los neutrinos muónicos son mucho más abundantes que los neutrinos electrónicos y la proporción de neutrinos a antineutrinos se mantiene cercana a uno.

Los neutrinos no se pueden separar de los antineutrinos en un telescopio de neutrinos como ORCA. Para ciertos parámetros INE, los efectos sobre las oscilaciones son opuestos para neutrinos y antineutrinos y, por lo tanto, podrían cancelarse parcialmente (nótese que en el flujo de neutrinos atmosféricos la relación $\nu/\bar{\nu}$ es cercana a uno para un amplio espectro de energía de neutrinos). Sin embargo, el impacto general todavía se puede observar gracias a la asimetría de la sección eficaz $\sigma_\nu/\sigma_{\bar{\nu}} \simeq 2$ en la materia ordinaria. El problema mencionado anteriormente es especialmente importante para el parámetro que viola el sabor $\epsilon_{\mu\tau}$, porque sus efectos son observables principalmente a través del canal de desaparición de neutrinos muónicos que se desacopla del estado de sabor de electrones para la energía de neutrinos $E_\nu > 20$ GeV. Esto significa que el efecto del potencial de materia estándar no interfiere mucho con el impacto potencial de $\epsilon_{\mu\tau}$ y la degeneración entre el signo $\epsilon_{\mu\tau}$ y la carga de leptones del neutrino es casi exacta. Sin embargo, la cancelación se espera solo en la región del espacio de fase donde los efectos NSI están dominados por los términos lineales del parámetro dado. Para las altas energías $E_\nu > 80$ GeV, el efecto $\epsilon_{\mu\tau}$ converge para neutrinos y anti-neutrinos a un déficit estable de eventos con respecto a las oscilaciones estándar. En el canal de desaparición de muones, la interferencia destructiva entre los efectos INE en $\nu\,\bar{\nu}$ no es prominente para el parámetro INE que viola sabor y que no involucra el sabor del muon, $\epsilon_{e\tau}$, y el no universal $\epsilon_{\tau\tau} - \epsilon_{\mu\mu}$.

Reconstrucción de eventos y resolución del detector

En ORCA normalmente se distinguen dos categorías generales de eventos: eventos tipo traza y eventos tipo cascada; llamados "trazas" y "cascadas" por brevedad. Las trazas son inducidas por eventos ν_μ-CC, muones atmosféricos e interacciones ν_τ-CC con el leptón tau que se descompone en un muon. Las cascadas generalmente pueden surgir de todo tipo de interacciones de neutrinos, porque incluso los ν_μ-CC tienen el componente hadrónico. Sin embargo, la mayoría de los eventos tipo cascada se esperan de ν_e-CC y todas las interacciones de sabor NC. Las trazas y las cascadas difieren significativamente en su topología: las cascadas dan una señal más isotrópica y localizada, mientras que las trazas dejan un rastro de DOMs activados en todo el detector a lo largo del camino del muon. Después de aplicar un conjunto adecuado de cortes para suprimir la contaminación por muones atmosféricos, la señal en forma de traza se convierte en la principal herramienta para la identificación del sabor de los neutrinos muónicos.

A la muestra de datos ORCA6 utilizada en esta tesis, solo se aplicó la reconstrucción de trazas, siendo la energía reconstruida evaluada directamente a partir de la longitud de la traza reconstruida. La longitud se traduce en energía con la relación simple de $0{,}25$ GeV/m que corresponde al régimen de partículas mínimamente ionizantes de un muon. Este enfoque no introduce un error significativo en el rango de energía del muon

hasta $\sim 100\,\mathrm{GeV}$. Sin embargo, las limitaciones geométricas del tamaño de ORCA6, que permiten la traza observable más larga de unos 200 metros, provocan una fuerte saturación de la energía reconstruida. Los neutrinos atmosféricos en un amplio espectro de energías por encima de $80\,\mathrm{GeV}$ se reconstruyen en solo unos pocos bines en el espacio de energía reconstruida, que por la construcción del proxy de energía reconstruida se restringe a $E_{reco} \sim 50\,\mathrm{GeV}$. Al mismo tiempo, la reconstrucción de la dirección es muy buena; las distribuciones del coseno del cenit verdadero reconstruido en un bin dado en el espacio reconstruido generalmente se alinean en el centro del bin con formas de tipo gaussiano. Como se esperaba de la cinemática, la resolución de reconstrucción de la dirección mejora con el aumento de la energía del neutrino y también, en las energías más bajas, muestra una ligera dependencia de la propia dirección verdadera.

Cálculo de la tasa de eventos con los métodos de Monte Carlo

Los datos se agrupan en un espacio de fase bidimensional de la energía reconstruida frente al coseno del cenit reconstruido. El modelo de análisis tiene que ser capaz de generar predicciones de manera similar basándose en los valores de los parámetros del modelo que puedan ser manipulados por el software de ajuste. Las predicciones de la tasa de eventos de Monte Carlo se generan utilizando el enfoque por etapas que desacopla el cálculo del flujo de neutrinos, la probabilidad de oscilación de neutrinos y el factor de resolución del detector, que incluye la sección eficaz y la aceptancia del detector. Para evaluar la resolución del detector en forma de matriz de respuesta, primero es necesario simular neutrinos y muones atmosféricos que interactúan en el sitio del detector, que posteriormente se tratan con los mismos algoritmos de trigger y reconstrucción que normalmente se aplican a los datos.

La predicción del conteo de eventos a nivel del detector se calcula con la siguiente fórmula:

$$
n^j_{reco}(E^j_{reco}, \cos\left(\theta^j_{reco}\right), E_{scale}) = \sum_i \sum_{\alpha \in \{e,\mu,\tau\}} \sum_{\nu,\bar\nu} \sum_{CC/NC} w^j_i \times
$$

$$
n_{tilt}(\Delta\gamma, \Delta d) \cdot [P(\nu_e \to \nu_\alpha)(\text{std osc}, \epsilon_{NSI}) \cdot \phi_e^{\zeta_{\mu e}}(E^i_{true}, \cos\left(\theta^i_{true}\right), \zeta_{\mu e}, \zeta_{e\bar e}, \zeta_{\mu\bar\mu}, \Delta\gamma, \Delta d) +
$$

$$
P(\nu_\mu \to \nu_\alpha)(\text{std osc}, \epsilon_{NSI}) \cdot \phi_\mu^{\zeta_{\mu e}}(E^i_{true}, \cos\left(\theta^i_{true}\right), \zeta_{\mu e}, \zeta_{e\bar e}, \zeta_{\mu\bar\mu}, \Delta\gamma, \Delta d)]
$$

$$
\times n_{tot} \times \delta_{\alpha\tau} n_{\sigma^{\nu_\tau}_{CC}} \times \delta_{xx,NC} n_{\sigma_{NC}} + n^\mu_{atm} \cdot N^\mu_{atm,j} \,,
$$

$$(32)$$

donde

- el bin reconstruido j tiene su centro en $\{E^j_{reco}, \cos\left(\theta^j_{reco}\right)\}$, potencialmente modificado por la E_{escala} parámetro de incertidumbre sistemática,

- la primera suma recorre todos los bines verdaderos i que contribuyen al bin j,

- las otras sumas van sobre la dimensión del canal de interacción de la matriz de respuesta: ν_e-CC, $\bar\nu_e$-CC, ν_μ-CC, $\bar\nu_\mu$-CC, ν_τ-CC, $\bar\nu_\tau$-CC, ν-NC y $\bar\nu$-NC,

- std osc = $\{\theta_{12}, \theta_{13}, \theta_{23}, \Delta m^2_{21}, \Delta m^2_{31}, \delta_{CP}\}$ denota los parámetros de oscilación estándar,

- ϵ_{NSI} denota todos los parámetros INE distintos de cero utilizados en el modelo de oscilación,

- $\delta_{\alpha\tau}$ y $\delta_{xx,NC}$ son deltas de Kronecker que aíslan el sabor del neutrino tau o las interacciones NC (tenga en cuenta que el sabor único que se usó para la simulación NC fue ν_μ, por lo que los deltas no introducen términos adicionales)

- $N^\mu_{atm,j}$ representa el número de muones atmosféricos encontrados en el bin reconstruido j.

Una predicción de la tasa de eventos de MC, también conocida como "template", representa una única hipótesis para valores dados de los parámetros del modelo, que son:

- parámetros de oscilación de neutrinos $\theta_{12}, \theta_{13}, \theta_{23}, \Delta m^2_{21}, \Delta m^2_{31}$ y δ_{CP} extendidos por

- Parámetros INE $\epsilon_{\alpha\beta}$ con $\alpha, \beta \in \{e, \mu, \tau\}$,

- sistemáticos del flujo: inclinación (tilt) de energía de flujo $\Delta\gamma$, inclinación del coseno cenital de flujo Δd, $\nu_e / \bar{\nu}_e$ "skew" $\zeta_{e\bar{e}}$, $\nu_\mu / \bar{\nu}_\mu$ skew $\zeta_{\mu\bar{\mu}}$, ν_μ / ν_e oblicuidad ζ_{mue},

- factores de normalización de la sección eficaz $n_{\sigma^{\nu\tau}_{CC}}$ y $n_{\sigma_{NC}}$,

- normalización global n_{tot},

- normalización de muones atmosféricos n^μ_{atm},

- escala de energía del detector E_{escala}

Entre los parámetros del modelo, sólo uno o dos parámetros INE a la vez son de interés intrínseco en nuestro análisis. Sin embargo, los parámetros restantes, a menudo denominados parámetros "nuisance", suelen estar correlacionados con los parámetros de interés. Los parámetros nuisance normalmente están diseñados para dar cuenta de las incertidumbres sistemáticas y mejorar la precisión del modelo, por lo que su exclusión podría introducir un sesgo en la medición. Para lograr una independencia aproximada de la verosimilitud de estos parámetros nuisance, se utiliza una verosimilitud "profiled".

Ajuste de modelos y métodos estadísticos

Los ajustes se realizan con el minimizador MINUIT [151] proporcionado por el paquete de software ROOT [153]. Todos los ajustes se realizan haciendo un "profile" sobre el orden de masas con los valores iniciales de Δm^2_{31} tomados de los valores de parámetros de oscilación de neutrinos estándar de NuFIT 5.0 [73]. La ambigüedad en el octante de θ_{23} se tiene en cuenta con dos valores iniciales de $\sin^2(\theta_{23})_{init} = \{0.4, 0.6\}$. Esto significa que para cada hipótesis ajustada, se prueban cuatro puntos de partida en el caso de los modelos INE reales. Todos los demás parámetros de oscilación estándar se fijan en sus valores de mejor ajuste de NuFIT y no se incluyen en los ajustes. En el caso de los modelos INE complejos, se agregan valores iniciales adicionales en $\delta^{init}_{\alpha\beta} = \{0, \pi/2, \pi, 3\pi/2\}$ resultantes en el total de 16 puntos de partida para cada ajuste.

El análisis estadístico se basa exclusivamente en el enfoque frecuentista. Para la estimación de los parámetros utilizamos el método de máxima verosimilitud. Para evaluar la *bondad del ajuste*, se explota el enfoque de chi-cuadrado, asumiendo el comportamiento asintótico del Chi-cuadrado de Poisson, que esencialmente es el cociente de log-verosimilitud calculada con la probabilidad de Poisson "binned" asumiendo que los contenidos en los bines de datos como la hipótesis alternativa. El enfoque de chi-cuadrado se coteja con la prueba de Kolmogorov-Smirnov. Algunos de los parámetros de incertidumbre sistemática están restringidos en el modelo con términos de penalización gaussiana, que reflejan el conocimiento previo de mediciones externas

y estudios teóricos. La forma final de la función de verosimilitud logarítmica negativa utilizada para ajustar los modelos INE a los datos es

$$-\ln\left(L(\overline{N}|\overline{\mu})\right) = \sum_{i}^{n_{reco}}(\mu_i - N_i \ln(\mu_i)) + \sum_{k}^{\eta^C}\frac{(\eta_k - \eta_k^0)^2}{2\sigma_{\eta_k}^2} + \text{const}, \tag{33}$$

donde $\overline{N}$ es un vector del contenido de los bines de datos, $\overline{\mu}$ es el vector de los valores esperados correspondientes al bin de las distribuciones de Poisson predichas por el modelo y η^C son los parámetros nuisance restringidos entre todos los parámetros nuisance η. La suma recorre los bines en el espacio reconstruido bidimensional de la energía reconstruida frente al cenit del coseno reconstruido. Los valores de $\overline{\mu}$ son en general funciones de los parámetros de interés, ϵ, y los parámetros nuisance, η. Los términos constantes que no dependen de μ se omiten ya que son irrelevantes para la minimización de la probabilidad logarítmica negativa y la prueba de hipótesis. La construcción del intervalo de confianza se basa en el estadístico de prueba del cociente de verosimilitudes "profiled"

$$-2\ln\frac{L(\overline{N}|\epsilon_0,\hat{\hat{\eta}})}{L(\overline{N}|\hat{\epsilon},\hat{\eta})}, \tag{34}$$

donde $\hat{\hat{\eta}}$ denota los valores "profiled" de η que minimizan la probabilidad logarítmica negativa para un valor dado de ϵ_0. $\hat{\epsilon}$ y $\hat{\eta}$ son las estimaciones de máxima verosimilitud de los parámetros de interés y los parámetros nuisance respectivamente. El principio de ordenación sigue el enfoque de Feldman y Cousins [150] y la aproximación χ^2 del test estadístico en la ecuación 34, proporcionada por el teorema de Wilks.

Resultados

Hay varios factores que hacen que nuestro análisis se centre en las INE en el sector $\mu - \tau$:

- Solo la reconstrucción de trazas está disponible por ahora para la muestra ORCA6,

- La resolución del detector ORCA6 no es fiable por debajo de energías reconstruidas de 10 GeV,

- Incluso por encima de 10 GeV, la reconstrucción de energía se satura rápidamente debido al método de reconstrucción de energía basado en la longitud de la traza reconstruida. Gracias a la fenomenología de la materia INE con término de violación de sabor $\mu - \tau$, esta saturación no deteriora significativamente la sensibilidad al parámetro $\epsilon_{\mu\tau}$,

- el flujo de neutrinos atmosféricos por encima de la energía de los neutrinos de 10 GeV y en las direcciones ascendentes con $\cos\theta_z < -0.84$, donde los efectos de la materia son los más importantes, se suprime para el sabor de los neutrinos electrónicos.

Los resultados de nuestro análisis son compatibles con la no observación de interacciones no estándar de neutrinos. Los límites de confianza obtenidos con la significancia estadística al 90% de nivel de confianza para todos los modelos de INE estudiados se resumen en la Tabla 12.

NSI Couplings	90% CL allowed regions
NSI real	
$\epsilon_{\mu\tau}$	$[-0.0087, 0.009]$
$\epsilon_{\tau\tau} - \epsilon_{\mu\mu}$	$[-0.021, 0.021]$
$\epsilon_{e\tau}$	$[-0.080, 0.081]$
$\epsilon_{e\mu}$	$[-0.069, 0.069]$
NSI complejo que viola el sabor	
$|\epsilon_{\mu\tau}|$	≤ 0.011
$\delta_{\mu\tau}$	$[0, 2\pi]$
$|\epsilon_{e\tau}|$	≤ 0.082
$\delta_{e\tau}$	$[0, 2\pi]$
$|\epsilon_{e\mu}|$	≤ 0.068
$\delta_{e\mu}$	$[0, 2\pi]$

Table 12: Resumen de los límites medidos en los acoplamientos INE con 355 días de datos ORCA6. La sección superior contiene los acoplamientos asumiendo que son reales. La sección inferior presenta medidas en las que se tiene en cuenta la posible naturaleza compleja de los parámetros INE que violan el sabor. Se supone que las INE se acoplan únicamente al quark d. Para parámetros NSI complejos, los límites de los módulos $|\epsilon_{\alpha\beta}|$ se obtienen haciendo un profile sobre las fases correspondiente $\delta_{\alpha\beta}$.

Se encontró que los datos ofrecen mejores restricciones en algunos de los parámetros nuisance de lo que se suponía con sus "priors" gaussianos. Ninguna de las mediciones introdujo un "pull" estadístico significativo en ninguno de los parámetros nuisance; todas las estimaciones de máxima verosimilitud se mantuvieron dentro de las distribuciones prior supuestas.

Los modelos INE que violan el sabor también se ampliaron con la introducción de sus correspondientes fases complejas. Se encontró que la posible naturaleza compleja de los parámetros INE tiene un impacto solo en la medida de $\epsilon_{\mu\tau}$, como se esperaba de la teoría. Las estimaciones de máxima verosimilitud de los parámetros nuisance en los ajustes a los modelos de INE complejos tenían casi exactamente los mismos valores que en el caso real.

Los resultados indicados en la tabla 12 se obtuvieron con la suposición de la aproximación del teorema de Wilks de que la relación de la log-verosimilitud "profiled" utilizada en la construcción del intervalo de confianza converge a la distribución χ^2. Sin embargo, la forma real del logaritmo del cociente de verosimilitudes "profiled" se puede derivar con pseudoexperimentos y el procedimiento que en la literatura se conoce habitualmente como el enfoque de Feldman y Cousins. Sin embargo, este es un procedimiento costoso desde el punto de vista computacional, por lo que se aplicó solo al parámetro real $\epsilon_{\mu\tau}$, para el que se esperaba que ORCA6 fuera el más sensible. Se obtuvo el nuevo intervalo de confianza exacto al 90% de nivel de confianza:

$$-0.009 \leq \epsilon_{\mu\tau} \leq 0.010. \tag{35}$$

El procedimiento se aplicó solo a un parámetro de ejemplo, porque no había razones significativas para creer que la aproximación de Wilks no debería cumplirse en ninguno de los modelos INE probados. La idea principal fue desarrollar un procedimiento para verificar la suposición del teorema de Wilks y que pueda aplicarse a futuros análisis con ORCA cuando la sensibilidad alcance los mejores límites competitivos a nivel mundial. De esta forma, las mediciones de ORCA podrán compararse con los resultados de otros experimentos de forma fiable.

Se investigó un tema que normalmente no recibe mucha atención en la investigación de las INE con neutrinos atmosféricos: el modelo de materia de la Tierra. Con respecto al perfil de densidad de las capas de la Tierra, el Modelo Preliminar de la Tierra (PREM) [52] es ampliamente utilizado debido a que su precisión, verificada con trabajos posteriores [131, 132], no introduce una fuente de incertidumbre sistemática. La característica ambigua de la materia de la Tierra es su composición química. Los modelos actuales no convergen a un resultado estable. La diferencia en la composición química afecta las densidades numéricas relativas de electrones, u-quarks y d-quarks, que son importantes especialmente cuando los límites obtenidos para un solo fermión se escalan para comparar. Al volver a ejecutar el análisis con un modelo alternativo de la Tierra adaptado del repositorio del software de cálculo de oscilación de neutrinos nuSQUiDS [167] disponible públicamente y comparar el resultado con los resultados obtenidos con el modelo predeterminado OscProb [58], se encontró que la diferencia era insignificante. Previamente se verificó que los modelos eran diferentes en la composición química.

Los límites obtenidos se compararon con los resultados más recientes de otros experimentos: ANTARES [77], IceCube [51] y DeepCore [81]. Se encontró que ORCA6 fue capaz de alcanzar límites solo de 2 a 3 veces peor que los mejores resultados actuales a nivel mundial. Teniendo en cuenta que la muestra de neutrinos seleccionada corresponde a solo 355 días de toma de datos, los resultados de este trabajo proporcionan una fuerte prueba de concepto para los futuros estudios de INE con el detector ORCA.

Conclusiones

No se observaron los INE y todos los modelos ajustados son consistentes entre sí y con el escenario de oscilación estándar. Sin embargo, los límites obtenidos en esta tesis proporcionan una fuerte evidencia de que las interacciones no estándar de los neutrinos pueden y deben estudiarse con las primeras etapas parciales del detector KM3NeT/ORCA. A pesar de la limitada resolución de reconstrucción de energía, ORCA6 pudo proporcionar resultados en los parámetros INE medidos solo un factor de 2 a 3 peores que los mejores límites actuales. Aunque la construcción del detector ha avanzado rápidamente en el último año y hay muchos componentes listos para instalarse en un futuro cercano, no es fácil predecir cuándo estará lista la etapa final del detector ORCA. No obstante, una gran ventaja del proyecto KM3NeT es que los detectores pueden recoger datos con cualquier número de líneas de detección ya instaladas, independientemente del estado de la construcción completa. Se están desarrollando varias mejoras en la reconstrucción y selección de eventos en base a la experiencia recopilada con el primer conjunto de datos ORCA6. La etapa actual del detector con siete unidades de detección adicionales probablemente podrá impulsar los resultados futuros de ORCA INE hacia una región competitiva.

Perspectiva

Una selección de eventos dedicada podría mejorar la sensibilidad a los parámetros $\epsilon_{\mu\tau}$ y $\epsilon_{e\mu}$. Estos representan un caso especial en el que la sensibilidad se beneficiaría significativamente del aumento de las estadísticas de los neutrinos muónicos de alta energía con $E_\nu > 100$ GeV. Normalmente, estos eventos no son el objetivo de la selección de eventos para ORCA, ya que las oscilaciones estándar y la mayoría de los fenómenos más allá del modelo estándar que pueden probarse con neutrinos atmosféricos se enfocan

en las energías en la escala del GeV. Se puede utilizar una resolución de energía mejorada en la región del espacio de fase de baja energía para derivar mejores restricciones para la fase compleja. En el caso del término INE diagonal, no universal $\epsilon_{\tau\tau} - \epsilon_{\mu\mu}$, se espera que la mayor parte de la mejora futura aumente las estadísticas con la exposición prolongada del detector. La modificación en la amplitud de oscilación parece ser ya medible.

Existe un gran potencial para la mejora en las mediciones de los parámetros INE que involucran el sabor electrónico. Esta mejora vendría de la adición de la muestra de cascadas, que daría acceso a canales de oscilación de neutrinos electrónicos como ν_μ a ν_e. Además, con una reconstrucción de las cascadas podría aparecer cierto potencial para $\epsilon_{ee} - \epsilon_{\mu\mu}$. Sin embargo, esta posibilidad debe investigarse más a fondo.

Debería mejorarse la predicción de la distribución de los muones atmosféricos que pasan por un conjunto de cortes de selección optimizados para la pureza de los neutrinos. Sin embargo, la generación de muones es la parte computacionalmente más costosa de la cadena de simulación KM3NeT. Una de las ideas investigadas en el pasado para el estudio de sensibilidad del detector ORCA completo fue primero relajar los cortes para obtener una distribución de muones atmosféricos más abundante y ampliamente distribuida y luego volver a normalizarla al número de eventos de muones presentes en la selección original de eventos de neutrinos. La tarea debería volverse más fácil de lograr con el uso futuro de los clasificadores de eventos basados en algoritmos de aprendizaje automático.

A Fits and their configuration

A.1 Detector response configuration

The detector response used for the analysis presented in Chapter 4 had the following configuration

- 30 bins evenly spaced in the logarithm of the reconstructed energy between 1 and 1000 GeV.

- 20 bins evenly spaced in $\cos\theta_{reco}$ between -1 and 1,

- 120 bins evenly spaced in the logarithm of the true energy between 1 and 1000 GeV.

- 40 bins evenly spaced in $\cos\theta_{true}$ between -1 and 1,

A.2 Fit range and MC statistics

Figure 1 shows all the available bins in the reconstructed energy versus reconstructed cosine zenith space in terms of effective MC events or equivalent unweighted events which would generate the statistical error of a given bin (weights calculated at NuFit 5.0 NO). This quantity is defined as:

$$N_{eff}^{MC} = \frac{(\sum_i w_i)^2}{\sum_i w_i^2},\tag{1}$$

where index i goes over all the weights w_i contributing to the given bin. The shape of the histogram is driven by the detector geometry and the usage of reconstructed track length as energy proxy. As can be seen, some of the bordering bins on the right side of the distribution have less than 10 Monte Carlo effective events and by a rule of thumb it would be safer to exclude from the fit. The problem could also be resolved by accounting for bin-by-bin Monte Carlo statistics using for example the Barlow-Beeston method. This feature in the MONA framework is still under development and not yet ready to be used in the analysis. However, these potentially problematic boundary bins are not expected to distort the results as they have minimal contribution to the $\Delta\chi^2$ in the NSI sensitivity study (more information in section 4.7). Therefore, it was decided to keep the full reconstructed space in the fits to leave space for the event migration caused by the energy scale systematic.

A.3 Best-fit event rates
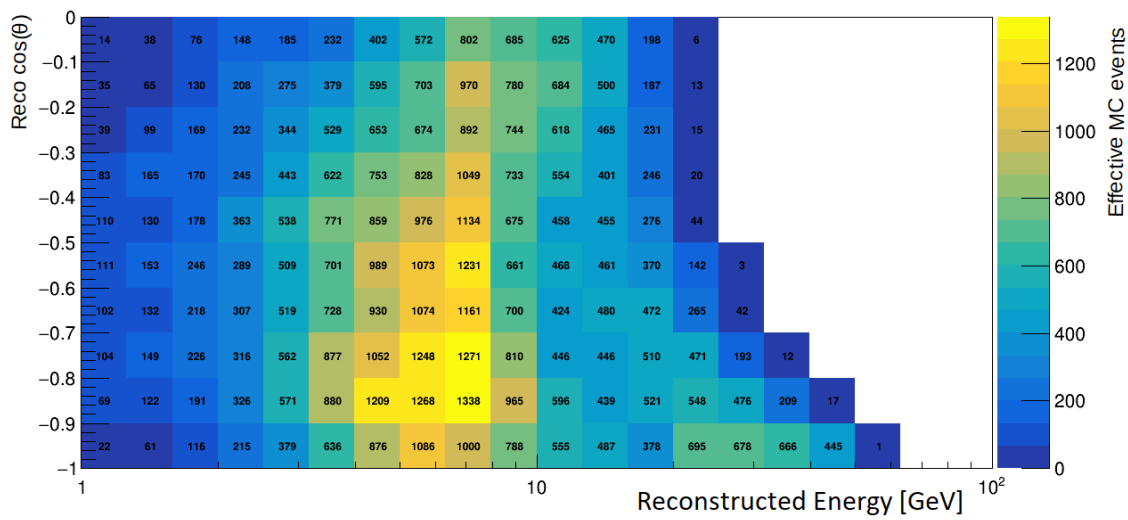
Figure 1: Number of equivalent events for the detector response used for the standard and the NSI analysis of ORCA6 ICRC21 sample. This number relates the sample of the number weighted events to the number of unweighted events (with w=1) that would have the same relative statistical fluctuation.

(a) The event rates from the MC prediction of the best-fit point of the real $\epsilon_{\tau\tau} - \epsilon_{\mu\mu}$ NSI model in 355 days of ORCA6 event selection portrayed in the two-dimensional space of reconstructed energy versus reconstructed cosine zenith.

(b) The event rates from the MC prediction of the best-fit point of the real $\epsilon_{e\tau}$ NSI model in 355 days of ORCA6 event selection portrayed in the two-dimensional space of reconstructed energy versus reconstructed cosine zenith.

(c) The event rates from the MC prediction of the best-fit point of the real $\epsilon_{e\mu}$ NSI model in 355 days of ORCA6 event selection portrayed in the two-dimensional space of reconstructed energy versus reconstructed cosine zenith.

(a) The event rates from the MC prediction of the best-fit point of the complex $\epsilon_{\mu\tau}$ NSI model in 355 days of ORCA6 event selection portrayed in the two-dimensional space of reconstructed energy versus reconstructed cosine zenith.

(b) The event rates from the MC prediction of the best-fit point of the real $\epsilon_{e\mu}$ NSI model in 355 days of ORCA6 event selection portrayed in the two-dimensional space of reconstructed energy versus reconstructed cosine zenith.

(c) The event rates from the MC prediction of the best-fit point of the real $\epsilon_{e\tau}$ NSI model in 355 days of ORCA6 event selection portrayed in the two-dimensional space of reconstructed energy versus reconstructed cosine zenith.

B   Oscillograms

This appendix shows the oscillograms for neutrino oscillations in vaccum, in Earth's matter without NSIs and with NSIs included. Transition probabilities between all the flavours are depicted. Survival probabilities are shown only for ν_e and ν_μ as only very small amounts of ν_τ are expected in the primary (non-oscillated) atmospheric neutrino flux.

B.1   Vacuum oscillations

In the case of neutrino oscillations in vacuum, the difference between the NO and IO scenarios should not be observable in principle as the neutrino oscillation probability in vacuum does not depend on the Δm_{ij}^2 signs. However, the current best-fit values for other oscillation parameters subtly vary between the two ordering scenarios (see Fig. 1.3), so a slight variation is visible. If δ_{CP} is different from 0 and π, we should be able to observe a difference between ν and $\bar{\nu}$ oscillations for the same configuration of the other oscillation parameters. Current best fits land at a CP violating δ_{CP}, but the allowed regions are still consistent with CP symmetry within 3σ (see Section 1.2.5).

(a) $P(\nu_e \to \nu_e)$ NO

(b) $P(\bar{\nu}_e \to \bar{\nu}_e)$ NO

(c) $P(\nu_e \to \nu_e)$ IO

(d) $P(\bar{\nu}_e \to \bar{\nu}_e)$ IO
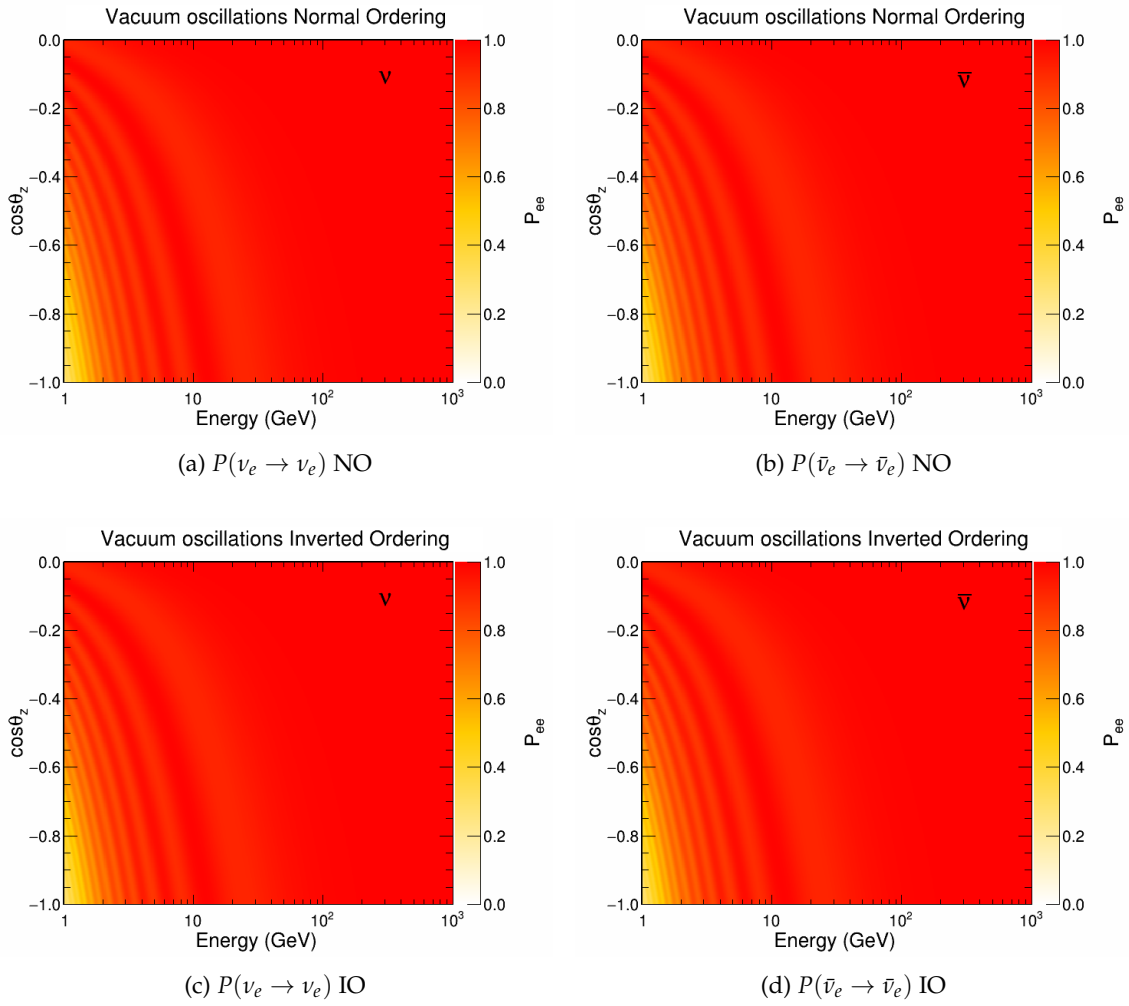
Figure 1: $P(\nu_e \to \nu_e)$ (left) and $P(\bar{\nu}_e \to \bar{\nu}_e)$ (right) survival probabilities in vacuum for normal (top) and inverted (bottom) ordering as a function of the neutrino true energy and $\cos(\theta_z)$.

(a) $P(\nu_e \to \nu_\tau)$ NO

(b) $P(\bar{\nu}_e \to \bar{\nu}_\tau)$ NO

(c) $P(\nu_e \to \nu_\tau)$ IO

(d) $P(\bar{\nu}_e \to \bar{\nu}_\tau)$ IO
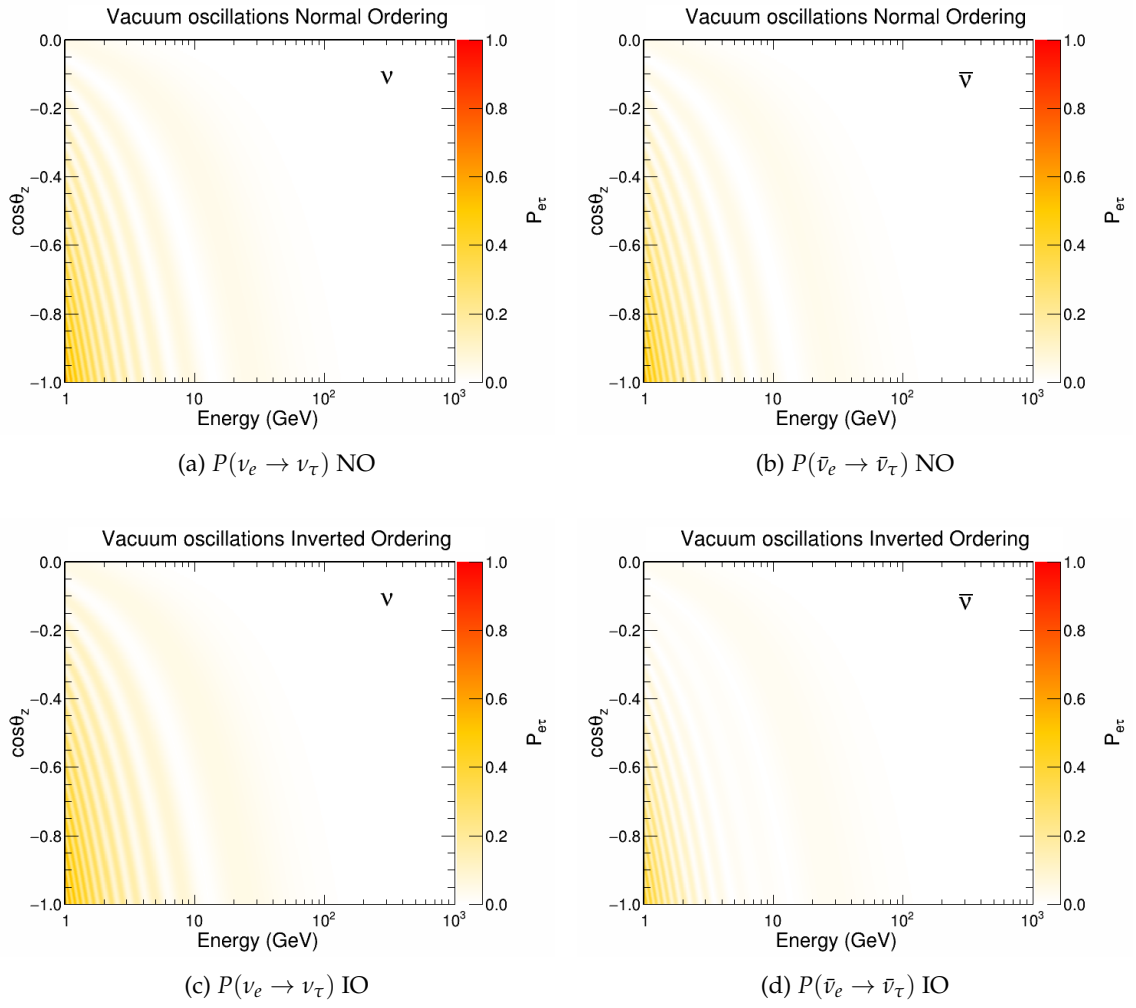
Figure 2: $P(\nu_e \to \nu_\tau)$ (left) and $P(\bar{\nu}_e \to \bar{\nu}_\tau)$ (right) transition probabilities in vacuum for normal (top) and inverted (bottom) ordering as a function of the neutrino true energy and $\cos(\theta_z)$.

(a) $P(\nu_\mu \to \nu_\mu)$ NO

(b) $P(\bar{\nu}_\mu \to \bar{\nu}_\mu)$ NO

(c) $P(\nu_\mu \to \nu_\mu)$ IO

(d) $P(\bar{\nu}_\mu \to \bar{\nu}_\mu)$ IO
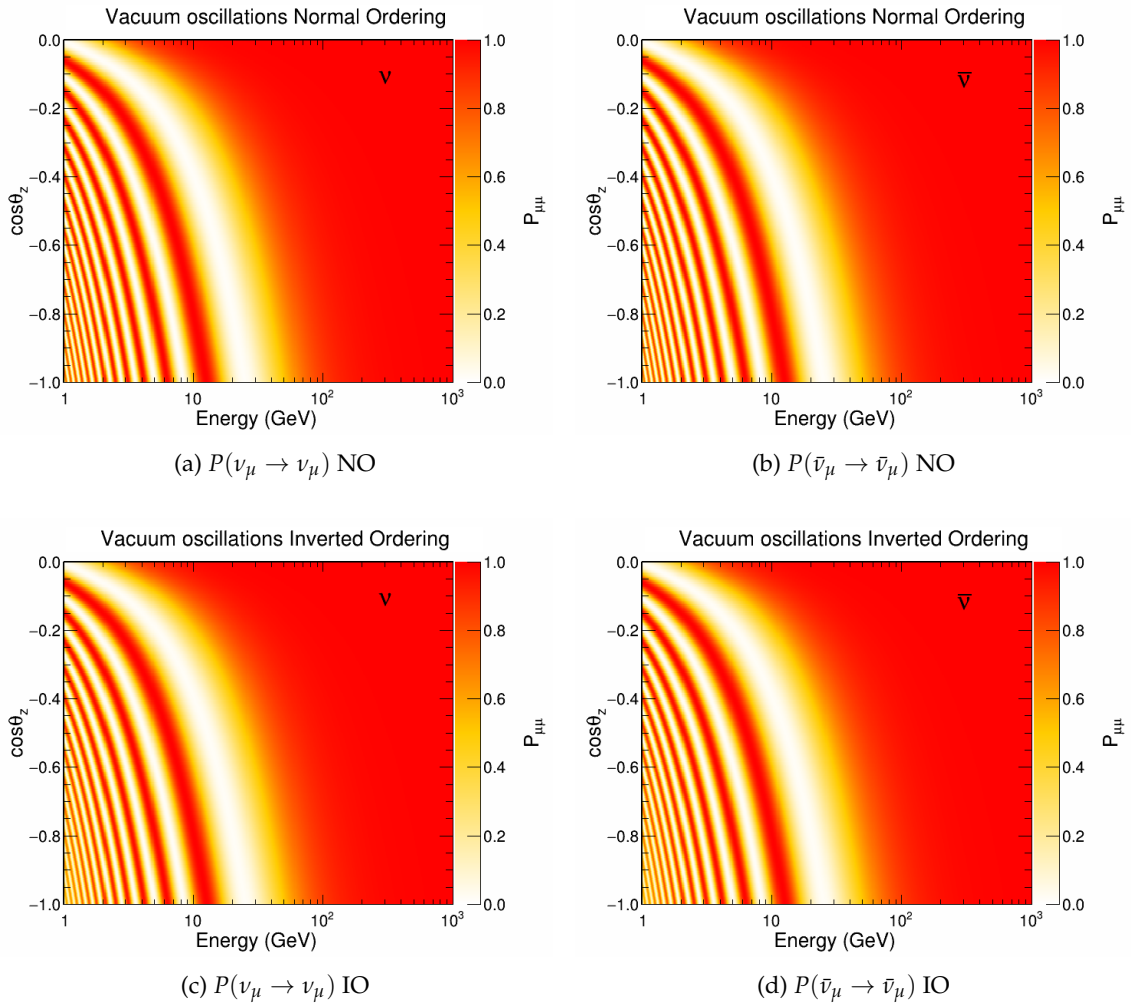
Figure 3: $P(\nu_\mu \to \nu_\mu)$ (left) and $P(\bar{\nu}_\mu \to \bar{\nu}_\mu)$ (right) survival probabilities in vacuum for normal (top) and inverted (bottom) ordering as a function of the neutrino true energy and $\cos(\theta_z)$.

(a) $P(\nu_\mu \to \nu_e)$ NO

(b) $P(\bar{\nu}_\mu \to \bar{\nu}_e)$ NO

(c) $P(\nu_\mu \to \nu_e)$ IO

(d) $P(\bar{\nu}_\mu \to \bar{\nu}_e)$ IO
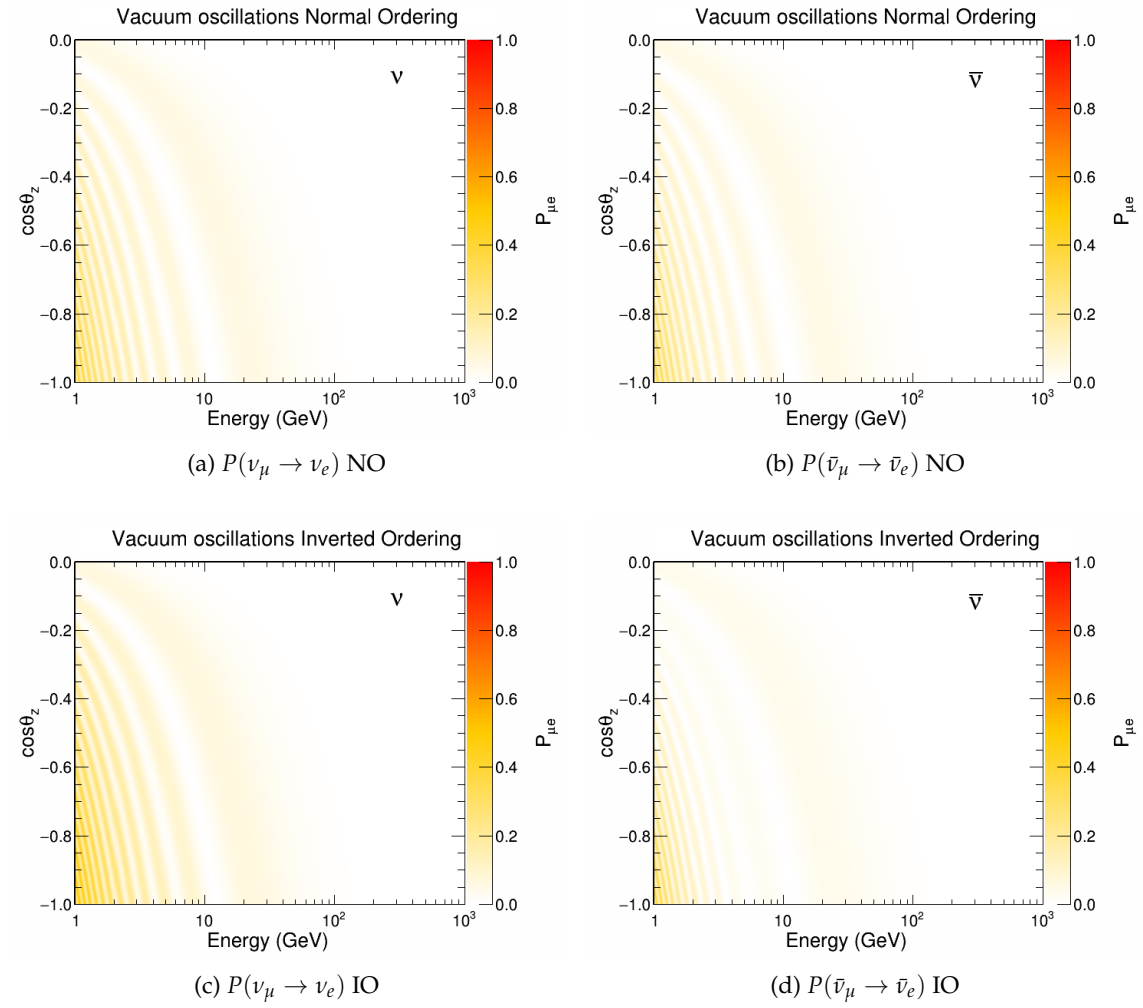
Figure 4: $P(\nu_\mu \to \nu_e)$ (left) and $P(\bar{\nu}_\mu \to \bar{\nu}_e)$ (right) transition probabilities in vacuum for normal (top) and inverted (bottom) ordering as a function of the neutrino true energy and $\cos(\theta_z)$.

(a) $P(\nu_\mu \rightarrow \nu_\tau)$ NO

(b) $P(\bar{\nu}_\mu \rightarrow \bar{\nu}_\tau)$ NO

(c) $P(\nu_\mu \rightarrow \nu_\tau)$ IO

(d) $P(\bar{\nu}_\mu \rightarrow \bar{\nu}_\tau)$ IO
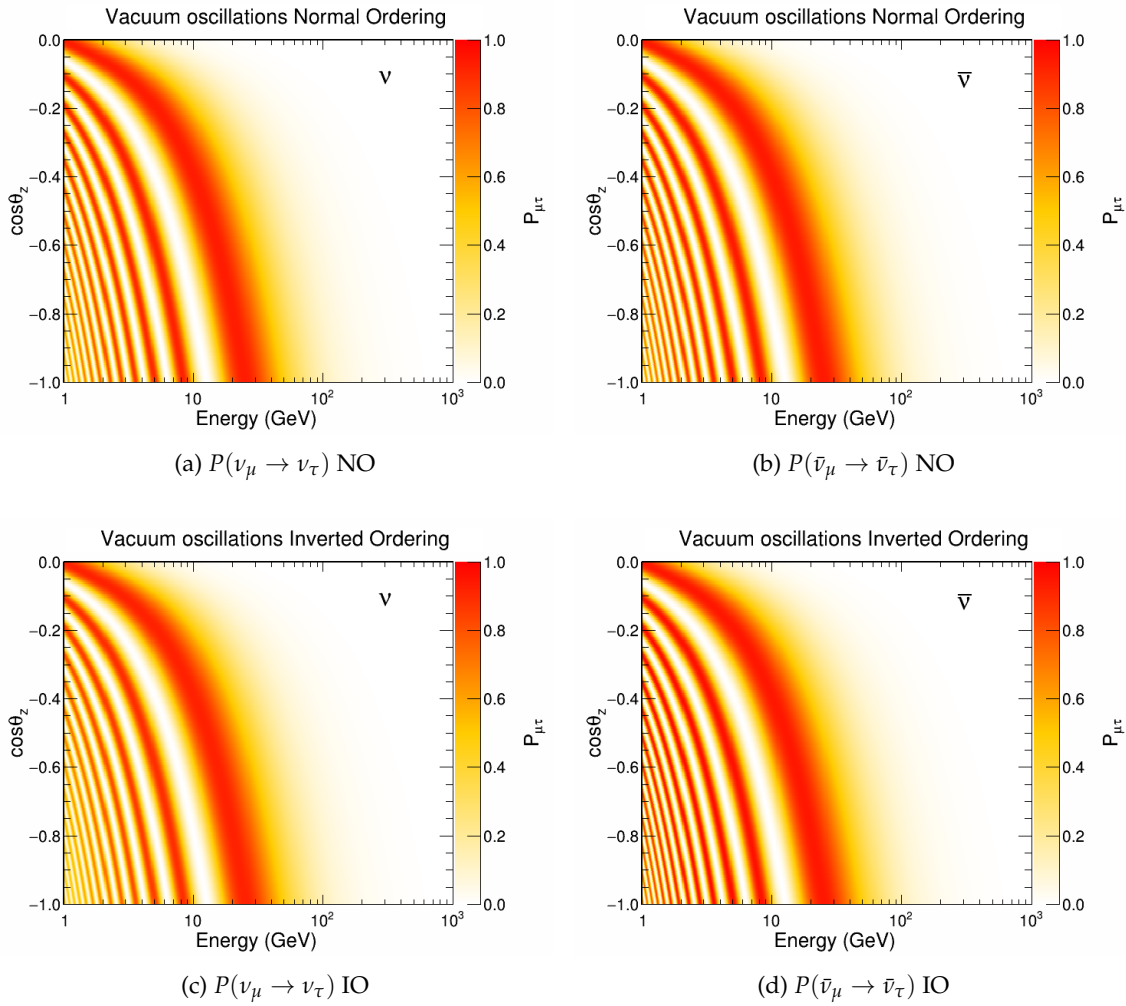
Figure 5: $P(\nu_\mu \rightarrow \nu_\tau)$ (left) and $P(\bar{\nu}_\mu \rightarrow \bar{\nu}_\tau)$ (right) transition probabilities in vacuum for normal (top) and inverted (bottom) ordering as a function of the neutrino true energy and $\cos(\theta_z)$.

B.2   Matter oscillations

Figures 6, 7, 8, 9 and 10 show matter oscillations for all the relevant flavour transitions. Neutrino oscillations in Earth's matter follow the formalism described in Section 1.2.2. As expected, in this case the oscillation patterns differ between NO and IO. The simultaneous change in the mass ordering and $\nu \leftrightarrow \bar{\nu}$ leads to the same results. The line around $\cos\theta_z \simeq -0.84$ corresponds to a drastic change in Earth density between the Core and the Mantle (see again Fig. 1.7).

(a) $P(\nu_e \to \nu_e)$ NO

(b) $P(\bar{\nu}_e \to \bar{\nu}_e)$ NO

(c) $P(\nu_e \to \nu_e)$ IO

(d) $P(\bar{\nu}_e \to \bar{\nu}_e)$ IO
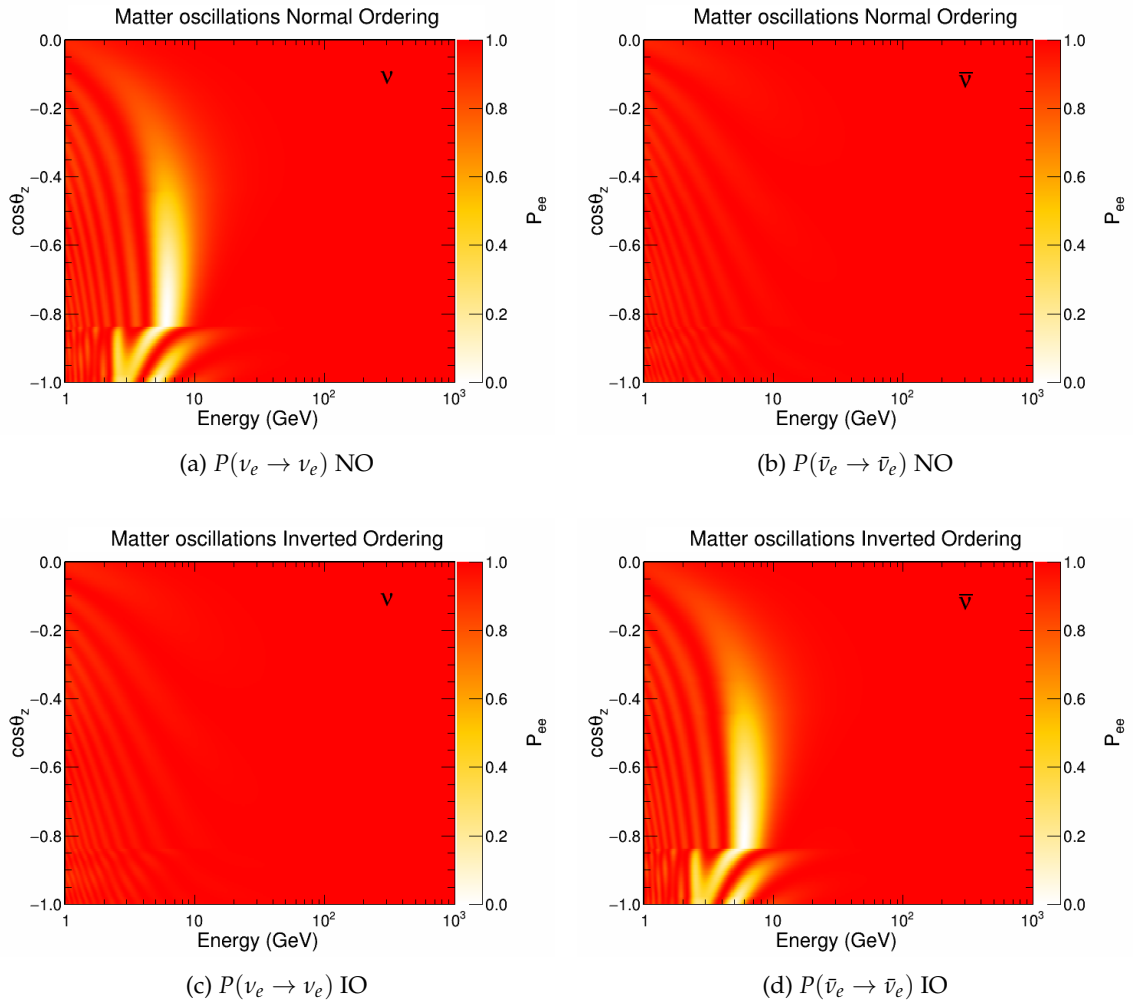
Figure 6: $P(\nu_e \to \nu_e)$ (left) and $P(\bar{\nu}_e \to \bar{\nu}_e)$ (right) survival probabilities in Earth's matter for normal (top) and inverted (bottom) ordering as a function of the neutrino true energy and $\cos(\theta_z)$.

(a) $P(\nu_e \to \nu_\tau)$ NO

(b) $P(\bar{\nu}_e \to \bar{\nu}_\tau)$ NO

(c) $P(\nu_e \to \nu_\tau)$ IO

(d) $P(\bar{\nu}_e \to \bar{\nu}_\tau)$ IO
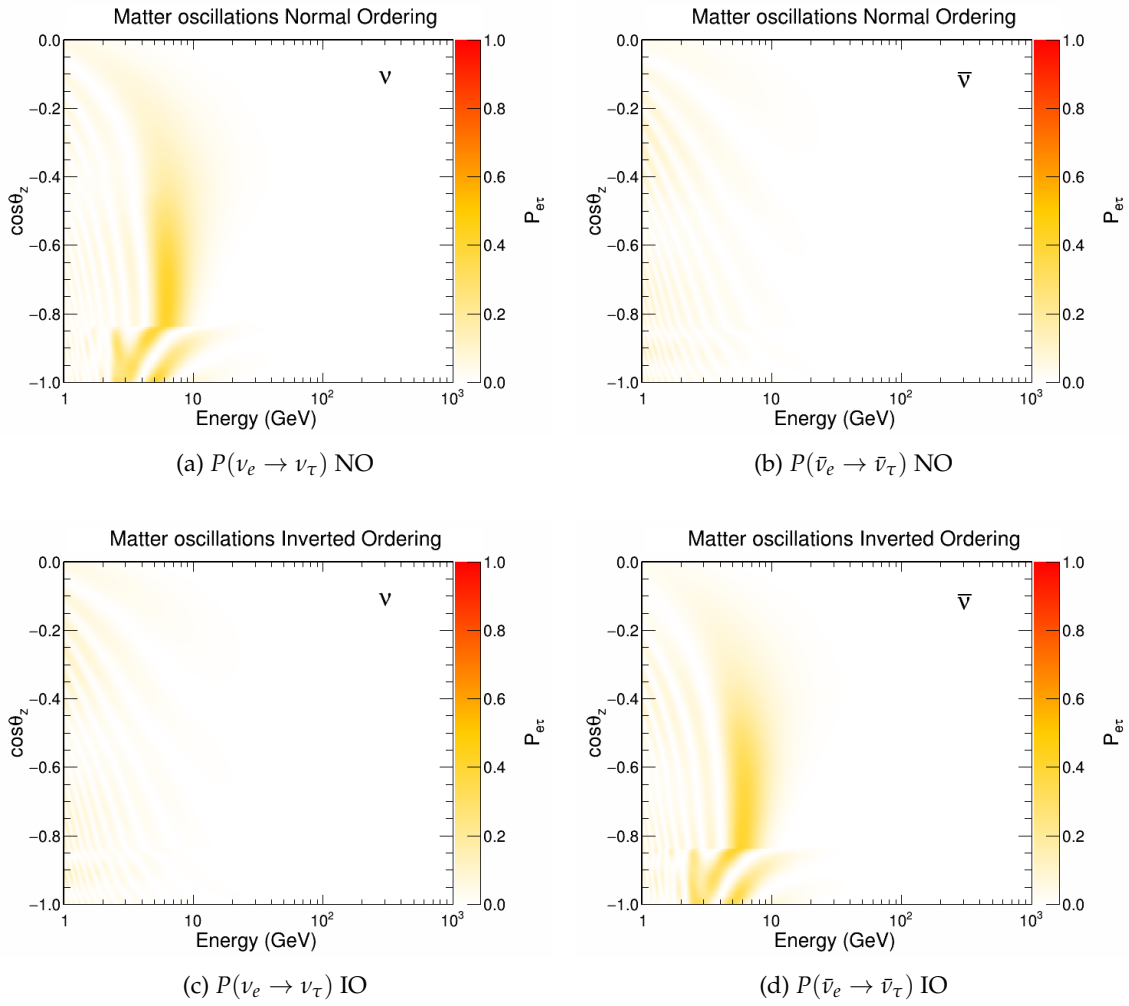
Figure 7: $P(\nu_e \to \nu_\tau)$ (left) and $P(\bar{\nu}_e \to \bar{\nu}_\tau)$ (right) transition probabilities in Earth's matter for normal (top) and inverted (bottom) ordering as a function of the neutrino true energy and $\cos(\theta_z)$.
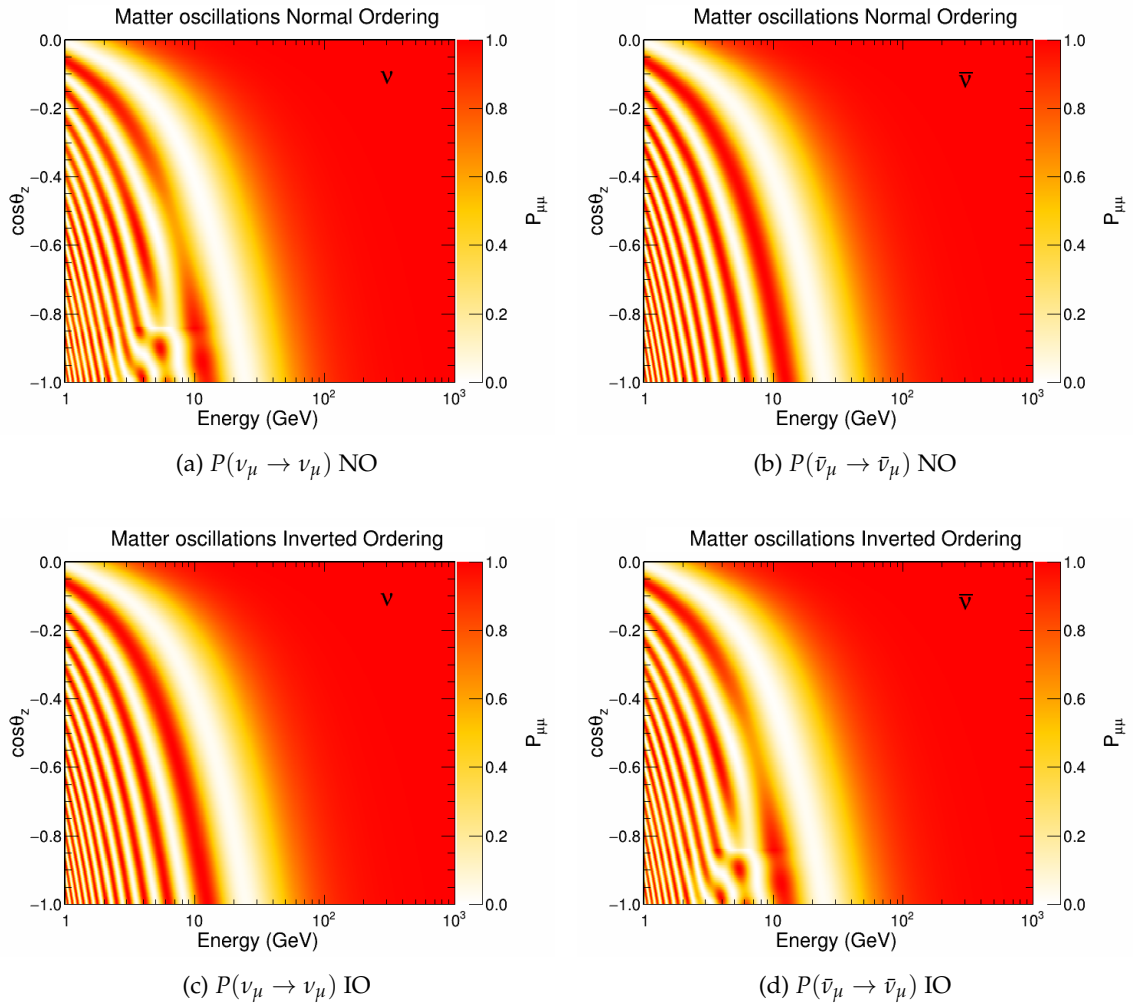
Figure 8: $P(\nu_\mu \to \nu_\mu)$ (left) and $P(\bar{\nu}_\mu \to \bar{\nu}_\mu)$ (right) survival probabilities in Earth's matter for normal (top) and inverted (bottom) ordering as a function of the neutrino true energy and $\cos(\theta_z)$.

(a) $P(\nu_\mu \to \nu_e)$ NO

(b) $P(\bar{\nu}_\mu \to \bar{\nu}_e)$ NO

(c) $P(\nu_\mu \to \nu_e)$ IO

(d) $P(\bar{\nu}_\mu \to \bar{\nu}_e)$ IO
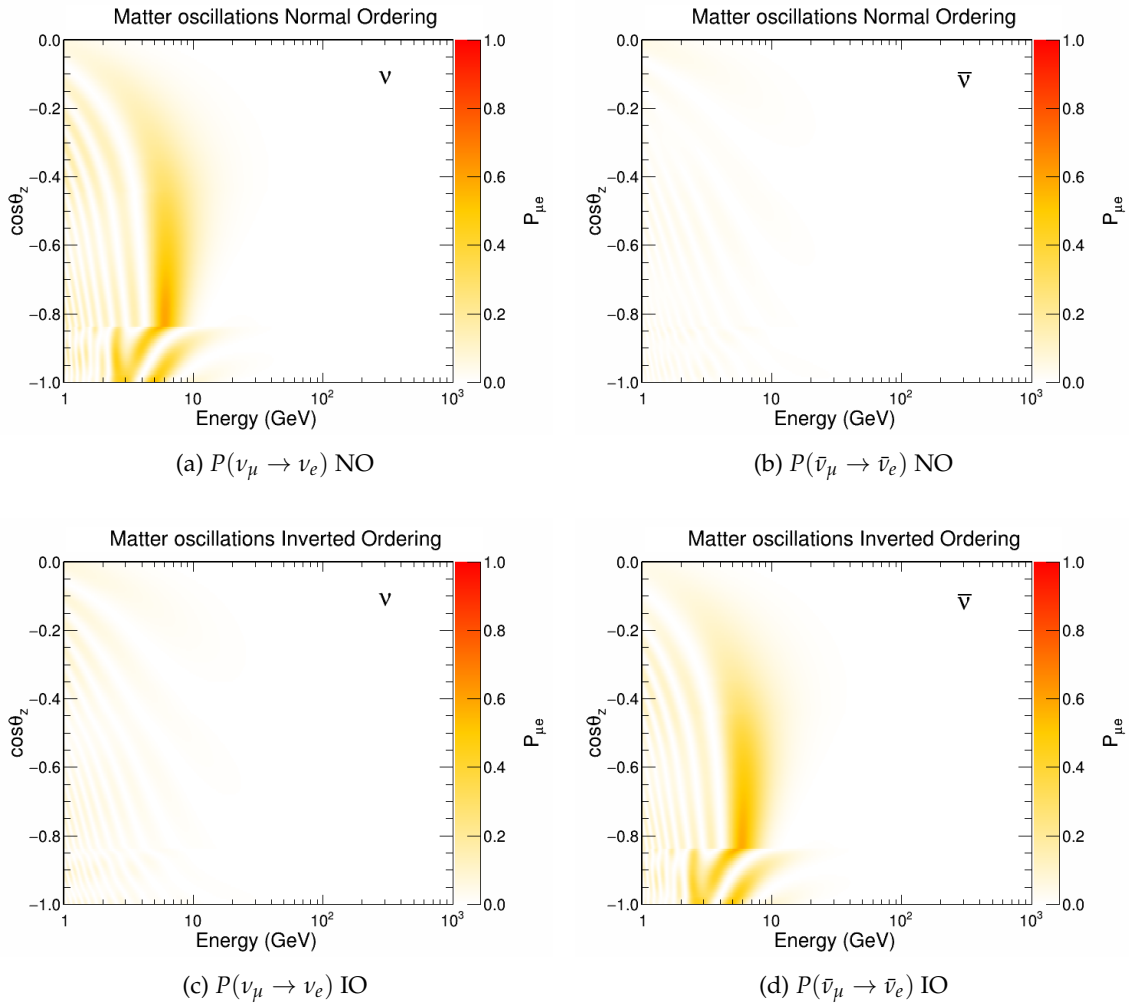
Figure 9: $P(\nu_\mu \to \nu_e)$ (left) and $P(\bar{\nu}_\mu \to \bar{\nu}_e)$ (right) transition probabilities in Earth's matter for normal (top) and inverted (bottom) ordering as a function of the neutrino true energy and $\cos(\theta_z)$.

(a) $P(\nu_\mu \to \nu_\tau)$ NO

(b) $P(\bar{\nu}_\mu \to \bar{\nu}_\tau)$ NO

(c) $P(\nu_\mu \to \nu_\tau)$ IO

(d) $P(\bar{\nu}_\mu \to \bar{\nu}_\tau)$ IO
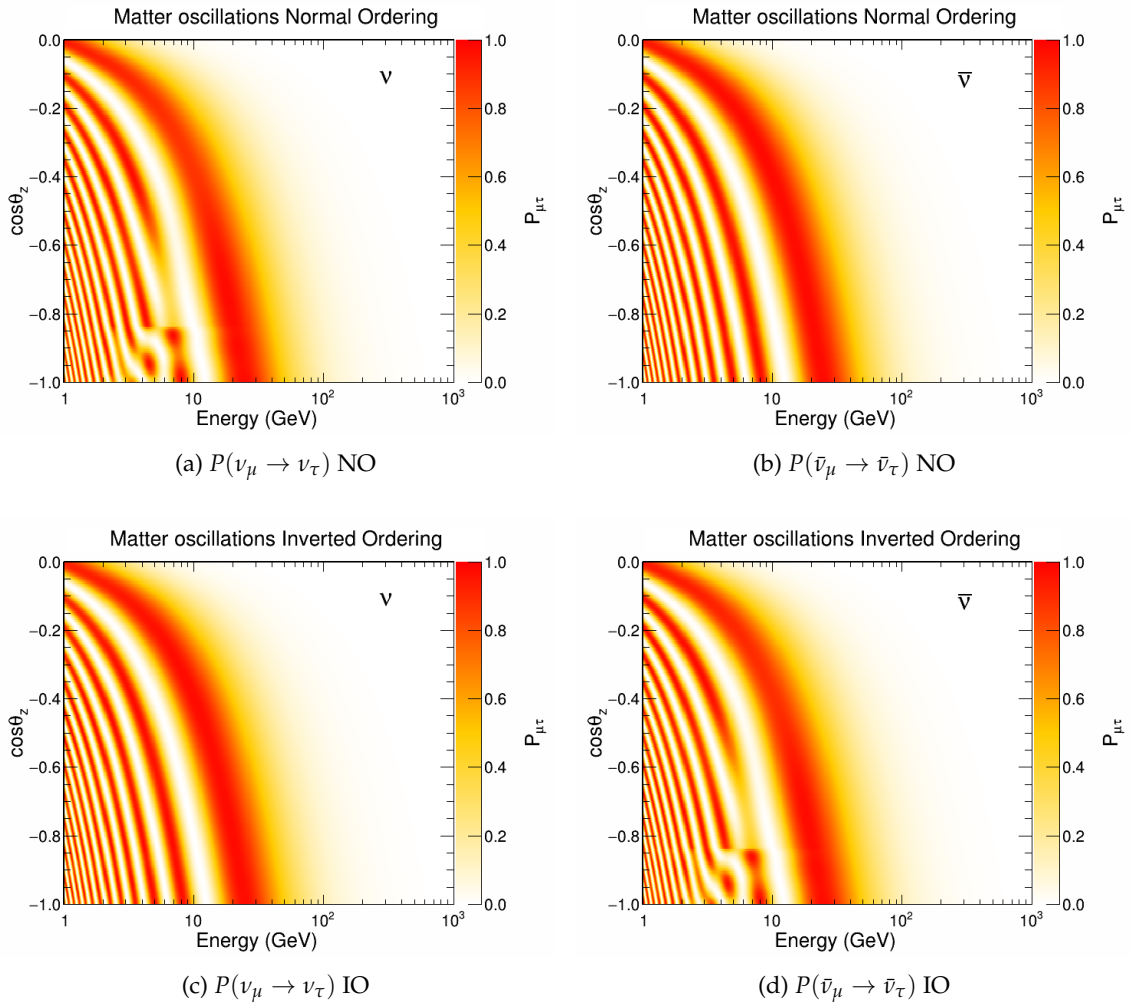
Figure 10: $P(\nu_\mu \to \nu_\tau)$ (left) and $P(\bar{\nu}_\mu \to \bar{\nu}_\tau)$ (right) transition probabilities in Earth's matter for normal (top) and inverted (bottom) ordering as a function of the neutrino true energy and $\cos(\theta_z)$.

B.3 Oscillograms with NSI

In this section, only the $\nu_\mu(\bar{\nu}_\mu)$ survival probabilities are shown as this is the most important channel for the NSI measurements with the ORCA6 configuration of the KM3NeT/ORCA detector. Only a single NSI parameter at the time is set to a non-zero value. The values of the NSI parameters are large (already excluded by current limits) in order to make the effect on the oscillation patterns clearly visible.

Flavour violating $\epsilon_{\mu\tau}$

Figures 11 and 12 show the $\nu_\mu(\bar{\nu}_\mu)$ survival probabilities for $\epsilon_{\mu\tau} \pm 0.02$. As can be seen, above the standard matter resonance ($E_\nu > 20\,\text{GeV}$) the probabilities are invariant under the simultaneous change in two of the following terms in the equation: the mass ordering, $\epsilon_{\mu\tau} \to -\epsilon_{\mu\tau}$ and $\nu \to \bar{\nu}$.

(a) $P(\nu_\mu \to \nu_\mu)$ NO $+ \epsilon_{\mu\tau} = -0.02$

(b) $P(\bar{\nu}_\mu \to \bar{\nu}_\mu)$ NO $+ \epsilon_{\mu\tau} = -0.02$

(c) $P(\nu_\mu \to \nu_\mu)$ IO $+ \epsilon_{\mu\tau} = -0.02$

(d) $P(\bar{\nu}_\mu \to \bar{\nu}_\mu)$ IO $+ \epsilon_{\mu\tau} = -0.02$
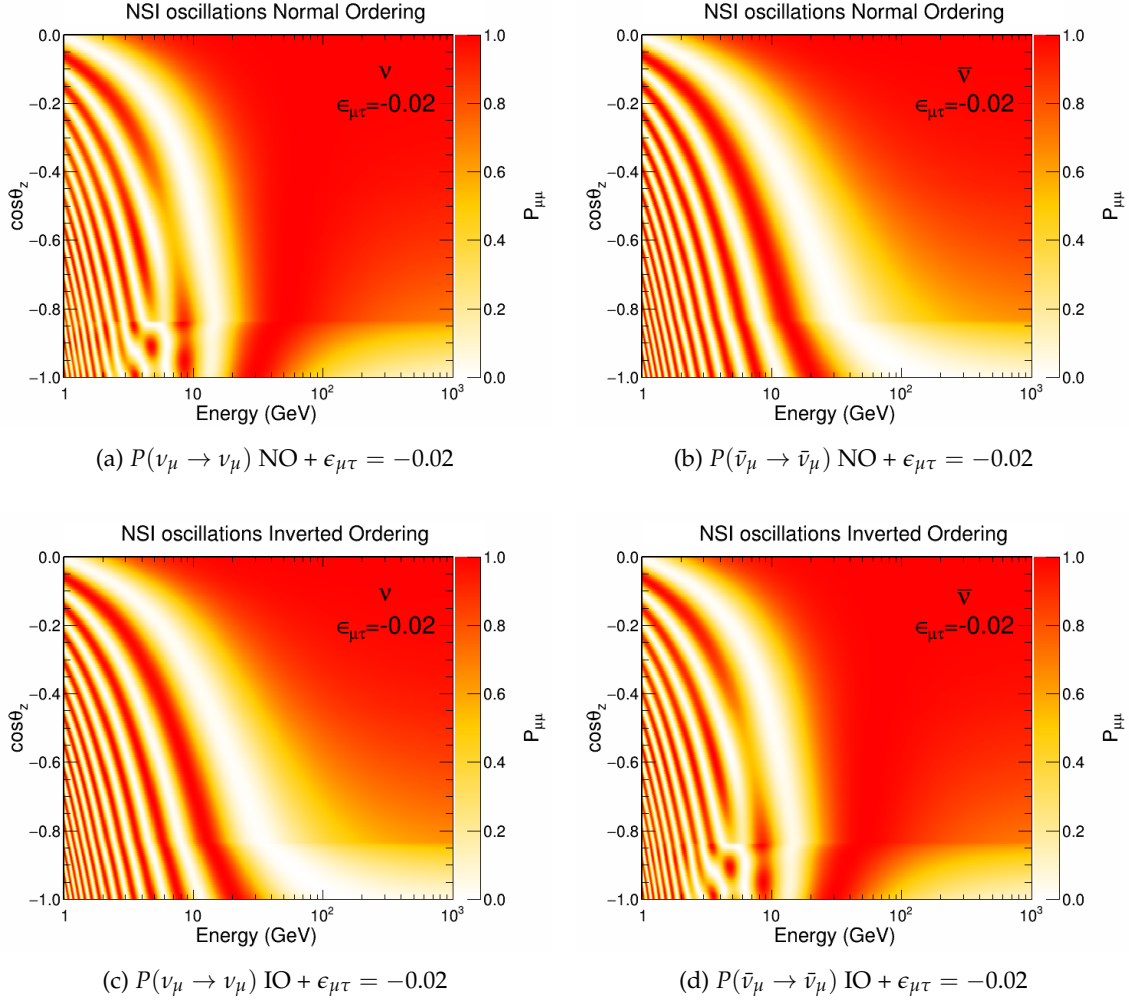
Figure 11: $P(\nu_\mu \to \nu_\mu)$ (left) and $P(\bar{\nu}_\mu \to \bar{\nu}_\mu)$ (right) survival probabilities in Earth's matter with NSI parameter $\epsilon_{\mu\tau} = -0.02$ for normal (top) and inverted (bottom) ordering as a function of the neutrino true energy and $\cos(\theta_z)$.

(a) $P(\nu_\mu \to \nu_\mu)$ NO $+ \epsilon_{\mu\tau} = 0.02$

(b) $P(\bar{\nu}_\mu \to \bar{\nu}_\mu)$ NO $+ \epsilon_{\mu\tau} = 0.02$

(c) $P(\nu_\mu \to \nu_\mu)$ IO $+ \epsilon_{\mu\tau} = 0.02$

(d) $P(\bar{\nu}_\mu \to \bar{\nu}_\mu)$ NO $+ \epsilon_{\mu\tau} = 0.02$
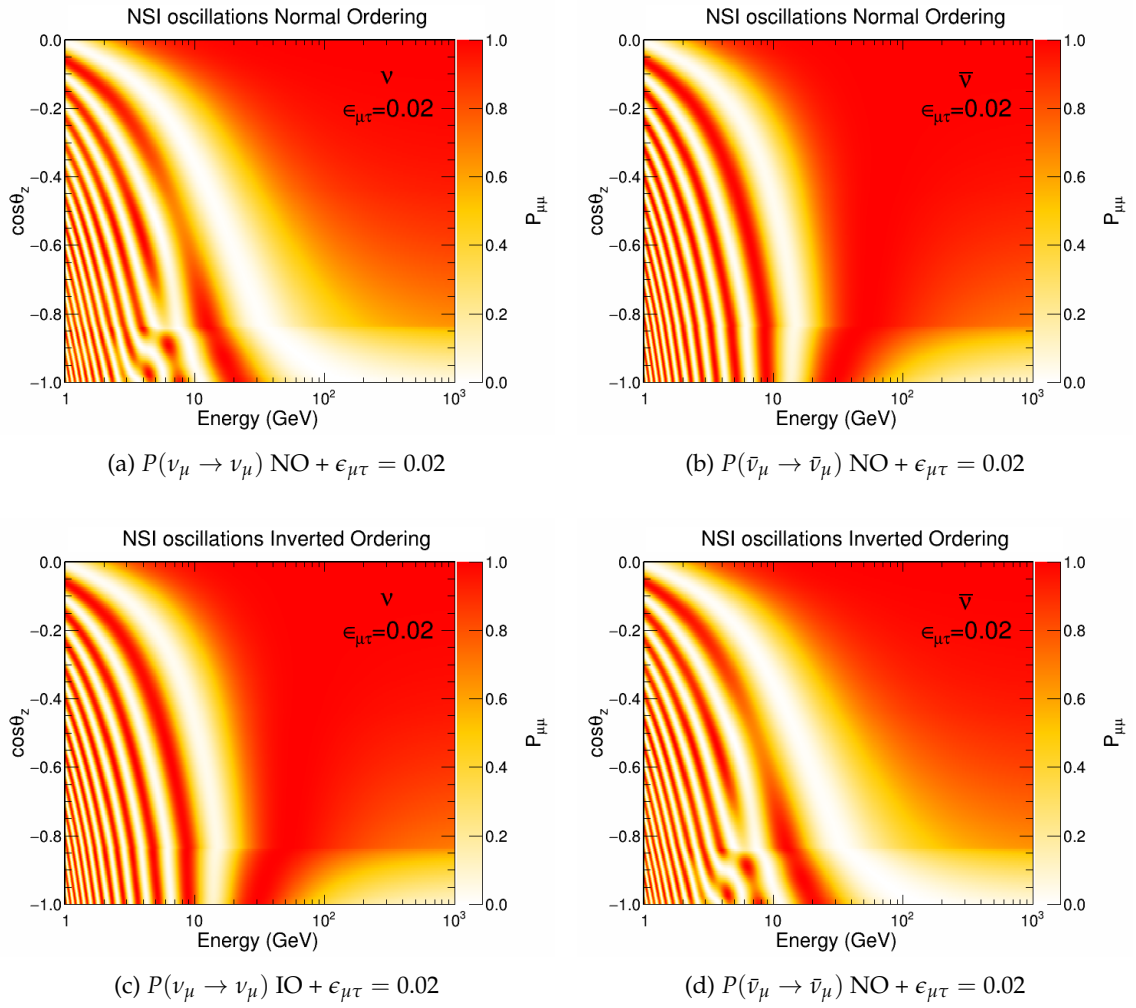
Figure 12: $P(\nu_\mu \to \nu_\mu)$ (left) and $P(\bar{\nu}_\mu \to \bar{\nu}_\mu)$ (right) survival probabilities in Earth's matter with NSI parameter $\epsilon_{\mu\tau} = 0.02$ for normal (top) and inverted (bottom) ordering as a function of the neutrino true energy and $\cos(\theta_z)$.

Appendix B. Oscillograms

Flavour violating $\epsilon_{e\tau}$

Figures 13 and 14 show $\nu_\mu(\bar{\nu}_\mu)$ survival probabilities for $\epsilon_{e\tau} \pm 0.15$.

(a) $P(\nu_\mu \to \nu_\mu)$ NO $+ \epsilon_{e\tau} = -0.15$

(b) $P(\bar{\nu}_\mu \to \bar{\nu}_\mu)$ NO $+ \epsilon_{e\tau} = -0.15$

(c) $P(\nu_\mu \to \nu_\mu)$ IO $+ \epsilon_{e\tau} = -0.15$

(d) $P(\bar{\nu}_\mu \to \bar{\nu}_\mu$ IO $+ \epsilon_{e\tau} = -0.15$
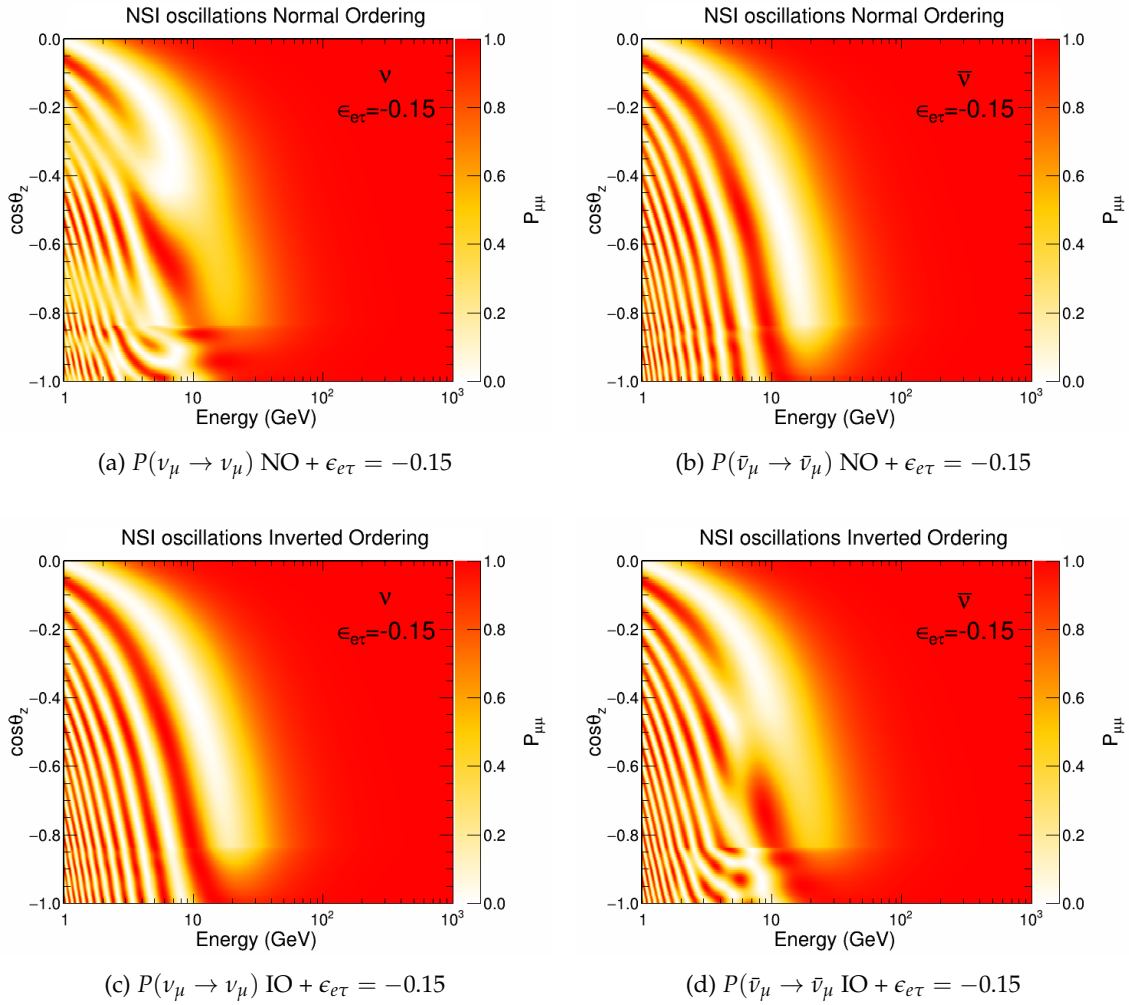
Figure 13: $P(\nu_\mu \to \nu_\mu)$ and $P(\bar{\nu}_\mu \to \bar{\nu}_\mu)$ survival probabilities in Earth's matter with NSI parameter $\epsilon_{e\tau} = -0.15$ for normal and inverted ordering as a function of the neutrino true energy and $\cos(\theta_z)$.

(a) $P(\nu_\mu \to \nu_\mu)$ NO $+ \epsilon_{e\tau} = 0.15$

(b) $P(\bar{\nu}_\mu \to \bar{\nu}_\mu)$ NO $+ \epsilon_{e\tau} = 0.15$

(c) $P(\nu_\mu \to \nu_\mu)$ IO $+ \epsilon_{e\tau} = 0.15$

(d) $P(\bar{\nu}_\mu \to \bar{\nu}_\mu)$ IO $+ \epsilon_{e\tau} = 0.15$
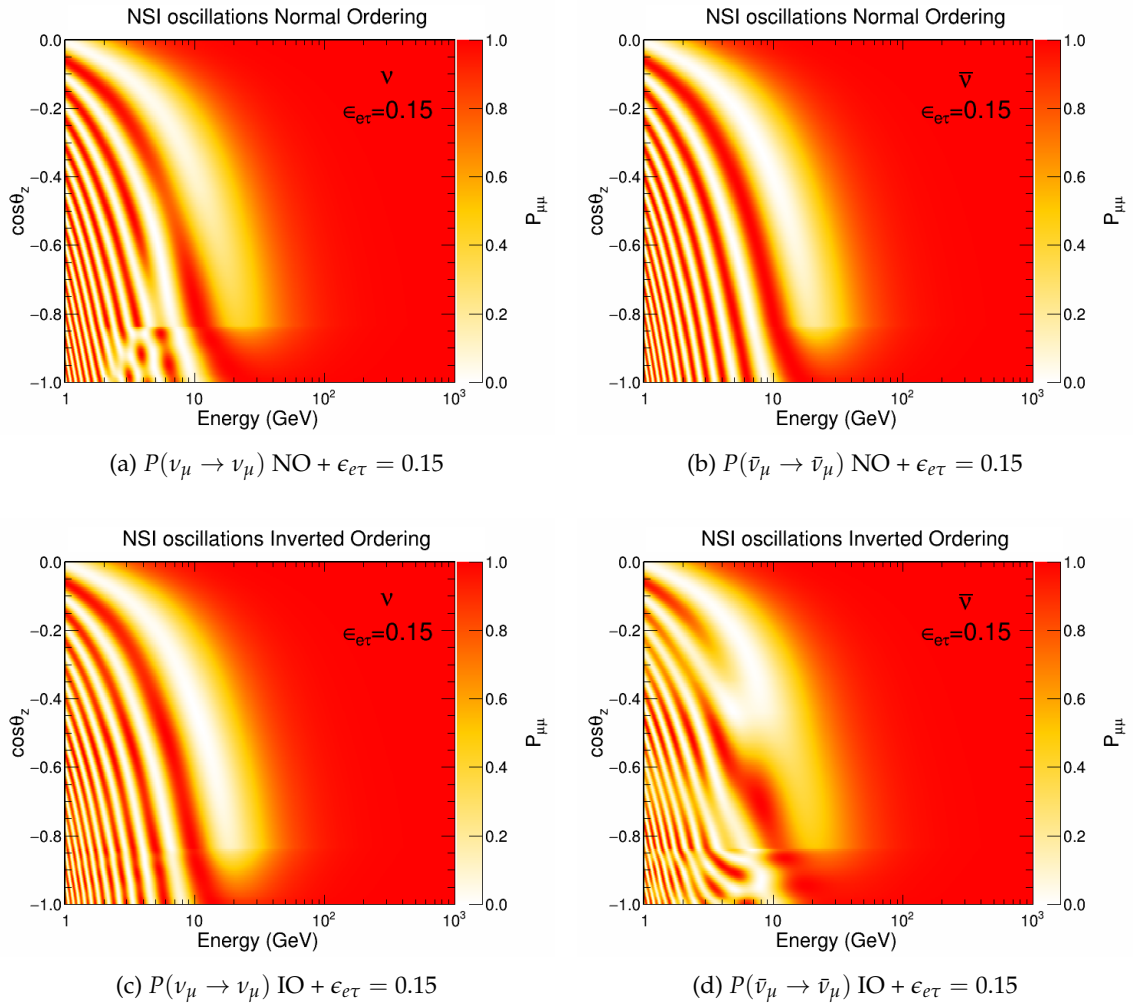
Figure 14: $P(\nu_\mu \to \nu_\mu)$ and $P(\bar{\nu}_\mu \to \bar{\nu}_\mu)$ survival probabilities in Earth's matter with NSI parameter $\epsilon_{e\tau} = 0.15$ for normal and inverted ordering as a function of the neutrino true energy and $\cos(\theta_z)$.

Flavour violating $\epsilon_{e\mu}$

Figures 15 and 16 show $\nu_\mu(\bar{\nu}_\mu)$ survival probabilities for $\epsilon_{e\mu} \pm 0.08$.

(a) $P(\nu_\mu \to \nu_\mu)$ NO $+ \epsilon_{e\mu} = -0.08$ (b) $P(\bar{\nu}_\mu \to \bar{\nu}_\mu)$ NO $+ \epsilon_{e\mu} = -0.08$

(c) $P(\nu_\mu \to \nu_\mu)$ IO $+ \epsilon_{e\mu} = -0.08$ (d) $P(\bar{\nu}_\mu \to \bar{\nu}_\mu)$ IO $+ \epsilon_{e\mu} = -0.08$
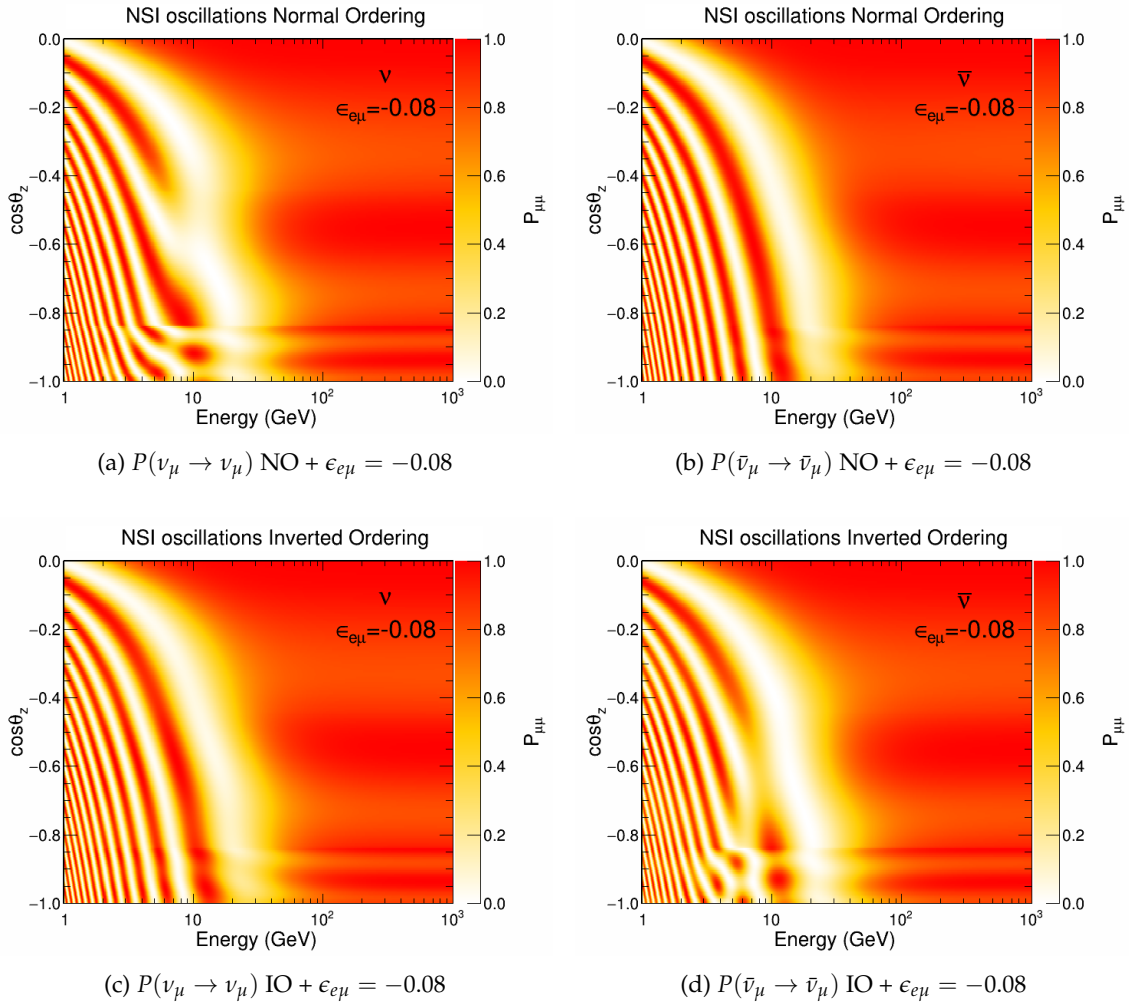
Figure 15: $P(\nu_\mu \to \nu_\mu)$ and $P(\bar{\nu}_\mu \to \bar{\nu}_\mu)$ survival probabilities in Earth's matter with NSI parameter $\epsilon_{e\mu} = -0.08$ for normal and inverted ordering as a function of the neutrino true energy and $\cos(\theta_z)$.

(a) $P(\nu_\mu \rightarrow \nu_\mu)$ NO + $\epsilon_{e\mu} = 0.08$

(b) $P(\bar{\nu}_\mu \rightarrow \bar{\nu}_\mu)$ NO + $\epsilon_{e\mu} = 0.08$

(c) $P(\nu_\mu \rightarrow \nu_\mu)$ IO + $\epsilon_{e\mu} = 0.08$

(d) $P(\bar{\nu}_\mu \rightarrow \bar{\nu}_\mu)$ IO + $\epsilon_{e\mu} = 0.08$
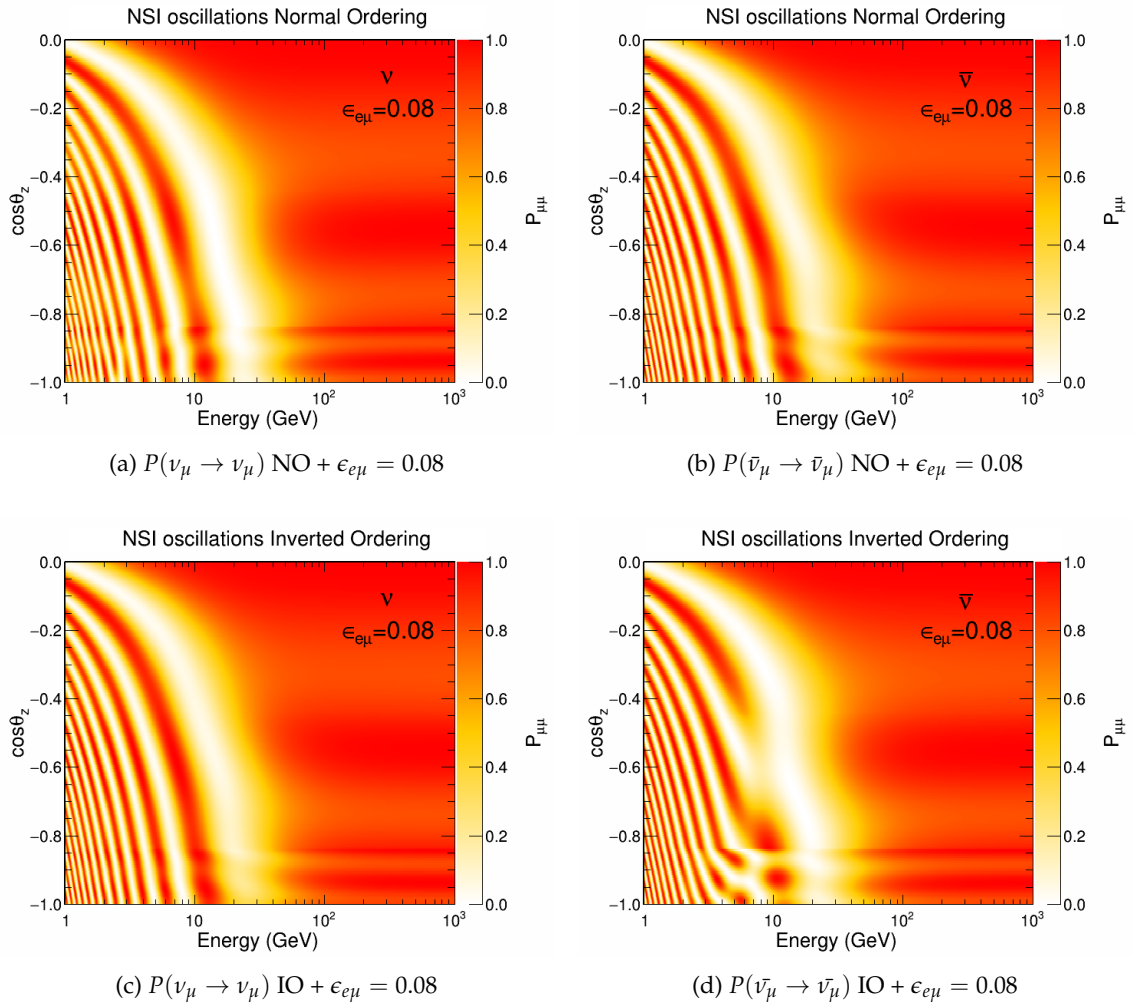
Figure 16: $P(\nu_\mu \rightarrow \nu_\mu)$ and $P(\bar{\nu}_\mu \rightarrow \bar{\nu}_\mu)$ survival probabilities in Earth's matter with NSI parameter $\epsilon_{e\tau} = 0.08$ for normal and inverted ordering as a function of the neutrino true energy and $\cos(\theta_z)$.

Flavour non-universal $\epsilon_{\tau\tau} - \epsilon_{\mu\mu}$

Figures 17 and 18 show $\nu_\mu(\bar{\nu}_\mu)$ survival probabilities for $\epsilon_{\tau\tau} - \epsilon_{\mu\mu} \pm 0.03$.

(a) $P(\nu_\mu \to \nu_\mu)$ NO $+ \epsilon_{\tau\tau} - \epsilon_{\mu\mu} = -0.03$

(b) $P(\bar{\nu}_\mu \to \bar{\nu}_\mu)$ NO $+ \epsilon_{\tau\tau} - \epsilon_{\mu\mu} = -0.03$

(c) $P(\nu_\mu \to \nu_\mu)$ IO $+ \epsilon_{\tau\tau} - \epsilon_{\mu\mu} = -0.03$

(d) $P(\bar{\nu}_\mu \to \bar{\nu}_\mu)$ IO $+ \epsilon_{\tau\tau} - \epsilon_{\mu\mu} = -0.03$
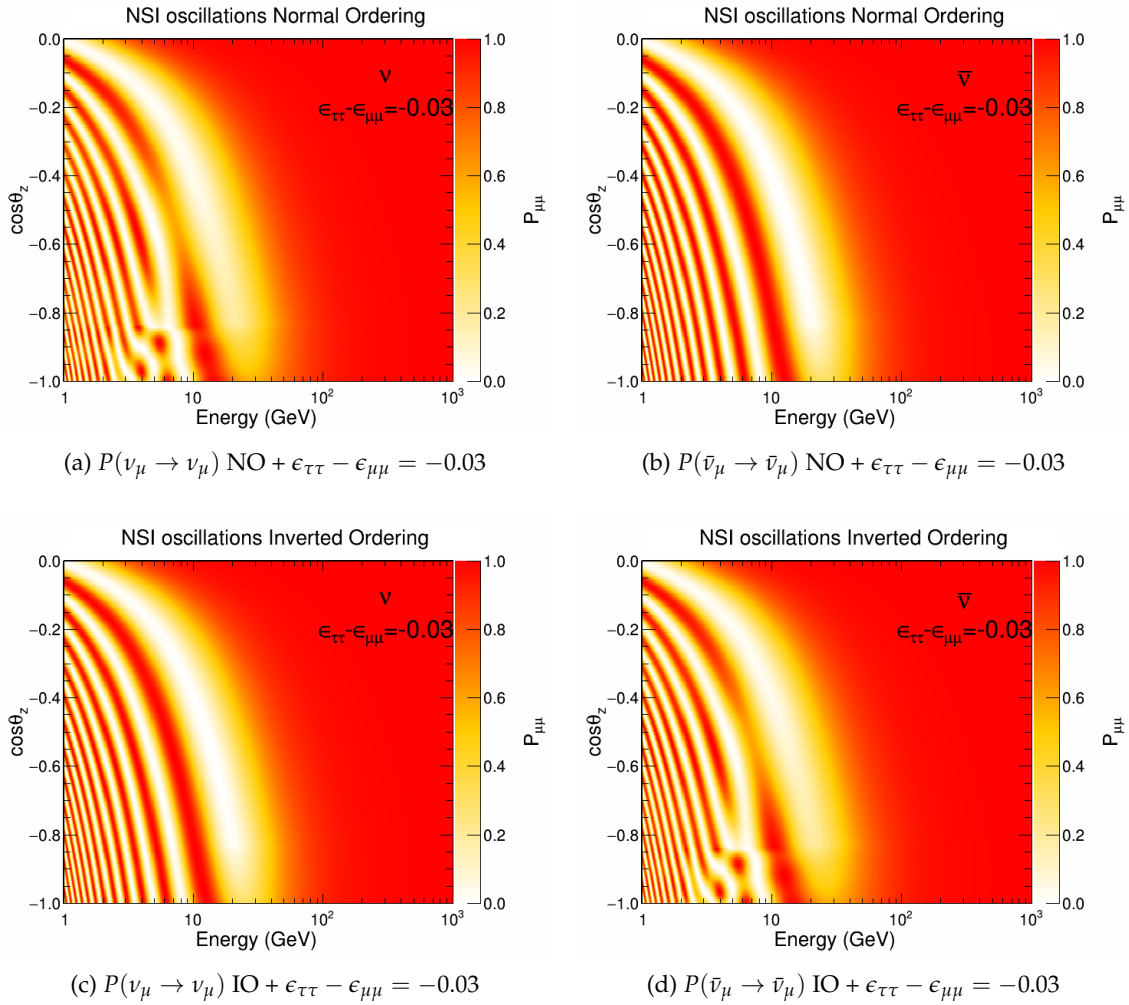
Figure 17: $P(\nu_\mu \to \nu_\mu)$ and $P(\bar{\nu}_\mu \to \bar{\nu}_\mu)$ survival probabilities in Earth's matter with NSI parameter $\epsilon_{\tau\tau} - \epsilon_{\mu\mu} = -0.03$ for normal and inverted ordering as a function of the neutrino true energy and $\cos(\theta_z)$.

(a) $P(\nu_\mu \rightarrow \nu_\mu)$ NO $+ \epsilon_{\tau\tau} - \epsilon_{\mu\mu} = 0.03$

(b) $P(\bar{\nu}_\mu \rightarrow \bar{\nu}_\mu)$ NO $+ \epsilon_{\tau\tau} - \epsilon_{\mu\mu} = 0.03$

(c) $P(\nu_\mu \rightarrow \nu_\mu)$ IO $+ \epsilon_{\tau\tau} - \epsilon_{\mu\mu} = 0.03$

(d) $P(\bar{\nu}_\mu \rightarrow \bar{\nu}_\mu)$ IO $+ \epsilon_{\tau\tau} - \epsilon_{\mu\mu} = 0.03$
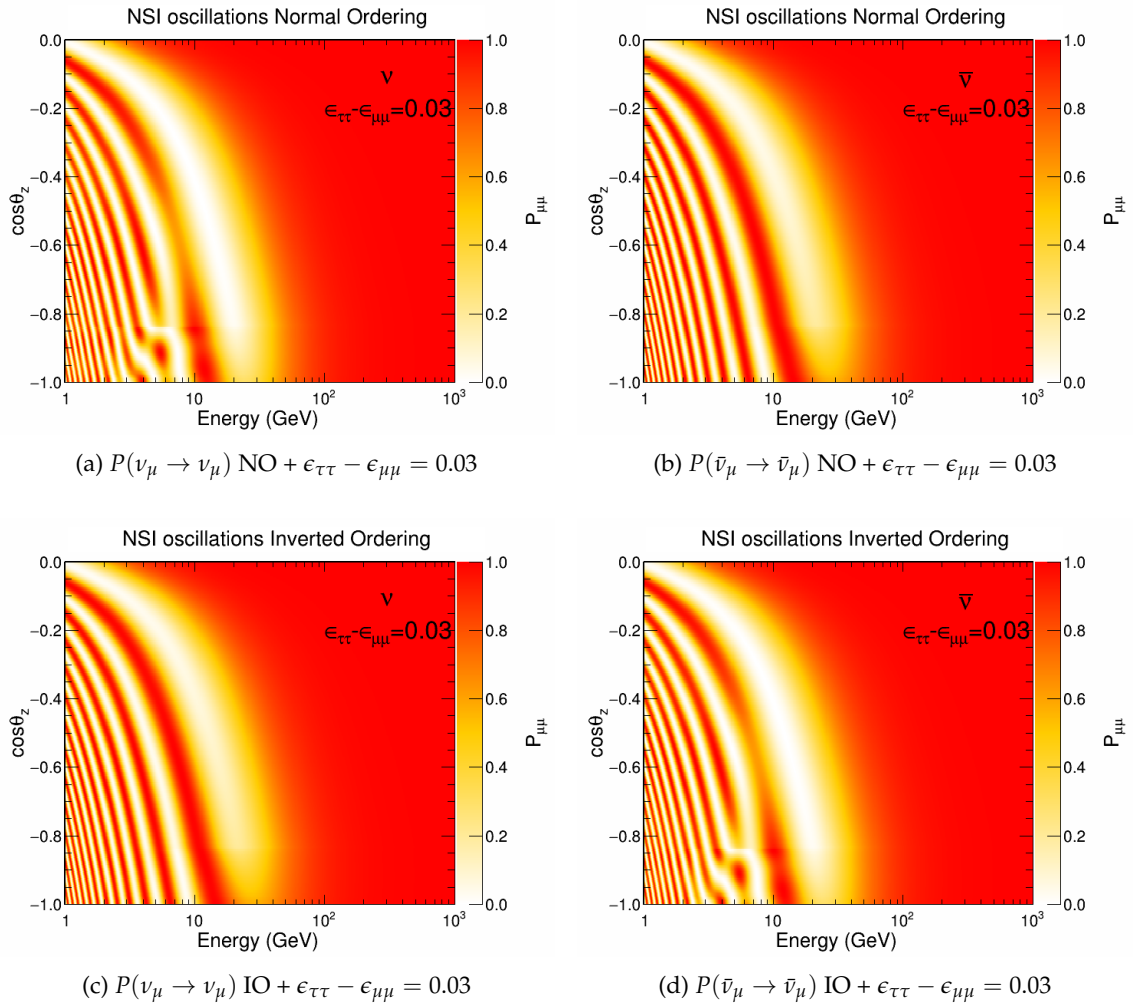
Figure 18: $P(\nu_\mu \rightarrow \nu_\mu)$ and $P(\bar{\nu}_\mu \rightarrow \bar{\nu}_\mu)$ survival probabilities in Earth's matter with NSI parameter $\epsilon_{\tau\tau} - \epsilon_{\mu\mu} = 0.03$ for normal and inverted ordering as a function of the neutrino true energy and $\cos(\theta_z)$.

B.4   Full picture versus two flavour approximation

Figure 19 shows the comparison between the 2-flavour approximation from Section 1.2.4 and the full 3-flavour probability calculation. As can be seen, the analytical formulas presented in Section 1.2.4 accurately describe the expected impact of NSI if the low neutrino energies, $E_\nu < 20$ GeV, are not considered. If we restrict the phase space only to the Earth Core crossing directions, where most of the matter is present on the neutrino path ($\cos\theta_z > -0.84$), then the energy threshold for a good approximation of the 2-flavour model can be lowered to $E_\nu > 10$ GeV.

(a) 2-flavour approximation $\epsilon_{\mu\tau} \neq 0$

(b) 3-flavour model $\epsilon_{\mu\tau} \neq 0$

(c) 2-flavour approximation $\epsilon' \neq 0$
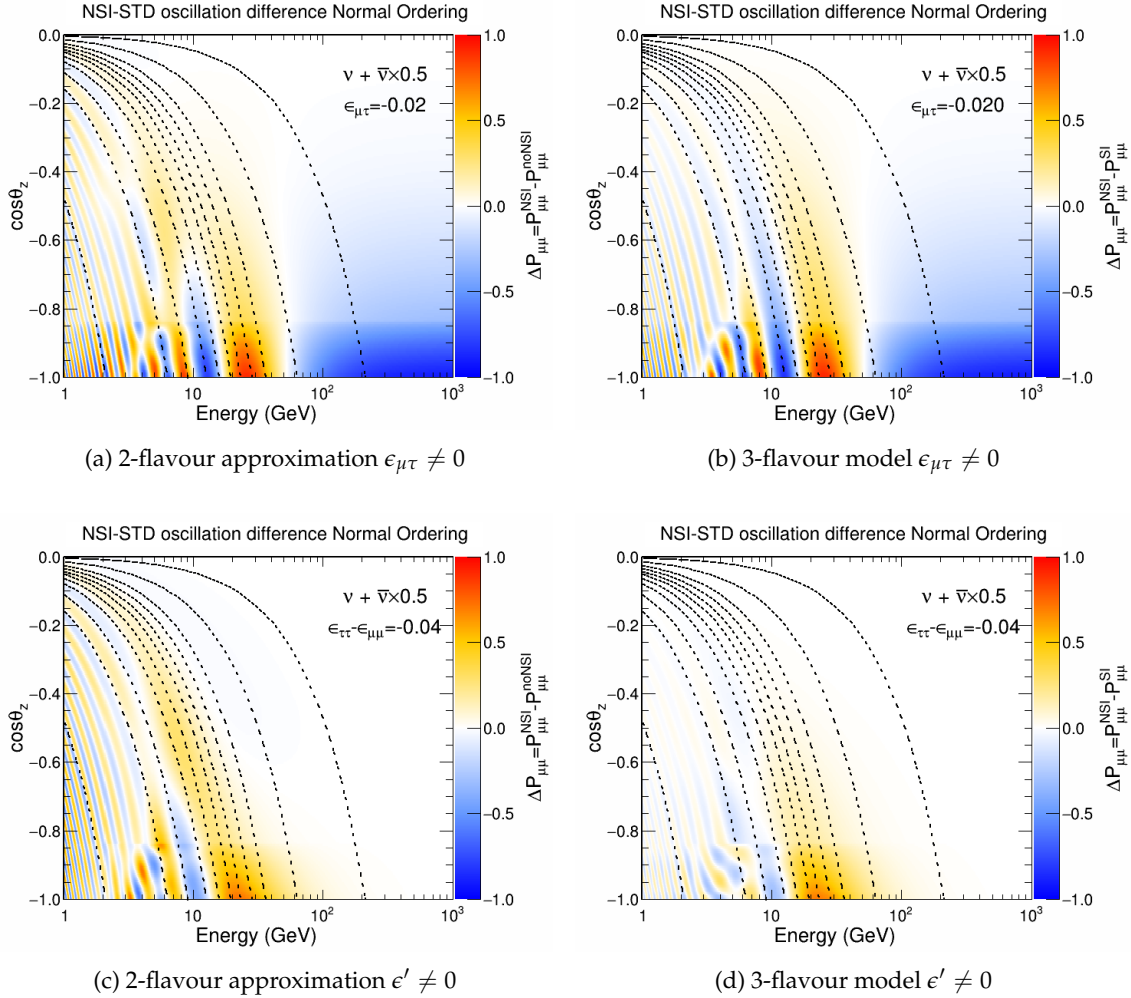
(d) 3-flavour model $\epsilon' \neq 0$

Figure 19: Comparison between the $\mu - \tau$ 2-flavour approximation model presented in section 1.2.4 and the full 3-flavour model.

List of Figures

List of Tables

Bibliography

[1] James Chadwick. "Intensitatsverteilung im magnetischen spektrum der beta-strahlen von radium B+C". In: *Verhandlungen der deutschen Physikalischen Gesellschaft* 16 (1914).
(Cited on p: 3.).

[2] Charles Drummond Ellis and W. A Wooster. "The average energy of disintegration of radium E". In: *Proc. Roy. Soc. Lond. A* 117.776 (1927), pp. 109–123.
(Cited on p: 3.).
DOI: 10.1098/rspa.1927.0168.

[3] Enrico Fermi. "Tentativo di una teoria dell'emissione dei raggi beta". In: *Ric. Sci.* 4 (1933), pp. 491–495.
(Cited on p: 4.).

[4] C. L. Cowan et al. "Detection of the free neutrino: A Confirmation". In: *Science* 124 (1956), pp. 103–104.
(Cited on p: 4.).
DOI: 10.1126/science.124.3212.103.

[5] G. Danby et al. "Observation of High-Energy Neutrino Reactions and the Existence of Two Kinds of Neutrinos". In: *Phys. Rev. Lett.* 9 (1962), p. 36.
(Cited on p: 4.).
DOI: 10.1103/PhysRevLett.9.36.

[6] Raymond Davis Jr., Don S. Harmer, and Kenneth C. Hoffman. "Search for neutrinos from the sun". In: *Phys. Rev. Lett.* 20 (1968), pp. 1205–1209.
(Cited on p: 4.).
DOI: 10.1103/PhysRevLett.20.1205.

[7] Q. R. Ahmad et al. "Measurement of the rate of $\nu_e + d \rightarrow p + p + e^-$ interactions produced by ^{8}B solar neutrinos at the Sudbury Neutrino Observatory". In: *Phys. Rev. Lett.* 87 (2001), p. 071301.
(Cited on p: 4.).
DOI: 10.1103/PhysRevLett.87.071301.
arXiv: nucl-ex/0106015.

[8] Y. Fukuda et al. "Evidence for oscillation of atmospheric neutrinos". In: *Phys. Rev. Lett.* 81 (1998), pp. 1562–1567.
(Cited on p: 4.).
DOI: 10.1103/PhysRevLett.81.1562.
arXiv: hep-ex/9807003.

[9] Salvatore Mele. "The Measurement of the Number of Light Neutrino Species at LEP". In: *Adv. Ser. Direct. High Energy Phys.* 23 (2015), pp. 89–106.
(Cited on p: 4.).
DOI: 10.1142/9789814644150_0004.

[10] K. Kodama et al. "Observation of tau neutrino interactions". In: *Phys. Lett. B* 504 (2001), pp. 218–224.
(Cited on p: 4.).
DOI: 10.1016/S0370-2693(01)00307-0.
arXiv: hep-ex/0012035.

[11] M. Goldhaber, L. Grodzins, and A. W. Sunyar. "Helicity of Neutrinos". In: *Phys. Rev.* 109 (3 Feb. 1958), pp. 1015–1017.
(Cited on p: 5.).
DOI: 10.1103/PhysRev.109.1015.
URL: https://link.aps.org/doi/10.1103/PhysRev.109.1015.

[12] S. Weinberg. "A Model of Leptons". In: *Phys. Rev. Lett.* 19 (Nov. 1967).
(Cited on p: 5.).
DOI: 10.1103/PhysRevLett.19.1264.

[13] S. L. Glashow. "Partial Symmetries of Weak Interactions". In: *Nucl. Phys.* 22 (1961), p. 579.
(Cited on p: 5.).
DOI: 10.1016/0029-5582(61)90469-2.

[14] A. Salam and J. C. Ward. "Electromagnetic and weak interactions". In: *Phys. Lett.* 13 (1964), p. 168.
(Cited on p: 5.).
DOI: 10.1016/0031-9163(64)90711-5.

[15] F. Englert and R. Brout. "Broken Symmetry and the Mass of Gauge Vector Mesons". In: *Phys. Rev. Lett.* 13 (9 Aug. 1964), pp. 321–323.
(Cited on p: 5.).
DOI: 10.1103/PhysRevLett.13.321.
URL: https://link.aps.org/doi/10.1103/PhysRevLett.13.321.

[16] P. W. Higgs. "Broken Symmetries and the Masses of Gauge Bosons". In: *Phys. Rev. Lett.* 13 (Oct. 1964), p. 508.
(Cited on p: 5.).
DOI: 10.1103/PhysRevLett.13.508.

[17] G. Aad et al. "Observation of a new particle in the search for the Standard Model Higgs boson with the ATLAS detector at the LHC". In: *Physics Letters B* 716.1 (2012), pp. 1–29. ISSN: 0370-2693.
(Cited on p: 5.).
DOI: https://doi.org/10.1016/j.physletb.2012.08.020.
URL: https://www.sciencedirect.com/science/article/pii/S037026931200857X.

[18] S. Chatrchyan et al. "Observation of a new boson at a mass of 125 GeV with the CMS experiment at the LHC". In: *Physics Letters B* 716.1 (2012), pp. 30–61. ISSN:

0370-2693.
(Cited on p: 5.).
DOI: https://doi.org/10.1016/j.physletb.2012.08.021.
URL: https : / / www . sciencedirect . com / science / article / pii /
S0370269312008581.

[19]   D. H. Perkins. *Introduction to high energy physics*. 1982. ISBN: 978-0-521-62196-0.
(Cited on p: 6.).

[20]   P.A. Zyla et al. "Review of Particle Physics". In: *PTEP* 2020.8 (2020), p. 083C01.
(Cited on pp: 8–10, 26, 52, 98, 100.).
DOI: 10.1093/ptep/ptaa104.

[21]   Jan T. Sobczyk. "Quasi-Elastic Neutrino Scattering - an Overwiew". In: *AIP Conf.
Proc.* 1405.1 (2011). Ed. by S. K. Singh et al., pp. 59–64.
(Cited on p: 9.).
DOI: 10.1063/1.3661558.
arXiv: 1108.0506 [hep-ph].

[22]   J. A. Formaggio and G. P. Zeller. "From eV to EeV: Neutrino cross sections across
energy scales". In: *Reviews of Modern Physics* 84.3 (Sept. 2012), p. 13071.
(Cited on pp: 9, 12.).
DOI: 10.1103/revmodphys.84.1307.

[23]   J. G. H. de Groot et al. "Inclusive Interactions of High-Energy Neutrinos and
anti-neutrinos in Iron". In: *Z. Phys. C* 1 (1979), p. 143.
(Cited on p: 11.).
DOI: 10.1007/BF01445406.

[24]   F. Halzen and Alan D. Martin. *QUARKS AND LEPTONS: AN INTRODUCTORY
COURSE IN MODERN PARTICLE PHYSICS*. Jan. 1984. ISBN: 978-0-471-88741-6.
(Cited on p: 11.).

[25]   A. A. Aguilar-Arevalo et al. "Measurement of the Antineutrino Neutral-Current
Elastic Differential Cross Section". In: *Phys. Rev. D* 91.1 (2015), p. 012004.
(Cited on p: 11.).
DOI: 10.1103/PhysRevD.91.012004.
arXiv: 1309.7257 [hep-ex].

[26]   Raj Gandhi et al. "Ultrahigh-energy neutrino interactions". In: *Astropart. Phys.* 5
(1996), pp. 81–110.
(Cited on p: 11.).
DOI: 10.1016/0927-6505(96)00008-4.
arXiv: hep-ph/9512364.

[27]   Raj Gandhi et al. "Neutrino interactions at ultrahigh-energies". In: *Phys. Rev. D* 58
(1998), p. 093009.
(Cited on p: 11.).
DOI: 10.1103/PhysRevD.58.093009.
arXiv: hep-ph/9807264.

[28]   Z. Li et al. "Measurement of the tau neutrino cross section in atmospheric neutrino oscillations with Super-Kamiokande". In: *Phys. Rev. D* 98.5 (2018), p. 052006.
(Cited on pp: 12, 107.).
DOI: 10.1103/PhysRevD.98.052006.
arXiv: 1711.09436 [hep-ex].

[29]   Hideyuki Takei. "Measurement of Neutrino-Nucleon Neutral-Current Elastic Scattering Cross-section at SciBooNE". PhD thesis. Feb. 2009.
(Cited on pp: 12, 107.).
DOI: 10.2172/957570.
URL: https://www.osti.gov/biblio/957570.

[30]   Kevin McFarland. *Neutrino Interactions*. 2008.
(Cited on p: 12.).
arXiv: 0804.3899 [hep-ex].

[31]   C. Andreopoulos et al. "The GENIE Neutrino Monte Carlo Generator". In: *Nucl. Instrum. Meth. A* 614 (2010), pp. 87–104.
(Cited on p: 12.).
DOI: 10.1016/j.nima.2009.12.009.
arXiv: 0905.2517 [hep-ph].

[32]   Simon Bourret. "Neutrino oscillations and earth tomography with KM3NeT-ORCA". PhD thesis. APC, Paris, 2018.
(Cited on pp: 12, 73.).
URL: https://hal.in2p3.fr/tel-02491394/.

[33]   L. Wolfenstein. "Neutrino Oscillations in Matter". In: *Phys. Rev. D* 17 (1978), pp. 2369–2374.
(Cited on pp: 12, 16.).
DOI: 10.1103/PhysRevD.17.2369.

[34]   Y. Farzan and M. Tortola. "Neutrino oscillations and Non-Standard Interactions". In: *Front. in Phys.* 6 (2018), p. 10.
(Cited on p: 13.).
DOI: 10.3389/fphy.2018.00010.
arXiv: 1710.09360 [hep-ph].

[35]   Tommy Ohlsson. "Status of non-standard neutrino interactions". In: *Reports on Progress in Physics* 76.4 (Mar. 2013), p. 044201.
(Cited on p: 13.).
DOI: 10.1088/0034-4885/76/4/044201.
URL: https://doi.org/10.1088/0034-4885/76/4/044201.

[36]   O. G. Miranda and H. Nunokawa. "Non standard neutrino interactions: current status and future prospects". In: *New J. Phys.* 17.9 (2015), p. 095002.
(Cited on p: 13.).
DOI: 10.1088/1367-2630/17/9/095002.
arXiv: 1505.06254 [hep-ph].

[37]   C. Biggio, M. Blennow, and E. Fernández-Martínez. "General bounds on non-standard neutrino interactions". In: *JHEP* 2009.08 (Aug. 2009), p. 090.
(Cited on p: 13.).
DOI: 10.1088/1126-6708/2009/08/090.

[38] Sanjib Kumar Agarwalla et al. "Probing Non-Standard Interactions at Daya Bay".
In: *JHEP* 07 (2015), p. 060.
(Cited on p: 13.).
DOI: 10.1007/JHEP07(2015)060.
arXiv: 1412.1064 [hep-ph].

[39] Chong Xing Yue and Xue Jia Cheng. "Constraints on the charged-current
non-standard neutrino interactions induced by the gauge boson W". In: *Nuclear
Physics B* 963 (2021), p. 115280. ISSN: 0550-3213.
(Cited on p: 13.).
DOI: https://doi.org/10.1016/j.nuclphysb.2020.115280.
URL: https : / / www . sciencedirect . com / science / article / pii /
S0550321320303655.

[40] Ziro Maki, Masami Nakagawa, and Shoichi Sakata. "Remarks on the Unified
Model of Elementary Particles". In: *Progress of Theoretical Physics* 28.5 (Nov. 1962),
pp. 870–880. ISSN: 0033-068X.
(Cited on p: 14.).
DOI: 10.1143/PTP.28.870.
eprint: https://academic.oup.com/ptp/article-pdf/28/5/870/5258750/28-
5-870.pdf.
URL: https://doi.org/10.1143/PTP.28.870.

[41] C. Giunti. "Neutrino wave packets in quantum field theory". In: *JHEP* 11 (2002),
p. 017.
(Cited on p: 14.).
DOI: 10.1088/1126-6708/2002/11/017.
arXiv: hep-ph/0205014.

[42] Q. R. Ahmad et al. "Direct evidence for neutrino flavor transformation from
neutral current interactions in the Sudbury Neutrino Observatory". In: *Phys. Rev.
Lett.* 89 (2002), p. 011301.
(Cited on p: 15.).
DOI: 10.1103/PhysRevLett.89.011301.
arXiv: nucl-ex/0204008.

[43] G. Bellini et al. "Final results of Borexino Phase-I on low energy solar neutrino
spectroscopy". In: *Phys. Rev. D* 89.11 (2014), p. 112007.
(Cited on p: 15.).
DOI: 10.1103/PhysRevD.89.112007.
arXiv: 1308.0443 [hep-ex].

[44] S. Mikheev and A. Y. Smirnov. "Resonance Oscillations of Neutrinos in Matter".
In: *Sov. Phys. Usp.* 30 (1987), p. 759.
(Cited on p: 16.).
DOI: 10.1070/PU1987v030n09ABEH002961.

[45] Andrea Donini, Sergio Palomares-Ruiz, and Jordi Salvado. "Neutrino
tomography of Earth". In: *Nature Phys.* 15.1 (2019), pp. 37–40.
(Cited on p: 17.).
DOI: 10.1038/s41567-018-0319-1.
arXiv: 1803.05901 [hep-ph].

[46]   Tommy Ohlsson and Hakan Snellman. "Three flavor neutrino oscillations in matter". In: *J. Math. Phys.* 41 (2000). [Erratum: J.Math.Phys. 42, 2345 (2001)], pp. 2768–2788.
        (Cited on p: 17.).
        DOI: 10.1063/1.533270.
        arXiv: hep-ph/9910546.

[47]   A. Yu. Smirnov. "The MSW effect and matter effects in neutrino oscillations". In: *Phys. Scripta T* 121 (2005). Ed. by L. Bergström et al., pp. 57–64.
        (Cited on p: 17.).
        DOI: 10.1088/0031-8949/2005/T121/008.
        arXiv: hep-ph/0412391.

[48]   M. C. Gonzalez-Garcia and M. Maltoni. "Determination of matter potential from global analysis of neutrino oscillation data". In: *Journal of High Energy Physics* 2013.9 (Sept. 2013).
        (Cited on p: 18.).
        DOI: 10.1007/jhep09(2013)152.

[49]   M. C. Gonzalez-Garcia et al. "Non-standard neutrino interactions in the Earth and the flavor of astrophysical neutrinos". In: *Astropart. Phys.* 84 (2016), pp. 15–22.
        (Cited on p: 18.).
        DOI: 10.1016/j.astropartphys.2016.07.001.
        arXiv: 1605.08055 [hep-ph].

[50]   M. G. Aartsen et al. "Search for Nonstandard Neutrino Interactions with IceCube DeepCore". In: *Phys. Rev. D* 97.7 (2018), p. 072009.
        (Cited on p: 18.).
        DOI: 10.1103/PhysRevD.97.072009.
        arXiv: 1709.07079 [hep-ex].

[51]   R. Abbasi et al. "Strong Constraints on Neutrino Nonstandard Interactions from TeV-Scale ν_μ Disappearance at IceCube". In: *Phys. Rev. Lett.* 129 (1 June 2022), p. 011804.
        (Cited on pp: 18, 29, 140, 152, 163.).
        DOI: 10.1103/PhysRevLett.129.011804.
        URL: https://link.aps.org/doi/10.1103/PhysRevLett.129.011804.

[52]   A. M. Dziewonski and D. L. Anderson. "Preliminary reference Earth model." In: *Physics of the Earth and Planetary Interiors* 25 (1981), p. 297.
        (Cited on pp: 18, 29, 71, 152, 163.).
        DOI: http://dx.doi.org/10.1016/0031-9201(81)90046-7.

[53]   Pilar Coloma and Thomas Schwetz. "Generalized mass ordering degeneracy in neutrino oscillation experiments". In: *Phys. Rev. D* 94.5 (2016). [Erratum: Phys.Rev.D 95, 079903 (2017)], p. 055005.
        (Cited on p: 18.).
        DOI: 10.1103/PhysRevD.94.055005.
        arXiv: 1604.05772 [hep-ph].

[54]   D. Meloni, T. Ohlsson, and H. Zhang. "Exact and approximate formulas for neutrino mixing and oscillations with non-standard interactions". In: *JHEP*

2009.04 (Apr. 2009), p. 033.
(Cited on p: 19.).
DOI: 10.1088/1126-6708/2009/04/033.

[55] F. J. Escrihuela Ferrándiz. "Phenomenology of Non-Standard Neutrino Interactions". PhD thesis. 2016.
(Cited on p: 19.).

[56] G. Mitsuka et al. "Study of Non-Standard Neutrino Interactions with Atmospheric Neutrino Data in Super-Kamiokande I and II". In: *Phys. Rev. D* 84 (2011), p. 113008.
(Cited on p: 19.).
DOI: 10.1103/PhysRevD.84.113008.
arXiv: 1109.1889 [hep-ex].

[57] Jordi Salvado et al. "Non-standard interactions with high-energy atmospheric neutrinos at IceCube". In: *JHEP* 01 (2017), p. 141.
(Cited on pp: 20, 25.).
DOI: 10.1007/JHEP01(2017)141.
arXiv: 1609.03450 [hep-ph].

[58] J. Coelho. "OscProb: The Oscillation Probability Calculator". In: *https://github.com/joaoabcoelho/OscProb/*. ().
(Cited on pp: 22, 23, 25, 29, 71, 152, 163.).

[59] Arman Esmaili and Alexei Yu. Smirnov. "Probing Non-Standard Interaction of Neutrinos with IceCube and DeepCore". In: *JHEP* 06 (2013), p. 026.
(Cited on p: 25.).
DOI: 10.1007/JHEP06(2013)026.
arXiv: 1304.1042 [hep-ph].

[60] Mattias Blennow and Tommy Ohlsson. "Approximative two-flavor framework for neutrino oscillations with non-standard interactions". In: *Phys. Rev. D* 78 (2008), p. 093002.
(Cited on p: 25.).
DOI: 10.1103/PhysRevD.78.093002.
arXiv: 0805.2301 [hep-ph].

[61] Alexander Friedland, Cecilia Lunardini, and Michele Maltoni. "Atmospheric neutrinos as probes of neutrino-matter interactions". In: *Phys. Rev. D* 70 (2004), p. 111301.
(Cited on p: 25.).
DOI: 10.1103/PhysRevD.70.111301.
arXiv: hep-ph/0408264.

[62] Joachim Kopp et al. "Non-standard neutrino interactions in reactor and superbeam experiments". In: *Phys. Rev. D* 77 (2008), p. 013007.
(Cited on p: 26.).
DOI: 10.1103/PhysRevD.77.013007.
arXiv: 0708.0152 [hep-ph].

[63] TseChun Wang and Ye-Ling Zhou. "Neutrino nonstandard interactions as a portal to test flavor symmetries". In: *Phys. Rev. D* 99.3 (2019), p. 035039.
(Cited on p: 26.).
DOI: 10.1103/PhysRevD.99.035039.
arXiv: 1801.05656 [hep-ph].

[64]   Wei-Jie Feng et al. "Nonstandard interactions versus planet-scale neutrino oscillations". In: *Phys. Rev. D* 100 (11 Dec. 2019), p. 115034.
(Cited on p: 26.).
DOI: 10.1103/PhysRevD.100.115034.
URL: https://link.aps.org/doi/10.1103/PhysRevD.100.115034.

[65]   F. Capozzi et al. "Status of three-neutrino oscillation parameters, circa 2013". In: *Phys. Rev. D* 89 (2014), p. 093018.
(Cited on p: 26.).
DOI: 10.1103/PhysRevD.89.093018.
arXiv: 1312.2878 [hep-ph].

[66]   M. C. Gonzalez-Garcia, Michele Maltoni, and Thomas Schwetz. "Global Analyses of Neutrino Oscillation Experiments". In: *Nucl. Phys. B* 908 (2016), pp. 199–217.
(Cited on p: 26.).
DOI: 10.1016/j.nuclphysb.2016.02.033.
arXiv: 1512.06856 [hep-ph].

[67]   Johannes Bergstrom et al. "Bayesian global analysis of neutrino oscillation data".
In: *JHEP* 09 (2015), p. 200.
(Cited on p: 26.).
DOI: 10.1007/JHEP09(2015)200.
arXiv: 1507.04366 [hep-ph].

[68]   D. V. Forero, M. Tortola, and J. W. F. Valle. "Neutrino oscillations refitted". In: *Phys. Rev. D* 90.9 (2014), p. 093006.
(Cited on p: 26.).
DOI: 10.1103/PhysRevD.90.093006.
arXiv: 1405.7540 [hep-ph].

[69]   F. Capozzi et al. "Neutrino masses and mixings: Status of known and unknown 3ν parameters". In: *Nucl. Phys. B* 908 (2016), pp. 218–234.
(Cited on p: 26.).
DOI: 10.1016/j.nuclphysb.2016.02.016.
arXiv: 1601.07777 [hep-ph].

[70]   I. Estebanet al. *Nufit4.1 at nufit webpage*. Accessed: 20.07.2022.
(Cited on p: 26.).
URL: http://www.nu-fit.org.

[71]   P. F. de Salas et al. "Status of neutrino oscillations 2018: 3σ hint for normal mass ordering and improved CP sensitivity". In: *Phys. Lett. B* 782 (2018), pp. 633–640.
(Cited on p: 26.).
DOI: 10.1016/j.physletb.2018.06.019.
arXiv: 1708.01186 [hep-ph].

[72]   F. Capozzi et al. "Current unknowns in the three neutrino framework". In: *Prog. Part. Nucl. Phys.* 102 (2018), pp. 48–72.
(Cited on p: 26.).
DOI: 10.1016/j.ppnp.2018.05.005.
arXiv: 1804.09678 [hep-ph].

[73] Ivan Esteban et al. "The fate of hints: updated global analysis of three-flavor neutrino oscillations". In: *JHEP* 09 (2020), p. 178.
(Cited on pp: 26, 27, 150, 160.).
DOI: 10.1007/JHEP09(2020)178.
arXiv: 2007.14792 [hep-ph].

[74] P. F. de Salas et al. "2020 global reassessment of the neutrino oscillation picture". In: *JHEP* 02 (2021), p. 071.
(Cited on p: 26.).
DOI: 10.1007/JHEP02(2021)071.
arXiv: 2006.11237 [hep-ph].

[75] Ivan Esteban et al. "Global analysis of three-flavour neutrino oscillations: synergies and tensions in the determination of θ_{23}, δ_{CP}, and the mass ordering". In: *JHEP* 01 (2019), p. 106.
(Cited on p: 27.).
DOI: 10.1007/JHEP01(2019)106.
arXiv: 1811.05487 [hep-ph].

[76] D. Akimov et al. "The COHERENT Experiment at the Spallation Neutron Source". In: (Sept. 2015).
(Cited on p: 27.).
arXiv: 1509.08702 [physics.ins-det].

[77] A. Albert et al. "Search for non-standard neutrino interactions with 10 years of ANTARES data". In: *JHEP* 07 (2022), p. 048.
(Cited on pp: 27, 29, 140, 152, 163.).
DOI: 10.1007/JHEP07(2022)048.
arXiv: 2112.14517 [hep-ex].

[78] Pilar Coloma et al. "Improved global fit to Non-Standard neutrino Interactions using COHERENT energy and timing data". In: *JHEP* 02 (2020). [Addendum: JHEP 12, 071 (2020)], p. 023.
(Cited on pp: 28, 134.).
DOI: 10.1007/JHEP02(2020)023.
arXiv: 1911.09109 [hep-ph].

[79] Ivan Esteban et al. "Updated constraints on non-standard interactions from global analysis of oscillation data". In: *JHEP* 08 (2018). [Addendum: JHEP 12, 152 (2020)], p. 180.
(Cited on pp: 28, 134.).
DOI: 10.1007/JHEP08(2018)180.
arXiv: 1805.04530 [hep-ph].

[80] D. Akimov et al. "COHERENT Collaboration data release from the first observation of coherent elastic neutrino-nucleus scattering". In: (Apr. 2018).
(Cited on p: 28.).
DOI: 10.5281/zenodo.1228631.
arXiv: 1804.09459 [nucl-ex].

[81] R. Abbasi et al. "All-flavor constraints on nonstandard neutrino interactions and generalized matter potential with three years of IceCube DeepCore data". In: *Phys.*

Rev. D 104.7 (2021), p. 072006.
(Cited on pp: 29, 107, 135, 141–143, 152, 163.).
DOI: 10.1103/PhysRevD.104.072006.
arXiv: 2106.07755 [hep-ex].

[82]   G. Mitsuka et al. "Study of nonstandard neutrino interactions with atmospheric neutrino data in Super-Kamiokande I and II". In: *Phys. Rev. D* 84 (11 Dec. 2011), p. 113008.
(Cited on p: 29.).
DOI: 10.1103/PhysRevD.84.113008.
URL: https://link.aps.org/doi/10.1103/PhysRevD.84.113008.

[83]   S. Adrian-Martinez et al. "Letter of intent for KM3NeT 2.0". In: *J. Phys. G* 43.8 (2016), p. 084001.
(Cited on pp: 43, 45, 57, 69, 108.).
DOI: 10.1088/0954-3899/43/8/084001.
arXiv: 1601.07459 [astro-ph.IM].

[84]   S. Aiello et al. "Determining the neutrino mass ordering and oscillation parameters with KM3NeT/ORCA". In: *Eur. Phys. J. C* 82.1 (2022), p. 26.
(Cited on pp: 44, 57, 69.).
DOI: 10.1140/epjc/s10052-021-09893-0.
arXiv: 2103.09885 [hep-ex].

[85]   M. Ageron et al. "Technical Design Report of the MEUST Infrastructure". In: (Jan. 2013).
(Cited on pp: 44, 45.).
URL: http://meust.cnrs.fr/TDR-MEUST_infrastructure.pdf.

[86]   Lodewijk Nauta et al. "First neutrino oscillation measurement in KM3NeT/ORCA". In: *Proceedings of 37th International Cosmic Ray Conference — PoS(ICRC2021)*. Vol. 395. 2021, p. 1123.
(Cited on p: 46.).
DOI: 10.22323/1.395.1123.

[87]   J. A. Aguilar et al. "ANTARES: the first undersea neutrino telescope". In: *Nucl. Inst. and Methods in Physics Research, A 656 (2011) pp. 11-38* (2011).
(Cited on pp: 46, 47.).
arXiv: 1104.1607v1.

[88]   S. Adrián-Martínez et al. "The prototype detection unit of the KM3NeT detector". In: *Eur. Phys. J. C* 76.2 (2016), p. 54.
(Cited on p: 46.).
DOI: 10.1140/epjc/s10052-015-3868-9.
arXiv: 1510.01561 [astro-ph.IM].

[89]   S. Aiello et al. "Deep-sea deployment of the KM3NeT neutrino telescope detection units by self-unrolling". In: *Journal of Instrumentation* 15.11 (Nov. 2020), P11027–P11027.
(Cited on p: 46.).
DOI: 10.1088/1748-0221/15/11/p11027.
URL: https://doi.org/10.1088/1748-0221/15/11/p11027.

[90] S. Aiello and other. "The KM3NeT multi-PMT optical module". In: *Journal of Instrumentation* 17.07 (July 2022), P07038.
(Cited on p: 47.).
DOI: 10.1088/1748-0221/17/07/p07038.

[91] *Photomultiplier tube, R12199*. Accessed: 26.06.2022.
(Cited on p: 47.).
URL: https://www.hamamatsu.com/eu/en/product/type/R12199/index.html.

[92] M. G. Aartsen et al. "The IceCube Neutrino Observatory: Instrumentation and Online Systems". In: *JINST* 12.03 (2017), P03012.
(Cited on p: 47.).
DOI: 10.1088/1748-0221/12/03/P03012.
arXiv: 1612.05093 [astro-ph.IM].

[93] S. Aiello et al. "Characterisation of the Hamamatsu photomultipliers for the KM3NeT Neutrino Telescope". In: *JINST* 13.05 (2018), P05035.
(Cited on p: 49.).
DOI: 10.1088/1748-0221/13/05/P05035.

[94] T. K. Gaisser and M. Honda. "Flux of atmospheric neutrinos". In: *Ann. Rev. Nucl. Part. Sci.* 52 (2002), pp. 153–199.
(Cited on pp: 49, 50.).
DOI: 10.1146/annurev.nucl.52.050102.090645.
arXiv: hep-ph/0203272.

[95] M. Honda et al. "Improvement of low energy atmospheric neutrino flux calculation using the JAM nuclear interaction model". In: *Phys. Rev. D* 83 (12 June 2011), p. 123001.
(Cited on p: 50.).
DOI: 10.1103/PhysRevD.83.123001.
URL: https://link.aps.org/doi/10.1103/PhysRevD.83.123001.

[96] M. Honda et al. "Calculation of atmospheric neutrino flux using the interaction model calibrated with atmospheric muon data". In: *Phys. Rev. D* 75 (4 2007), p. 043006.
(Cited on p: 50.).
DOI: 10.1103/PhysRevD.75.043006.
URL: https://link.aps.org/doi/10.1103/PhysRevD.75.043006.

[97] G. D. Barr et al. "Three-dimensional calculation of atmospheric neutrinos". In: *Phys. Rev. D* 70 (2 July 2004), p. 023006.
(Cited on p: 50.).
DOI: 10.1103/PhysRevD.70.023006.
URL: https://link.aps.org/doi/10.1103/PhysRevD.70.023006.

[98] G. Battistoni et al. "The FLUKA atmospheric neutrino flux calculation". In: *Astropart. Phys.* 19 (2003). [Erratum: Astropart.Phys. 19, 291–294 (2003)], pp. 269–290.
(Cited on p: 50.).
DOI: 10.1016/S0927-6505(02)00246-3.
arXiv: hep-ph/0207035.

[99]   Yusuke Koshio. "Observation of Atmospheric Neutrinos". In: *Universe* 6.6 (2020).
       ISSN: 2218-1997.
       (Cited on p: 50.).
       DOI: 10.3390/universe6060080.
       URL: https://www.mdpi.com/2218-1997/6/6/80.

[100] Rikard Enberg, Mary Hall Reno, and Ina Sarcevic. "Prompt neutrino fluxes from
       atmospheric charm". In: *Phys. Rev. D* 78 (2008), p. 043005.
       (Cited on p: 51.).
       DOI: 10.1103/PhysRevD.78.043005.
       arXiv: 0806.0418 [hep-ph].

[101] M. Honda et al. "Atmospheric neutrino flux calculation using the NRLMSISE-00
       atmospheric model". In: *Phys. Rev. D* 92 (2 July 2015), p. 023004.
       (Cited on pp: 51, 72.).
       DOI: 10.1103/PhysRevD.92.023004.
       URL: https://link.aps.org/doi/10.1103/PhysRevD.92.023004.

[102] T. Gluesenkamp. "On the Detection of Subrelativistic Magnetic Monopoles with
       the IceCube Neutrino Observatory". PhD thesis. 2010.
       (Cited on p: 52.).

[103] T.J. Petzold. "Volume scattering functions for selected ocean waters". In: *Scripts
       Inst. Oceanogr. Report SIO* 72-78 (1972).
       (Cited on p: 53.).
       URL: https://www.oceanopticsbook.info/packages/iws_l2h/conversion/
       files/Petzold_VSF_SIO72-78.pdf.

[104] L. G. Henyey and J. L. Greenstein. "Diffuse radiation in the Galaxy." In: *APJ* 93
       (Jan. 1941). Provided by the SAO/NASA Astrophysics Data System, pp. 70–83.
       (Cited on p: 53.).
       DOI: 10.1086/144246.
       URL: https://ui.adsabs.harvard.edu/abs/1941ApJ....93...70H.

[105] O.V. Kopelevich. "Small-parameter model of optical properties of sea water". In:
       Ocean Optics, vol 1: Physical Ocean Optics. Ed. by A.S. Monin. Moscow: Nauka Pub.,
       1983. Chap. 8.
       (Cited on p: 53.).

[106] J.A. Aguilar et al. "Transmission of light in deep sea water at the site of the
       Antares neutrino telescope". In: *Astroparticle Physics* 23.1 (2005), pp. 131–155. ISSN:
       0927-6505.
       (Cited on p: 53.).
       DOI: https://doi.org/10.1016/j.astropartphys.2004.11.006.
       URL: https://www.sciencedirect.com/science/article/pii/
       S0927650504001902.

[107] G Riccobene et al. "Deep seawater inherent optical properties in the Southern
       Ionian Sea". In: *Astroparticle Physics* 27.1 (Feb. 2007), p. 1.
       (Cited on p: 54.).
       DOI: 10.1016/j.astropartphys.2006.08.006.

[108] Paul H. Barrett et al. "Interpretation of Cosmic-Ray Measurements Far Underground". In: *Rev. Mod. Phys.* 24 (3 July 1952), pp. 133–178.
(Cited on p: 54.).
DOI: 10.1103/RevModPhys.24.133.
URL: https://link.aps.org/doi/10.1103/RevModPhys.24.133.

[109] DONALD E. GROOM, NIKOLAI V. MOKHOV, and SERGEI I. STRIGANOV. "MUON STOPPING POWER AND RANGE TABLES 10 MeV100 TeV". In: *Atomic Data and Nuclear Data Tables* 78.2 (2001), pp. 183–356. ISSN: 0092-640X.
(Cited on p: 55.).
DOI: https://doi.org/10.1006/adnd.2001.0861.
URL: https://www.sciencedirect.com/science/article/pii/S0092640X01908617.

[110] C. Kopper. "Performance Studies for the KM3NeT Neutrino Telescope". PhD thesis. 2010.
(Cited on p: 56.).
URL: http://antares.in2p3.fr/Publications/thesis/2010/Claudio-Kopper-phd.pdf.

[111] Jannik Hofestädt. "Measuring the neutrino mass hierarchy with the future KM3NeT/ORCA detector". PhD thesis. Friedrich-Alexander-Universität Erlangen-Nürnberg (FAU), 2017.
(Cited on pp: 57, 108.).

[112] C. H Wiebusch. "The Detection of Faint Light in Deep Underwater Neutrino Telescopes." PhD thesis. RHEINISCH WESTFÄLISCHE TECHNISCHE HOCHSCHULE AACHEN, 1995.
(Cited on p: 57.).
URL: https://web.physik.rwth-aachen.de/~wiebusch/Publications/Various/phd.pdf.

[113] Jun Chen. "Nuclear Data Sheets for A=40". In: *Nuclear Data Sheets* 140 (2017), pp. 1–376. ISSN: 0090-3752.
(Cited on p: 58.).
DOI: https://doi.org/10.1016/j.nds.2017.02.001.
URL: https://www.sciencedirect.com/science/article/pii/S0090375217300169.

[114] S. Adrián-Martínez et al. "Deep sea tests of a prototype of the KM3NeT digital optical module". In: *Eur. Phys. J. C* 74.9 (2014), p. 3056.
(Cited on p: 58.).
DOI: 10.1140/epjc/s10052-014-3056-3.
arXiv: 1405.0839 [astro-ph.IM].

[115] Steven H.D. Haddock, Mark A. Moline, and James F. Case. "Bioluminescence in the Sea". In: *Annual Review of Marine Science* 2.1 (2010). PMID: 21141672, pp. 443–493.
(Cited on p: 58.).
DOI: 10.1146/annurev-marine-120308-081028.
eprint: https://doi.org/10.1146/annurev-marine-120308-081028.
URL: https://doi.org/10.1146/annurev-marine-120308-081028.

[116]   M. Ageron et al. "Dependence of atmospheric muon flux on seawater depth measured with the first KM3NeT detection units: The KM3NeT Collaboration". In: *Eur. Phys. J. C* 80.2 (2020), p. 99.
(Cited on p: 58.).
DOI: 10.1140/epjc/s10052-020-7629-z.
arXiv: 1906.02704 [physics.ins-det].

[117]   Y. Becherini et al. "A Parameterisation of single and multiple muons in the deep water or ice". In: *Astropart. Phys.* 25 (2006), pp. 1–13.
(Cited on p: 59.).
DOI: 10.1016/j.astropartphys.2005.10.005.
arXiv: hep-ph/0507228.

[118]   T. Chiarusi and M. Spurio. "High-energy astrophysics with neutrino telescopes". In: *The European Physical Journal C* 65.3-4 (Jan. 2010), pp. 649701. ISSN: 1434-6052.
(Cited on p: 59.).
DOI: 10.1140/epjc/s10052-009-1230-9.
URL: http://dx.doi.org/10.1140/epjc/s10052-009-1230-9.

[119]   Dídac D.Tortosa. "Monitoring and Reconstruction of the Shape of the Detection Units in KM3NeT Using Acoustic and Compass Sensors". In: *Sensors* 20.18 (2020). ISSN: 1424-8220.
(Cited on p: 61.).
DOI: 10.3390/s20185116.
URL: https://www.mdpi.com/1424-8220/20/18/5116.

[120]   Miguel Ardid et al. "Acoustic Transmitters for Underwater Neutrino Telescopes". In: *Sensors* 12.4 (2012), pp. 4113–4132. ISSN: 1424-8220.
(Cited on p: 61.).
DOI: 10.3390/s120404113.
URL: https://www.mdpi.com/1424-8220/12/4/4113.

[121]   Karel Melis. "In-Situ Calibration of KM3NeT". In: *Proceedings of 35th International Cosmic Ray Conference — PoS(ICRC2017)*. Vol. 301. 2017, p. 1059.
(Cited on p: 61.).
DOI: 10.22323/1.301.1059.

[122]   S. Aiello et al. "gSeaGen: The KM3NeT GENIE-based code for neutrino telescopes". In: *Computer Physics Communications* 256 (2020), p. 107477. ISSN: 0010-4655.
(Cited on pp: 64, 65.).
DOI: https://doi.org/10.1016/j.cpc.2020.107477.
URL: https://www.sciencedirect.com/science/article/pii/S0010465520302241.

[123]   C. Andreopoulos et al. "The GENIE Neutrino Monte Carlo Generator: Physics and User Manual". In: (Oct. 2015).
(Cited on p: 64.).
arXiv: 1510.05494 [hep-ph].

[124]   G. Carminati, A. Margiotta, and M. Spurio. "Atmospheric MUons from PArametric formulas: A Fast GEnerator for neutrino telescopes (MUPAGE)". In:

Comput. Phys. Commun. 179 (2008), pp. 915–923.
(Cited on p: 66.).
DOI: `10.1016/j.cpc.2008.07.014`.
arXiv: `0802.0562 [physics.ins-det]`.

[125] G. Carminati et al. "MUPAGE: a fast atmospheric MUon GEnerator for neutrino telescopes based on PArametric formulas". In: (July 2009).
(Cited on p: 66.).
arXiv: `0907.5563 [astro-ph.IM]`.

[126] S. Navas and L. Thompson. "Km3 user guide and reference manual". In: *KM3NeT internal note, KM3NeT-SIM/2015-001* (2015).
(Cited on p: 66.).

[127] S. Agostinelli et al. "GEANT4–a simulation toolkit". In: *Nucl. Instrum. Meth. A* 506 (2003), pp. 250–303.
(Cited on p: 66.).
DOI: `10.1016/S0168-9002(03)01368-8`.

[128] L. Quinn. "Determining the Neutrino Mass Hierarchy with KM3NeT-ORCA". In: *Ph.D. Thesis, CPPM, Aix-Marseille University* (2018).
(Cited on p: 67.).
URL: `https://hdl.handle.net/11245.1/36457c73-2ef4-4a73-bbb8-bdd2c8e3f364`.

[129] Alba Domi. "SHOWER RECONSTRUCTION AND STERILE NEUTRINO ANALYSIS WITH KM3NeT/ORCA AND ANTARES". PhD thesis. Universitá degli studi di Genova, 2019.
(Cited on p: 69.).
URL: `http://hdl.handle.net/11567/985989`.

[130] Wouter Verkerke and David Kirkby. *The RooFit toolkit for data modeling*. 2003.
(Cited on pp: 70, 100.).
DOI: `10.48550/ARXIV.PHYSICS/0306116`.
URL: `https://arxiv.org/abs/physics/0306116`.

[131] Jessica C. E. Irving, Sanne Cottaar, and Vedran Leki. "Seismically determined elastic parameters for Earth’s outer core". In: *Science Advances* 4.6 (2018), eaar2538.
(Cited on pp: 71, 152, 163.).
DOI: `10.1126/sciadv.aar2538`.
eprint: `https://www.science.org/doi/pdf/10.1126/sciadv.aar2538`.
URL: `https://www.science.org/doi/abs/10.1126/sciadv.aar2538`.

[132] Guy Masters and David Gubbins. "On the resolution of density within the Earth". In: *Physics of the Earth and Planetary Interiors* 140.1 (2003). Geophysical and Geochemical Evolution of the Deep Earth, pp. 159–167. ISSN: 0031-9201.
(Cited on pp: 71, 152, 163.).
DOI: `https://doi.org/10.1016/j.pepi.2003.07.008`.
URL: `https://www.sciencedirect.com/science/article/pii/S0031920103001705`.

[133]   Hubert Staudigel et al. "Geochemical Earth Reference Model (GERM): description of the initiative". In: *Chemical Geology* 145.3 (1998), pp. 153–159. ISSN: 0009-2541.
(Cited on p: 71.).
DOI: https://doi.org/10.1016/S0009-2541(97)00141-1.
URL: https://www.sciencedirect.com/science/article/pii/S0009254197001411.

[134]   W.F. McDonough. "2.15 - Compositional Model for the Earth's Core". In: *Treatise on Geochemistry*. Ed. by Heinrich D. Holland and Karl K. Turekian. Oxford: Pergamon, 2003, pp. 547–568. ISBN: 978-0-08-043751-4.
(Cited on p: 71.).
DOI: https://doi.org/10.1016/B0-08-043751-6/02015-6.
URL: https://www.sciencedirect.com/science/article/pii/B0080437516020156.

[135]   Edouard Kaminski and Marc Javoy. "A two-stage scenario for the formation of the Earth's mantle and core". In: *Earth and Planetary Science Letters* 365 (2013), pp. 97–107. ISSN: 0012-821X.
(Cited on p: 71.).
DOI: https://doi.org/10.1016/j.epsl.2013.01.025.
URL: https://www.sciencedirect.com/science/article/pii/S0012821X13000423.

[136]   M. Javoy et al. "The chemical composition of the Earth: Enstatite chondrite models". In: *Earth and Planetary Science Letters* 293.3 (2010), pp. 259–268. ISSN: 0012-821X.
(Cited on p: 71.).
DOI: https://doi.org/10.1016/j.epsl.2010.02.033.
URL: https://www.sciencedirect.com/science/article/pii/S0012821X10001445.

[137]   L. Nauta. "Quantum Effects on a Planetary Scale - The First Neutrino Oscillation Measurement with KM3NeT/ORCA". PhD thesis. Univesiteit van Amsterdam, 2022. ISBN: 978-94-6419-498-2.
(Cited on pp: 73, 90, 91, 93, 143, 145, 155.).
URL: https://hdl.handle.net/11245.1/36457c73-2ef4-4a73-bbb8-bdd2c8e3f364.

[138]   Louis Lyons. "Unfolding: Introduction". In: *PHYSTAT 2011*. Geneva: CERN, 2011, pp. 225–228.
(Cited on p: 75.).
DOI: 10.5170/CERN-2011-006.225.

[139]   M. G. Aartsen et al. "Computational techniques for the analysis of small signals in high-statistics neutrino oscillation experiments". In: *Nucl. Instrum. Meth. A* 977 (2020), p. 164332.
(Cited on p: 77.).
DOI: 10.1016/j.nima.2020.164332.
arXiv: 1803.05390 [physics.data-an].

[140]   Glen Cowan et al. "Asymptotic formulae for likelihood-based tests of new physics". In: *Eur. Phys. J. C* 71 (2011). [Erratum: Eur.Phys.J.C 73, 2501 (2013)],

p. 1554.
(Cited on pp: 93, 98.).
DOI: 10.1140/epjc/s10052-011-1554-0.
arXiv: 1007.1727 [physics.data-an].

[141] Joseph Berkson. "Minimum Chi-Square, not Maximum Likelihood!" In: *The Annals of Statistics* 8.3 (1980), pp. 457–487. ISSN: 00905364.
(Cited on p: 97.).
URL: http://www.jstor.org/stable/2240587 (visited on [visited on 07/04/2022]).

[142] Steve Baker and Robert D. Cousins. "Clarification of the use of CHI-square and likelihood functions in fits to histograms". In: *Nuclear Instruments and Methods in Physics Research* 221.2 (1984), pp. 437–442. ISSN: 0167-5087.
(Cited on p: 98.).
DOI: https://doi.org/10.1016/0167-5087(84)90016-4.
URL: https://www.sciencedirect.com/science/article/pii/0167508784900164.

[143] Rene Andrae, Tim Schulze-Hartung, and Peter Melchior. *Dos and don'ts of reduced chi-squared*. 2010.
(Cited on p: 98.).
DOI: 10.48550/ARXIV.1012.3754.
URL: https://arxiv.org/abs/1012.3754.

[144] A. N. Kolmogorov. "Sulla Determinazione Empirica di Una Legge di Distribuzione". In: *Giornale dellIstituto Italiano degli Attuari* 4 (1933), pp. 83–91.
(Cited on p: 98.).

[145] N. V. Smirnov. "Table for Estimating the Goodness of Fit of Empirical Distributions". In: *Annals of Mathematical Statistics* 19 (1948), pp. 279–281.
(Cited on p: 98.).

[146] Marvin Karson. "Handbook of Methods of Applied Statistics. Volume I: Techniques of Computation Descriptive Methods, and Statistical Inference. Volume II: Planning of Surveys and Experiments. I. M. Chakravarti, R. G. Laha, and J. Roy, New York, John Wiley; 1967, $9.00." In: *Journal of the American Statistical Association* 63.323 (1968), pp. 1047–1049.
(Cited on p: 98.).
DOI: 10.1080/01621459.1968.11009335.
eprint: https://doi.org/10.1080/01621459.1968.11009335.
URL: https://doi.org/10.1080/01621459.1968.11009335.

[147] René Brun and and. "HBOOK : Statistical Analysis and Histogramming : Reference Manual". In: (1998). CERN Program Library Long Writeups.
(Cited on p: 98.).
URL: http://cds.cern.ch/record/2296378.

[148] S. S. Wilks. "The Large-Sample Distribution of the Likelihood Ratio for Testing Composite Hypotheses". In: *Annals Math. Statist.* 9.1 (1938), p. 60.
(Cited on p: 99.).
DOI: 10.1214/aoms/1177732360.

[149] J. Neyman. "Outline of a Theory of Statistical Estimation Based on the Classical
       Theory of Probability". In: *Phil. Trans. Roy. Soc. Lond. A* 236.767 (1937), p. 333.
       (Cited on p: 99.).
       DOI: 10.1098/rsta.1937.0005.

[150] Gary J. Feldman and Robert D. Cousins. "Unified approach to the classical
       statistical analysis of small signals". In: *Phys. Rev. D* 57 (7 Apr. 1998),
       pp. 3873–3889.
       (Cited on pp: 99, 103, 151, 161.).
       DOI: 10.1103/PhysRevD.57.3873.
       URL: https://link.aps.org/doi/10.1103/PhysRevD.57.3873.

[151] F. James. "MINUIT Function Minimization and Error Analysis: Reference Manual
       Version 94.1". In: (1994).
       (Cited on pp: 100, 150, 160.).

[152] R. Brun and F. Rademakers. "ROOT: An object oriented data analysis framework".
       In: *Nucl. Instrum. Meth. A* 389 (1997). Ed. by M. Werlen and D. Perret-Gallix, p. 81.
       (Cited on p: 100.).
       DOI: 10.1016/S0168-9002(97)00048-X.

[153] Fons Rademakers et al. *root-project/root: v6.20/06*. Version v6-20-06. June 2020.
       (Cited on pp: 100, 150, 160.).
       DOI: 10.5281/zenodo.3895852.
       URL: https://doi.org/10.5281/zenodo.3895852.

[154] M. G. Aartsen et al. "Measurement of Atmospheric Neutrino Oscillations at 6–56
       GeV with IceCube DeepCore". In: *Phys. Rev. Lett.* 120 (7 Feb. 2018), p. 071801.
       (Cited on p: 103.).
       DOI: 10.1103/PhysRevLett.120.071801.
       URL: https://link.aps.org/doi/10.1103/PhysRevLett.120.071801.

[155] K. Abe et al. "Measurements of neutrino oscillation in appearance and
       disappearance channels by the T2K experiment with 6.6×10^{20} protons on target".
       In: *Phys. Rev. D* 91.7 (2015), p. 072010.
       (Cited on p: 103.).
       DOI: 10.1103/PhysRevD.91.072010.
       arXiv: 1502.01550 [hep-ex].

[156] Sara Algeri et al. "Searching for new phenomena with profile likelihood ratio
       tests". In: *Nature Rev. Phys.* 2.5 (2020), pp. 245–252.
       (Cited on p: 103.).
       DOI: 10.1038/s42254-020-0169-5.
       arXiv: 1911.10237 [physics.data-an].

[157] Bradley. Efron, Society for Industrial, and Applied Mathematics. *The jackknife, the
       bootstrap, and other resampling plans / Bradley Efron*. English. Society for Industrial
       and Applied Mathematics Philadelphia, Pa, 1982, vii, 92 p. : ISBN: 0898711797.
       (Cited on p: 105.).
       URL: http://www.loc.gov/catdir/enhancements/fy0726/81084708-t.html.

[158] G. D. Barr et al. "Uncertainties in atmospheric neutrino fluxes". In: *Phys. Rev. D*
       74.9 (Nov. 2006).
       (Cited on pp: 106, 107.).
       DOI: 10.1103/physrevd.74.094009.

[159] Justin Evans et al. "Uncertainties in atmospheric muon-neutrino fluxes arising from cosmic-ray primaries". In: *Phys. Rev. D* 95 (2 Jan. 2017), p. 023012.
(Cited on pp: 107, 108.).
DOI: 10.1103/PhysRevD.95.023012.
URL: https://link.aps.org/doi/10.1103/PhysRevD.95.023012.

[160] M. G. Aartsen et al. "Measurement of atmospheric tau neutrino appearance with IceCube DeepCore". In: *Phys. Rev. D* 99 (3 Feb. 2019), p. 032007.
(Cited on p: 107.).
DOI: 10.1103/PhysRevD.99.032007.
URL: https://link.aps.org/doi/10.1103/PhysRevD.99.032007.

[161] Brían Ó Fearraigh. "Tuning parametric models of the atmospheric muon flux in MUPAGE to data from the KM3NeT detector". In: *PoS* ICRC2021 (2021), p. 1176.
(Cited on p: 108.).
DOI: 10.22323/1.395.1176.

[162] O. Buss et al. "Transport-theoretical Description of Nuclear Reactions". In: *Phys. Rept.* 512 (2012), pp. 1–124.
(Cited on p: 108.).
DOI: 10.1016/j.physrep.2011.12.001.
arXiv: 1106.1344 [hep-ph].

[163] Johannes Schumann and Bouke Jung. "GiBUU based neutrino interaction simulations in KM3NeT". In: *JINST* 16.09 (2021), p. C09022.
(Cited on p: 108.).
DOI: 10.1088/1748-0221/16/09/C09022.
arXiv: 2107.13947 [hep-ex].

[164] Georges Aad et al. "Measurement of the $t\bar{t}$ production cross-section in the lepton+jets channel at $\sqrt{s} = 13$ TeV with the ATLAS experiment". In: *Phys. Lett. B* 810 (2020), p. 135797.
(Cited on p: 109.).
DOI: 10.1016/j.physletb.2020.135797.
arXiv: 2006.13076 [hep-ex].

[165] O.G. Sorokhtin, G.V. Chilingar, and N.O. Sorokhtin. "Chapter 2 - Structure and Composition of Modern Earth". In: *Evolution of Earth and its Climate: Birth, Life and Death of Earth*. Ed. by O.G. Sorokhtin, G.V. Chilingarian, and N.O. Sorokhtin. Vol. 10. Developments in Earth and Environmental Sciences. Elsevier, 2011, pp. 13–60.
(Cited on p: 133.).
DOI: https://doi.org/10.1016/B978-0-444-53757-7.00002-7.
URL: https://www.sciencedirect.com/science/article/pii/B9780444537577000027.

[166] K. Lodders and B. Fegley Jr. *The Planetary Scientists Companion*. New York: Oxford University Press, 1998.
(Cited on p: 133.).

[167] Carlos A. Argüelles, Jordi Salvado, and Christopher N. Weaver. "nuSQuIDS: A toolbox for neutrino propagation". In: *Computer Physics Communications* 277

(2022), p. 108346. ISSN: 0010-4655.
(Cited on pp: 134, 152, 163.).
DOI: https://doi.org/10.1016/j.cpc.2022.108346.
URL: https : / / www . sciencedirect . com / science / article / pii / S0010465522000649.

Acknowledgements